

Silicon Microwire Photovoltaics

Thesis by
Michael David Kelzenberg

In Partial Fulfillment of the Requirements
for the Degree of
Doctor of Philosophy



California Institute of Technology
Pasadena, California

2010

(Defended May 19, 2010)

To the memory of my grandfather

Andrew J. Kraus

1917–2009

For instilling in me a curious desire to take things apart

Acknowledgements

To describe my experience at Caltech as merely positive would be an understatement. As I pause to reflect on the five years I've spent here, I am overwhelmed by a sense of achievement and personal growth that would not have been possible without the guidance, support, and assistance of countless people both on and off campus. To list everybody to whom I owe thanks could fill as many pages as a chapter of this thesis. To those I omit here, please know that my gratitude is no less sincere.

First and foremost I must acknowledge my advisor Harry Atwater. His mentorship has been tremendously helpful, and his vision and insight never cease to surprise me. I cannot overstate my gratitude towards Harry for accepting my application to Caltech and supporting me throughout my endeavors here—particularly during the earlier days of my research when I admittedly struggled to reach the proficiency I would need to succeed as a graduate student. Over the years I sometimes joked that I was afraid to ask Harry why he accepted me into his research group, for fear that he might realize his mistake and send me away. But in all earnestness, it has been his encouragement and enthusiasm, not fears of disappointment, which have inspired my interest and enjoyment of science.

I must also acknowledge the members of my candidacy and thesis committees, which have included Professors Nathan Lewis, Changhuei Yang, Amnon Yariv, and Pietro Perona. In particular, Nate Lewis has been a remarkable mentor over the years—in many regards playing the role of a second advisor. His meticulous attention to detail has been essential to the quality of the research presented herein, and his active role in reviewing each of the resulting publications is greatly appreciated. Without the fruitful collaboration existing between the Atwater and Lewis groups, many of the results herein would never have been achieved. I would also like to acknowledge my option representatives, which have included Yu-Chong Tai, P. P. Vaidyanathan, Babak Hassibi, Ali Hajimiri, and Changhuei Yang.

Over the years, I have enjoyed collaboration and camaraderie with many talented people at Caltech. In particular, I would like to acknowledge Morgan Putnam, with whom I have worked closely since day one; and Dan Turner-Evans, whose involvement with this project actually began a year before he joined the group as a graduate student: with a summer undergraduate project in which we achieved the first significant results of my research efforts. Morgan's and Dan's contributions are visible throughout this thesis, and more importantly, their friendship has made the journey all the more enjoyable. I must also acknowledge the contributions of my present and past colleagues of the Si wire team. Brendan Kayes and Michael Filler laid much of the groundwork for this research, helped me author my first paper, and served as role models for the early development of my scientific technique. And, although two years have passed since they departed the group, each nonetheless deserves specific thanks with regard to this thesis: Brendan, for providing me with the source files for his own thesis (which served as the starting point for typesetting this document); and Michael, for giving me his old laptop computer (which I am using to type these words from the comforts of home). In more recent years, Shannon Boettcher provided

much-appreciated guidance and enthusiasm during the course of his brief but fruitful appointment as a postdoctoral scholar. I have also enjoyed friendship and collaboration with Matthew Bierman, Ryan Briggs, Ron Grimm, Emily Kosten, Jim Maiolo, Stephen Maldonado, Katherine Plass, Liz Santori, Joshua Spurgeon, Nick Strandwitz, Adele Tamboli, Michael Walter, Emily Warren, and the rest of the Si wire team. I am honored to have been part of such a collaborative group of talented researchers. Furthermore, I would like to express special thanks to the undergraduate students I've had the pleasure of mentoring over the past three years: Dan Turner-Evans (then from Yale University), Jan Petykiewicz (Caltech), and Claire Baek (Stanford University). And although it causes his name to be listed a third time in this paragraph, I cannot neglect to mention that Dan Turner-Evans provided an extremely helpful review of this thesis that has greatly improved its quality.

Describing my gratitude towards the ever-growing number of students, postdocs, and alumni of the Atwater research group has proven to be the most difficult task of writing these acknowledgments. To keep this section within reasonable dimensions, I will simply state that it has been an honor and a pleasure to be a part of this group, and that virtually every member has contributed to my research in meaningful ways over the years. The list of contributors includes, in addition to those already mentioned: Robb Walters, Luke Sweatlock, Domenico Pacifici, Jenn Dionne, Henri Lezec, Julie Biteen, Ken Diest, Matt Dicken, Gerald Miller, Krista Langeland, Michael Decegelie, Greg Kimball, Melissa Archer, Carrie Hofmann, Imogen Pryce, Emily Warmann, Andrew Leenheer, Vivian Ferry, Stanley Burgos, and Deirdre O'Carroll (in no particular order, and likely omitting some). Of course, I can't thank the Atwater group without also thanking our administrative assistants April Neidholdt, Lyra Haas, and Sherry Feick.

There are also many people to thank for providing me with experimental insight, equipment training, and instrument/facility support over the years. These include Bruce Brunshwig of the Molecular Materials Research Center, Ali Ghafari of the Applied Physics Micro/Nano Lab, Chi Ma of the Division of Geological and Planetary Sciences, and the entire staff of the Kavli Nanoscience Institute, including Guy DeRose, Melissa Melendes, Bophan Chhim, and Carol Garland. Many of our experiments also benefited from the expert capabilities of the Caltech machine shops. I would especially like to thank Mike Roy and Steve Olson of the Instrument Shop for the many parts they've made (and sometimes remade) at my request; for their helpful advice and assistance with instrument design and repair; and for allowing us the use of their fume hood to coat the components of our integrating sphere.

I would also like to express particular thankfulness to those who have looked out for my personal well-being—keeping me registered, insured, salaried, and generally out of harm's way despite my seemingly endless abilities to miss instructions and deadlines. This list includes Linda Dozsa, Tanya Owen, and Janet Couch in Electrical Engineering, Tess Legaspi in the Registrar's office, Natalie Gilmore and Icy Ma in the Graduate Office, Eleonora Vorobieff and Connie Rodriguez in Applied Physics, and of course, the entire staff of the Student Health Center. Additional thank are due to the Allie Akmal, who proofread this thesis for the Graduate Office.

One of the most enlightening experiences of my graduate career didn't occur in the lab. Rather, it occurred on the rooftop above it. When Morgan Putnam informed me in mid-2008 of his plans to lead students in installing solar panels on campus, I'll admit I was initially skeptical. But his ambition, combined with the tremendous enthusiasm and support that the project received from the Caltech community, led to the formation of the Caltech Student Solar Initiative (CSSI) and the installation of a 14 kW photovoltaic array over our heads by the end of that year. The many hours of my involvement with this project gave me an unanticipated crash course in photovoltaics installation, as well as the pleasure of working outdoors and with talented people I might not have otherwise met. This project would not have been possible without the generous support provided by the Moore-Hufstedler Fund for Student Life and Caltech Facilities, as well as the enthusiasm and hard work of many people, including John Onderdonk, Jim Cowell, Mike Anchando, Nick Grewal, Nathan Braden, Alta Fang, Amy Hofmann, and Heidrun Mumper-Drumm.

My gratitude must also extend beyond the boundaries of Caltech. My undergraduate education at Iowa State University provided me with a decidedly useful skill set that very well complemented those of my colleagues in the lab. I would especially like to thank my undergraduate adviser, Vikram Dalal, who saw a potential in me that I didn't know existed; for his support and the active role he played in preparing me for Caltech. I have no doubt that I would not be here today if not for his encouragement. Furthermore, the proficiency I gained in using the *LabVIEW* and *MATLAB* programming environments under the mentorship of Adin Mann has time and time again proven to be one of the most useful skills I acquired as an undergraduate student.

Last, but certainly not least, I would like to acknowledge my friends and family. I feel the need to single out Evan and April Neidholdt, who have become close friends over the past several years (and, as April will tell you if she gets the chance, were responsible for introducing me to the woman I now know as my wife). I also need to acknowledge my father David for some much-needed last-minute proofreading of this thesis. I would certainly not be the man I am today if not for the dedication (and remarkable patience) of him and my mother Anne Marie, who along with my sister Jenny, I have missed greatly in moving to California. Luckily I have been blessed with fantastic in-laws: I could not feel more welcomed by the Roberts family, and a home-cooked meal is once again only a short drive away. Finally, to my wonderful wife Jessica: thank you for your unwavering love and support. I couldn't have done this without you. And now that I'm done, I will finally agree to clean off my desk.

Michael Kelzenberg
May 2010
Pasadena, CA

Abstract

The favorable bandgap and natural abundance of Si, combined with the large expertise base for semiconductor wafer processing, have led to the use of wafer-based crystalline Si in the vast majority of photovoltaic cells and modules produced worldwide. However the high cost of purifying, crystallizing, and sawing Si wafers has inhibited these photovoltaic energy sources from approaching cost parity with fossil fuels. Crystalline Si microwires, grown by the catalytic vapor-liquid-solid (VLS) chemical vapor deposition process, have recently emerged as promising candidate materials for thin-film photovoltaics—combining low-cost Si deposition techniques with mechanically flexible, high-performance device geometries.

This thesis presents several achievements that have helped to establish the viability of high-performance Si microwire photovoltaics. We begin by developing a comprehensive numerical model of Si microwire-array solar cells, combining finite-element device physics simulations with time-domain optical methods to predict that these devices can exceed 17% solar energy conversion efficiency. We then turn our attention to the optical properties of Si microwire arrays, concerned that the sparsely packed wires might not absorb enough sunlight. However our experiments reveal that simple light-trapping techniques can dramatically improve their absorption, not only permitting them to effectively absorb sunlight using 1/100th as much Si as a wafer, but also leading to an unexpected and fundamentally advantageous absorption enhancement over classical light trapping in planar materials. Techniques are then presented to characterize the material quality of VLS-grown Si wires. Although the growth of these wires is catalyzed by notoriously undesirable metal impurities for crystalline Si (e.g., Au, Ni, and Cu), we find it is nonetheless possible to synthesize high-quality material with remarkable diffusion lengths. By combining these materials with effective surface-passivation and a novel junction-fabrication technique, we realize single-wire solar cells that achieve open-circuit voltages of ~600 mV and with fill factors exceeding 80%. These observations suggest that Si microwires may offer a promising alternative to wafers for cost-effective crystalline Si photovoltaics.

Contents

List of Figures	xv
List of Tables	xix
List of Publications	xxi
1 Introduction	1
1.1 Global photovoltaics perspective	2
1.1.1 Photovoltaic technologies	2
1.2 Reducing the cost of solar energy	4
1.3 Fundamentals of photovoltaic energy conversion	5
1.3.1 Theoretical efficiency limits	7
1.4 Non-planar solar cell geometries	8
1.5 Silicon microwire photovoltaics	10
1.5.1 The vapor-liquid-solid growth process	10
1.5.2 The radial p-n junction	12
1.5.3 Peel-off and wafer reuse	12
2 Optoelectronic modeling of Si wire photovoltaics	15
2.1 Introduction	15
2.2 Device-physics model	16
2.2.1 Choice of simulation software	16
2.2.2 Overview of simulation procedure	17
2.2.3 Single-wire solar cell model	18
2.2.4 Numerical optimization	24
2.2.5 Effects of core depletion	25
2.3 Comprehensive optoelectronic model	31
2.3.1 Optical absorption simulation	32
2.3.2 Extracting optical generation profiles	36
2.3.3 Device physics simulation	37
2.4 Discussion	40
2.4.1 Future work	40
3 Optical absorption in Si wire arrays	43
3.1 Introduction	43
3.1.1 Sunlight and fundamental optical absorption in semiconductors	43
3.1.2 Observing optical absorption	46
3.1.3 Absorption and light-trapping in planar solar cells	47
3.1.4 Absorption in wire arrays	51

3.2	Optical measurement technique	52
3.2.1	Integrating sphere apparatus	53
3.2.2	Determining optical absorption	56
3.2.3	Quantifying useful absorption for photovoltaics	57
3.2.4	Sub-bandgap absorption	60
3.3	Effects of array geometry on optical absorption	64
3.3.1	Disordered arrays	64
3.3.2	Ordered microwire arrays	67
3.4	Light-trapping in Si wire arrays	72
3.4.1	Fabrication of light-trapping structures	74
3.4.2	Optical absorption enhancement	76
3.4.3	Comparison to planar absorbers	78
3.5	Photoelectrochemical characterization of carrier collection	80
3.5.1	Determination of internal quantum efficiency	84
3.5.2	Enhanced E.Q.E. via light-trapping	86
3.6	Discussion and outlook	88
4	Bulk electrical properties of Si microwires	91
4.1	Introduction	91
4.2	Fabrication of single-wire test structures	93
4.2.1	Electron-beam lithography	94
4.2.2	Nanoprobe	95
4.2.3	Photolithography	96
4.3	Properties of Si wires grown from SiH_4	98
4.4	Properties of Si wires grown from SiCl_4	102
4.4.1	Induced rectifying-contact devices	105
4.5	Measurement of minority-carrier recombination rate	109
4.5.1	Au-catalyzed Si wires	110
4.5.2	Ni-catalyzed Si wires	114
4.5.3	Cu-catalyzed Si wires	116
4.6	Discussion	117
4.6.1	Catalyst choice for photovoltaic applications	117
5	Radial p-n junction microwire solar cells	121
5.1	Formation of radial p-n junctions	121
5.2	Fabrication of single-wire devices	124
5.2.1	Current-voltage behavior	125
5.2.2	Scanning photocurrent microscopy	125
5.3	Passivation of wire surfaces	127
5.3.1	Passivation with buffered hydrofluoric acid	130
5.3.2	Passivation with PECVD a-Si:H	131
5.3.3	Passivation with PECVD a-SiN _x :H	133
5.4	Photovoltaic performance of single-wire test structures	135
5.4.1	Spectral response	136
5.5	Predicted efficiency of large-area solar cells	139
5.5.1	Horizontally aligned wires	140
5.5.2	Vertically aligned wires	142

6	Conclusion and outlook	145
6.1	Advantages of Si microwire photovoltaics	145
6.2	Toward efficient Si microwire-array solar cells	147
6.3	Outlook	148
A	Supplementary information	151
A.1	Optical properties of PECVD films	151
A.2	Spreading resistance analysis of diffused p-n junction profiles in planar control wafers	152
A.3	Selected <i>Sentaurus</i> command files	155
A.3.1	<i>Sentaurus Structure Editor</i> command file	155
A.3.2	<i>Sentaurus Device</i> command file	158
A.3.3	<i>Inspect</i> command file	164
B	Integrating <i>Lumerical FDTD</i> within <i>Sentaurus TCAD</i>	165
B.1	Introduction	165
B.1.1	Requirements	167
B.2	Understanding the mesh files	167
B.2.1	Generating custom data files	169
B.3	Step 1: Generating the mesh	169
B.3.1	Meshing strategy	170
B.4	Step 2: Simulating optical generation profiles using Lumerical FDTD	171
B.4.1	Partial spectral averaging	174
B.5	Step 3: Generating the external-profile data file	175
B.6	Step 4: Loading the external profile in <i>Sentaurus</i>	178
B.7	Tool integration within SWB	178
B.8	Simulating solar illumination	180
B.8.1	Tips	182
B.9	Tool information	183
B.9.1	Lumerical CAD (<i>lumcad</i>)	183
B.9.2	Shell	184
B.9.3	MATLAB	184
B.10	Selected source code	185
B.10.1	<i>tooldb</i> file	185
B.10.2	Lumerical structure generation script	188
B.10.3	FDTD execution shell script	189
B.10.4	MATLAB mesh conversion script	190
B.11	Solar spectrum weightings for discrete simulations	197
C	SPCM instrument	203
C.1	System description	203
C.2	Operating procedures	208
C.3	Extended capabilities	211

D Spectrophotometer instrument	215
D.1 Illumination source and optical path	217
D.2 Specimen stage	221
D.3 Detection instrumentation	223
D.4 Integrating sphere	227
D.4.1 Transmission measurements	228
D.4.2 Reflection measurements	230
D.4.3 Absorption measurements	232
D.5 Photoelectrochemical cell	234
D.5.1 E.Q.E. measurements	237
D.5.2 Calibration issues	237
D.5.3 Mass transport issues	239
D.6 Computer software	240
D.6.1 Data acquisition software	240
D.6.2 Alignment utilities	241
D.6.3 Data processing software	241
D.7 Operating procedures	244
D.7.1 Laser operation guidelines	244
D.7.2 Source alignment	247
D.7.3 Illumination beam alignment	250
D.7.4 Specimen stage alignment	251
D.7.5 Reflection-mode configuration	252
D.7.6 Reflection measurements	255
D.7.7 Transmission-mode configuration	256
D.7.8 Transmission measurements	260
D.8 Supplementary information	262
D.8.1 Data processing program	262
D.8.2 Diagrams of custom parts	266
Bibliography	269

List of Figures

1.1	Cost distribution for Si photovoltaic modules and wafers	3
1.2	Cost per peak-watt (W_p) of a photovoltaic system	4
1.3	Structure and $I-V$ characteristics of a typical solar cell	6
1.4	Schematic diagram of the VLS growth process	10
1.5	Images of VLS-grown Si microwire arrays	11
1.6	Radial p-n junction, wire-array solar cell schematic	12
1.7	Polymer-embedded Si microwire arrays	13
2.1	Illustration of simulated single-wire solar cell	19
2.2	Simulated performance of single-wire radial junction solar cells	21
2.3	Simulated performance of radial- vs. planar-junction solar cells	22
2.4	Simulated current density and SRH recombination profiles	23
2.5	Effect of wire radius on simulated efficiency of radial-junction structures	27
2.6	Recombination rates in depleted vs. nondepleted wires	28
2.7	Physical state of the center of fully depleted vs. nondepleted radial p-n junction solar cells	29
2.8	Modes of operation in radial p-n junction solar cells	30
2.9	Advanced Si microwire-array solar cell geometry.	32
2.10	Schematic diagram of simulated wire-array unit cell geometry	34
2.11	Simulation source intensities used to approximate sunlight	35
2.12	Simulated absorption of wire-array solar cell	36
2.13	Simulated optical generation profiles for the wire-array solar cell	38
2.14	Simulated terminal behavior of wire-array solar cell	39
3.1	The solar spectrum and limiting J_{sc} of semiconductor solar cells	44
3.2	Absorption length and front-surface reflectivity of silicon	45
3.3	Schematic diagram of optical transmission and reflection	47
3.4	Specular vs. textured surfaces in planar solar cells	49
3.5	Limiting short-circuit current density as a function of planar silicon solar cell thickness	50
3.6	Structure of Si wire arrays prepared for optical measurements	53
3.7	Illustration of integrating sphere apparatus	54
3.8	Example absorption measurements	57
3.9	Schematic diagram for figure of merit calculation	58
3.10	Example figure of merit calculations	59
3.11	Measured absorption of a commercial silicon solar cell	60
3.12	Optical properties of PDMS and back-reflector materials	61
3.13	Example of scaling procedure	62
3.14	Removal of Au catalyst tips	63

3.15	Catalyst tip structure and removal	63
3.16	Disordered Si wire arrays grown from SiH_4	65
3.17	Measured optical absorption of disordered Si wire films	66
3.18	Representative composition and optical properties of each wire-array tiling pattern	69
3.19	Absorption figures of merit vs. array geometry	71
3.20	Schematic diagram of light-trapping elements	72
3.21	Optical micrograph of light-trapping wire array	73
3.22	Determination of nitride thickness	74
3.23	SEM image of a wire array infilled with Al_2O_3 particles	75
3.24	Measured optical absorption of PDMS-embedded Al_2O_3 particles	76
3.25	Effects of light-trapping elements on optical absorption	77
3.26	A_{avg} of light-trapping Si microwire arrays	78
3.27	Measured absorption of a light-trapping Si wire array vs. the theoretical absorption limits for equivalently thick planar Si	79
3.28	Schematic diagram of photoelectrochemical cell configuration	80
3.29	Photoelectrochemical $J-V$ and spectral response of a p-Si wire-array electrode	81
3.30	Spatial uniformity of the E.Q.E. of a wire-array electrode	82
3.31	Angle- and wavelength-resolved photoresponse of a Si wire-array electrode	82
3.32	Angle-resolved photoresponse of a Si wire-array electrode	83
3.33	Internal quantum efficiency of a Si wire-array electrode	85
3.34	Control measurements performed on a recovered growth-substrate electrode	86
3.35	Effect of light-scattering particles on wire array electrode E.Q.E.	87
3.36	E.Q.E. figures of merit for Si wire-array electrodes	88
4.1	Typical single-wire device fabricated by e-beam lithography	94
4.2	Single Si wire contacted by tungsten nanoprobe tips	95
4.3	SiH_4 -grown wires and single-wire devices	98
4.4	$I-V$ characteristics of a single SiH_4 -grown wire device	99
4.5	Field-effect resistance modulation in a SiH_4 -grown device	100
4.6	Effective doping concentration of SiH_4 -grown wires	101
4.7	SiCl_4 -grown wires and single-wire devices	102
4.8	Electrical characteristics of a single SiCl_4 -grown wire device	103
4.9	Effective doping concentration of unintentionally doped wires grown from SiCl_4	104
4.10	Effective doping concentration of Cu-catalyzed, B-doped wires grown from SiCl_4	105
4.11	$I-V$ behavior of an induced-rectifying-contact device	106
4.12	Photovoltaic response of an induced-rectifying-contact device	107
4.13	Spectral response of a single-wire solar cell	108
4.14	Schematic diagram of SPCM measurements	110
4.15	SPCM characterization of a Au-catalyzed wire	111
4.16	SPCM profiles and extracted minority-collection length	112
4.17	Effective carrier lifetime vs. bulk and surface recombination	113

4.18	SPCM characterization of a Ni-catalyzed single-wire device . . .	115
5.1	Fabrication procedure for radial junction Si microwire arrays . .	122
5.2	Si wire array following the radial junction formation procedure .	123
5.3	Single-wire, radial p-n junction devices	124
5.4	I - V characteristics of a typical single-wire radial p-n junction device	125
5.5	SPCM characterization of a radial p-n junction single-wire device	126
5.6	SPCM characterization of radial p-n junction single-wire devices with various surface passivation treatments	128
5.7	Characterization of single-wire devices passivated by immersion in hydrofluoric acid	130
5.8	SPCM characterization of an a-Si:H-coated single-wire device . .	131
5.9	Images of an a-Si _x :H-coated wire array and individual wires . .	132
5.10	SPCM characterization of an a-Si _x :H-coated single-wire device	133
5.11	Determining the junction position within the a-Si _x :H-coated single-wire devices	134
5.12	Invariance of L_{eff} at reduced carrier injection levels	134
5.13	Photovoltaic J - V behavior of champion single-wire solar cells . .	135
5.14	Spectral response of champion single-wire solar cells	137
5.15	Proposed large-area solar cell comprising horizontal Si wires . . .	140
5.16	Simulated absorption of horizontally oriented Si microwires . . .	141
5.17	Proposed large-area solar cell comprising vertical Si wires	142
5.18	Projected efficiency of large-area wire-array solar cell	143
6.1	Si microwire-array solar cell	148
A.1	Optical properties of PECVD a-Si _x :H	151
A.2	Optical properties of PECVD a-Si:H	151
A.3	Junction profile, 10 min P diffusion, $T = 850$ °C	153
A.4	Junction profile, 5 min P diffusion, $T = 850$ °C	154
A.5	Radial p-n junction structure for two-dimensional cylindrical simulations	156
B.1	Schematic diagram of simulated structures	166
B.2	Screenshot of simulation meshes produced by each tool	172
B.3	Effect of partial spectral averaging (PSA) on Lumerical FDTD simulations	174
B.4	Result of running the MATLAB script on a <code>noffset3d</code> -generated mesh	176
B.5	Use of Delaunay triangulation to improve the accuracy of profile conversion	177
B.6	Screenshot of SWB project that integrates <i>Lumerical</i> and <i>MATLAB</i> processing steps	179
B.7	Discrete solar spectrum script output	182
C.1	Schematic illustration of SPCM instrumentation	204

C.2	Cantilevered NSOM tips	205
C.3	Printed circuit board layout for SPCM switch box	206
C.4	Transimpedance amplifier circuit schematic	207
C.5	Confocal SPCM focusing procedures	210
D.1	Schematic illustration of spectrophotometer instrumentation	216
D.2	Spatial transmission map of the edge of a Si wire-array film	220
D.3	Illumination spectra for spectrophotometry measurements	221
D.4	Specimen stage	223
D.5	Internal configuration of integrating sphere	228
D.6	Transmission-mode integrating sphere configuration	229
D.7	Reflection-mode integrating sphere configuration	231
D.8	Integrating sphere absorption measurement configurations	233
D.9	Photoelectrochemical cell configuration: front view	234
D.10	Photoelectrochemical cell configuration: top view	236
D.11	Opacity of photoelectrochemical cell with methyl viologen electrolyte	238
D.12	Photograph of photoelectrochemical cell configuration	239
D.13	Screenshot of transmission-mode software	240
D.14	Data processing utility for one-dimensional sweeps	243
D.15	Data processing utility for two-dimensional sweeps	243
D.16	Fianium laser master source waveforms	246
D.17	Aligning the laser to the monochromator input slits	250
D.18	Reflection-mode configuration	254
D.19	Artifacts in two-angle transmission scans	258
D.20	Transmission-mode configuration	259
D.21	Mechanical drawing: Reflection-mode specimen stage	267
D.22	Mechanical drawing: Transmission-mode specimen holder	268

List of Tables

1.1	Global photovoltaic technologies	3
2.1	Numerical optimization of a radial-junction solar cell structure	25
2.2	Geometry of simulated wire-array solar cell	33
2.3	Optical properties used for FDTD simulations	35
2.4	Simulated performance of the Si wire-array solar cell	39
4.1	Typical minority carrier diffusion lengths for silicon	92
4.2	Growth conditions for SiH ₄ -grown Si wires	98
4.3	Summary of minority-carrier lifetime measurements	118
4.4	Selected properties of Au, Ni, and Cu as VLS growth catalysts	119
5.1	Measured properties of single-wire solar-cell test structures	136
5.2	Measured vs. calculated J_{sc} of champion single-wire solar cells	139
5.3	Performance of single-wire solar cell under horizontal vs. projected wire-array illumination levels	143
A.1	Optical properties of PECVD films	152
B.1	Discrete solar spectrum, 100 nm bins	197
B.2	Discrete solar spectrum, 50 nm bins	197
C.1	Typical instrument settings for SPCM measurements	209
D.1	Monochromator gratings	218
D.2	Monochromator passband values	218
D.3	Specimen stage axes	222
D.4	Default normalization modes of data processing script	244

List of Publications

Portions of this thesis have been drawn from the following publications:

Photovoltaic measurements in single-nanowire silicon solar cells.

M. D. Kelzenberg, D. B. Turner-Evans, B. M. Kayes, M. A. Filler, M. C. Putnam, N. S. Lewis, and H. A. Atwater.

Nano Letters **8** 710–714 (2008)

Single-nanowire Si solar cells.

M. D. Kelzenberg, D. B. Turner-Evans, B. M. Kayes, M. A. Filler, M. C. Putnam, N. S. Lewis, and H. A. Atwater.

Conference Record of the Thirty-third IEEE Photovoltaic Specialists Conference, San Diego, CA (2008)

Predicted efficiency of Si wire array solar cells.

M. D. Kelzenberg, M. C. Putnam, D. B. Turner-Evans, N. S. Lewis, and H. A. Atwater.

Conference Record of the Thirty-fourth IEEE Photovoltaic Specialists Conference, Philadelphia, PA (2009)

Enhanced absorption and carrier collection in Si wire arrays for photovoltaic applications.

M. D. Kelzenberg, S. W. Boettcher, J. A. Petykiewicz, D. B. Turner-Evans, M. C. Putnam, E. L. Warren, J. M. Spurgeon, R. M. Briggs, N. S. Lewis, and H. A. Atwater.

Nature Materials **9**, 239–244 (2010)

High-performance Si microwire photovoltaics.

M. D. Kelzenberg, D. B. Turner-Evans, M. C. Putnam, S. W. Boettcher, R. M. Briggs, J. Y. Baek, N. S. Lewis, and H. A. Atwater.

Energy & Environmental Science **4**, 866–871 (2011)

Introduction

We live in an age of unsurpassed technological prosperity made possible by our ability to harness energy. Global energy consumption has reached ~ 15 TW, the vast majority of which is supplied by fossil fuels. The continued growth of the world's population, combined with the rapidly increasing quality of life sought by its inhabitants, implies that energy demand will continue to grow for decades to come, easily reaching 60 TW within our lifetimes. [1]

The future of energy production is one of the greatest, if not the greatest, challenges facing the human race. Continued reliance on fossil-fuel-based energy sources poses a great threat to the global climate, economy, and geopolitical stability. The irregular global distribution of energy demand and fossil fuel resources—especially petroleum—has been cited as a frequent cause of conflict and warfare, and supply shortages have caused great economic turmoil in recent times (e.g., the U.S. oil crises of the 1970s). Global petroleum production trends are foreshadowing that the supply of easily extractable (i.e., inexpensive) oil may soon “peak” and subsequently decline, due to the alarming rate at which is consumed. [2] Furthermore, many scientists fear that rising CO_2 levels, as a direct result of the continued consumption of fossil fuels, will cause irreversible global warming and destruction of the earth's environment. [3] Other externalities are borne by the victims of accidents and conflicts resulting from fossil fuel production: The writing of this thesis has witnessed two catastrophic accidents in the U.S. alone, causing the loss of human lives at coal-mining and oil-drilling operations, as well as what threatens to become the worst oil spill in U.S. history.

Renewable energy sources provide an enduring, distributed means of carbon-free power generation, and are widely regarded as the most strategically desirable option with which to meet future energy demand. Human civilizations have utilized renewable energy sources for millennia (e.g., sailing vessels), but today, renewable energy provides only a minuscule fraction of global energy usage. In fact, it has been shown that many renewable energy sources (e.g., wind, biofuels, or hydroelectricity) are simply not abundant enough to replace fossil fuels at today's rate of energy consumption—for example, most of the world's economically feasible hydroelectric sites are already dammed, producing less than 1 TW of power. [3] On the other hand, sunlight has been striking the Earth at a rate exceeding 100,000 TW throughout human history, making solar energy not only the most abundant, but also the most widely distributed renewable energy resource. The promise of solar energy becomes clear when one considers that the entire U.S. energy demand could be satisfied (electrically) by 15%-efficient solar panels covering an area on par with that of the interstate highway system.

To date, the high cost of solar electricity ($\sim \$0.25/\text{kWh}$, vs. $\$0.03\text{--}0.05/\text{kWh}$ for conventional utility-scale electricity) has prevented its widespread adoption as an energy source, and it presently accounts for less than 0.1% of worldwide energy usage. [4] Thus the key challenge facing the adoption of photovoltaic power is to lower the cost of energy generation—by reducing the cost of photovoltaic systems and increasing their energy output. In the following sections, we examine why photovoltaics have remained so expensive despite decades of intense research and development. We then describe why Si microwire solar cells have emerged as promising candidates for reducing the cost of photovoltaic energy, providing the framework and motivation for this thesis work.

1.1 Global photovoltaics perspective

The global photovoltaic industry has experienced remarkable growth in recent times—exceeding 40% annually throughout the past decade. Photovoltaics are the world’s fastest-growing energy source, and are expected to provide 11% of global energy by 2050. [5] However, the cost of photovoltaic energy remains several times above the average retail price of electricity, and to date, the growth of the solar marketplace has been sustained only through the aid of government subsidies. A learning-curve analysis of the industry has predicted that existing photovoltaic technologies will not achieve cost-parity with conventional energy sources until ~ 2020 or later, requiring billions of dollars of additional subsidies to reach this point. [6] This presents a tremendous opportunity for disruptive technologies to bring about transformative changes within the solar industry, and to accelerate the progress towards cost-effective renewable energy sources.

1.1.1 Photovoltaic technologies

One of the greatest technological achievements of the 20th century was the development of the crystalline silicon (Si) wafer, which has enabled such technologies as integrated circuits, computers, and solar cells. In 1954, the world’s first modern photovoltaic panel was made from several dozen Si wafer solar cells soldered together to form a circuit. [7] Since then, the solar industry has grown by leaps and bounds, but the predominant fundamental technology remains the same. Si wafer-based photovoltaics are in production today, with efficiencies of up to 23%, [8] and with warranted lifetimes of 25 years or longer. No other photovoltaic technology offers the proven efficiency and durability of crystalline Si—except those that cost hundreds of times more per unit area, and are thus used only in extreme environments such as aerospace applications, or in conjunction with focusing lenses that focus intense sunlight onto small cell areas.

Crystalline Si wafers are cumbersome, fragile, and tremendously expensive and energy-intensive to produce. Roughly one-third to one-half of the cost of module production arises from the purification, crystallization, and sawing procedures required to produce Si wafers. [10] This ratio was even higher a few years ago due to a shortage of solar-grade Si feedstock (see Fig. 1.1). [9] One promising

Table 1.1. Global photovoltaic technologies.

Technology	Market share (%)	Material	Efficiency range (%)
Wafered	85–90	Monocrystalline Si	14–20
		Multicrystalline Si	13–15
Thin-film	10–15	a/ μ c-Si	6–9
		CdTe	9–11
		CIGS	10–12

Source: International Energy Agency, 2010 [5]

alternative to wafer-based Si solar cells is a broad class of technologies known as “thin-film” photovoltaics, including amorphous hydrogenated Si (a-Si:H), CIGS, CdTe, and dye-sensitized solar cells. Instead of sawing large crystals to produce wafers, these materials are typically deposited on inexpensive substrates, such as glass or aluminum foil. These technologies cost less and are easier to produce than Si wafers, but typically suffer from lower efficiencies and accelerated degradation in sunlight. For this reason, crystalline Si wafer-based photovoltaics continue to dominate the terrestrial photovoltaic market. The approximate market share and efficiency of each leading photovoltaic technology is shown in Table 1.1.

Only recently has the market share of crystalline Si photovoltaics dropped below 90%, due mostly to the rapid growth of the thin-film photovoltaics company *First Solar*, which manufactures CdTe modules at extremely low costs. First Solar is now the largest solar company in the U.S., and its modules have recently reached 11% efficiency, which, although markedly below the efficiencies offered by crystalline Si photovoltaics, is remarkable considering that their manufacturing costs have dropped to below \$1/W_p. [11] Nonetheless, the efficiencies of mass-produced thin-film photovoltaics today leave substantial room for improvement in comparison with those of crystalline Si technologies.

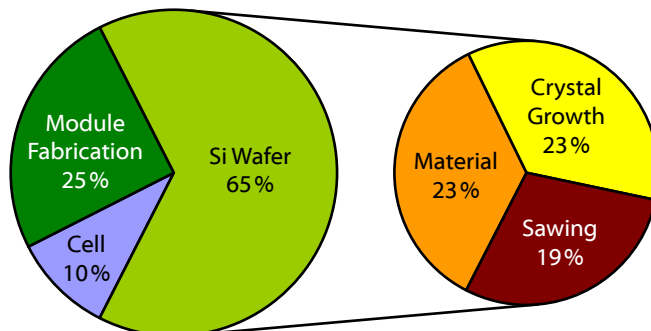


Figure 1.1. Cost distribution for Si photovoltaic modules and wafers.

Adapted from [9, p. 223] (2003 data).

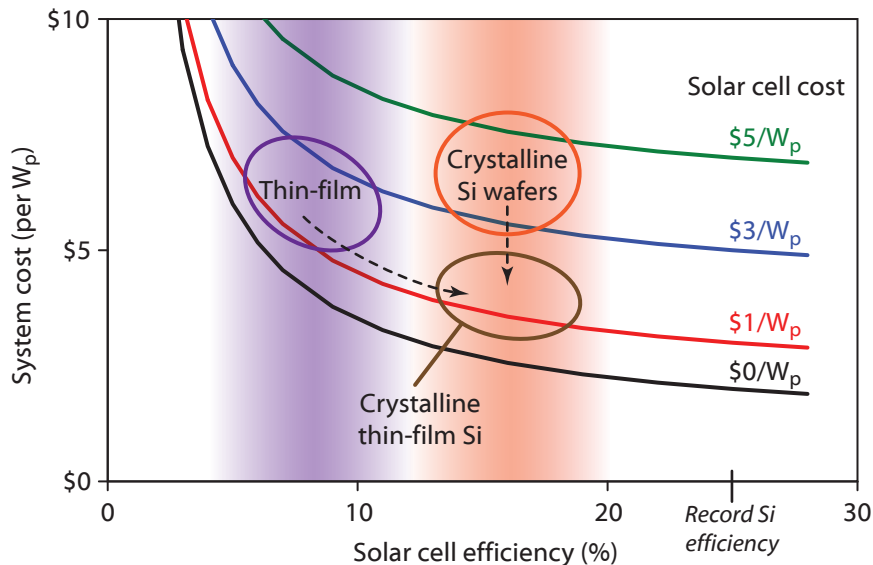


Figure 1.2. Cost per peak-watt (W_p) of a photovoltaic system, assuming balance of system costs of $\$1/W_p$ and $\$250/m^2$. The shaded regions indicate the typical efficiency range for commercial thin-film vs. crystalline Si wafer-based solar cells, and the circled regions show the approximate cost range. The brown circle indicates the cost and efficiency target for thin-film crystalline Si photovoltaics.

1.2 Reducing the cost of solar energy

Photovoltaic systems are typically rated in terms of their total cost per watt-peak ($\$/W_p$) of energy generation capacity.* In the U.S., it is widely believed that the total installed cost of photovoltaic systems must approach $\sim \$1/W_p$ in order for solar electricity to become cost-competitive with retail electricity prices—a condition known as *grid parity*. The most obvious cost of a photovoltaic system (and historically the most expensive component) is the cost of the solar panels themselves. In recent years, however, thin-film photovoltaic modules have been produced at costs below $\sim \$1/W_p$ (whereas crystalline Si wafer-based photovoltaics have struggled to reach $\sim \$1.50/W_p$, and cost much more for higher-efficiency modules). As the cost of solar cells decreases, other costs of photovoltaic systems become increasingly important. Known as *balance of systems* (BOS), these costs include the labor, electronics (interconnects and inverters), mounting hardware, land, and other overhead required to establish and operate a photovoltaic energy system. It is because of these BOS costs that thin-film solar cells have thus far been unable to displace more costly (but more efficient) crystalline Si photovoltaics.

*The watt-peak is a standardized rating for photovoltaic systems; a measure of the power it produces under laboratory 1-sun conditions. Power output in real conditions depends on the local solar insolation, climate, and many other factors.

To illustrate the effects of balance of system costs, we consider a simple example in which a photovoltaic installation requires $\$1.00/W_p$ for electrical inverters, interconnects, permitting, etc.; and $\$250/m^2$ for land and development or roof modifications, mounting hardware, labor, and other costs. These costs might be typical for specialized residential or small-commercial installations in southern California. BOS costs can vary greatly between projects, depending on the size and location of the system as well as local codes and labor rates. While our simple calculation thus does not model the real-world cost any specific photovoltaic installation, it does illustrate a key principal that is true for virtually all photovoltaic systems: the importance of cell efficiency. Figure 1.2 plots the total installed system cost (per W_p) as a function of cell efficiency, for solar cell costs ranging from $\$0$ to $\$5/W_p$.^{*} It may seem surprising, but for the assumed BOS costs, a 15%-efficient, $\$3/W_p$ solar cell is more economical than a 5%-efficient solar cell at *any* price—even free. Figure 1.2 also indicates the approximate efficiency and price range for modern commercial thin-film and crystalline Si photovoltaic technologies. This comparison makes it clear why inefficient thin-film technologies have not been widely adopted, despite their markedly lower cost per peak-watt compared to wafer-based Si photovoltaics.

Terrestrial photovoltaic technologies have historically straddled a continuum ranging from cheap, inefficient devices to expensive, high-performance devices. Incremental improvements and the scaling of the industry continue to inch existing technologies towards cost-effectiveness, but to date, no large-scale commercial photovoltaic technologies have succeeded in combining the low cost of thin-film processing with the high efficiency and reliability of wafer-based crystalline Si solar cells. For many years, researchers have sought to achieve this goal with *thin-film crystalline Si solar cells*, [12, 13] which were suggested to be “the first thin-film technology able to challenge the supremacy of bulk Si.” [14] Although thin-film crystalline Si photovoltaics have not yet achieved widespread commercial success, their potential to transform the photovoltaics industry is clear when their anticipated cost and efficiency are plotted in Figure 1.2. The combination of high efficiency and low cost would give such solar cells a definitive advantage over virtually all existing photovoltaic technologies. Combined with aggressive reductions in BOS costs, such a technology would enable solar electricity to be produced at grid parity. This fact has motivated our study of Si microwires, a novel approach to thin-film crystalline Si photovoltaics.

1.3 Fundamentals of photovoltaic energy conversion

The functional element of a semiconductor solar cell is the *p-n junction*. When the solar cell absorbs sunlight, electrons and holes (collectively known as photo-carriers) are excited within the semiconductor material. The junction separates these electrons and holes, and provides the electrical potential to drive them through an external circuit as current. The better the junction is at separating charge, the higher a voltage the solar cell can produce.

^{*}Our calculation assumes that the system power rating is simply the sum of the cell power ratings, and that the system area is simply equal to the solar panel area.

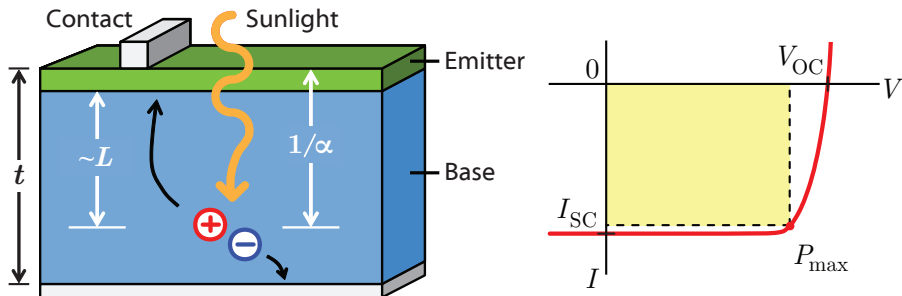


Figure 1.3. Structure and I - V characteristics of a typical solar cell.

A typical planar p-n junction solar cell is depicted in Figure 1.3. This device consists of a thick n- or p-type slab of semiconductor (called the *base* region) with a thin p- or n-type (oppositely doped) layer at the top of the device (called the *emitter* region). Current is extracted by electrical contacts to each region. When sunlight is incident from the top of the device, the current-voltage (I - V) behavior of an ideal p-n junction solar cell is:

$$I \approx I_0 e^{\frac{qV}{kT}} - I_L \quad (1.1)$$

The quantity I_L is the *light current* (or *photocurrent*), and is determined by how many photocarriers are excited and collected by the device. The quantity I_0 is the *dark current* (or *saturation current*) of the device, and describes how “leaky” the junction is. The larger the I_0 , the worse the junction is at separating the photocarriers. Figure 1.3 depicts the I - V behavior described by equation (1.1), from which we can identify the key descriptors of photovoltaic performance. At short-circuit conditions ($V = 0$), the solar cell’s current is simply equal to $-I_L$, and known as the *short-circuit current* (I_{sc}). As the voltage is increased ($V > 0$), the solar cell generates electrical power ($P = -IV$). Above a certain voltage, however, the current becomes positive, and the device instead dissipates electrical power. This voltage is the *open-circuit voltage* (V_{oc}), and can be expressed as:

$$V_{oc} = \frac{kT}{q} \ln \left(\frac{I_L}{I_0} \right) \quad (1.2)$$

The maximum amount of power that the solar cell can produce, P_{max} , occurs at a voltage slightly less than V_{oc} and a current slightly less than I_{sc} . This determines the cell’s solar energy conversion efficiency, η :

$$\eta = \frac{P_{max}}{P_{in}} = \frac{FF \cdot I_{sc} \cdot V_{oc}}{P_{in}} \quad (1.3)$$

The quantity FF is the *fill factor* of the cell, which describes how closely the cell can operate to I_{sc} and V_{oc} . P_{in} is simply the total amount of optical power (sunlight) incident on the device. The amount of sunlight striking a solar cell at any given time can vary greatly—depending on the time of day, weather con-

ditions, etc. For this reason, solar cell efficiency is almost universally measured under a standard reference spectrum of sunlight.*

Considering these equations, one can identify the three key requirements for an efficient solar cell:

1. The cell must *absorb* as much light as possible, so that the maximal number of photocarriers are excited. For a planar cell, this means that the cell must be thicker than the *absorption length*, $1/\alpha$, which for crystalline Si, can be 100 μm or more. Absorption can also be limited by reflection and transmission of light, and by parasitic processes that absorb energy without producing any photocarriers. We will measure and then optimize the optical absorption of Si microwire photovoltaics in Chapter 3.
2. The cell must *collect* as many of the photocarriers as possible. In most solar cells, the carriers must diffuse to the junction from deep within the base region in order to be collected. The length over which carriers can diffuse before they lose their energy to recombination is the *minority-carrier diffusion length*, L . Thus solar cells should have L as long as possible; and at minimum, L should be greater than the thickness (t) of the device. We will measure and then maximize the minority-carrier diffusion length of Si microwire solar cells in Chapter 4.
3. The cell must achieve *high operating voltage*, which requires as low a dark current (I_0) as possible, as well as good electrical contacts with low series resistance. We will measure and then maximize the V_{oc} and FF of Si microwire photovoltaics in Chapter 5.

1.3.1 Theoretical efficiency limits

Because a solar cell operates in thermodynamic equilibrium with the sun, it acts not only as an absorber, but also as a radiator of energy. Given that the sun's surface temperature is approximately 6000 K, the laws of thermodynamics therefore dictate that terrestrial solar cells ($T \approx 300$ K) can be no more than 95% efficient at absorbing solar energy. However, the principles of the semiconductor p-n junction solar cell discussed above impose much more stringent limitations on the efficiency at which sunlight can be converted into photovoltaic power.

Sunlight is inherently a diffuse source of energy, irradiating the earth's surface with a typical power density of $\sim 100 \text{ mW}\cdot\text{cm}^{-2}$. The amount of solar power striking a cell (P_{in}) thus depends directly on its area. This is a key concept of photovoltaics: performance is always normalized to the cell's area, and electrical current is usually reported as *current density* (J). For crystalline Si photovoltaics,

*The most common reference spectra are known as "Air Mass 1.5," and represent sunlight that has traveled through the earth's atmosphere at an incidence angle of 37° , traversing $1.5\times$ the normal thickness of the atmosphere. [15] The *global* spectrum (AM 1.5G) has a power density of $100 \text{ mW}\cdot\text{cm}^{-2}$, and represents typical sunlight that would strike a solar cell facing the sun—including diffuse light from the sky. The *direct* spectrum (AM 1.5D), represents only the light coming directly from the sun (and a small region around it).

the quantized nature of light-matter interaction limits the maximum possible short-circuit current density (J_{sc}) to $\sim 43 \text{ mA}\cdot\text{cm}^{-2}$ under one-sun (AM 1.5G) illumination. Similarly, thermodynamic equilibrium considerations dictate that the minimum dark current density (J_0) is approximately $0.27 \text{ fA}\cdot\text{cm}^{-2}$ at 300 K. Together, these values imply a theoretical V_{oc} limit of nearly 850 mV (equation 1.2) and a limiting efficiency of around 33%. [16, 17] Champion Si solar cells have already approached the theoretical maximum value of J_{sc} , but have thus far exhibited J_0 much larger than the thermodynamic minimum value. A more practical efficiency limit of $\sim 29.8\%$ has been established for Si solar cells, based on intrinsic loss mechanisms in crystalline Si. [18] The present 1-sun efficiency record for crystalline Si photovoltaics ($\eta = 25\%$) has stood for over 10 years, [19] and is unlikely to be greatly surpassed due to several well-understood, yet seemingly unavoidable, loss mechanisms in real devices. [17]

These considerations reveal that it is possible to increase the efficiency of solar cells by employing *optical concentration*, which we can conceptualize in two alternative but equivalent ways. Geometrically, we can define an optical concentrator as an *external* focusing optic (e.g., a magnifying glass) placed above a conventional solar cell. The solar cell's minimum J_0 is not affected, but the focused sunlight enables much greater J_{sc} from the same device area. Alternatively, we can define an optical concentrator as an *internal* part of a solar cell that reduces its thermodynamic light acceptance angle. In this case, the solar cell's J_{sc} remains limited by the power density of unfocused sunlight. However, because the thermodynamic radiation angle is also reduced, the device may have much lower J_0 . The achievable concentration ratio (or minimum acceptance angle) is limited by the size of the solar disk, leading to a theoretical efficiency limit of $\sim 37\%$ for crystalline Si photovoltaics under optical concentration. [20]

Despite the higher efficiencies enabled by optical concentration, the cost and challenges of optical concentrating systems have limited their widespread use in terrestrial applications. This is because concentrating solar panels must be precisely pointed at the sun at all times, and thus require complex motorized mounts to track the sun across the sky. The vast majority of today's commercial solar panels are designed for non-concentrating (one-sun) operation, and are typically mounted in fixed or simplified tracking configurations.

1.4 Non-planar solar cell geometries

Although the theoretical efficiency limits described above apply to all crystalline Si solar cells, numerous non-planar solar cell geometries have been developed to realize very practical gains in performance or utility compared to the simple planar solar cell described above. Non-planar solar cell geometries can alter the ratios between the device volume, illumination area, and junction area, which in turn can manipulate the effective values of J_{sc} and J_0 . The following list describes several solar cells having non-planar morphology or junction geometries that embody many of the principles of Si microwire photovoltaics.

Parallel multijunction (PMJ) solar cells provide a short minority-carrier collection path, enabling high J_{sc} even when L is less than the wafer thickness. However, for low-diffusion-length materials, J_0 usually scales directly with junction area, which for a n -layer cell, is approximately n -fold larger than the illumination area. Thus, PMJ cells suffer from lower operating voltages than simple planar-junction solar cells, but offer overall efficiency benefits for a certain range of low-diffusion-length materials. [21]

Vertical multijunction (VMJ) solar cells were investigated in the 1970s for producing radiation-hardened photovoltaics for space applications. [22, 23, 24] (The ionizing radiation encountered in outer space induces damages in crystalline Si, reducing L even in high-purity material.) VMJ cells are similar to parallel multijunction devices in that they tolerate low-diffusion-length materials. One fabrication route involves etching ridges in Si wafers and diffusing p-n junctions. [25] Like PMJ cells, their increased junction area leads to lower operating voltages.

Point-contact solar cells. At the opposite extreme, point-contact devices have a very small junction area in order to achieve very high operating voltages. [26, 27] This is accomplished by using a lithographic technique to define small, heavily doped n- and p-type regions (alternating) and contacts on the back of a wafer. The rest of the wafer is only lightly doped and has well-passivated surfaces, allowing it to operate in high-level injection. Point-contact solar cells require high-quality Si wafers, as the carriers must diffuse across the device thickness to reach the back-side junction. However, their all-backside contact geometry also eliminates shading loss due to front-side contact grids. Point-contact cells are one of the most efficient crystalline Si photovoltaic technologies in large-scale commercial production today.

Sliver cells are initially fabricated in a manner similar to etched VMJ cells, by micromachining thin (e.g., 50 μm) ridges or “slivers” from thick Si wafers. The slivers are then removed from the handle wafer and assembled into bifacial modules. The small size of each sliver permits some degree of mechanical flexibility, and allows the modules to consume $\sim 10\times$ less Si than conventional wafer-based photovoltaics. [28]

Silicon microcells are ultrathin (sub-micron) solar cells that are exfoliated from crystalline Si wafers using a controlled fracture technique. Arrays of microcells can be assembled to form flexible, lightweight, and visually aesthetic modules with very low Si utilization. Several such devices can be exfoliated from a single Si wafer. [29]

Spherical solar cells use miniature parabolic reflectors to concentrate sunlight onto sparsely packed Si spheres ($\sim\text{mm}$ in diameter), each of which contains a p-n junction. The low density of the spheres enables efficient Si utilization and moderate optical concentration levels. [30]

1.5 Silicon microwire photovoltaics

Silicon microwire photovoltaics provide an intriguing alternative to planar, wafer-based crystalline Si solar cells. The fundamental appeal of Si microwire photovoltaics is twofold: First, the microwires enable novel cell geometries that have unique performance benefits compared to equivalent planar structures. Secondly, Si microwire-array solar cells can be produced using traditionally low-cost, high-throughput fabrication techniques that are synergistic with the existing infrastructure and supply chain of the crystalline Si photovoltaics industry.

Wire-based solar cells were first discussed many years ago. A photoconverter based on crystalline Si wires (which were then typically called “whiskers” or “filamentary crystals”) was reported in the Soviet literature in 1978, [31] and a Si whisker solar cell was patented in the U.S. in 1979. [32] However, to our knowledge, these concepts received little attention until the past decade’s surge in renewable energy research, combined with the revival of whisker growth techniques for producing new types of nanowire devices, led to a flourishing field of nanowire-based solar cell research (many results of which are cited throughout this thesis). The work presented here began as part of an effort at Caltech to examine photovoltaic applications of semiconductor nanorods, and as a result of the insight gathered therein, has evolved to focus on crystalline Si microwire photovoltaics.

1.5.1 The vapor-liquid-solid growth process

Crystalline Si wires, ranging in diameter from nanometers to millimeters, can be grown by a catalytic chemical vapor deposition (CVD) technique known as the *vapor-liquid-solid* (VLS) process, depicted in Figure 1.4. First reported by Wagner and Ellis in 1964, the VLS process can produce defect-free crystalline material directly from gaseous precursors (e.g., producing Si from SiH_4 , SiCl_4 , or HSiCl_3). [33, 34, 35] During VLS Si growth, the precursor gas decomposes

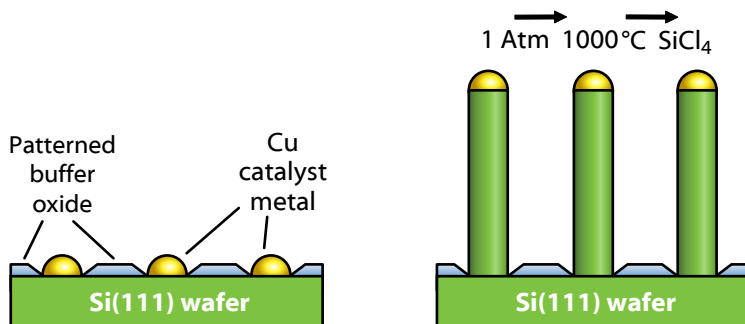


Figure 1.4. Schematic diagram of the VLS growth process. The patterned growth wafer (left), and VLS growth (right).

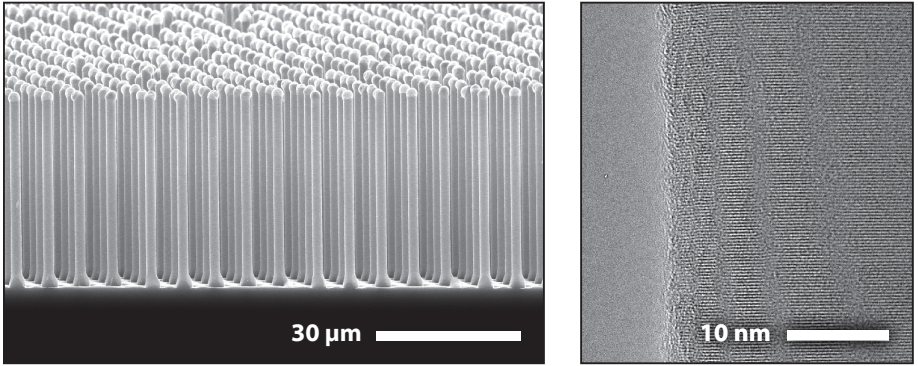


Figure 1.5. Images of VLS-grown Si microwire arrays. SEM image (left) and TEM image (right), both provided by Brendan Kayes. [39]

at the surface of a liquid metal catalyst droplet, forming a eutectic metal/Si alloy. Au is the most commonly studied VLS catalyst metal, although at least 11 other metals (including Cu and Ni) also lead to VLS growth. [36] As the catalyst droplet becomes supersaturated, the Si precipitates at the solid interface. In this manner, an approximately cylindrical column of crystalline material is produced, elevating the catalyst droplet above it as it grows. Because precursor decomposition is favored at the catalyst surface, negligible conformal deposition occurs, and substantially faster growth rates are observed than for non-catalytic processes.

During the course of this thesis work, efforts led by Brendan Kayes and Michael Filler resulted in a high-fidelity patterned VLS growth technique for producing Si microwire arrays. [37] This process was used extensively throughout the course of this work, and is depicted in Figure 1.4. Si(111) growth wafers are prepared by thermal oxidation to produce a ~ 300 nm thick buffer layer that confines the catalyst metal at growth temperatures. Using standard photolithography, holes are etched in the buffer oxide, through which the catalyst metal (e.g., Cu) is evaporated (or electrodeposited) onto the Si surface. VLS growth is performed under atmospheric pressure at temperatures of ~ 1000 °C, using SiCl_4 precursor gas diluted in H_2 . The wire position and diameter are determined by the photolithographic pattern and catalyst metal thickness, whereas the wire length is determined by growth conditions and duration, with typical 20-minute growths producing wires ranging from 50 to 200 μm in length. Representative SEM and TEM images of a wires grown by this technique are shown in Figure 1.5. SiCl_4 is a particularly favorable precursor gas because it is presently an unwanted by-product of the *Siemens process*, which supplies a majority of the polysilicon feedstock for today's photovoltaic and microelectronics industries. [9, 38]

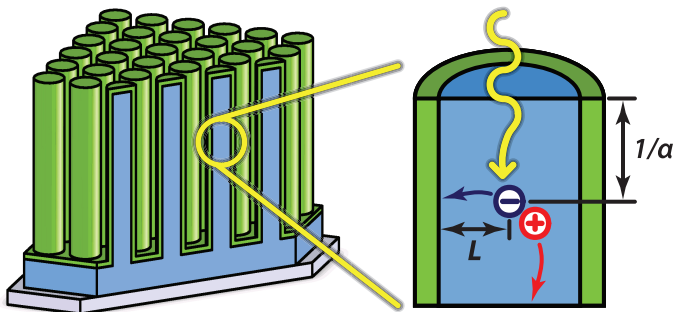


Figure 1.6. Schematic diagram of a Si wire-array solar cell and the radial p-n junction geometry.

1.5.2 The radial p-n junction

A unique advantage of wire-based solar cells is the ability to produce *radial p-n junctions*, as depicted in Figure 1.6. Radial junctions can be fabricated, for example, by thermal dopant diffusion [39] or by conformal deposition of an oppositely doped material. [40]

The virtue of the radial p-n junction is that it decouples the direction of light absorption from that of carrier collection. Solar cells should be sufficiently thick to absorb all incident light, which for crystalline Si, can require 100 μm of material or more. In planar cells (see Fig. 1.3), the minority-carrier diffusion length, L , must be at least this long so that photocarriers can reach the junction and be collected. This places extreme purity requirements on the Si material (as impurities can drastically reduce L) and results in high costs. Radial junctions, however, can provide an arbitrarily short collection path equal to the wire radius. This geometry ensures both high absorption and high carrier collection efficiency, and permits the use of lower-quality materials with lower minority-carrier diffusion lengths. Like the vertical and parallel multijunction solar cell concepts, however, this tradeoff comes at the cost of operating voltage due to increased junction area.

Brendan Kayes presented an analytical model of radial p-n junction solar cells in 2005, [41] which played a seminal role in motivating our study of Si wire-based photovoltaics. His study indicated that reasonable efficiencies (e.g., $\eta \sim 13\%$ – 15%) could be obtained even in low-diffusion-length Si material ($L \sim 1$ – $10 \mu\text{m}$).

1.5.3 Peel-off and wafer reuse

Remarkable structures and processing methods for Si microwire arrays were also developed concurrent to this thesis work. Efforts led by Katherine Plass and Michael Filler showed that the VLS-grown microwire arrays can be embedded in a transparent polymer and then peeled intact from the growth substrate as a flexible, highly ordered film of crystalline Si wires. [42] Images of a polymer-embedded Si microwire array appear in Figure 1.7.

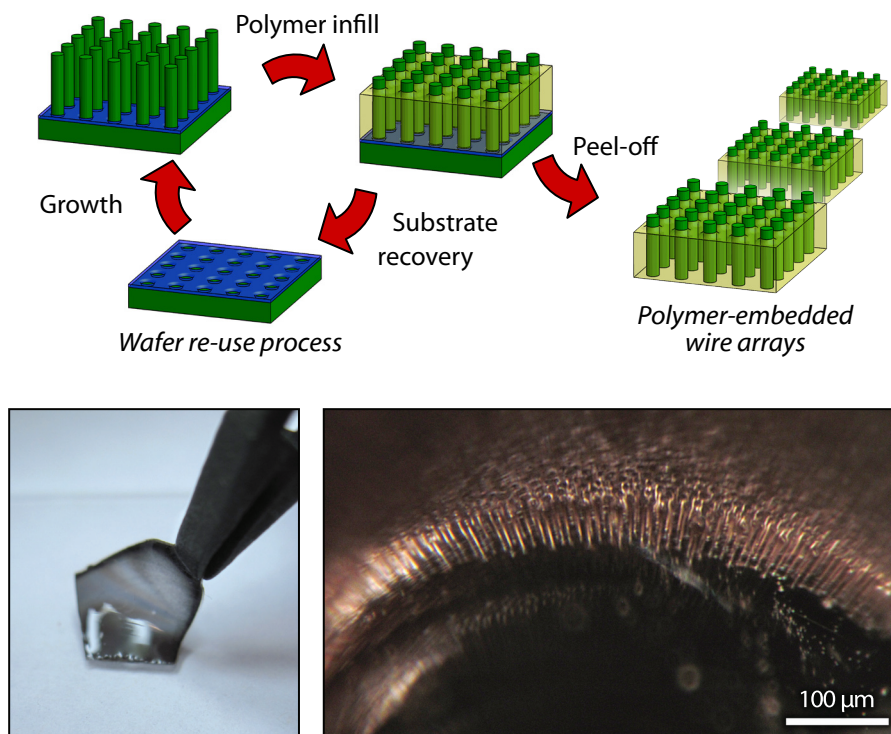


Figure 1.7. Wire array peel-off and wafer reuse diagram (above) and images of polymer-embedded Si microwire arrays (below).

The wire-array peel-off technology opens the possibility of producing flexible, lightweight solar cells made from Si microwires. Equally importantly, this technique preserves the integrity of the patterned growth wafer, allowing each wafer to be reused to produce a multitude of wire-array solar cells—without repatterning the oxide template layer, as depicted in Figure 1.7. Following peel-off, the growth substrates are cleaned in KOH at 80 °C, which selectively etches residual polymer material and the remaining wire stubs, but which otherwise leaves the oxide template layer intact. New catalyst metal can then be redeposited using electrodeposition. This research, led by Joshua Spurgeon, has demonstrated up to four wire-array growths from a single patterned wafer. [43] Continued research to improve the number of regrowths, combined with the ability to touch-polish, oxidize, and repattern wafers after pattern fidelity is lost, is expected to enable 1000 or more growths from each Si wafer. The ability to grow high-quality Si wire arrays without consuming expensive Si wafers offers the potential to produce high-efficiency, low-cost Si microwire photovoltaics.

Optoelectronic modeling of Si wire photovoltaics

The unyielding progress of today's semiconductor industry is made possible by the use of computer simulation at virtually every level of technology development. Numerical modeling has become equally indispensable to the understanding and optimization of modern photovoltaic technologies [44] and has developed such complexity and precision that it has been used in the design of the world's most efficient Si solar cells. [45, 46] In this chapter, we will develop a comprehensive numerical model for Si microwire photovoltaics, and address the fundamental phenomena that make them such intriguing structures for solar energy conversion.

2.1 Introduction

In principal, the silicon solar cell is a relatively simple semiconductor device. Its salient characteristics are indeed well described by analytical approaches to the underlying device physics of p-n junctions. Classical (Shockley) behavior of the abrupt p-n junction is obtained by partitioning the structure into conceptual regions of quasi-neutrality and depletion. By virtue of the simplifying assumptions and approximations applied to each region, this analysis gives way to the well-known closed-form expressions that relate the behavior of a diode to its morphology. [47, §2.3.1] This provides valuable intuition for the design of solar cells.

In practice, however, solar cells rarely manifest behavior as predicted by classical diode theory. Analytical approaches must be modified to account for nonidealities of real device structures, such as edge effects and nonabrupt p-n junctions; as well as to address the inadequacies of first-order simplifying assumptions, such as considering recombination/generation in the depletion region. [48, §5.2.4] Even for one-dimensional structures, analytical solutions quickly become difficult if not impossible when taking into account, for example, the doping profile of diffused or arbitrarily graded p-n junctions, the electrostatics of surface or bulk trap states, or the dependence of mobility and carrier lifetime on doping concentration in crystalline Si. Analytical approaches are further compounded in complexity when extended to nonplanar junction geometries, such as vertical multijunctions, [24] radial junctions, [41] or point-contact solar cells. [26] These geometries decouple the direction of majority- and minority-carrier transport, and require numerous simplifying approximations to be made in order to obtain closed-form equations describing their behavior—for example, by neglecting axial minority-carrier transport in the analysis of radial p-n junctions. Computational approaches need not make simplifying approximations to solve

the equations of device physics, and thus produce *numerically exact* solutions. When properly implemented, the accuracy of numerical methods is limited only by the accuracy with which the input equations and parameters can model the underlying physics and structure of a device.

Nonplanar geometries also present tremendous challenge to the understanding of optical absorption within solar cells. Photogeneration profiles within planar structures can be easily calculated by assuming one-dimensional Beer-Lambert absorption, and can even be adapted for the case of randomized (ergodic) light trapping (see section 3.1.3). More complex approaches (such as numerical raytracing) are required to describe optical absorption within nonrandomly textured solar cells [49] and, for example, optical microconcentrator solar cells. [50] However, as our experiments in Chapter 3 will show, the photonic dimensions of Si microwire arrays manifest novel optical properties that cannot be described by classical ray-optics. Thus these structures require full-wave numerical solutions of Maxwell's equations to accurately describe their optical behavior. Although several full-wave approaches have been employed to model the optical properties of smaller Si nanowire-array solar cells, [51, 52, 53, 54, 55, 56, 57] the optical properties of our Si microwire arrays for photovoltaic applications have thus far not been modeled numerically.

The above considerations frame our development of techniques to model Si microwire photovoltaics in this chapter. We will begin by employing a state-of-the-art device physics simulator to model the electrical behavior of radial p-n junction solar cells. Our simulations will not only affirm the findings of prior analytical studies, but will also enable us to explore and optimize new realms of device operation such as full-core-depletion and hybrid radial/axial junction geometries. We will then turn our attention to modeling the optical properties of Si microwire arrays, and study geometries that lead to optimal absorption of sunlight. Finally, we will combine the device physics and optical simulation techniques to produce a comprehensive model of the photovoltaic behavior of Si microwire-array solar cells. These simulation techniques will be used throughout the remainder of this thesis to gain insight from experimental measurements, and ultimately, to guide the development of high-performance Si microwire photovoltaics.

2.2 Device-physics model

2.2.1 Choice of simulation software

Numerical methods for solving the constitutive equations of device physics phenomena in one dimension were described by Gummel and Scharfetter in the 1960s, [58, 59] and had found applications in modeling and optimizing the performance of Si photovoltaics by the following decade. [60] The advent of personal computers in the 1980s made numerical methods available to researchers throughout the world, and device physics modeling soon became an integral aspect of photovoltaics research. Several groups developed and distributed one-dimensional solar cell simulators that remain widely used to this day. Notable

examples include *PC1D*, developed at Iowa State University (and later maintained at UNSW); [61] *AMPS*, developed at Pennsylvania State University; [62] and more recently, *AFORS-HET*, developed at the Hahn-Meitner-Institut in Berlin. [63] Advances in numerical methods and computational power have now made two- and even three-dimensional device physics simulations feasible for photovoltaics research, enabling complex nonplanar junction geometries to be modeled. Example applications have included the study of perimeter effects in high-efficiency solar cells, [64] pyramidal front-surface texturing, [49] point- and buried-contact cell geometries, [27, 65, 66] and optimization of contact grid resistance and shading loss. [45]

Whereas some of the most popular one-dimensional solar cell simulators were developed as freely available research tools for the photovoltaics community, many of today’s most robust and widely used three-dimensional device-physics simulators have been developed and commercialized for the semiconductor microelectronics industry by *electronics design automation* (EDA) software firms. Device-physics simulation is integral to the process known as *technology computer-automated-design* (TCAD), which seeks to model the fabrication and behavior of semiconductor devices at the physical level. For this study we have employed the Synopsys *TCAD Sentaurus* software suite,* which includes *Sentaurus Device*, a state-of-the-art device physics simulator. Through years of consolidation within the EDA industry, the lineage of Sentaurus can be traced back to several other commercial simulation tools that were prominently featured in prior solar cell modeling, including ISE DESSIS and SIMUL.

2.2.2 Overview of simulation procedure

Sentaurus Device employs a numerical discretization method to solve the constitutive equations of device physics over a finite-element mesh that represents a semiconductor device. [67, 68] The mesh stores the values of all physical quantities throughout the device, including impurity concentrations (N_D , N_A), carrier concentrations (n , p), and electrostatic potential (φ); and also specifies which boundaries of the device are electrodes. Upon calculating the state of the mesh that satisfies the device-physics equations, Sentaurus records the current and voltage of each electrode. By repeating this procedure over a swept range of electrode biases, the I – V behavior of the device can be simulated.

The device-physics equations that are solved by Sentaurus depend on the type of simulation and on which carrier-transport model is employed. Our simulations sought steady-state solutions under drift-diffusion carrier transport, for which the constitutive equations of device physics are:

1. The Poisson equation,

$$\nabla \cdot \epsilon \nabla \varphi = -q(p - n + N_D - N_A) - \rho_T \quad (2.1)$$

*The following versions of Sentaurus were used in this thesis: A-2007.12, A-2008.09, and C-2009.06-SP2.

where ϵ is the electrical permittivity, q is the electron charge, and ρ_T is the charge density due to traps.

2. The electron continuity equation,

$$-\nabla \cdot (\mu_n n \nabla E_{Fn}) = q (U_{R/G} - G_{opt}) \quad (2.2)$$

where E_{Fn} is the electron quasi-Fermi level, μ_n is the electron mobility, $U_{R/G}$ is the net recombination rate due to recombination/generation processes, and G_{opt} is the optical generation rate.

3. The hole continuity equation,

$$\nabla \cdot (\mu_p p \nabla E_{Fp}) = q (U_{R/G} - G_{opt}) \quad (2.3)$$

where E_{Fp} is the hole quasi-Fermi level and μ_p is the hole mobility.

Sentaurus offers models for most known device-physics phenomena, which it can take into account while evaluating the above equations. For example, our work required that the doping dependence of carrier mobility be considered; thus, our command file instructed Sentaurus to employ its built-in model to calculate the values of μ_n and μ_p at each mesh point according to the accepted parameters for this phenomena in crystalline Si. [69] Sentaurus includes default parameters for most device-physics phenomena in crystalline Si. [68] For each simulation presented herein, we will describe which models were employed, and will note if parameter values other than defaults were used. An example set of command files for a simple radial p-n junction solar cell is included in Appendix A.3.1.

2.2.3 Single-wire solar cell model

Brendan Kayes presented a quasi-analytical approach to the device physics of radial p-n junction solar cells in 2005. [41] This study has played a seminal role in the development of Si wire-array photovoltaics, and has attracted attention from research groups around the world. To further expand the understanding of radial-junction solar cells, and to explore modes of device operation that could not be studied analytically, a single-Si-wire radial p-n junction solar cell was modeled using the Sentaurus TCAD software suite. Figure 2.1a illustrates a proposed Si wire-array solar cell geometry, from which the single-wire-equivalent model shown in Figure 2.1b was derived. The numerical model was implemented in two-dimensional cylindrical coordinates, thus simulating three-dimensional quantities under the assumption of cylindrical symmetry. Like Kayes' analytical study, this model assumed top-down illumination following a simple Beer-Lambert absorption profile, and did not model any optical effects of a wire array.* Accordingly, the photovoltaic performance of this structure was normalized to the circular area of illumination, rather than the unit cell of a proposed wire-array device.

*This was implemented using OptBeam generation in Sentaurus (see Appendix A.3.1).

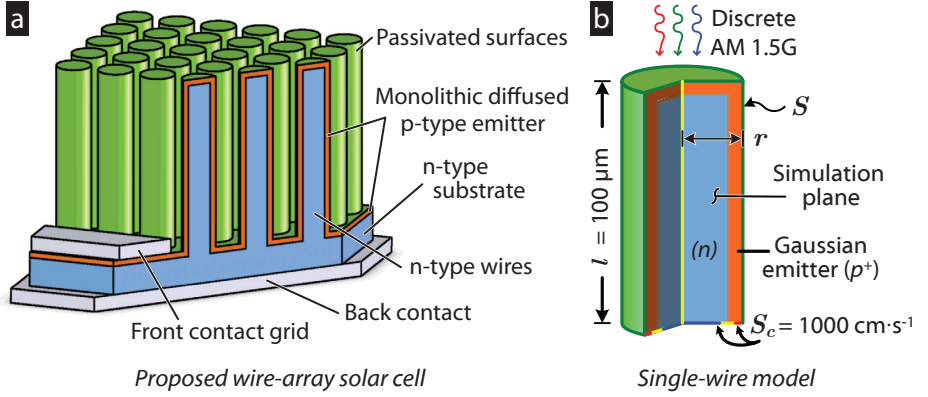


Figure 2.1. Illustration of simulated single-wire solar cell. (a) Proposed Si wire-array solar cell. (b) Single-wire structure for device-physics simulations.

The simulated single-wire device had an n-type core with $N_D = 10^{18} \text{ cm}^{-3}$, corresponding to the experimentally observed doping levels in our early single-wire solar cells that were grown by a Au-catalyzed VLS process (see section 4.4.1). A Gaussian p-type (boron) emitter profile was assumed, with a surface concentration of $N_{A,\text{surf}} = 5 \times 10^{18} \text{ cm}^{-3}$ and a junction depth of $x_j = 50 \text{ nm}$, corresponding to an approximate junction profile that could be produced by thermal B diffusion. A wire length of $100 \mu\text{m}$ was selected as a compromise between the length required for complete optical absorption, and the increased computational resources required to model larger structures. This thickness absorbed $\sim 90\%$ of incident solar power and thus limited the maximally obtainable current density to $\sim 38 \text{ mA}\cdot\text{cm}^{-2}$. A 5 nm oxide was placed along the side and top surface of the wire to allow surface recombination to be modeled at these interfaces, and ideal ohmic contacts to the base and emitter regions were placed at the bottom of the structure. Contact electrodes are typically associated with extremely high surface recombination velocities ($S \sim 10^7 \text{ cm}\cdot\text{s}^{-1}$ or larger). However, as shown in Figure 2.1, each individual wire in the proposed wire-array device would be interconnected via monolithic planar n- and p-type regions of the substrate, rather than directly contacted by metallic electrodes. Thus it was estimated that an effective minority-carrier surface recombination velocity of $S = 1000 \text{ cm}\cdot\text{s}^{-1}$ could be used at the electrodes of the simulated single-wire structure, to approximate the distributed effect of back-surface field and a distant metallic contact electrode.

Using Sentaurus Device, the terminal J - V behavior of the single-wire solar cell device was simulated. The model included the effects of doping-dependent mobility and Auger recombination, using default parameters for both. Homogeneous bulk and surface Shockley-Read-Hall (SRH) recombination were also considered. For the purpose of generality, the bulk SRH recombination was assumed to arise from a single midgap SRH trap having minority carrier lifetimes $\tau_n = \tau_p$. This implementation gave rise to carrier recombination dynamics

as predicted by SRH theory (namely, producing the intended minority-carrier lifetime τ_p within the base region of the device) but did not model the electrostatics of an actual trap state. Similarly, surface SRH recombination was implemented at the Si/SiO₂ interface, assumed to arise from a mid-gap surface-trap state with minority-carrier surface recombination velocities $S_n = S_p$. Solar illumination was modeled using a 20-point discrete approximation of the above-bandgap AM 1.5G [15] spectrum, which preserved the incident power density, photon flux, and overall shape of the relevant AM 1.5G spectrum. (Similar discrete solar spectra for simulations can be found in Appendix B.11.) Simple Beer-Lambert optical absorption profiles were assumed, using the optical beam absorption model within Sentaurus, and default values for the absorption coefficient of Si. One-sun J - V behavior was simulated for devices of varying radius ($r = 0.2$ – 20 μm), minority-carrier lifetime ($\tau = 10^{-11}$ – 10^{-5} s), and surface recombination velocity ($S = 100, 1300, \text{ and } 10^5$ $\text{cm}\cdot\text{s}^{-1}$). Within the n-type (base) region of the solar cell, the chosen τ values corresponded to minority-carrier diffusion lengths (L_p) ranging from 60 nm to 60 μm .*

Figure 2.2 shows the simulated efficiency contours of the single-wire solar cell structures, indicating that the modeled device would be capable of conversion efficiencies in excess of $\eta = 20\%$ within the considered parameter space (although we note that this model has not yet considered any optical or contact-related losses). The V_{oc} and J_{sc} contours are also shown. As predicted by radial p-n junction theory, the simulated device was capable of obtaining high J_{sc} at arbitrarily low minority-carrier diffusion lengths, as long as the wire radius r was kept smaller than the diffusion length. However, the V_{oc} (and FF , not shown) decreased markedly at low values of L , particularly for smaller wire radius. Thus, for any given diffusion length, optimal cell efficiency occurred when $r \sim L_p/2$. The structure was remarkably insensitive to surface recombination on the top and sides of the wire, owing to the fact that most of the light was absorbed within the base (core) of the device, and was thus shielded from all surfaces by the emitter layer. Only in cases of extreme recombination velocity ($S = 10^5$ $\text{cm}\cdot\text{s}^{-1}$) was performance affected. This was caused by a loss of collection efficiency at the top of the cell, as well as a dramatic increase in junction dark current for longer-lifetime devices.

To obtain an estimate of achievable photovoltaic efficiencies for VLS-grown Si wire solar cells, based on experimentally inferred minority-carrier lifetimes (see section 4.5), we considered the case of $\tau_p = 20$ ns (the highest value observed for Au-catalyzed wires) and $\tau_p = 140$ ns (the highest value observed for Ni-catalyzed wires). These values correspond to L_p values of 2.8 and 7.5 μm , respectively, within the base region of the simulated structure. In both cases, the experimentally inferred upper limit on surface recombination velocity was also assumed ($S = 1300$ $\text{cm}\cdot\text{s}^{-1}$ for Au-catalyzed wires, and $S = 300$ $\text{cm}\cdot\text{s}^{-1}$ for Ni-catalyzed wires). The radius of each device was chosen to be near the optimal radius predicted by Figure 2.2: 1.5 and 5 μm , respectively. These simulated cells

* $L_p = \sqrt{D_p \tau_p}$, where D_p is the minority-carrier (hole) diffusion coefficient. $D_p = 4$ $\text{cm}^2\cdot\text{s}^{-1}$ for Si having $N_D = 10^{18}$ cm^{-3} .

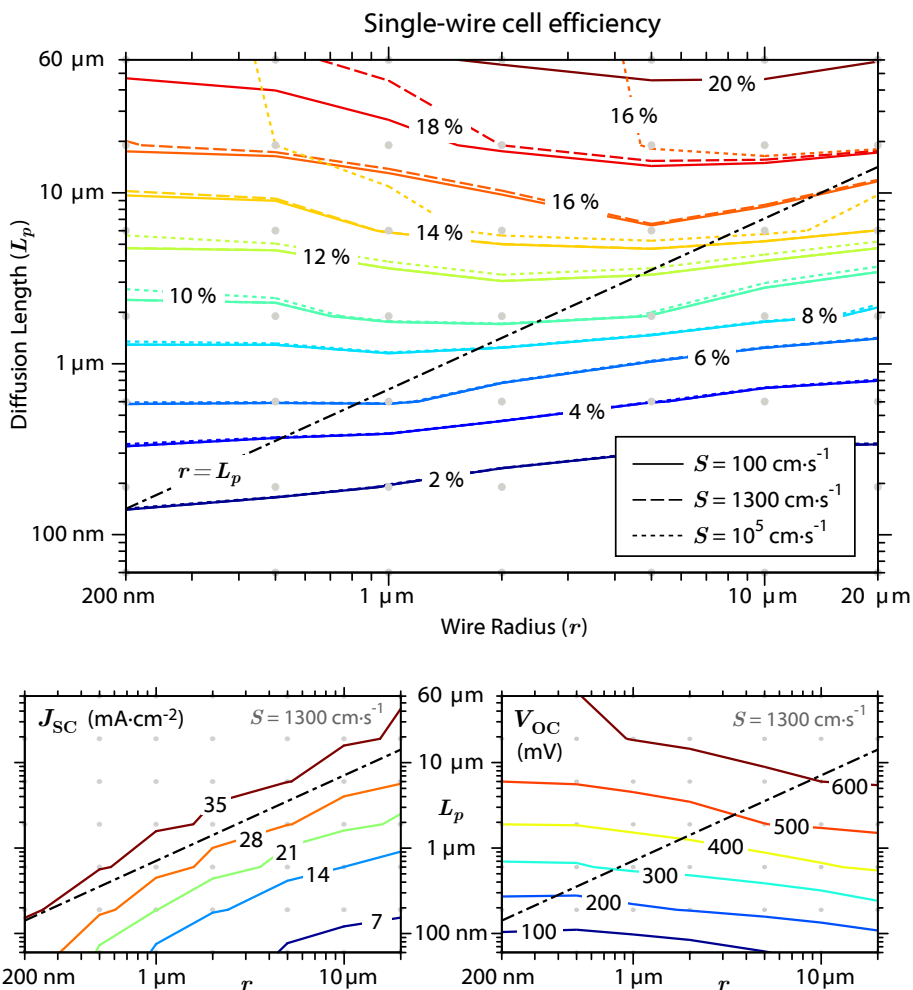


Figure 2.2. Simulated performance of single-wire radial junction solar cells. Efficiency (η , top), short-circuit current density (J_{sc} , lower left), and open-circuit voltage (V_{oc} , lower right) contours for simulated devices as a function of wire radius (r) and minority-carrier diffusion length (L_p). Efficiency contours are shown for all three simulated surface recombination velocities (S), whereas V_{oc} and I_{sc} contours correspond to $S = 1300 \text{ cm}\cdot\text{s}^{-1}$. Gray dots indicate simulated devices.

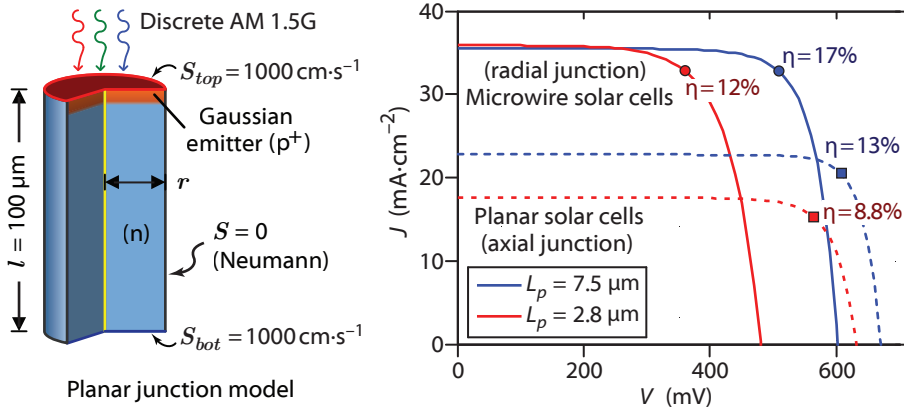


Figure 2.3. Simulated performance of radial- vs. planar-junction solar cells. **Left:** Structure for planar-junction solar cell simulations. **Right:** Simulated one-sun J - V behavior of radial- and planar-junction devices for $L_p = 2.8 \mu\text{m}$ and $L_p = 7.5 \mu\text{m}$.

exhibited energy conversion efficiencies of 12% and 17%, respectively, as shown in Figure 2.3.

For comparison, the performance of planar-junction solar cells having identical emitter doping profiles, contact surface recombination velocities, and carrier lifetimes was simulated. The planar-junction structures were implemented within Sentaurus by modifying the radial-junction model as follows: The radial emitter profile was removed, leaving only the axial junction at the top of the wire. The contact electrodes were defined as shown in Figure 2.3, and the SiO_2 shell was removed from the outside of the cylindrical structure. In the absence of an interface at the edge of the structure, Sentaurus applied ideal (Neumann) boundary conditions; thus this structure effectively simulated a cylindrical “plug” of a planar-junction device. Comparing the simulated J - V performance of these structures to that of the radial-junction solar cells (Figure 2.3), the advantage of radial minority-carrier collection becomes clear: Although the planar-junction devices achieved higher V_{oc} , their poor carrier-collection efficiency for the studied diffusion lengths led to greatly reduced J_{sc} , and notably lower efficiency than the radial-junction devices.

Although these device physics simulations did not use a realistic optical model for light absorption in Si microwires, it nonetheless provided much insight into carrier transport and design considerations for Si microwire solar cells. The simulation mesh can be plotted, for example, to study the distribution of carrier recombination (U_{SRH}) and current densities (J_n and J_p) as shown in Figure 2.4. The selected streamtraces shown in the graphs of J_n and J_p illustrate the transport path of each carrier type, revealing that the minority-hole transport was somewhat complex, having both both an axial and radial components. This is

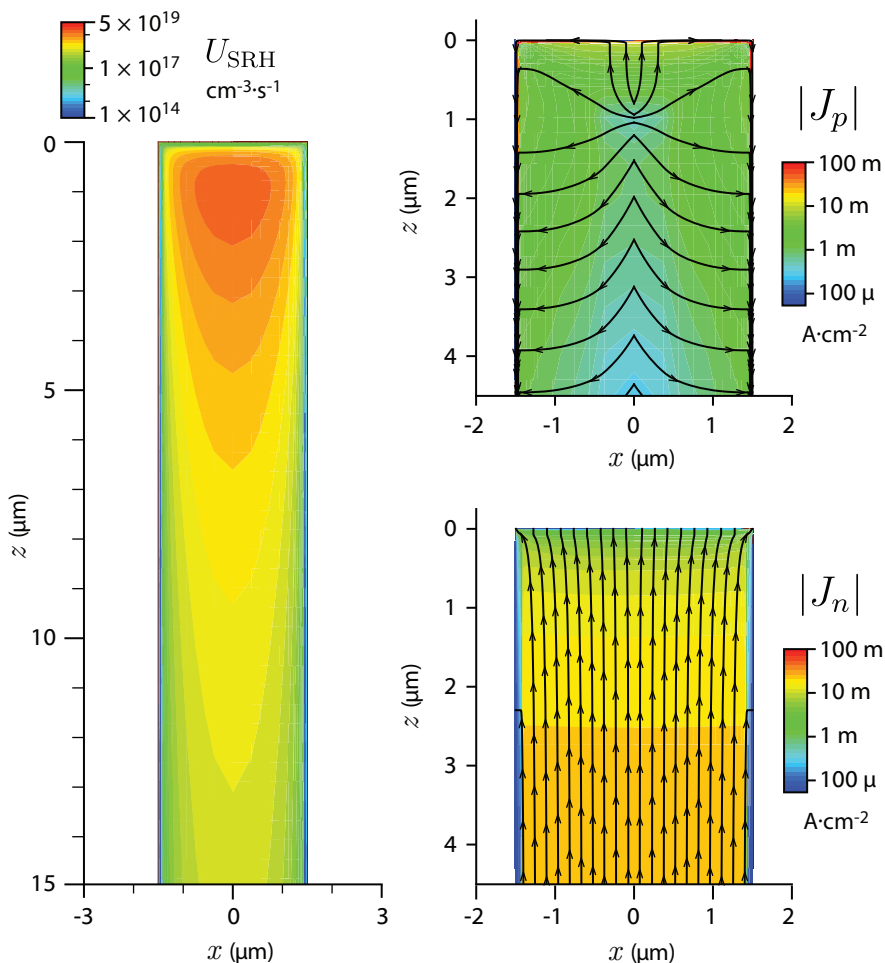


Figure 2.4. Simulated current density and SRH recombination profiles for the $r = 1.5 \mu\text{m}$ radial junction solar cell device whose J - V behavior is shown in Fig. 2.3. The simulation plane has been mirrored to show the full cross section of the simulated cylindrical device (only the upper portion of the wire is shown). Streamtraces have been added to the electron and hole current-density plots to illustrate the path of carrier transport. All plots correspond to short-circuit one-sun illumination.

not surprising near the top of the wire, where our model featured an axial p-n junction. Below the region of axial collection, the exponential optical generation profile also gave rise to a downward component to the hole diffusion path. This two-dimensional transport behavior had not been addressed in Kayes' analytical modeling, which only considered minority-carrier transport in the radial direction. However, the numerical simulations yielded strikingly similar results, in terms of device performance, as predicted by the analytical modeling. In fact, when the results of the two approaches were compared for several different device parameters, we found that both predicted the same solar energy conversion efficiency to within a few percent. Thus our numerical simulations largely confirmed the validity of the assumptions that had been made in the prior analytical approach to radial p-n junctions.

Ultimately, gaining further insight into the realistic efficiency potential of wire-array solar cells would require optical (as well as electrical) modeling—which is presented in the next section of this thesis. However, even without complex optical generation profiles, the numerical device physics model afforded new opportunities to explore modes of device operation that had not been possible under the assumptions of the analytical model, as well as to leverage the capabilities of TCAD to improve the design of Si wire solar cells. The following discussions highlight some of these efforts.

2.2.4 Numerical optimization

Although the device physics model presented above enabled us to study the effects of device geometry on the simulated photovoltaic efficiency of radial-junction solar cells, it did not necessarily provide us with insight as to which dimensions would yield optimal performance. While we were able to select reasonable dimensions by performing a large parametric sweep of the two key variables r and L_p , the Sentaurus TCAD software also offered the option of performing numerical optimization of the device structure. This has the advantage of requiring fewer simulations than a parametric sweep, and is capable of considering more variables at one time.

To explore this technique, we employed numerical optimization to determine a more favorable device structure for a radial-junction solar cell subject to low minority-carrier diffusion length ($L_p = 2.8 \mu\text{m}$) and moderate surface recombination velocity ($S = 1300 \text{ cm}\cdot\text{s}^{-1}$). The modeled structure was identical to that presented in the previous section, except that an electrode surface recombination velocity of $S = 10^4 \text{ cm}\cdot\text{s}^{-1}$ was assumed. The wire radius (r), length (l), and base doping (N_D) were chosen as free variables. Table 2.1 lists the initial values and permitted range of each parameter, as well as the unoptimized efficiency of the cell ($\eta = 12.6\%$). Using Sentaurus Workbench, an iterative optimization task was defined to maximize η , using a face-centered central composite experimental design, and a second-degree response surface model. [70]

Over the course of ~ 160 individual simulations, the optimizer was able to improve the simulated efficiency to $\eta = 13.4\%$, a significant increase over the

Table 2.1. Numerical optimization of a radial-junction solar cell structure.

Parameter	Initial value	Optimization range	Final value
r (μm)	1.5	0.9–2.2	1.72
l (μm)	100	30–150	45
N_D (cm^{-3})	1×10^{18}	10^{16} – 10^{19}	1×10^{18}
V_{oc} (mV)	483	—	530
J_{sc} ($\text{mA}\cdot\text{cm}^{-2}$)	37.9	—	35.2
FF (%)	69.3	—	72.5
η %	12.6	—	13.4

$L_p = 2.8 \mu\text{m}$ and $S = 1300 \text{ cm}\cdot\text{s}^{-1}$.

initially chosen value considering the simplicity of the optimization space. From this starting point, it is likely that additional improvements could be made by freeing more parameters, such as the emitter doping profile ($N_{A,\text{surf}}$ and x_j). However, our initial numerical optimizations were of limited practical use, due to the lack of a realistic optical absorption model, as well as uncertainty about which (if any) structures could actually be fabricated. Given the recent breakthroughs with regards to both of these challenges (as will be highlighted in section 2.3 and Chapter 5, respectively), numerical optimization now has the potential to play a prominent role in the future development of high-performance Si microwire photovoltaics.

2.2.5 Effects of core depletion

One of the more puzzling questions posed of the theory of radial junctions was how they would behave if their core regions were fully depleted. Tsakalagos et al. suspected that this may have contributed to the relatively poor performance of early Si wire-array solar cells, the cores of which were estimated to be nearly or fully depleted. [40] Depletion may also have been to blame for other early reports of low-efficiency Si wire-array solar cells, due either to extremely small wire diameters [71] or to inadequate core doping levels. [72] Our numerical device physics model enables us to simulate and understand this behavior.

One might not initially predict that core depletion could pose a threat to the performance of radial p-n junction solar cells. After all, the conventional wisdom of crystalline Si solar cells is that the minority carriers are “collected” as soon as they reach the depletion region. Carriers are rarely lost within the depletion region because the built-in electric field quickly sweeps them to the opposite side of the junction, where as majority carriers, they are essentially immune to recombination. The rapid speed of this transit is often exploited, for example, by p-i-n photodiodes to achieve high frequencies of operation, as well as by p-i-n a-Si:H solar cells, whose extremely low lifetime and mobility make

efficient carrier-collection nearly impossible without the help of an electric field. And aside from this perceived certainty of collection within depletion regions, the radial junction geometry can still provide arbitrarily short collection paths for minority carriers.

However, it is not the radial collection of minority carriers that turns out to limit the performance of fully depleted devices; rather, it is lack of *majority* carriers to facilitate *axial* carrier transport. This becomes clear when the electrostatics of a fully depleted device are considered. Because the depletion extends from the base to the tip of a fully depleted wire (which for the structures considered herein, is three orders of magnitude longer than the nominal depletion width of the junction), its axial electric field component must be essentially zero throughout most of the device. This fact, combined with the low concentration of equilibrium free carriers caused by depletion, effectively disables carrier drift as a transport mechanism to sustain current through the device. Furthermore, with no vertical electric field to assist the collection of what normally would be majority photocarriers, are instead left stranded as minority carriers in the depletion region, beset by a short lifetime and a long distance over which to diffuse before reaching the base of the wire.

To further investigate this behavior, we performed numerical device-physics simulations as shown in Figure 2.5. To simulate a fully depleted wire, the above radial-junction model was modified as follows: The doping of the n-type core was lowered to $N_D = 10^{17} \text{ cm}^{-3}$ so that full depletion would occur at a radius of $r \sim 100 \text{ nm}$. The emitter profile was changed to an abrupt junction with $N_A = 5 \times 10^{18} \text{ cm}^{-3}$ and $x_j = 50 \text{ nm}$, to avoid a subtle variation in junction depth that occurs for diffused cylindrical junctions in small-diameter wires. To ensure that the depletion would not extend to the contact electrode, the model was extended to include a $1 \text{ }\mu\text{m}$ long cylindrical “plug” of identical n-type material as the core, and the electrode was defined at the bottom of this region. Finally, to reduce the computational complexity of the simulations, the wire length was reduced to $50 \text{ }\mu\text{m}$, and a 5-point (vs. 20-point) discretization of the solar spectrum was used to calculate the optical generation profiles (again using the simple Beer-Lambert absorption model).

The photovoltaic performance of the single-wire structure was simulated for wire radii ranging from 70 nm to $31 \text{ }\mu\text{m}$, assuming three possible values of minority-carrier lifetime: 5 ns ($L_p = 2 \text{ }\mu\text{m}$), 100 ns ($L_p = 9 \text{ }\mu\text{m}$), and $5 \text{ }\mu\text{s}$ ($L_p = 64 \text{ }\mu\text{m}$). The effect of core depletion was immediately apparent in the simulation results, as shown in Figure 2.5: The carrier collection (J_{sc}), and thus the photovoltaic efficiency, both plummeted to zero at small wire diameters—even for the structures with L_p longer than the length of the wire. Figure 2.6 plots the Shockley-Read-Hall recombination profiles (U_{SRH}) for $L_p = 64 \text{ }\mu\text{m}$ wires of 160 nm diameter (fully depleted) and 400 nm diameter (normal operation), illustrating the dramatic increase in recombination within fully depleted radial junctions.

Further insight is gained by examining the simulated physical state of a depleted vs. a nondepleted device. Figure 2.7 plots the axial component of the electric field, E_z , along the center of the $L_p = 64 \text{ }\mu\text{m}$ wire, for wires with

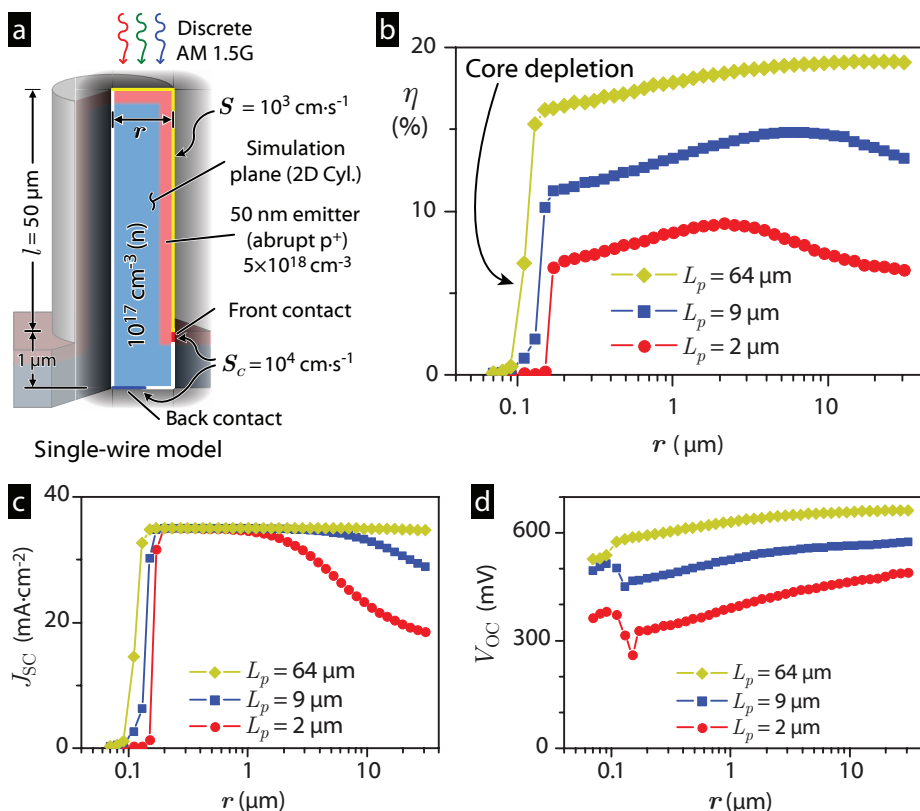


Figure 2.5. Effect of wire radius on simulated efficiency of radial-junction structures. (a) Schematic diagram of simulated structure. (b-d) Simulated η , V_{oc} , and J_{sc} as a function of wire radius (r) and minority-carrier diffusion length (L_p).

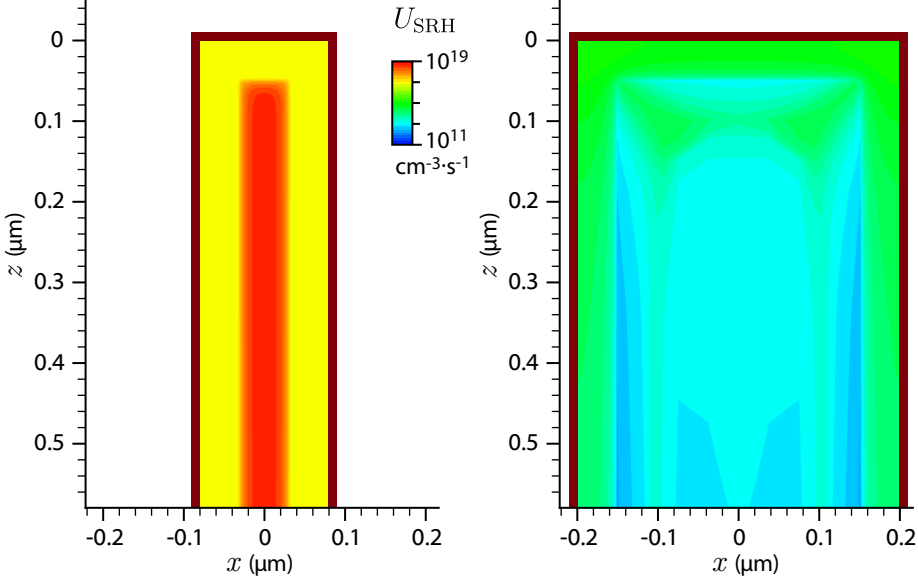


Figure 2.6. Recombination rates in depleted vs. nondepleted wires. Shockley-Read-Hall recombination (U_{SRH}) plotted for $L_p = 64 \mu\text{m}$ wires of 160 nm diameter (left, fully depleted) and 400 nm diameter (right, normal operation). Only the top of each wire is shown. The simulation planes have been mirrored about $x = 0$ to illustrate the full cross section of each wire.

$r = 90 \text{ nm}$ (depleted) and $r = 170 \text{ nm}$ (nondepleted). For the depleted wire, E_z was indeed very small throughout the entire length of the wire—requiring a log-scale plot to even be seen. In fact, the vertical electric field was smaller within the depleted wire’s core than it was within the nondepleted ‘quasi-neutral’ core of the larger-diameter wire. Furthermore, the depletion of the small-diameter wire led to a very low concentration of free electrons within the core ($n \leq 10^{14} \text{ cm}^{-3}$). These factors combined to effectively cut off the flow of electron drift, resulting in essentially zero electron current ($J_{n,z}$) reaching the base of the wire. This behavior can also be expressed in terms of recombination rates. Given the free-electron concentration n , as well as the rate of SRH recombination, [68, p. 309]

$$U_{\text{SRH}} = \frac{np - n_i^2}{\tau_p(n + n_1) + \tau_n(p + p_1)} \quad (2.4)$$

where here, $\tau_p = \tau_n = 5 \mu\text{s}$, and $n_1 \approx p_1 \approx n_i$; we can define an *effective electron recombination lifetime*,* $\mathcal{T}_{n,\text{eff}}$, as:

$$\mathcal{T}_{n,\text{eff}} = \frac{n}{U_{\text{SRH}}} \quad (2.5)$$

*Note that this definition neglects Auger recombination, which was not significant here.

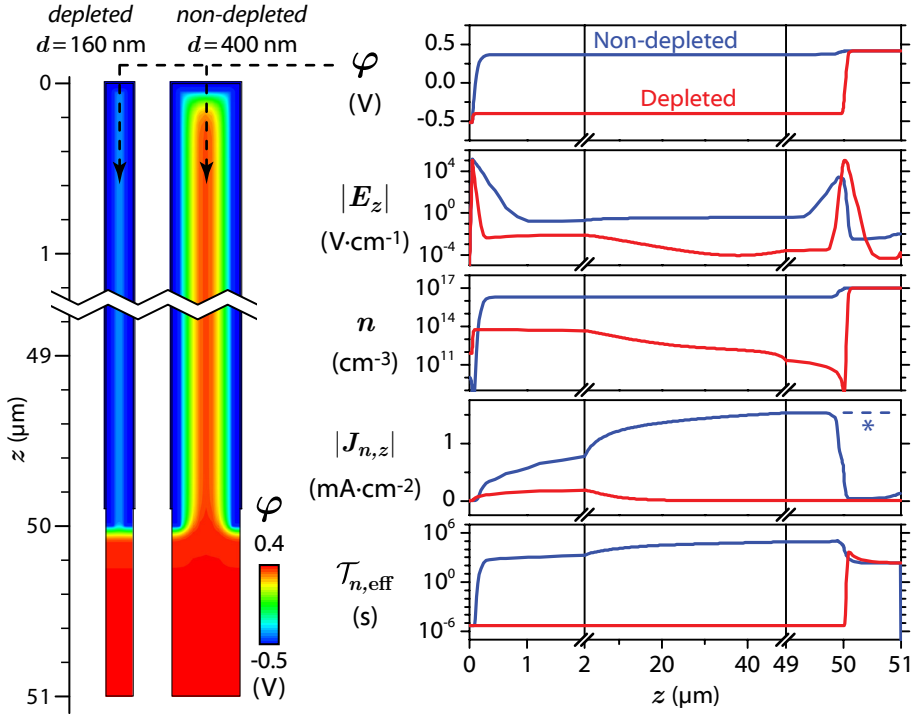


Figure 2.7. Physical state of the center of fully depleted vs. nondepleted radial p-n junction solar cells. **Left:** Electrostatic potential profiles (ϕ) for $L_p = 5 \mu\text{m}$ wire devices with 160 nm diameter (fully depleted) and 400 nm diameter (nondepleted). **Right:** Plots of electrostatic potential (ϕ), vertical electric field magnitude ($|E_z|$), free-electron concentration (n), vertical component of the electron current density ($J_{n,z}$), and effective electron recombination lifetime ($\mathcal{T}_{n,\text{eff}}$); at the center of the two simulated wires; as a function of axial position from the top of the wire (z). *Note: The decrease in $J_{n,z}$ for $z > 50 \mu\text{m}$ in the nondepleted wire is due to the expansion of the conduction channel, not a loss in total vertical current.

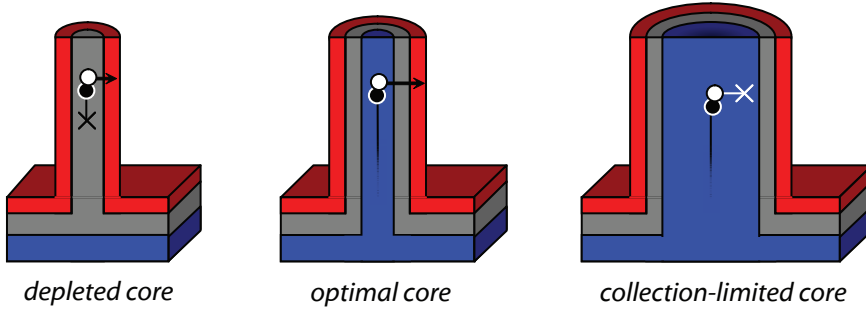


Figure 2.8. Modes of operation in radial p-n junction solar cells.

Examining the values of $\mathcal{T}_{n,\text{eff}}$, it is clear that the electrons recombine at the rate of minority carriers for the depleted wires, whereas they enjoy the practically infinite lifetime of majority carriers in the core of a nondepleted wire.

This analysis makes it clear why, for the wire structures studied here, the occurrence of core depletion is not tolerable in radial p-n junction solar cells. Interestingly, we note that the threshold for cutoff occurred at increasingly smaller wire radii as the minority-carrier lifetime was increased. We suspect this was because the extended carrier lifetimes enabled the steady-state population of photoexcited carriers to reach high enough concentrations to sustain drift current through an increasingly depleted core of the wire. This suggests that it may be possible to engineer a structure to operate under full core depletion by virtue of long minority-carrier lifetimes or perhaps under high-level injection. However for the device parameters considered, there seems to be little reason to attempt such a feat—unless the benefit could outweigh the inevitable scaling of dark current (and thus reduction in V_{oc}) that occurred as the wires were made smaller.

Examining the J_{sc} behavior of the simulated radial-junction structures, three modes of operation can be identified: Cutoff due to core depletion (at small wire radii), optimal collection (when $r \sim L$), and lifetime-limited collection (for $r \gtrsim L$). These modes of operation are conceptually illustrated in Figure 2.8. One more conclusion can be drawn from the results of this study: not only must the wire radius be properly chosen to obtain optimal efficiency for a given minority-carrier diffusion length, but also, variation in wire radius should be minimized for the multiwire devices. This is evident from examining the variation in V_{oc} as a function of r (Figure 2.5), and considering that wires will be parallel-connected in the proposed wire-array devices. A one-decade variation in r results in a simulated V_{oc} variation of ~ 100 mV. Just as series-connected solar cells are binned based on I_{sc} to improve photovoltaic module efficiency, each parallel-connected wire in a wire-array device should operate at similar V_{oc} . This will require that the wires are consistent both in electrical quality as well in physical dimensions.

2.3 Comprehensive optoelectronic model

The device physics model presented in the previous section provided a solid foundation on which a comprehensive optoelectronic modeling technique for Si microwire-array photovoltaics was built. Here, we present this modeling technique, and employ it to simulate the operation of a state-of-the-art Si microwire-array solar cell design.

The proposed Si microwire-array solar cell structure is shown in Figure 2.9. The evolution of this device geometry has been guided by years of experimental research and development of Si microwire-array photovoltaics, and is has been made possible only through the combined efforts of several researchers in addition to this author. These achievements have resulted in the following design features of the proposed microwire-array solar cell:

Ordered Si microwire arrays. The ordered arrays of Si microwires can be grown using the patterned VLS growth technique developed by Brendan Kayes, Michael Filler, and others, as described in section 1.5.1. [37]

Wafer-free, mechanically flexible structure. The proposed device structure differs from that considered in our prior modeling (Fig. 2.1) in that it does not call for an underlying growth wafer to provide mechanical support or electrical contact. This is made possible by the wire-array peel-off technique described by Kate Plass, Michael Filler, and others, as described in section 1.5.3. [42] Not only does this procedure yield flexible arrays of crystalline Si wires for photovoltaic applications, but as demonstrated by Joshua Spurgeon and colleagues, also allows the crystalline Si growth-wafers to be re-used for further production of wire arrays. [43]

Selectively formed, diffused radial p-n junctions. Chapter 5 describes a masked dopant diffusion procedure that has been developed to produce radial p-n junctions that do not extend to the bottom of each wire. This achievement enables peeled-off wire arrays to be contacted with simple top- and bottom-side contacts, as shown, without the risk of shunting the p-n junctions with the electrode material.

Embedded light-scattering particles. Adding dielectric light-scattering particles to the polymer infill material enhances the optical absorption of Si microwire arrays (as described in Chapter 3) by scattering the light passing between the wires into the Si material where it can be absorbed. This is particularly effective for normal-incidence illumination, where microwire arrays typically exhibit poorest absorption.

Metallic back contact. A metallic back contact not only provides high electrical conductivity, but also serves as an efficient optical back-reflector.

Antireflective coating. By depositing an antireflective coating onto the side-walls of the wires, in addition to the use of light-scattering particles and back-reflectors, microwire arrays have been engineered to achieve absorption comparable to wafer-based Si photovoltaics while using only 1/100th as much Si material; as described in Chapter 3.

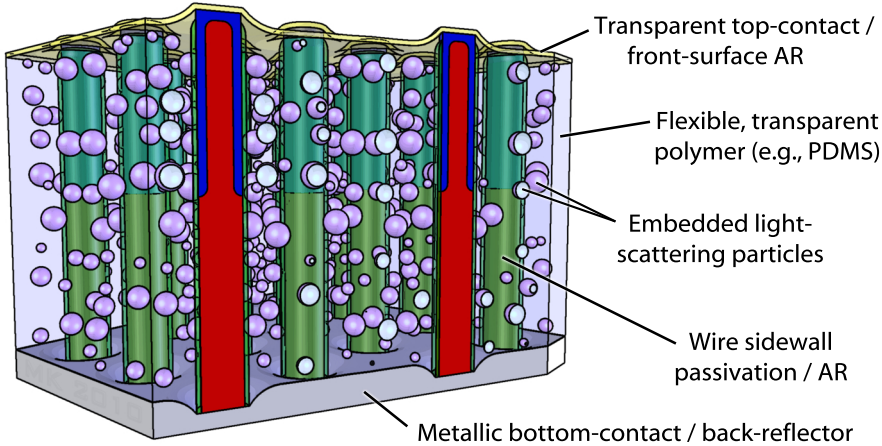


Figure 2.9. Advanced Si microwire-array solar cell geometry.

Surface passivation. The same surface coating that provides enhanced optical absorption as an antireflective coating, has also been used to achieve the lowest-reported surface recombination velocities to date for Si microwire photovoltaics, as described in Chapter 5.

Transparent top contact. Recent efforts led by Morgan Putnam have produced a high-yield technique that enables the tops of polymer-embedded wire-array solar cells to be contacted with a transparent conductive oxide (ITO).

The above design features have been combined in the proposed wire-array solar cell to yield a potentially low-cost, high-performance photovoltaic device. The dimensions and parameters of the simulated device were chosen based on two primary design objectives: that the structure absorb as much above-bandgap incident sunlight as possible, and that it collect nearly all excited photocarriers while operating at maximal photovoltaic potential. The experimental results of our optical studies (Chapter 3), our electrical characterization (Chapter 4), and our fabrication of single-wire solar cells (Chapter 5) were integral to the choice of parameter values for the simulations. The primary dimensions of the simulated wire-array device are listed in Table 2.2. We now turn our attention to developing a comprehensive optoelectronic model to predict the solar energy conversion efficiency of this device.

2.3.1 Optical absorption simulation

The photonic dimensions of Si microwire arrays lead to optical behavior that is not well described by a classical ray-optics approaches. Many phenomena affect the optical behavior of microwire-array structures, including scattering, diffraction, and waveguiding. Si *nanowire* arrays have recently received widespread

Table 2.2. Geometry of simulated wire-array solar cell.

Array pitch (p)	$7 \times 7 \text{ } \mu\text{m}$ (square-tiled)
Wire length (l)	$75 \text{ } \mu\text{m}$
Wire diameter (d)	$1.6 \text{ } \mu\text{m}$ (not including AR coating)
Geometric packing fraction (η_f)	4.1% ($\eta_f = \frac{\pi d^2}{4p^2}$)
Equivalent planar thickness (t_{eq})	$3.1 \text{ } \mu\text{m}$ ($t_{eq} = l \cdot \eta_f$)

attention, both experimentally and theoretically, resulting in a large body of work devoted to understanding their optical properties. Approaches have included finite-difference time-domain (FDTD) methods, [52, 55] finite-element frequency-domain methods, [51, 53, 54, 56, 57] and scattering theory. [73, 74] Numerous freely available as well as commercial software solutions are available to implement these methods. In fact, Sentaurus TCAD includes a variety of robust optical absorption models, including the transfer-matrix method (TMM), ray-tracing, and FDTD—in addition to the simple Beer-Lambert absorption model we have employed up to this point. Here, we have employed the commercial FDTD simulation software *FDTD Solutions* (Lumerical, version 6.5) to perform three-dimensional simulations of the interaction of sunlight with the proposed Si microwire-array solar cell. Briefly, this method iteratively calculates the full-field (\vec{E}, \vec{H}) solutions to Maxwell’s equations in the time domain, at each point on a three-dimensional simulation grid.

The optical simulation geometry is depicted in Figure 2.10. By placing periodic (or Bloch)* boundary conditions in the x and y directions, the simulations carried out within this unit cell effectively modeled the periodic square-array wire structure from Figure 2.9. The back contact was modeled as a perfect metallic boundary condition for simplicity (although some losses would be expected at a real metal back-reflector). The antireflective coating consisted of a uniformly thick (80 nm) SiN_x layer along the sidewalls of the wires, and the infill material consisted of the polymer PDMS. The light-scattering particles were implemented as randomly sized Al_2O_3 spheres (0.2–1.0 μm in diameter), randomly distributed within the lower 50 μm of the array, at a density of 400 spheres per unit cell.† A slight curvature (as depicted) was assumed for the top surface of the PDMS infill, mimicking an experimentally observed morphology, and the transparent conductive top contact material consisted of 60 nm ITO. Table 2.3 lists the optical constants that were used to model each material within the structure. The simulation volume was bounded above by a perfectly matched layer (PML), allowing reflected light to escape the simulation volume. A plane

*Bloch boundary conditions permitted excitation at off-normal incidence angles, which have not been presented here. Periodic boundary conditions were used for normal-incidence simulations. Symmetry was applied to quarter the simulation volume at normal incidence, or to halve the simulation volume at single tilt angles of incidence.

†The spheres were randomly positioned by a greedy algorithm that prevented them from overlapping with one another or other non-PDMS regions (but allowed them to span the boundary of the unit cell). Identical particle placement was used for all simulations.

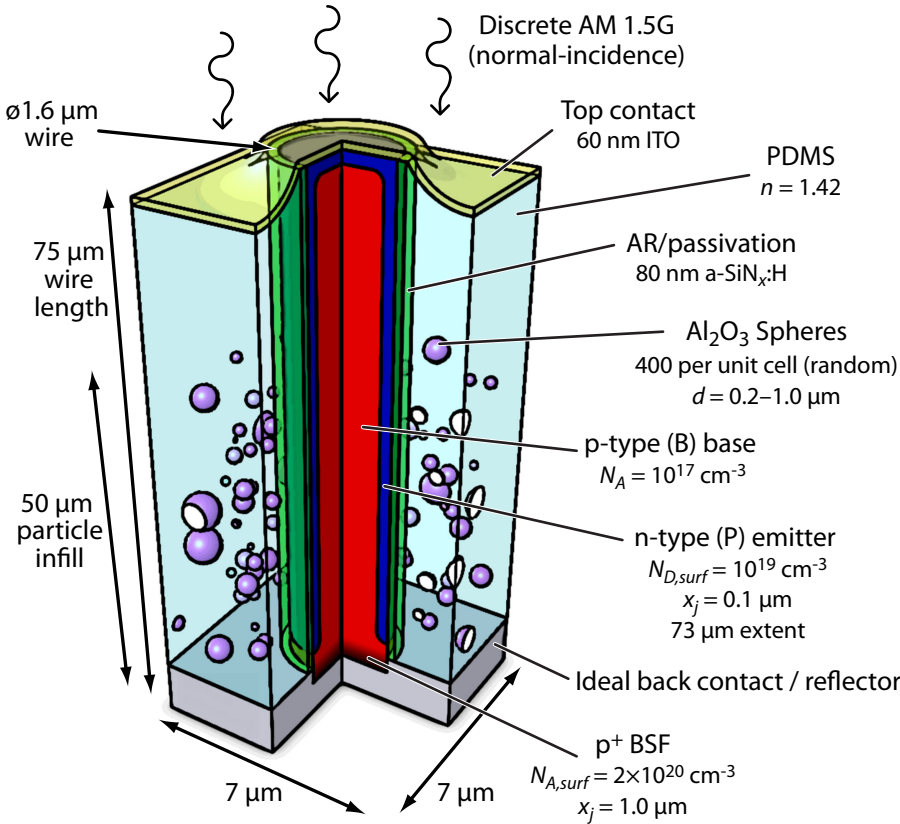


Figure 2.10. Schematic diagram of the wire-array unit cell geometry employed to simulate the device proposed in Figure 2.9. *Diagram is not drawn to scale.*

wave source was placed several microns above the top surface of the wire array, and a reflection monitor was placed above this source to record the total power reflected by the wire array (R). Monitors were also placed to record the refractive index and steady-state electric field phasors throughout the simulation volume.

Each simulation was performed using $1 \text{ mW}\cdot\text{cm}^{-2}$ of quasi-monochromatic (i.e., single-wavelength) illumination at normal incidence. To simulate sunlight, the above-bandgap AM 1.5G [15] spectrum was divided into discrete (monochromatic) ‘beams,’ using an algorithm that preserved the total incident photon flux within each beam’s spectral range (see Appendix B.11), and a separate simulation was performed for each wavelength. Computational resources limited the number of simulations that could be processed; thus, seven discrete wavelengths were chosen to span the solar spectrum ($\lambda = 450, 550, \dots, 1050 \text{ nm}$) and the results of each simulation were weighted to yield the same equivalent source photocurrent ($43.5 \text{ mA}\cdot\text{cm}^{-2}$) and similar spectral power density as the $\lambda = 280-1100 \text{ nm}$ AM 1.5G spectrum, as shown in Figure 2.11. All simulation monitors

Table 2.3. Optical properties used for FDTD simulations.

Material	Optical properties
Si	Aspnes [75]
SiN _x	Ellipsometry (see Appendix A.1)
PDMS	Fixed index, $n = 1.42$
ITO	Woollam [76]
Al ₂ O ₃	Palik [77]
Back contact	Metallic boundary condition

employed partial spectral averaging ($\Delta\lambda \sim 25$ nm) to suppress coherence artifacts (see section B.4.1), and an auto shutoff criteria was used to ensure that each simulation proceeded until all field intensities had decayed to 10^{-6} times the initial value. A variable-pitch simulation grid was used, with a minimum of ~ 10 grid points per material wavelength (λ/n).

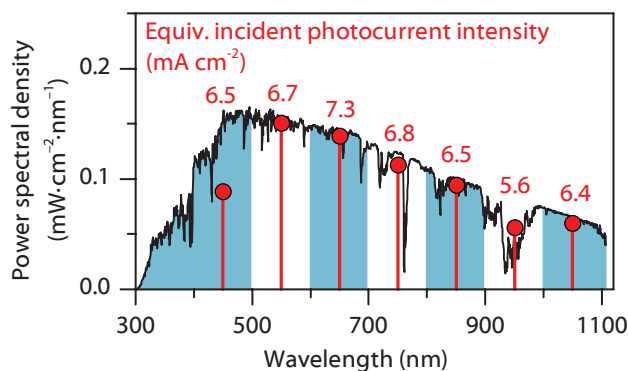


Figure 2.11. Source intensities used to approximate AM 1.5G ($100 \text{ mW}\cdot\text{cm}^{-2}$) illumination with single-wavelength simulations.

After each simulation, the integrated Poynting power flowing through the reflection monitor was extracted in order to determine the absorption, $A = 1 - R$, as plotted in Figure 2.12. Integrating this absorption across the solar spectrum yields a photoabsorption current of $J_{\text{abs}} = 32.8 \text{ mA}\cdot\text{cm}^{-2}$, which is slightly below that which we experimentally observed in similar wire-array structures (described in Chapter 3). This discrepancy was primarily due to the fact that the FDTD simulations modeled an ITO top contact, which slightly increased the front-surface reflectance losses. The experimentally studied structures had no such ITO layer.

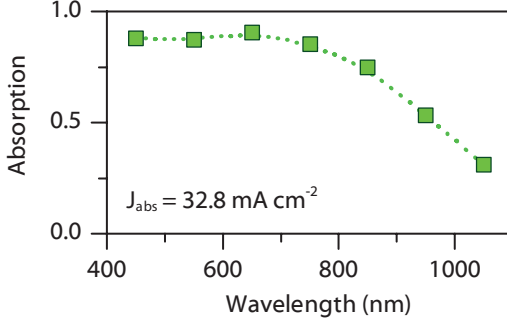


Figure 2.12. Simulated absorption of the Si microwire-array solar cell.

2.3.2 Extracting optical generation profiles

In addition to calculating the overall absorption of light, the FDTD simulations can be used to determine the optical generation rate within the wires, G_{opt} , thus providing the necessary input for device-physics modeling of photovoltaic J - V behavior. In general, semiconductors can act both as absorbers and emitters of radiation, requiring that device physics simulations be coupled with optical simulations. However for Si photovoltaics, re-radiation of light is negligible due to the material's indirect bandgap and trap-dominated recombination.

The process of fundamental optical absorption in a semiconductor transfers energy from a propagating electromagnetic wave to excite a free electron-hole pair within the semiconductor band structure; a transfer which is quantized by the photon energy, $E_{\text{ph}} = \frac{hc}{\lambda}$, where h is Planck's constant and c is the speed of light. Thus in the absence of other processes, the photogeneration rate can be determined from the divergence of Poynting vector $\vec{P} = \vec{E} \times \vec{H}$. Under steady-state harmonic conditions, this can be expressed in terms of the electric field magnitude $|\vec{E}|$ and the imaginary part of the material's permittivity, $\epsilon'' = 2nk$:

$$G_{\text{opt}} = \frac{\Re\{\nabla \cdot \vec{P}\}}{2E_{\text{ph}}} = \frac{\pi\epsilon'' |\vec{E}|^2}{h} \quad (2.6)$$

Throughout the three-dimensional FDTD simulation volume, monitors recorded the steady-state electromagnetic field phasor \vec{E} as well as the complex refractive index, allowing G_{opt} to be calculated at each grid point.

Whereas the FDTD simulations (Lumerical) operated on a three-dimensional rectangular grid, our device physics model (Sentaurus) operated on a two-dimensional (cylindrical) finite-element mesh. Although Sentaurus was capable of simulating a device in three dimensions, it was suspected that this would not provide insight worthy of the increased computational complexity. The three-dimensional photogeneration profiles calculated by FDTD were not strictly cylindrically symmetric; however, the fourfold symmetry of the array (combined with the randomization caused by the light-scattering particles) ensured that the absorption was never concentrated more strongly on one side of the wire than the

other. Thus, the three-dimensional optical generation profiles, $G_{\text{opt}}(x, y, z)$ were ‘flattened’ to a two-dimensional cylindrical grid by numerical interpolation and integration:

$$G_{\text{opt}}(r, z) = \frac{\int_0^{2\pi} r \cdot G_{\text{opt}}(r \cos \theta, r \sin \theta, z) d\theta}{2\pi r} \quad (2.7)$$

This flattening procedure conserved the total photogeneration current within the device model; so that the resulting absorption, when integrated throughout the wire volume, agreed well with the absorption inferred from the FDTD reflection monitor data. As a final step, the photogeneration profile was interpolated onto the finite-element mesh for the device physics simulations.*

Figure 2.13 plots the vertical cross-section of the photogeneration profiles within the Si wire in response to $1 \text{ mW}\cdot\text{cm}^{-2}$ illumination at each simulated wavelength. These profiles have been flattened as described above, and mirrored about $r = 0$ for ease of viewing. The generation profiles were concentrated near the center of the wire, as a result of the waveguiding and focusing effect of the cylindrical geometry. Prior simulations performed at higher photon energies (e.g., $\lambda = 400 \text{ nm}$) have shown that the absorption profiles become concentrated nearer the wire surface, due to the shorter extinction length at these wavelengths. However, the large dimensions of the proposed wire-array solar cell prevented us from simulating ultraviolet wavelengths with available computational resources.

2.3.3 Device physics simulation

Using the optical generation profiles calculated above, device physics simulations were performed for the device structure depicted in Figure 2.14. This model was derived from our prior work (section 2.2.3).

The material parameters for the simulated structure were selected based on recent experimental measurements performed on single-wire solar cells (see Chapter 5). The doping levels and junction profiles were inferred from four-point I - V measurements as well as spreading resistance measurements of planar control wafers. The base doping was $N_A = 10^{17} \text{ cm}^{-3}$, and the emitter surface concentration was $N_{D,\text{surf}} = 10^{19} \text{ cm}^{-3}$ with a junction depth of $x_j = 100 \text{ nm}$. The simulated structures were assumed to have radial p-n junctions extending throughout all but the bottommost $2 \text{ }\mu\text{m}$ of each wire. Recombination parameters were conservatively chosen based on the single-wire experiments: $S = 70 \text{ cm}\cdot\text{s}^{-1}$ at the wire sidewalls and $\tau = 500 \text{ ns}$ throughout the wire. A standard surface recombination velocity of $S = 10^7 \text{ cm}\cdot\text{s}^{-1}$ was assumed for the (ohmic) top and bottom contacts. Our measurements actually indicated a surprisingly low effective S at the bottom (base-region) contacts to single-wire solar cells. We hypothesize that these contacts were effectively passivated by a p^+ back-surface field, which would have formed by thermal B diffusion from the p-type growth substrates ($\rho < 0.001 \text{ }\Omega\cdot\text{cm}$) during the 2 hr thermal oxidation ($1100 \text{ }^\circ\text{C}$) used to fabricate these devices. Accordingly, the modeled device structure includes a back-surface field with $N_{A,\text{surf}} = 2 \times 10^{20} \text{ cm}^{-3}$ and $x_j = 1 \text{ }\mu\text{m}$.

*Details of this procedure are presented in Appendix B.

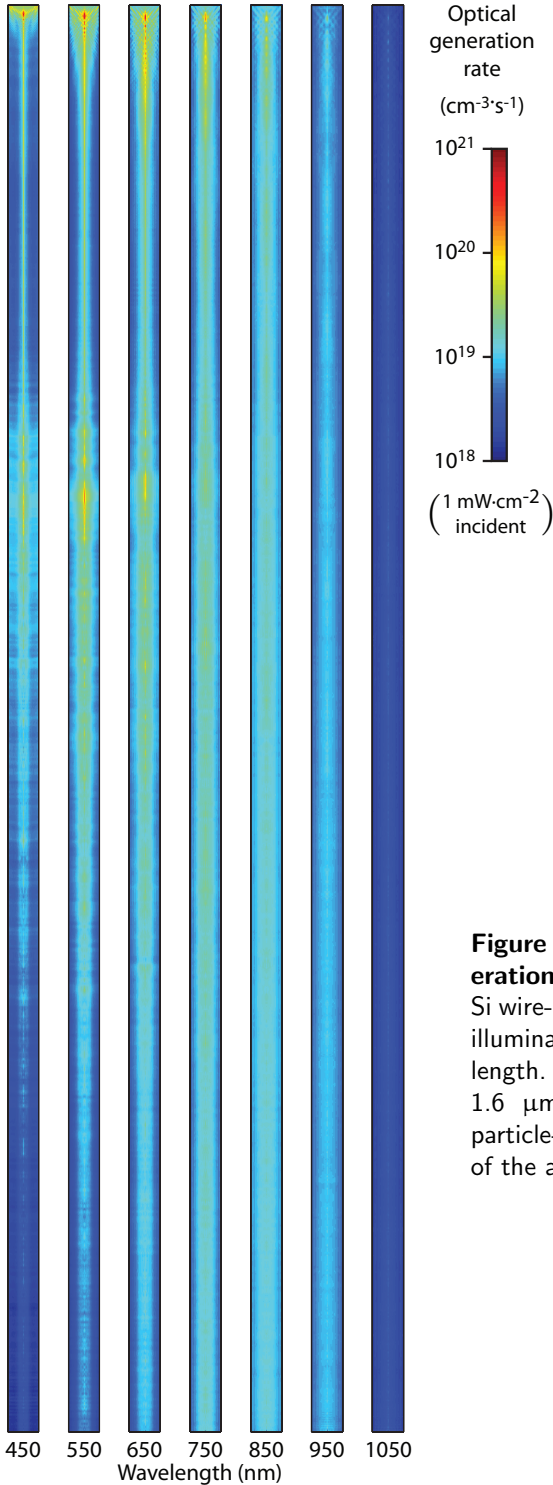


Figure 2.13. Simulated optical generation profiles within the wires of the Si wire-array solar cell under $1 \text{ mW}\cdot\text{cm}^{-2}$ illumination at each simulated wavelength. The wires are $75 \mu\text{m}$ in length, $1.6 \mu\text{m}$ in diameter, and the Al_2O_3 particle-infill occupies the lower $50 \mu\text{m}$ of the array.

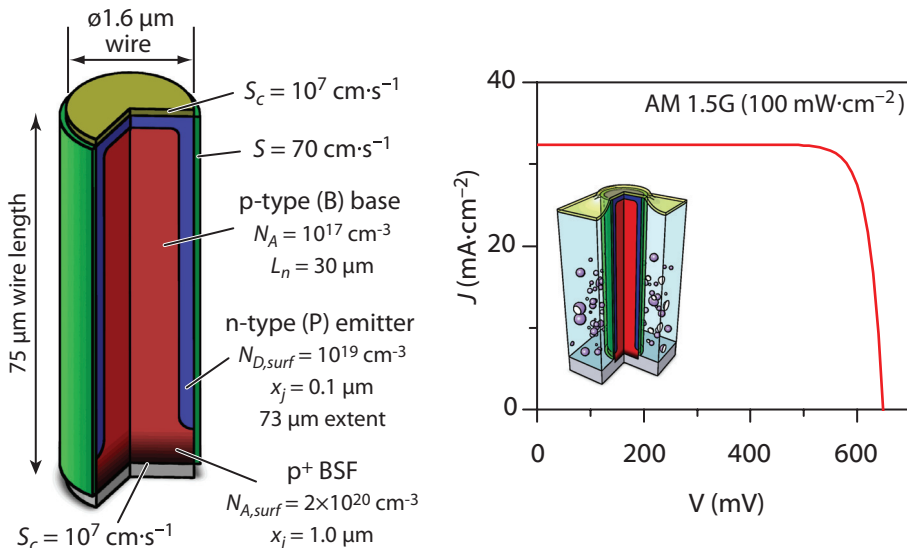


Figure 2.14. Simulated terminal behavior of wire-array solar cell. Left: Schematic diagram of the cylindrical model used for device-physics simulations. **Right:** Simulated J – V behavior under one-sun illumination.

The terminal I – V characteristics were simulated under each monochromatic illumination profile as well as the combined AM 1.5G illumination profile. The simulated current magnitude was normalized to the $49 \mu\text{m}^2$ area of the wire-array unit cell to determine current density and photovoltaic efficiency of the wire array, as plotted in Figure 2.14 (right). The operating parameters of the simulated device are listed in Table 2.4. At each monochromatic simulation wavelength, the structure exhibited $>99\%$ carrier collection efficiency; thus, J_{sc} was limited solely by incomplete optical absorption of sunlight by the Si wires. Maximizing absorption (and minimizing losses due to front-surface reflection or parasitic absorption) will remain a key requirement for the design of efficient Si wire-array solar cells, and has the potential to significantly increase efficiencies significantly above that simulated here.

Table 2.4. Simulated performance of the Si wire-array solar cell.

Open-circuit voltage	649 mV
Short-circuit current density	$32.4 \text{ mA}\cdot\text{cm}^{-2}$
Fill factor	83%
Efficiency	17.4%

2.4 Discussion

The development of an optoelectronic model has led to an encouraging result: Si microwire-array solar cells are predicted to reach efficiencies exceeding 17%. This performance was simulated using *experimentally measured* values for the most important parameters to photovoltaic performance—namely, minority-carrier diffusion length and surface recombination velocity. While our model has neglected to consider several key challenges facing real solar cells, including contact resistance, grid shading, and yield loss; the results nonetheless leave little doubt as to the underlying capability of Si microwire photovoltaics to reach high solar energy conversion efficiencies. The remainder of this thesis will highlight progress that has been made toward realizing these structures, and will ultimately culminate with an experimental affirmation of the promising potential of Si microwire photovoltaics.

2.4.1 Future work

We can identify several opportunities to improve the scope and utility of the optoelectronic model presented above, including:

Dopant-induced lifetime degradation. In this initial modeling work, we assumed that bulk recombination would be dominated solely by defects inherent to VLS growth (e.g., residual catalyst metal impurities). While this is likely reasonable for Au-catalyzed wires, the experiments performed during the course of this thesis work have placed an ever-increasing lower limit on minority-carrier lifetimes in Cu-catalyzed wires. Thus far, our modeling has assumed only conservative lifetime values inferred from these measurements. In order to consider longer “VLS-limited” lifetimes, one must also consider recombination due to dopants—particularly in heavily doped regions such as the emitter layer. [60, 78, 79] Dopant-dependent SRH lifetimes can be implemented in Sentaurus using, e.g., the Scharfetter model [68, p. 311] or an external profile grid (see Appendix B).

Improved recombination models. The above simulations used a simple SRH recombination model based on a fixed mid-gap trap level that was assumed to have equal electron and hole recombination lifetimes. Further insight could be gained by understanding and modeling the actual recombination processes in VLS-grown Si wires. For example, our knowledge of the Au concentration in our Au-catalyzed wires [80], combined with literature values for the energy levels and capture cross-sections of Au traps in Si, enabled us to model the bulk trap activity and electrostatics of Au-catalyzed wires (see section A.3.2). However, modeling the trap electrostatics of Cu-catalyzed wires has not been attempted, in part because the Cu concentration in our wires is not known, but also because the recombination activity of Cu impurities can vary greatly depending on device processing steps (as discussed in section 4.6.1). Nonetheless, an improved understanding of the recombination processes (both bulk and surface) in

Cu-catalyzed wires will increase the utility of the model, particularly in cases of high-level injection.

Expanded optical modeling. FDTD simulations provided the optical absorption profiles that were necessary to obtain our first realistic estimate of the performance of wire-array solar cells. However, computational resources limited our simulations to consider only normal-incidence illumination of a single device structure, using seven discrete wavelengths to approximate AM 1.5G sunlight. Future modeling efforts will benefit from considering off-normal incidence angles and from varying the device structure to obtain optimal absorption. Performing such simulations with the FDTD method, although not infeasible, would likely require more computer power than presently available in our labs. Alternatively, other simplified approaches (such as raytracing) may prove suitably accurate for photovoltaics simulations. Sentaurus includes a number of internal optical solvers, including raytracing and the beam propagation method, which may prove useful in future studies.

Multi-wire simulations. A particularly important challenge for the design of wire-array photovoltaics will be to understand how variations in dimensions, placement, or quality of the wires will affect the ensemble performance of the array. From an electrical standpoint, this can be approached in a straightforward manner: each wire is simply an independent, parallel-connected circuit element. This permits each wire's I - V characteristics can be calculated independently, then summed to determine the performance of the ensemble device.* From an optical standpoint, however, the problem is greatly complicated because of multiple scattering within the array: the absorption of each wire is affected by its surroundings. For example, if a single wire is missing from an otherwise perfect array, our intuition suggests that some (but not all) light reaching its intended location would instead be scattered to adjacent wires and absorbed. Quantifying the sensitivity of device efficiency to variations in wire yield or geometry will thus help establish fidelity tolerances for wire-array growth.

Sensitivity and loss analysis. In addition to numerical optimization, sensitivity and loss analysis will be instrumental in designing future wire-array solar cells by identifying the key parameters that are most critical to performance. Such calculations could be used, for example, to prioritize research on the process steps that are more likely to produce higher-efficiency devices, or to establish strategic checkpoints in the fabrication process to ensure that the key parameters fall within range. Fossum [60] presented a one-dimensional model for Si solar cells that he used to identify the sources of recombination by device region (i.e., front surface, emitter, depletion region, base, and back surface). This was used to identify routes to higher efficiency, for example, by reducing the doping and thickness of the emitter region.

*This motivated our conclusion in section 2.2.5 that, neglecting optical considerations, wires should be of similar radius in a radial-junction wire-array device.

Optical absorption in Si wire arrays

The most fundamental, yet conceptually simple requirement of an efficient solar cell, is that it absorb nearly all incident sunlight. A perfect solar cell would appear completely black. However the broad spectral distribution of sunlight, combined with the wide range of angles at which it strikes the earth's surface, poses a formidable challenge for the design of solar cells with optimal light absorption properties.

The pursuit of ideal absorption has spawned the diverse field of photovoltaics engineering known as *light-trapping*, and is integral to the design of every modern solar cell. This task may seem particularly daunting for Si microwire-array solar cells because of the large voids of space between the wires, through which light might pass without striking any photovoltaic material. In this chapter, we will show that the principles of light-trapping can be applied to Si wire arrays to yield a novel structure that not only overcomes the shortcomings of sparsely packed photovoltaic material, but which provides an unexpected and fundamentally advantageous absorption enhancement over classical light-trapping in planar materials.

3.1 Introduction

The study of optical absorption in Si wire arrays necessitates a discussion of sunlight and how it is absorbed by semiconductor solar cells to produce photovoltaic energy. This section introduces the concepts of optical absorption, describes how it can be experimentally observed, and discusses the fundamental optical absorption limits of planar vs. wire-array solar cells.

3.1.1 Sunlight and fundamental optical absorption in semiconductors

When light is absorbed in a semiconductor solar cell, its energy is transferred to excite free carriers (electron-hole pairs) within the semiconductor band structure in a process known as *fundamental* optical absorption. The photoexcited free carriers can in turn be separated by a junction and collected as electrical current at the terminals of the device, providing photovoltaic energy to the external circuit. The fundamental absorption process is quantized by the photon energy, $E_{\text{ph}} = \frac{hc}{\lambda}$, where h is Planck's constant, c is the speed of light, and λ is the free-space wavelength of the illumination. The absorption of each photon produces a

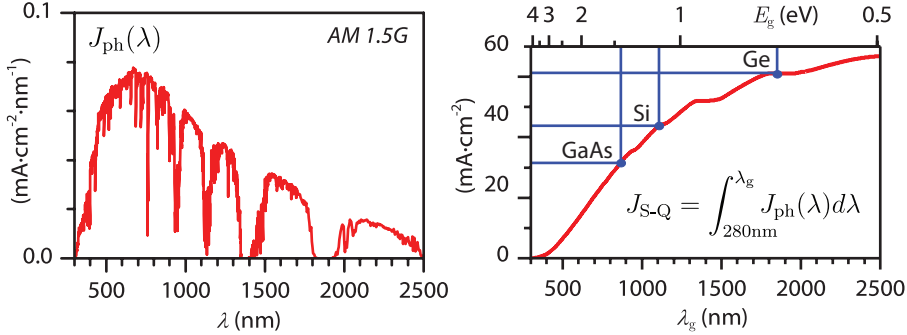


Figure 3.1. The solar spectrum and the limiting J_{sc} of semiconductor solar cells. **Left:** Equivalent spectral photocurrent density, $J_{ph}(\lambda)$, for the AM 1.5G reference spectrum ($100 \text{ mW}\cdot\text{cm}^{-2}$). [15] **Right:** Limiting short-circuit current density of semiconductor p-n junction solar cells as a function of bandgap energy ($E_g = \frac{hc}{\lambda_g}$), under the Shockley-Queisser detailed balance limit. [16]

single electron-hole pair.* Thus for semiconductor solar cells, the most relevant property of sunlight is not necessarily the amount of power it contains, but rather the number of incident photons that can be absorbed. For this reason, it is convenient to consider the *equivalent photocurrent density* of sunlight, $J_{ph} = q\Gamma$, where q is the electron charge and Γ is the incident photon flux. The equivalent photocurrent density spectrum, $J_{ph}(\lambda)$, corresponding to the AM 1.5G reference spectrum is plotted in figure 3.1 (left).

Integrating the $J_{ph}(\lambda)$ spectrum throughout all wavelengths of the solar spectrum ($\lambda = 280\text{--}4000 \text{ nm}$) yields $\sim 69 \text{ mA}\cdot\text{cm}^{-2}$, the maximal short-circuit current density (J_{sc}) that a 100%-absorbing semiconductor solar cell could produce under AM 1.5G illumination. In real solar cells, the obtainable J_{sc} is further reduced by incomplete absorption of sunlight. We define this value as the *limiting short-circuit current density*, J_{abs} :

$$J_{abs} = \int \Gamma(\lambda) \cdot A(\lambda) d\lambda \quad (3.1)$$

where $A(\lambda)$ is the optical absorption spectrum of the device.

To first order, the optical absorption of any semiconductor can be approximated as 100% for above-bandgap photon energies ($E_{ph} > E_g$) and 0% for below-bandgap photon energies. This approximation is employed by the well-known Shockley-Queisser detailed balance limit of solar cell efficiency to calculate the theoretical limiting short-circuit current density, J_{S-Q} , as well as

*This is true for fundamental band-to-band optical absorption process in semiconductor solar cells. There exist numerous other absorption processes that can produce multiple free-carrier pairs from each single photon (or vice versa), as well as parasitic absorption processes that absorb optical energy without exciting any free carriers. However, these absorption processes are extremely weak in intrinsic Si and can safely be ignored here. The relevant non-fundamental and extrinsic absorption processes (e.g., parasitic absorption and impurity-band absorption) are discussed later in this chapter.

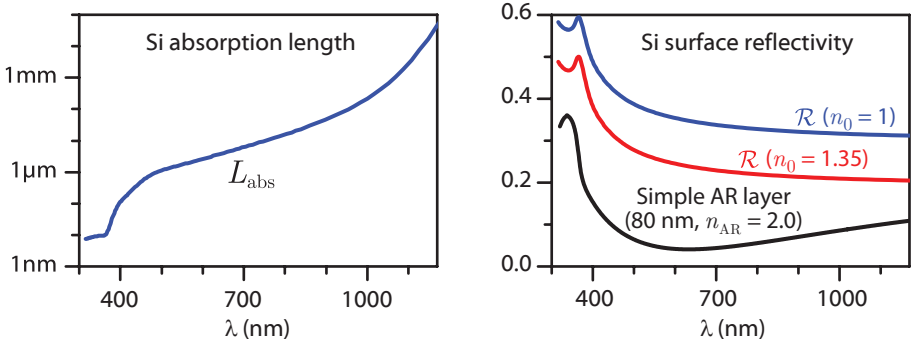


Figure 3.2. Absorption length and front-surface reflectivity of silicon. Reflectance (\mathcal{R}) is plotted for planar Si surfaces in a surrounding medium of refractive index of $n_0 = 1.0$ (i.e., in air) or $n_0 = 1.35$ (i.e., immersed/encapsulated in a material like H_2O or PDMS). Also plotted is the front surface reflectivity (in air) of Si coated with an 80 nm thick antireflective (AR) layer of $n = 2.0$. Calculations based on tabulated optical constants of Si. [75]

the thermodynamic efficiency limit, for single-homojunction semiconductor solar cell. [16] Figure 3.1 (right) plots $J_{\text{S-Q}}$ as a function of the semiconductor bandgap, showing the values for GaAs, Si, and Ge. The Shockley-Queisser limit predicts that optimal semiconductor bandgap for a single-homojunction solar cell, in the absence of material-specific processes (such as non-radiative recombination), is very near that of Si (~ 1.1 eV). Here, a value of $E_g = 1.12$ eV is assumed for Si, which in conjunction with the AM 1.5G spectrum ($100 \text{ mW}\cdot\text{cm}^{-2}$), yields a value of $J_{\text{S-Q}} \approx 44 \text{ mA}\cdot\text{cm}^{-2}$. This approach provides a reasonable approximation of the limiting J_{abs} for an ideal semiconductor solar cell: The present world record for Si photovoltaic efficiency has achieved $J_{\text{sc}} = 42.0 \text{ mA}\cdot\text{cm}^{-2}$. [19]

In reality, the absorption of light in semiconductors is not as simple as the approximation of the Shockley-Queisser limit. Rather, the probability that a photon will be absorbed as it passes through matter depends strongly on its energy and on the band structure of the semiconductor. Optical absorption follows the Beer-Lambert law, which describes the exponential decay in light intensity along its propagation path in a material:

$$I_{\text{ph}}(\lambda, x) = I_{\text{ph}}(\lambda, x = 0)e^{-\alpha(\lambda)x} \quad (3.2)$$

where the *absorption coefficient*, $\alpha(\lambda)$, describes the rate of attenuation within the material. The absorption coefficient can also be expressed as an *absorption length*, $L_{\text{abs}} = 1/\alpha$; which is the thickness of material through which light can propagate before being attenuated to $1/e$ ($\sim 37\%$) its original intensity. This and serves as a convenient indicator of the approximate material thickness (or more accurately, optical path length) required to absorb light. The L_{abs} of Si is plotted in Figure 3.2. This figure also plots the front-surface reflectivity of Si surfaces, which is discussed in greater detail in section 3.1.3.

3.1.2 Observing optical absorption

All optical absorption processes involve the conversion of incident light into some other form of energy, such as heat or the excitation of free-carriers in a semiconductor solar cell. Thus there are two fundamental ways to observe optical absorption in solar cells: directly, by measuring the energy that is absorbed (i.e., the photovoltaic response of the cell), or indirectly, by measuring the energy that is *not* absorbed (i.e., the light reflected and transmitted from the cell). We will refer to the latter as “optical” measurements, and the former as “electrical” measurements (although there exist numerous non-electrical means by which to directly observe absorption in semiconductors, such as photoluminescence or calorimetry). Our study employs both optical and electrical absorption measurement techniques.

Electrical measurement techniques provide accurate means of quantifying the useful optical absorption in photovoltaic devices, particularly in the presence of parasitic absorption processes. For example, at wavelengths near and beyond the Si band-edge ($\lambda > 1 \mu\text{m}$), the rate of free-carrier absorption can exceed that of fundamental absorption in heavily doped Si. [81] This effect increases the extinction rate within the material, but does not excite electron-hole pairs (and in fact, dissipates energy that might otherwise have been useful to the solar cell). Electrical absorption measurements via photocurrent or photoconductivity only detect the generation of electron-hole pairs, thus providing a more accurate gauge of useful absorption at these wavelengths. In fact, such techniques have been used to measure values of the band-to-band absorption coefficient of Si as low as $\alpha = 10^{-7} \text{ cm}^{-1}$ (at room temperature), four orders of magnitude lower than values that had been measured using optical measurement techniques. [82] However, electrical measurements can easily underestimate the true absorption of a solar cell, because they do not count the energy that is successfully absorbed but then lost due to recombination. Thus, these techniques are best suited for solar cells with near-unity carrier collection efficiency, and generally provide a lower limit on the true optical absorption of a solar cell. In this study, electrical absorption measurements were performed by operating Si wire arrays as electrodes in a photoelectrochemical cell, as presented in section 3.5.

Optical measurement techniques provide a straightforward and widely used means of determining the optical absorption of virtually any material, based directly on the principal of energy conservation: any light that is not absorbed by an object must be either reflected or transmitted from it. Absorption (A) is thus determined by measuring the reflection (R) and transmission (T):

$$A = 1 - R - T \tag{3.3}$$

Accurate optical absorption measurements require meticulous photon bookkeeping, so to speak, in that the technique will typically overestimate true absorption unless *all* reflected and transmitted photons are precisely accounted for in the measurements. Figure 3.3 depicts how the hemispheres of reflected and trans-

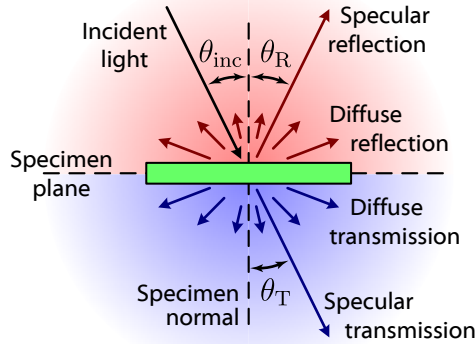


Figure 3.3. Schematic diagram of optical transmission and reflection.

mitted light were defined with respect to the specimen plane for this study.* Reflected and transmitted light can be classified as either *specular* or *diffuse*. Specular reflection and transmission occur at smooth surfaces (i.e., $< \lambda/10$ surface roughness) such as polished Si wafers, and preserve the collimation and angle of the reflected and transmitted beams (unless refracted by non-parallel interfaces). Rough or textured surfaces scatter the incident light and cause diffuse behavior, which we define to include all non-specular light. A special case of ideal diffusivity occurs at randomly textured surfaces, and is known as *Lambertian* behavior. Regardless of incidence angle (θ_{inc}), Lambertian surfaces distribute the intensity of reflected or transmitted light as:

$$I(\theta) \propto I_{\text{inc}} \cos(\theta) \quad (3.4)$$

In this study, disordered films of randomly oriented Si wires exhibited Lambertian behavior (section 3.3.1). However, arrays of ordered, vertically oriented Si wires exhibited highly non-Lambertian behavior due to diffraction (section 3.3.2). The wide range of specular and diffuse behaviors encountered in this study necessitated the use of an integrating sphere to accurately measure the total hemispherical transmission and reflection of each specimen (section 3.2).

3.1.3 Absorption and light-trapping in planar solar cells

Virtually all solar cells produced today are of a planar geometry; that is, composed of a continuous sheet of light-absorbing material with approximately uniform thickness, t , over their entire area. Conventional Si wafer-based solar cells have thicknesses of 200–500 μm , whereas a large class of cells known as *thin-film* solar cells have thickness of several microns or less. Regardless of thickness, the maximization of optical absorption plays a key role in the design of all solar cells,

*Reflection and transmission need not necessarily be differentiated by the specimen plane, so long as together they deterministically account for all non-absorbed light.

and has resulted in a number of widely used light-trapping techniques. Here, we consider two key limiting cases for optical absorption in planar solar cells: Specular absorption, in which the surfaces are ideally smooth, and ergodic light-trapping, in which the surfaces are randomly textured so as to fully randomize the direction of light within the material. These absorption configurations are depicted in Figure 3.4.

Specular absorption. The optical properties of planar structures with specular surfaces are determined by reflection and refraction at each interface, by absorption within each material, and depending on the thickness of the layer and coherence of the illumination, by Fabry-Perot interference effects. Figure 3.4 (left) depicts the multiple reflections experienced by a beam incident on a simple planar slab of absorbing material. Let us first consider the case of normal-incidence illumination and ignore interference effects.

When light is normally incident on a material interface, the power is reflected and transmitted with coefficients of reflectance (\mathcal{R}) and transmittance (\mathcal{T}):

$$\mathcal{R} = \left(\frac{n_0 - n}{n_0 + n} \right)^2$$

$$\mathcal{T} = 1 - \mathcal{R} = \frac{4n_0n}{(n_0 + n)^2} \quad (3.5)$$

where n is the (complex*) refractive index of the material on which it is incident, and n_0 is the refractive index of the surrounding media. From (3.5), the reflection coefficient at the front (\mathcal{R}_f) and back (\mathcal{R}_b) of a planar solar cell can be calculated. Crystalline Si exhibits a front surface reflectivity of $\mathcal{R}_f = 34\% - 50\%$ at visible wavelengths (see Figure 3.2). As depicted in Figure 3.4, the front surface splits an incident beam of photocurrent I_0 into a reflected beam of photocurrent $\mathcal{R}_f I_0$, and a transmitted beam of photocurrent $(1 - \mathcal{R}_f)I_0$ that is then attenuated by $e^{-\alpha t}$ due to absorption as it traverses the device. A similar reflection and transmission occur at the rear surface, and again upon each subsequent traversal of the device, eventually leading to an infinite series of contributions to the reflected, transmitted, and absorbed power.

For the simple case of Si in air ($n_0 = 1$), then $\mathcal{R}_f = \mathcal{R}_b = \mathcal{R}$, and the series of reflected and transmitted beams sum to:

$$R = \frac{\mathcal{R} + (\mathcal{R} - 2\mathcal{R}^2)e^{-2\alpha t}}{1 - \mathcal{R}^2 e^{-2\alpha t}}$$

$$T = \frac{(1 - \mathcal{R})^2 e^{-\alpha t}}{1 - \mathcal{R}^2 e^{-2\alpha t}} \quad (3.6)$$

The limiting case for specular absorption occurs when $\mathcal{R}_f = 0$ and $\mathcal{R}_b = 1$. This would correspond to an ideal antireflective (AR) layer at the top surface,

*For crystalline Si, the extinction coefficient (k) is negligible for $\lambda \gtrsim 400$ nm.

and an ideal back-reflector at the bottom surface. The back-reflector effectively doubles the optical absorption path length within the material:

$$R = e^{-2\alpha t}$$

$$T = 0 \quad (3.7)$$

Figure 3.5 plots the limiting J_{sc} of a Si solar cell with specular surfaces as a function of thickness, for the above two cases, obtained by evaluating (3.1) using the AM 1.5G reference spectrum. The high front-surface reflectance of bare polished Si limits the attainable J_{sc} well below $30 \text{ mA}\cdot\text{cm}^{-2}$, which is why all modern solar cells feature AR coatings.

The above approach is easily extended to include the effects of coherence (i.e., thin-film interference), or to consider non-normal-incidence illumination. To account for coherence effects, one must sum the transmitted and reflected field amplitude phasors (i) rather than optical power or photocurrent (I). At normal incidence, the reflection and transmission of the field amplitude phasors is described by the Fresnel coefficients:

$$r = \frac{n - n_0}{n + n_0} \quad (3.8)$$

$$t = \frac{2n_0}{n + n_0} \quad (3.9)$$

Furthermore, each traversal of the material attenuates and advances the field amplitude phasor as:

$$i(t) = i(0)e^{-\frac{\alpha t}{2} + j2\pi\frac{nt}{\lambda}} \quad (3.10)$$

Upon summing the series of reflected and transmitted field amplitude phasors, the quantities then are squared to obtain the total reflected and transmitted power. In this study, these calculations were performed numerically. Due to the broad spectral range of sunlight, coherence effects do not significantly affect the limiting J_{sc} of Si solar cells, even for relatively thin devices. However,

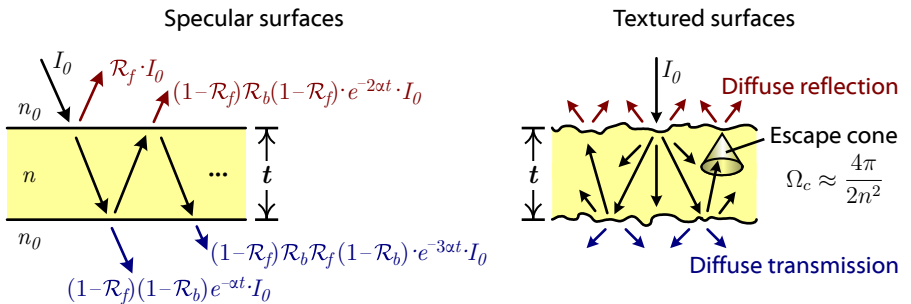


Figure 3.4. Specular vs. textured surfaces in planar solar cells.

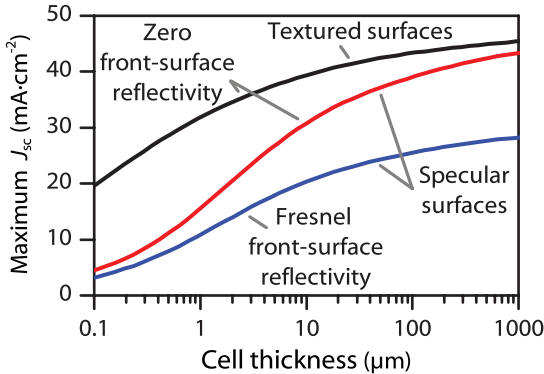


Figure 3.5. Limiting short-circuit current density as a function of planar silicon solar cell thickness. J_{abs} calculated based on optical absorption of the AM 1.5G reference spectrum ($100 \text{ mW}\cdot\text{cm}^{-2}$) assuming specular or textured surfaces with ideal (unity) back-surface reflectivity and either Fresnel (eqn. 3.5) or ideal (zero) front-surface reflectivity, using tabulated optical properties of Si. [75]

where appropriate, interference effects were taken into consideration elsewhere in this work (for example, see Fig. 4.13). This approach was also employed to calculate the front-surface reflectance of Si coated with a simple quarter-wave antireflective layer, plotted in Figure 3.2. These concepts can be further extended to consider off-normal-incidence illumination by considering refraction and the angle-dependent Fresnel coefficients; and can also be generalized to multi-layer structures via the transfer matrix method. [83, Ch. 4]

Ergodic light-trapping. Ergodic behavior occurs if the surfaces of a solar cell are suitably textured so as to fully randomize the light within the material, as depicted in Figure 3.4 (right). It has been shown that Lambertian surfaces produce this behavior. [84] The randomization of the light effectively increases its average path length within the material, leading to increased absorption. Furthermore, light reaching either interior surface at too shallow an angle will be totally internally reflected. The material’s refractive index (n) reduces the range of angles at which light can escape the material, or the “escape cone” as shown in Figure 3.5. Yablonovitch has shown that these factors increase the effective absorption path length by a factor of $2n^2$ (i.e., from t to $2n^2t$), or by a factor of $4n^2$ with a reflecting back surface. [85] This can amount to $\sim 25\times$ or $\sim 50\times$ for crystalline Si, respectively. In the case of weak absorption (that is, $\alpha t \ll 1$), this behavior manifests directly as a $4n^2$ increase in the absorption of a solar cell. Assuming an ideal non-reflecting front surface, and a perfectly reflecting back surface, the absorption achievable under ergodic light-trapping is approximately: [18]

$$A_{\text{LT}} \approx \frac{\alpha}{\alpha + (4n^2t)^{-1}} \quad (3.11)$$

Figure 3.5 compares the achievable 1-sun J_{sc} for Si solar cells under assumptions of ergodic vs. specular behavior, as a function of the cell thickness. The

effectiveness of ergodic light-trapping is particularly dramatic for thin layers ($t \sim 1 \mu\text{m}$ or less), where it enables the same absorption as $>10\times$ thicker specular layers.

The ergodic absorption limit has been seminal in the understanding of photovoltaic efficiency limits, and places a theoretical efficiency limit of 29.8% for planar Si solar cells under non-concentrated sunlight (AM 1.5). [18] Exceeding this limit with randomly textured planar solar cells requires external optical concentration, or equivalently, that the solar cell's acceptance angle be reduced. [20] The pursuit of broadband, isotropic light-trapping structures that exceed the ergodic absorption limit in planar solar cells has remained an active area of research for many years. For example, pyramidal texturing or orthogonal front- and rear-surface ridge texturing can provide a few-percent advantage over ergodic absorption at normal (but not at oblique) incidence, [86] and periodic back-reflectors such as photonic crystals can provide extreme enhancements at certain angles or wavelengths. [87, 88] But aside from various concentrator-optics schemes, commercial planar solar cells to date do not achieve injection levels above that predicted by the ergodic limit.

3.1.4 Absorption in wire arrays

The three-dimensional structure of Si wire arrays presents a fundamentally different absorption geometry than planar devices. Whereas the limiting optical absorption for planar Si devices ultimately depends on a single geometric parameter (the thickness, t), the interaction of light with Si wire arrays can depend on a large number of geometric factors. In fact, the tremendous diversity of non-planar Si microstructures that have been devised and fabricated for photovoltaic applications make it difficult to define quantitative parameters that can describe all morphologies. Thus it is instructive to considering the following qualitative properties which have been shown to affect optical absorption in Si wire arrays:

Size The diameters of VLS-grown Si wires can vary from $\sim\text{nm}$ to $\sim\text{mm}$ —a range that spans vastly different regimes of light-matter interaction. Wires of millimeter dimensions exhibit the mirrorlike appearance of crystalline Si, [89] whereas arrays of subwavelength nanowires exhibit optical properties determined by their size and shape rather than their material composition. For example, arrays of vertically oriented carbon have been engineered to achieve the lowest reflectance of any known material. [90] Because of this capability to engineer novel optical properties, Si nanowire arrays have received particular interest as potential photovoltaic materials. Wires of deeply sub-wavelength diameter ($\leq 100 \text{ nm}$) behave as an effective medium with a refractive index better-matched to that of air, [51] and thus exhibit greatly reduced reflectivity compared bare planar Si. [52, 91, 72, 73] Arrays of vertically oriented nanowires can exceed the absorption of specular films of equal thickness, even if they occupy as little as $\sim 50\%$ of the specimen plane. [51, 54] Absorption can be further enhanced by tuning the array dimensions to maximize dielectric resonances or Bloch modes. [56, 55]

Shape Most theoretical studies have approximated Si wires as ideal cylinders. However, deviations from this geometry are not only unavoidable with most fabrication techniques, but are also of great potential significance to the ensemble optical properties of the array. For example, arrays of tapered nanowires (i.e., nanocones) have exhibited superior absorption compared to arrays of cylindrical nanowires—both in magnitude and in acceptance angle, [92] and resemble the surface morphology of “black silicon.” [93] Hierarchical branching nanowire geometries are also under investigation as novel light-absorbing structures. [94]

Order A wide variety of Si wire array morphologies have been reported, ranging from disordered mattes of kinked, irregular, and randomly oriented wires; to pristine arrays of identically sized, vertically oriented pillars tiled over large areas. Randomly oriented wires ensure isotropic (i.e., Lambertian) optical behavior, but studies have shown that they exhibit much lower overall absorption than vertically oriented nanowires. [52, 74] Randomly oriented wires cannot be as densely packed as vertical wires, and furthermore, they exhibit high diffuse reflectivity due to strong multiple scattering. [74, 73] Disordered arrays of VLS-grown Si nanowires have also been reported to have curiously high sub-bandgap absorption, [52, 95] which may suggest that the growth conditions leading to disordered wires also produce poor-quality materials (see section 3.3.1).

The above considerations and studies clearly demonstrate that Si nanowire arrays provide beneficial optical absorption properties for photovoltaic applications, owing to sub-wavelength scale of the nanowires. Producing high-efficiency solar cells from such materials, however, will require not only that they provide optimal absorption of sunlight over a broad range of incidence angles, but also that the wires be optimally sized for efficient carrier collection and operating voltage. To date, the reported efficiencies of VLS-grown Si nanowire-array solar cells have not exceeded $\sim 2\%$, [40, 95, 96] whereas our device physics modeling in Chapter 2 indicated that efficiencies exceeding 17% should be possible for wires of *micron*-scale diameters. It was also shown that the open-circuit voltage of radial p-n junctions varies with the diameter and length of the wires, and thus, that wires should be of uniform size in wire-array solar cells. This framework motivates the study of the optical absorption of ordered arrays of vertically oriented Si microwires, which interact with light differently from nanowires, and until now, have received little attention as photovoltaic materials.

3.2 Optical measurement technique

To study the optical absorption of Si wire arrays independently from the optical effects of the growth substrate or growth catalyst metal, following growth, they were chemically etched to remove the metal catalyst, and then embedded in the transparent polymer polydimethylsiloxane (PDMS) and peeled intact from the growth wafer as flexible films (Fig. 3.6, left). Because PDMS has negligible

absorption throughout the measured wavelength range, these films enabled the indirect observation of optical absorption within the Si wires by measuring the hemispherical reflection and transmission of light through the arrays. The pliability of the polymer-embedded wire-array films also enabled each array to be repeatedly measured upon a variety of non-absorbing support substrates, including transparent quartz slides as well as specular (Ag) and Lambertian (BaSO_4) back-reflectors. All measurements were performed using an integrating sphere, as a function of illumination wavelength and polar incidence angles θ_x and θ_y , as illustrated in Figure 3.6 (right). By convention of this study, normal-incidence illumination corresponded to $\theta_x = 0^\circ$ and $\theta_y = 0^\circ$.

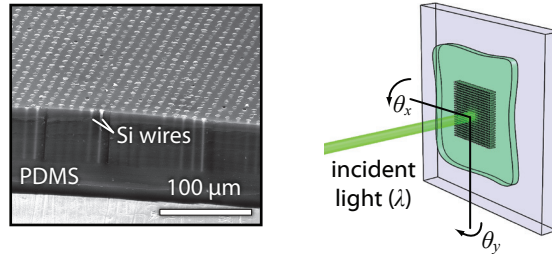


Figure 3.6. Structure of Si wire arrays prepared for optical measurements. **Left:** SEM image of peeled-off, polymer-embedded wire array, viewed upside down (at 60° tilt) to illustrate the order and fidelity of the embedded wires. **Right:** Schematic of illumination conditions and definition of incidence angles θ_x and θ_y .

3.2.1 Integrating sphere apparatus

Integrated reflection and transmission measurements were performed with a custom-built 4" integrating sphere apparatus, depicted in Figure 3.7 (see Appendix D). This instrument was designed by applying the theory of integrating spheres [97] to produce a photospectrometer capable of measuring hemispherical reflection and transmission over a wide range of incidence angle, while maximizing the sphere efficiency, spectral resolution, and absolute accuracy of the measurements. The design is similar to that described by Edwards et al. [98], with notable differences including the use of a supercontinuum laser illumination source (vs. an incandescent lamp filament), the use of a baffled photodetector (vs. an opal-glass-covered detector), and the fully motorized articulation of the sphere assembly. Although this implementation provided fewer degrees of kinematic freedom than Edwards' design (notably lacking azimuthal sample rotation capability), it also added a second (orthogonal) polar tilt capability in transmission measurements. Most importantly, the computerized automation of the entire measurement sequence enabled the full spectral and angular scan capabilities of the instrument to be spanned with consistency and measurement densities far beyond the capabilities of a manually operated instrument.

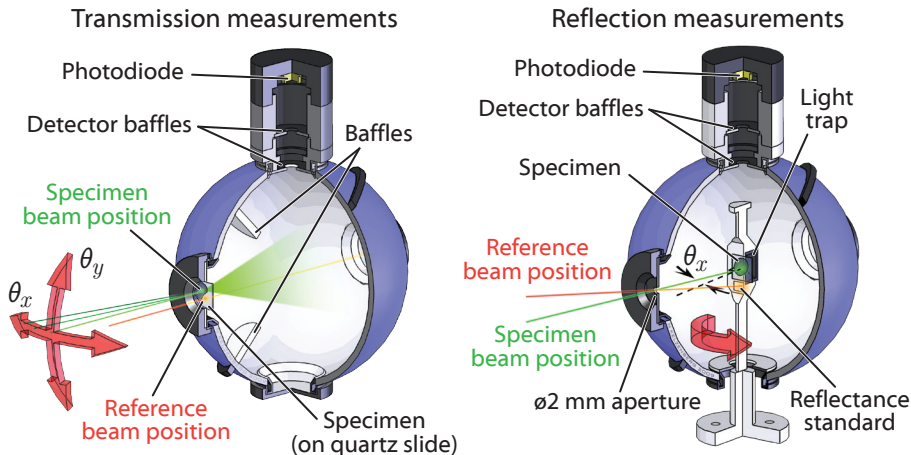


Figure 3.7. Illustration of integrating sphere apparatus. **Left:** Configuration for transmission measurements. The incidence beam angle variation was achieved by the eucentric tilt of the entire sphere apparatus. **Right:** Configuration for reflection measurements. The incidence beam angle variation was achieved by rotation of the reflection stage within the sphere.

Fabrication of the integrating sphere apparatus began with a standard 4-port (stationary) integrating sphere. Custom-designed specimen stages, baffles, and adapters were fabricated from aluminum at the Caltech machine shops. The internal surfaces of the sphere, baffles, port apertures, and stages were sandblasted, cleaned, and then coated with a BaSO_4 integrating sphere coating (6080 White Reflectance Coating; LabSphere) to achieve nearly ideal Lambertian reflectivity. The light traps and external baffles were coated with a low-reflectance black paint (Black-S Coating; Avian Technologies). To enable automated articulation of the integrating sphere assembly, a six-axis motorized stage, comprising two rotational axes and four translational axes, was designed and built using computer-controlled stepper motors (Thorlabs). The stage also included four manually operated translation stages to allow eucentric alignment of both rotational axes with respect to the incidence beam. The operation of the stepper motors, monochromator, and detection circuitry was fully automated using a custom LabVIEW program, which typically performed between 10,000 and 40,000 individual transmission and reflection measurements on each specimen over the course of 2–12 hours.

Monochromatic illumination was provided by a chopped supercontinuum laser source (Fianium SC-2) coupled to a 1/4 m monochromator (Oriel), which produced tunable excitation from $\lambda = 400\text{--}2600$ nm with a typical passband of <0.5 nm. The illumination beam was focused and collimated to produce a 1 mm spot size with $<0.1^\circ$ of beam divergence. Measurements were typically performed from $\lambda = 400\text{--}1150$ nm in 2 nm increments, except between 1058 and 1070 nm where the reported values were interpolated from measurements at either endpoint due to an unstable peak in the illumination intensity at 1064 nm.

Initially, a linear polarizer was placed in the beam path, and the response of each specimen to s - and p -polarized illumination was averaged in the reported absorption. However, little difference was observed between the averaged s - and p -polarized response of the wire arrays and that obtained without the polarizer in place. Thus for simplicity, the polarization state of the illumination beam was generally not controlled.

At the beginning of each measurement sequence, the response spectrum of the sphere was measured in the *reference position*, in which the beam illuminated a reference sample of known reflectance (R_{ref}) or transmittance (T_{ref}). The sphere was then moved to the *specimen position*, in which the beam illuminated the desired area of the specimen, and the response spectrum was measured at each desired illumination incidence angle. At each measurement point, a pair of calibrated Si (400–1150 nm) or Ge (1000–1600 nm) photodiodes simultaneously recorded (using lock-in detection) the relative intensity of the incident beam, I_{inc} (sampled via a thin quartz beamsplitter in the beam path), and the relative intensity of light within sphere, I_{sph} . These measurements enabled the absolute reflectance (R) or transmittance (T) of each specimen to be determined as:

$$R = \left(\frac{I_{\text{sph}}}{I_{\text{inc}}} \right)_{\text{Specimen position}} \cdot \left(\frac{I_{\text{inc}}}{I_{\text{sph}}} \right)_{\text{Reference position}} \cdot R_{\text{ref}} \quad (3.12)$$

This approach ensured that all spectral variations in the sphere and detector response, as well as all spectral and temporal variations in the light source intensity, were canceled out in the calculation of R and T . In fact, the only inherent sources of error with this technique (aside from experimental noise) arise from the non-infinitesimal size of the port apertures, non-idealities of the sphere surface, and non-linear or directional sensitivity of the detectors. Edwards originally estimated the precision of this type of integrating-sphere photospectrometer to be $\pm 1.5\%$, [98] and more recent studies have reported improved accuracies with similar instrument designs. [99] In our instrument, the supercontinuum laser source allowed the use of an extremely small port aperture in reflection mode ($\Omega \approx 3 \text{ msr}$). The internal surfaces of the integrating sphere were frequently re-coated to ensure consistent performance, and detector linearity was periodically confirmed by re-performing measurements under varying illumination intensities. Furthermore, because the sequential acquisition of the specimen and reference spectra under computer automation bypassed the need to open, touch, or otherwise disturb the integrating sphere between the two measurement sequences, the possibility of operator-induced alignment error was greatly reduced.

In transmission mode, each specimen was placed over a 10 mm diameter entrance port of the integrating sphere (Fig. 3.7, left). Motorized operation permitted eucentric tilt and translation in two dimensions with 0.1° and $100 \mu\text{m}$ resolution, respectively. The transmission spectrum of each wire array was referenced to that of an exposed area of the quartz slide on which it was placed ($T_{\text{ref}} \approx 0.92$), utilizing motorized translation of the sphere assembly to reach the

reference beam alignment at the beginning of each measurement sequence. In reflection mode, each specimen was placed on a specially designed rotation stage at the center of the sphere, which had a 5 mm diameter light trap centered beneath the specimen to absorb any transmitted light (Fig. 3.7, right). Motorized rotation of the specimen stage permitted eucentric tilt in one direction (θ_x) with 0.1° resolution. The tilt in the second direction (θ_y) was typically fixed at $\sim 0.5^\circ$ to prevent the specular reflection from escaping the sphere through the 2 mm diameter illumination port aperture. The reflection spectrum of each wire array was referenced to that of an adjacently located reflectance standard (Lab-Sphere, $R_{\text{ref}} \approx 0.99$), utilizing motorized translation and rotation of the entire sphere assembly to reach the reference beam alignment at the beginning of each measurement.

The integrating sphere specimen stages were designed for a $0.5''$ square form factor; the size of the quartz microscope slides on which the wire arrays were placed for measurements. Typical wire arrays were ~ 5 mm square. To measure the arrays with a specular back-reflector, they were transferred onto slides which had been coated with > 100 nm of evaporated Ag. In both cases, the wire-array films were held in place by the adhesion between the PDMS and the quartz or Ag surface. For measurements performed on Lambertian back-reflectors, each wire array film was attached to a piece of $0.5''$ -square BaSO_4 -coated Al sheet metal (similar to the internal surfaces of the integrating sphere) using two-sided tape at opposite edges of the sample. The tape was placed as far from the point of beam incidence as possible.

3.2.2 Determining optical absorption

For non-opaque specimens (e.g. wire arrays placed on quartz slides), absorption was calculated from the wavelength- and angle-resolved hemispherical transmission and reflection measurements, $R(\lambda, \theta)$ and $T(\lambda, \theta)$, as:

$$A(\lambda, \theta) = 1 - R(\lambda, \theta) - T(\lambda, \theta) \quad (3.13)$$

For opaque specimens (e.g. wire arrays placed on back-reflectors, and the commercial Si solar cell), absorption was calculated from hemispherical reflection measurements only:

$$A(\lambda, \theta) = 1 - R(\lambda, \theta) \quad (3.14)$$

Example transmission, reflection, and resulting absorption measurements of a triangular-tiled microwire array ($\eta_f = 8.8\%$, $68 \mu\text{m}$ wire length) are shown in Figure 3.8. Similar measurements were performed on all wire arrays in this study.

In Equations (3.13) and (3.14), θ represents the direction of tilt during measurements, which was usually θ_x as defined in Figure 3.6. Due to the angularly anisotropic optical properties of the periodic (e.g. square- or triangular-tiled) microwire arrays, it was important that each array be tilted in the same direction with respect to the lattice pattern of the wires—particularly when combining the angle-resolved reflection and transmission measurements to calculate absorption. For this reason, fiducial markings at the corner of each array were used to

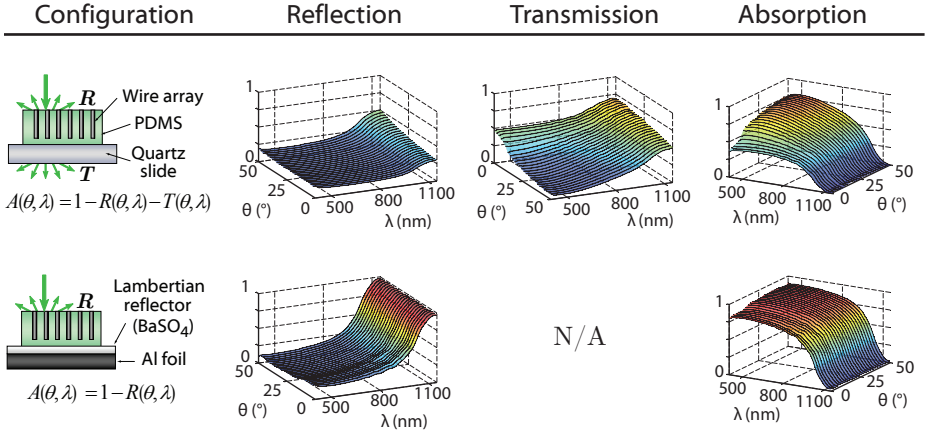


Figure 3.8. Example absorption measurements. Schematic (left), reflection and transmission measurements (center), and calculated absorption (right) of a triangular-tiled wire array ($\eta_f = 8.8\%$), placed on a quartz slide (top row) and on a Lambertian back-reflector (bottom row).

position them in a consistent orientation between measurements, and the specular beam reflection from each sample was used to precisely align the equipment to normal-incidence prior to each measurement. Furthermore, to ensure reproducible orientation of the periodic arrays with respect to the tilt plane, their transmitted (or reflected) diffraction patterns were also used to align each array's lattice pattern orientation to a consistent convention (which will be shown in Figure 3.18).

3.2.3 Quantifying useful absorption for photovoltaic applications

Having measured the angle- and wavelength-dependent optical properties of Si wire arrays, it was desired to define a figure of merit (FOM) to succinctly quantify their overall absorption of sunlight, and thereby determine their relative performance potential as photovoltaic devices. To this end, we calculated the approximate fraction of above-bandgap sunlight that each wire array might absorb in a day of operation as a non-tracking solar cell. This calculation combined the wire-array absorption measurements at each wavelength and angle, $A(\lambda, \theta)$, with a standard reference spectrum that specified the photon flux of direct normal radiation (Γ) at each hour (t) and wavelength (λ) throughout the day. [100] This spectrum represents solar insolation conditions typical of a summer day in the southwestern United States.

Figure 3.9 depicts the FOM calculation and the associated simplifying conditions. We considered an absorbing device oriented at *global tilt*: oriented so as to directly face the sun at noon, but which does not otherwise track the sun. The path of the sun across the sky was simplified as an equatorial arc;

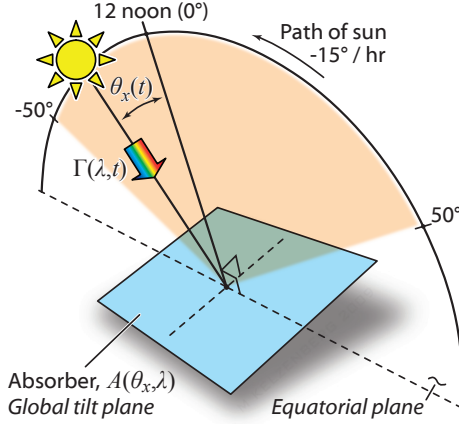


Figure 3.9. Schematic diagram for figure of merit calculation.

that is, confined within the equatorial plane of the earth.* Under these assumptions, determining the incidence angle of direct sunlight as a function of time was greatly simplified: $\theta_x = 0^\circ$ at noon and progresses at $15^\circ/\text{hr}$, while $\theta_y = 0^\circ$ throughout the day. The fraction of above-bandgap incident photons that would be absorbed from this reference spectrum, A_{avg} , could then be expressed as:

$$A_{\text{avg}} = \frac{\iint \Gamma(t, \lambda) A(\theta_x(t), \lambda) \cos(\theta_x(t)) d\lambda dt}{\iint \Gamma(t, \lambda) \cos(\theta_x(t)) d\lambda dt} \quad (3.15)$$

This calculation was performed for each wire array, over the wavelength range $400 < \lambda < 1100$ nm and angle range $-50^\circ < \theta_x < 50^\circ$ (corresponding to the time interval from 08:40 to 15:20). These integration limits were imposed by the spectral range of the illumination source ($\lambda_{\text{min}} = 400$ nm) and the Si band edge ($\lambda_{\text{max}} \approx 1100$ nm), and by the mechanical rotation limits of the integrating sphere apparatus. Despite the lack of absorption data for ultraviolet wavelengths or incidence angles greater than 50° from normal, this integration range accounts for $255 \text{ mAh}\cdot\text{cm}^{-2}$ (84%) of the $305 \text{ mAh}\cdot\text{cm}^{-2}$ of above-bandgap photon-equivalent charge that would strike the global tilt plane throughout the entire day under this reference spectrum and associated simplifying assumptions. An example A_{avg} calculation (resolved by time of day) is plotted in Figure 3.10, corresponding to the example absorption measurements shown in Figure 3.8. The effectiveness of the Lambertian back-reflector is evident from the dramatic improvement in optical absorption, particularly near normal incidence.

The calculation of A_{avg} is convenient in that it reduces an extensive amount of angle- and wavelength-resolved absorption data for each wire array into a sin-

*Note that this procession of the sun would occur only on the spring or fall equinoxes, whereas the chosen reference spectrum corresponded to summertime illumination conditions. Further note that, in our calculations, we time shifted the reference spectrum data so that the peak direct-normal irradiation intensity occurred at 12 noon, to approximately correct for differences between solar noon and local noon of the reference conditions.

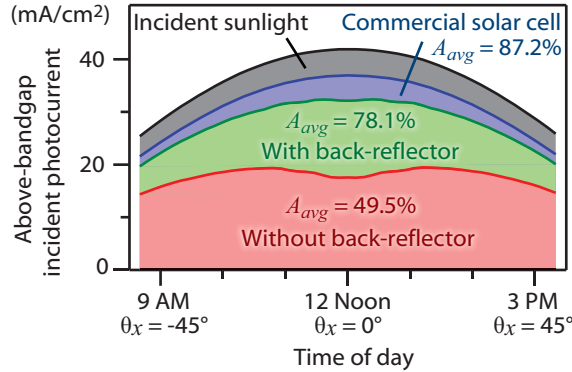


Figure 3.10. Example figure of merit calculations corresponding to the wire array absorption data shown in Figure 3.8 (measured with and without a Lambertian back-reflector) as well as the calculation corresponding to the measured absorption of a commercial multicrystalline silicon solar cell.

gle figure of merit, allowing straightforward comparisons to be made. However it is important to note that this calculation is measure of the *quantum* (rather than energy-conversion) efficiency of the absorption process. Some recent studies [54, 55] have instead reported the *ultimate efficiency* of absorption: the theoretical energy-conversion efficiency limit imposed by the fact that photon energy exceeding the bandgap energy is wasted (thermalized) in semiconductor solar cells (which is one of the constitutive assumptions of the principal of detailed balance). Aside from different spectral weighting of the absorption data, however, both types of calculations provide equivalent information, and neither take into account the practical aspects of solar cell efficiency such as operating voltage or varying carrier-collection efficiency as a function of incidence angle. [101] One practical advantage of the A_{avg} calculation presented here is that it calculates the day-integrated (rather than peak or normal-incidence) absorption of direct sunlight, which is particularly important for photovoltaic structures with non-isotropic response. However, note that we have not modeled the absorption of diffuse sunlight, which can be a major portion of total solar irradiation in cloudy climates such as northern Europe. The development of a diffuse illumination profile to use in our calculations would depend heavily on location-specific atmospheric conditions, [102] and the lack of absorption data for incidence angles greater than 50° from normal might limit the validity of such a figure of merit. In our study, the omission of diffuse irradiation considerations was partially mitigated by the choice of a reference spectrum representative of a desert climate: Diffuse irradiation accounted for only $\sim 10\%$ of the total above-bandgap photon flux striking the global tilt plane in the reference data set. Furthermore, since a substantial portion of diffuse sunlight occurs at shorter (blue) wavelengths and oblique incidence angles, where wire arrays exhibited increasing absorption, it is not unreasonable to surmise that wire arrays would absorb diffuse sunlight at least as well as direct sunlight. Experimental techniques have

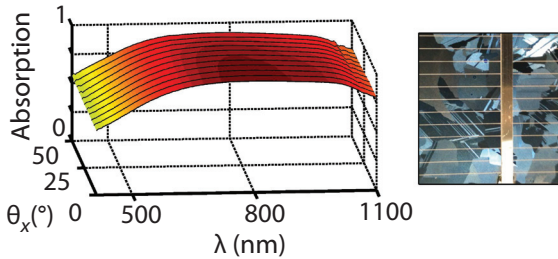


Figure 3.11. Measured absorption of 280 μm thick, commercial multicrystalline Si solar cell with dielectric AR-coating. Right: Photograph of ~ 2 cm-square area of this solar cell.

been described for measuring the response of other photovoltaic materials under diffuse illumination, [103] and such methods might find use in future studies on the solar-energy-conversion potential of Si wire arrays.

To provide a reference point for this figure of merit calculation, the absorption characteristics of a commercial, antireflective-coated, multicrystalline Si solar cell were also measured using the integrating sphere apparatus (Fig. 3.11). The calculation of this cell's A_{avg} (0.87) is also shown in Figure 3.10.

3.2.4 Sub-bandgap absorption

Spectrally resolved measurements of the wire arrays were also performed at wavelengths exceeding the Si band edge (1150–1200 nm), where virtually no band-to-band absorption is expected. In the absence of a back-reflector, the observed sub-bandgap absorption of the wire arrays did not exceed -4% to $+12\%$, and was typically below 5% .^{*} Some deviation from zero absorption (negative values in particular) can be attributed to an experimental artifact arising from the spatial variation in the array's optical density, because the transmission and reflection measurements were not necessarily performed at the same location on each wire array specimen. Variations of up to 0.08 in absolute transmission were observed across the wire arrays; however this artifact alone could not account for the larger instances of sub-bandgap absorption, nor that observed when the arrays were placed on the back-reflector (1% – 16%). Thus, this sub-bandgap absorption may be indicative of parasitic (non-photovoltaically useful) absorption processes. If present, parasitic absorption at above-bandgap wavelengths would be detrimental to any photovoltaic device, and must be addressed in this absorption study.

Free-carrier absorption is an intrinsic source of parasitic absorption within Si solar cells. [18, 104, 81] However the absorption due to free carriers was likely negligible at these wavelengths, because most wires were nominally undoped, and the illumination levels were low (\ll one-sun equivalent intensity). Absorption

^{*}This discussion pertains to the Si microwire arrays grown from SiCl_4 . Si wire films that were grown from SiH_4 exhibited dramatically higher sub-bandgap absorption (see section 3.3.1).

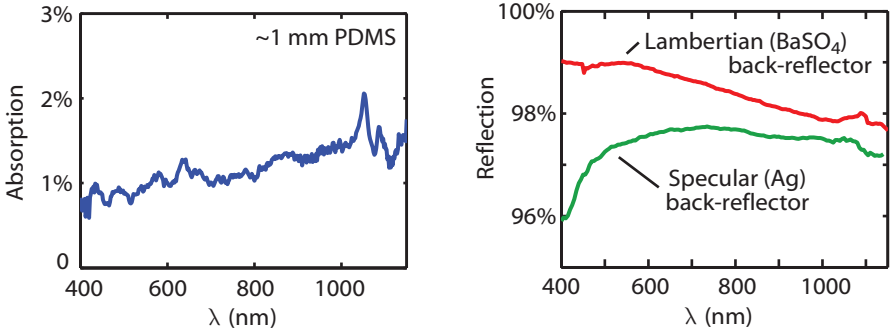


Figure 3.12. Normal-incidence optical absorption of ~ 1 mm thick PDMS film, and hemispherical reflectance of the specular (Ag) and Lambertian (BaSO_4) back-reflectors used in this study.

due to the PDMS or the back-reflectors was also negligible, as measured in Figure 3.12.

Others have reported sub-bandgap absorption in Au-catalyzed, VLS-grown Si wire arrays (up to ~ 0.6 at these wavelengths), and this has been primarily attributed to the presence of surface states, defects, or catalyst metal particles. [40, 52, 95] It is well-known that certain defects or impurities introduce energy levels or bands within a semiconductor's bandgap, and can give rise to extrinsic (trap-assisted) sub-bandgap absorption. [104] Known as the *impurity photovoltaic effect* (IPV), this theoretically useful sub-bandgap absorption mechanism has been proposed and studied as route to exceed the efficiency limit of single-junction solar cells, particularly in non-planar junction geometries. [105, 16, 71, 106, 107]

The IPV effect has been experimentally observed at roughened Si surfaces [108] as well as for Au traps in bulk Si, [109, 110] both of which may be present in Au-catalyzed, VLS-grown Si wires. However, IPV absorption has not yet been shown to produce an overall increase in efficiency vs. comparable conventional Si solar cells. Moreover, no sub-bandgap photogeneration has been reported for either surface-state-induced or Au-trap-induced IPV absorption within a purely photovoltaic device, and it has been argued that any potential increase in solar cell J_{sc} due to IPV absorption would be more than offset by a reduction in operating voltage. [111] Because of this, and the well-known deleterious properties of surface damage and deep-level traps within Si solar cells, we conclude that IPV absorption, if present, should not presently be considered useful for the purpose of estimating potential photovoltaic performance from absorption measurements.

Thus in this study it was assumed that any observed sub-bandgap absorption was indicative of parasitic processes, which should be excluded from the estimation of a solar cell's performance potential (A_{avg}) as well as when comparing a wire array's absorption to theoretical absorption limits of planar devices. However, for above-bandgap photon energies, the magnitude of parasitic absorption

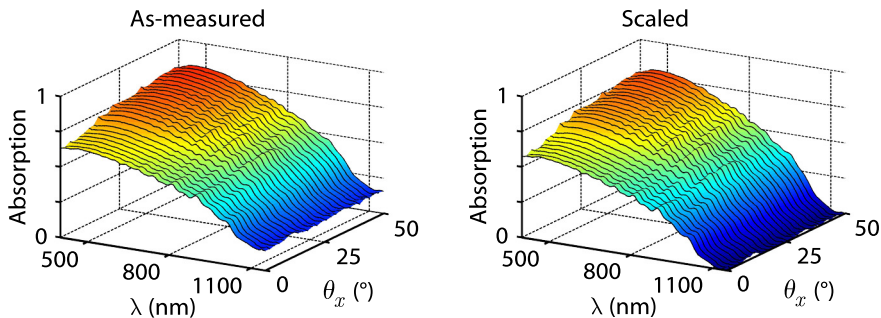


Figure 3.13. Example of scaling procedure to correct for sub-bandgap absorption, applied to the measurements of a triangular-tiled wire array ($\eta_f = 4.9\%$) that exhibited $\sim 14\%$ sub-bandgap absorption (measured with a Lambertian back-reflector).

cannot be determined from optical measurements because, if present, it would be indistinguishable from the normal band-to-band absorption of Si. In an attempt to minimize the inclusion of potential (but unknown) parasitic absorption at above-bandgap energies (as well as to mitigate the experimental artifact described above), the reported absorption of each wire array was scaled based on its observed sub-bandgap absorption. This was achieved by uniformly scaling (by up to $1.19\times$) the transmission and reflection measurements of each wire array, so as to produce a reported absorption (averaged around 1150 nm) equal to that of a PDMS film with no wires ($\sim 1.5\%$). An example of one of the more extreme cases of this scaling is shown in Figure 3.13.

Note that this scaling procedure was only utilized for the purpose of calculating A_{avg} from the indirect (optical) absorption measurement data, as well as when comparing this data to the theoretical absorption limits of planar solar cells. Outside of this context, all absorption data plotted in this thesis appears unscaled except where noted. In the case of direct observations of absorption via photoelectrochemical measurements (which will be discussed in section 3.5), no such scaling was necessary because the approach did not measure parasitic absorption. Also note that no scaling was applied to any of the control measurements (e.g. the measurement of PDMS absorption in Figure 3.12) or to the measurements of non-wire-array absorbers (e.g. the commercial Si solar cell of Figs. 3.10 and 3.11).

It was not clear what caused some wire-array samples to exhibit substantial sub-bandgap absorption, while others were nearly 100% transparent at these wavelengths. This perplexing variation in behavior was observed regardless of array geometry (e.g. diameter or packing fraction) or catalyst metal choice (Au, Cu, or Ni). The wire arrays of each catalyst type were processed identically to remove residual surface metals following growth (see section 3.3.2). Figure 3.14 shows the effect of the catalyst removal procedure on a typical Au-catalyzed

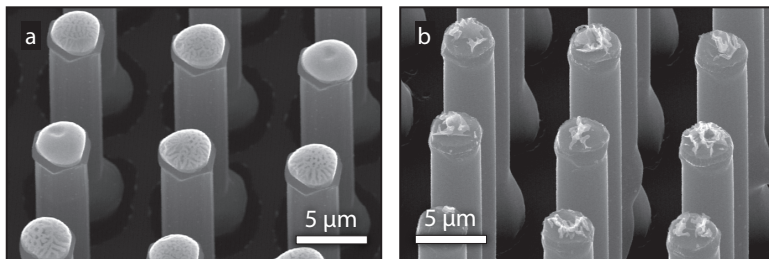


Figure 3.14. Removal of Au catalyst tips. SEM images of an Au-catalyzed wire array, taken (a) before and (a) after catalyst tip removal.

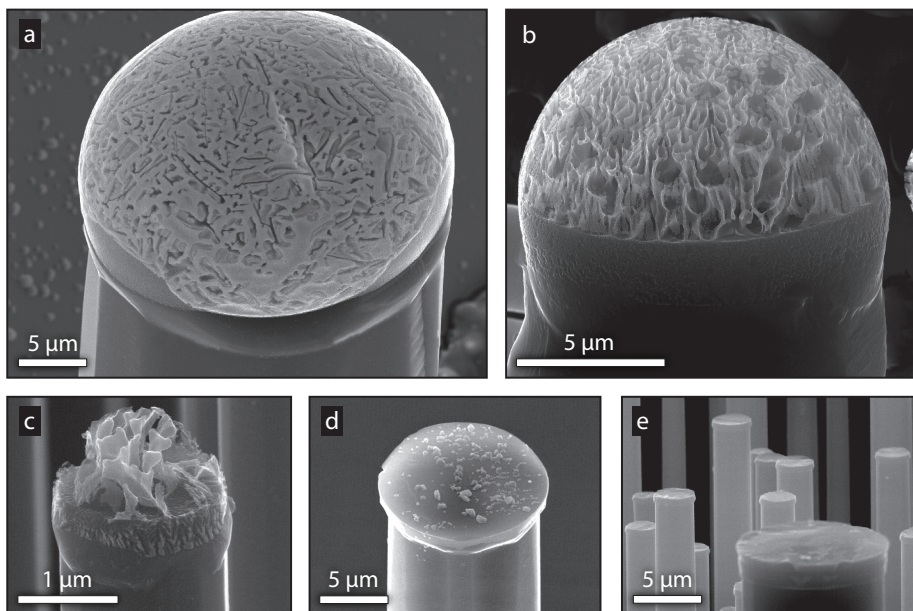


Figure 3.15. Catalyst tip structure and removal. a, SEM image of an Au catalyst tip on a large-diameter Si microwire. b–e, SEM images of the residual tip structures observed on several wire arrays following chemical catalyst removal, exemplifying fairly incomplete (b) to complete (e) removal of the tip material. All wire arrays were subject to identical catalyst-removal procedures.

wire array. Given the similarity in chemical processing between the arrays of each catalyst type, it is unlikely that the *intermittent* sub-bandgap absorption could be attributed to the presence of specific surface states, or to specific bulk trap states associated with homogeneously distributed (interstitial/substitutional) catalyst metal impurities within the Si.

We suspect that the sub-bandgap absorption, when present, was due to catalyst metal precipitates within the wires, or to portions of the catalyst metal tips that were not effectively removed by our chemical etch procedure. Depending on the rate of cooling, the solidification of the supersaturated catalyst eutectic produces dendritic recrystallization of the Si (or silicides), which can potentially entrap metallic catalyst material. [112] A wide variety of dendritic structures were observed on our Si microwires following catalyst removal (Fig. 3.15), indicating varying degrees of success at removing this material. Others have found that residual Si can completely entrap the catalyst metal regions on Si nanowires, and thus prevent removal via chemical etching. [113] Furthermore, catalyst metal inclusions have been observed within the bulk of Au-catalyzed VLS-grown Si wires, [35] and it is well-known that Cu and Ni impurities readily precipitate upon rapid cooling due to their high solubility and diffusivity in crystalline Si. [114, 115, 116] Unfortunately, the cooling rates following VLS growth was not controlled in this study, and varied greatly between samples. A policy of slowly cooling samples to 700 °C prior to unloading them from the reactor has since been adopted, and although no conclusive study has been performed, recent results indicate that this procedure yields Si wires that have improved electrical properties, and which do not exhibit sub-bandgap absorption.

3.3 Effects of array geometry on optical absorption

3.3.1 Disordered arrays

Prior to the development of the patterned SiCl_4 VLS growth technique that was used to produce ordered arrays of vertically aligned microwires throughout most of this study, our Si wires had been synthesized from SiH_4 in a low-pressure CVD reactor, at relatively low temperatures (~ 500 °C), using non-patterned (bare) Si $\langle 111 \rangle$ growth wafers and thermally evaporated Au to produce the VLS catalyst particles. This produced films of disordered, randomly oriented (kinked) crystalline Si nano- or microwires of similar morphology to those studied by Tsakalakos [52] and Stelzner. [95] Although these films contained wires of widely varying lengths and diameters, the growth conditions and Au film thickness provided some control over the range of wire lengths and diameters within each film. The wire growths were performed by Brendan Kayes, and further details of the methods can be found in his PhD thesis. [39, Ch. 3]

Figure 3.16 shows two Si wire films that were grown from SiH_4 at 500 °C for optical absorption studies. The first film, denoted “disordered nanowires,” was ~ 8 μm thick and consisted of 30–800 nm diameter wires (left). The second film, denoted “disordered microwires,” was ~ 14 μm thick and consisted of 0.1–3.0 μm

diameter wires (right). The differing morphologies of these two wire films were evident from their visual appearance: The disordered nanowires were yellow in color, while the disordered microwires were dark brown in color. These films also differed greatly in visual appearance from the ordered microwire arrays, such as that shown in the previous section (Fig. 3.6). Both disordered wire films had a flat (non-specular) appearance at all angles, whereas the ordered arrays exhibited angle-dependent optical properties, including transmitted and reflected diffraction patterns.

To enable optical measurements, the disordered wire films were embedded in PDMS and peeled off following the same procedure that was used to prepare the ordered, SiCl_4 -grown microwire arrays (section 3.3.2). Figure 3.17 compares the integrated normal-incidence optical absorption of the disordered SiH_4 -grown wire films to that of an ordered SiCl_4 -grown microwire array (a square-tiled array resembling that shown in Fig. 3.6). The disordered wire films exhibited nearly identical absorption spectra throughout the measured range of incidence angle ($\theta_x = 0^\circ - 50^\circ$); thus, only the normal-incidence absorption is plotted. The ordered microwire array exhibited dramatically different absorption spectra throughout this range of incidence angle; measurements are shown corresponding to normal incidence and $\theta_x = 50^\circ$ illumination.

The absorption of the disordered Si wires generally resembled that reported for Au-catalyzed Si nanowire films of similar morphologies by Tsakalakos [40] and Stelzner. [95] The disordered films exhibited very high absorption (up to 85%) at blue wavelengths, which gradually decreased with increasing wavelength. And, although the disordered films were several times thinner than the lengths of the ordered microwires ($\sim 60 \mu\text{m}$), they both achieved greater optical absorption at

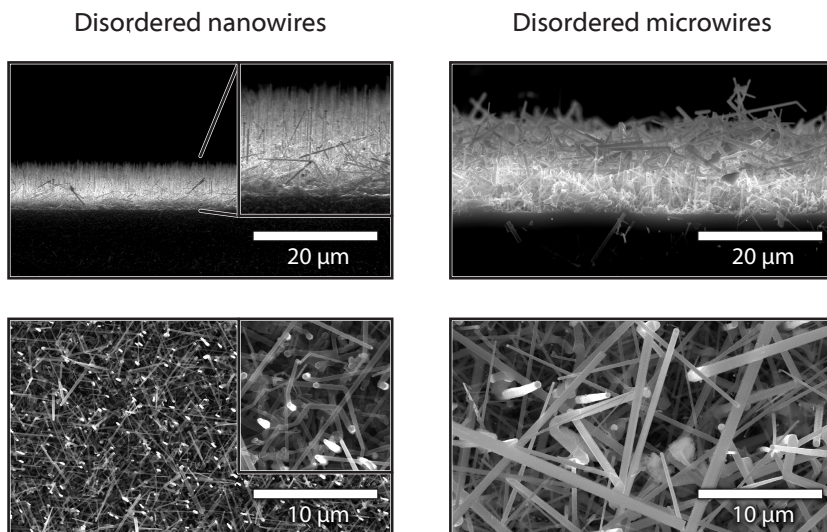


Figure 3.16. Disordered Si wire arrays grown from SiH_4 .

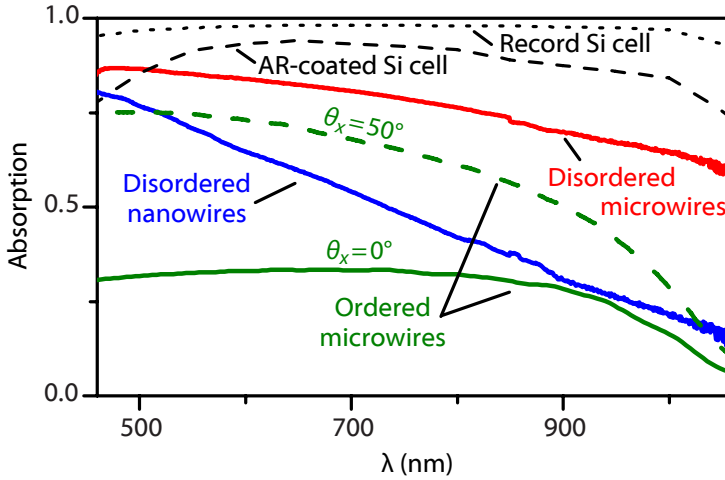


Figure 3.17. Measured optical absorption of disordered Si wire films, comparing the (approximately isotropic) absorption of the disordered Si nanowires (blue) and microwires (red) from Fig. 3.16, to the normal- and 50° -incidence absorption of the ordered, square-tiled Si microwire array (green) from Fig. 3.6. Shown for reference are the published absorption data for the record Si solar cell, [117] and for a multicrystalline Si solar cell with a single-layer SiN_x antireflective coating. [118]

normal incidence. In fact, the disordered microwires exhibited greater absorption than the ordered microwires at all incidence angles. These observations suggested that disordered wires may present a more advantageous geometry for optical absorption: the vertical orientation of the ordered microwires permitted most light to pass between the wires without changing course; whereas the dense mattes of disordered micro- or nanowires ensured that nearly all incident light was randomly scattered within the film. However, other studies have shown that multiple light-scattering events within disordered nanowire arrays substantially increase their diffuse reflectivity compared to vertically oriented nanowire arrays, [74, 73] suggesting that the poor absorption of our ordered microwire array may have been caused by its low ($<5\%$) packing fraction. And, as shown in Figure 3.17, the optical absorption of the disordered Si wires still fell short of that achievable by wafer-based Si solar cells with even simple antireflective coatings.

Of greater concern was that the absorption of our disordered arrays did not approach zero at the Si band edge. In fact, the absorption of the disordered microwires was $\sim 50\%$ even at $\lambda = 1200$ nm, where virtually no band-to-band absorption should be expected—potentially indicating strong parasitic absorption within the SiH_4 -grown material. Residual catalyst metal has been suggested as the culprit behind such sub-bandgap absorption [40], and transmission electron microscopy analysis of our SiH_4 -grown wires revealed a high concentration of Au particles on or near the wire surfaces. [39, p. 58] Thus, it was unclear how much of the measured optical absorption could be of use to a photovoltaic device.

These observations, combined with the slow growth rate and poor morphologies of the SiH₄-grown Si wires, shifted the focus of our studies to the high-quality microwire arrays grown by high-temperature SiCl₄ CVD and alternate VLS catalyst metals.

3.3.2 Ordered microwire arrays

The development of a photolithographically patterned, SiCl₄-based VLS growth technique (see section 1.5.1) enabled the fabrication of high-fidelity arrays of vertically oriented Si microwires over large areas, with explicit control over the positioning of the wires within the array. Combined with the ability to control the length and diameter of the microwires by adjusting the catalyst metal thickness and growth conditions, this provided an unprecedented opportunity to synthesize Si microwire arrays of widely varying packing fraction and tiling patterns using the VLS growth process. The following procedure was used to produce the ordered Si microwire arrays for this study:

Growth. Ordered arrays of Si microwires were grown from SiCl₄ by the photolithographically patterned VLS process described in section 1.5.1. [37] The wires were grown on p-type <111> Si wafers ($\rho < 0.001 \text{ } \Omega\text{-cm}$) using a 300 nm thermal oxide for catalyst confinement and evaporated Au, Cu, or Ni (400–700 nm thickness, 5N purity) as the VLS catalyst. (Most arrays were grown using Au catalyst. No notable differences were observed between the optical properties of wires grown using Au, Cu, or Ni catalyst metal.)

Catalyst removal. Following growth, the wire arrays were etched in 5% HF(aq) for 30 s. To remove the catalyst metal, Au-catalyzed wires were then etched for 30 min in a solution of 9:1 Gold Etchant TFA (Transene) to 36% HCl(aq) and then rinsed for 30 s in 5% HCl(aq). Cu- and Ni-catalyzed wires were instead etched for 20 min at 70 °C in a 6:1:1 solution of H₂O:H₂O₂:HCl. Both groups of wires were etched in 10% HF(aq), dried, and momentarily dipped in a 50% (wt) solution of KOH(aq) at 55 °C to remove ~20 nm of Si, which has been shown to remove a metal-rich surface layer from similarly grown wires. [80]

Polymer infill. The wire arrays were then infilled with polydimethylsiloxane (PDMS) using the method described in section 1.5.3. [42] A 10:1 (wt) mixture of PDMS and curing agent (Sylgard 184, Dow Corning) was drop-cast onto the wire arrays and spun at 1000 rpm for 30 s, and then cured for ≥ 1 hr at 120 °C, producing a smooth film whose overall thickness ranged from 10 to 50 μm greater than the height of the wire array.

Peel-off. The polymer-embedded wire arrays were carefully peeled from the growth substrate as flexible films using a razor blade.

For this study, 28 unique Si wire arrays were grown based on seven tiling patterns: periodic (square, triangular); chirped-periodic (square and triangular lattices where each wire was randomly displaced by up to $\pm 1 \mu\text{m}$); quasi-periodic (Penrose, dodecagonal); and quasi-random (a greedy packing of randomly placed wires constrained by a minimum center-to-center distance criteria). The photomask used to pattern the wire arrays featured four $\sim 5 \times 5 \text{ mm}$ square hole-array patterns for each of the seven tilings, printed with diameters of 3 or 5 μm and minimum pitch (center-to-center distance between adjacent holes) of 7, 9, or 12 μm .* The length of the wires was nominally controlled by VLS growth time, however, arrays with higher areal packing fraction exhibited slower growth rates than those with lower packing fractions. In total, wire arrays of each of the 28 unique tiling patterns were successfully grown, with packing fractions ranging from 1.6% to 16%, wire diameters ranging from 1.4 to 4.0 μm , and wire lengths ranging from 24 to 97 μm . Following growth, the lengths, diameters, and areal fractions of each wire array were determined by computer-processing of high-resolution SEM images, taken from a $200 \times 200 \mu\text{m}$ area at the center of each array. Arrays with more than one defect (i.e., a missing wire or spurious growth) within this area were discarded.

Figure 3.18 shows the 9 μm -pitch wire array of each of the seven tiling patterns, as grown (top rows). Following growth, the arrays were etched to remove the catalyst metal, embedded in PDMS and peeled-off, and then placed upon quartz slides for transmission measurements. The transmitted optical diffraction patterns (Fig. 3.18, third row) were used to orient the wire lattice patterns relative to the tilt directions (θ_x, θ_y), and angularly resolved transmission measurements were performed (bottom row).

Because periodic arrangements offered the most efficient packing of wires within the plane, the square- and triangular-tiled wire arrays were fabricated with greater areal packing fractions than the quasi-periodic- and random-tiled arrays, and thus generally achieved highest optical absorption. However, the well-aligned rows and columns of wires within the periodic arrangements also caused these arrays to exhibit strongly anisotropic angular transmission profiles, including high transmission (and thus low absorption) at incidence angles aligned with the array lattice. This behavior would lead to undesirable “dead zones” in the performance of a solar cell. The mild randomization of the wire position within the chirped-periodic arrays was not sufficient to eliminate the obvious optical absorption minima at certain angles of incidence. In fact, even the quasi-periodic arrays exhibited mild variations in azimuthal angular transmission, manifesting the underlying order of these array lattices. Most importantly, however, all wire arrays exhibited very high transmission (> 0.7) at normal incidence ($\theta_x, \theta_y = 0^\circ$), owing to the vertical orientation of the wires. This behavior

*To facilitate writing the photomask in an optical stepper, each $\sim 5 \text{ mm}$ square hole-array field was produced by tiling $\sim 200 \mu\text{m}$ -square generating patterns. The periodic and chirped-periodic generating patterns were tiled at integral multiples of the wire-to-wire pitch in each direction, so as to preserve periodicity over the entire device area. The quasi-periodic and random generating patterns were tessellated by tiling them with a slight overlap between each tile, then deleting the holes that violated the minimum pitch criteria.

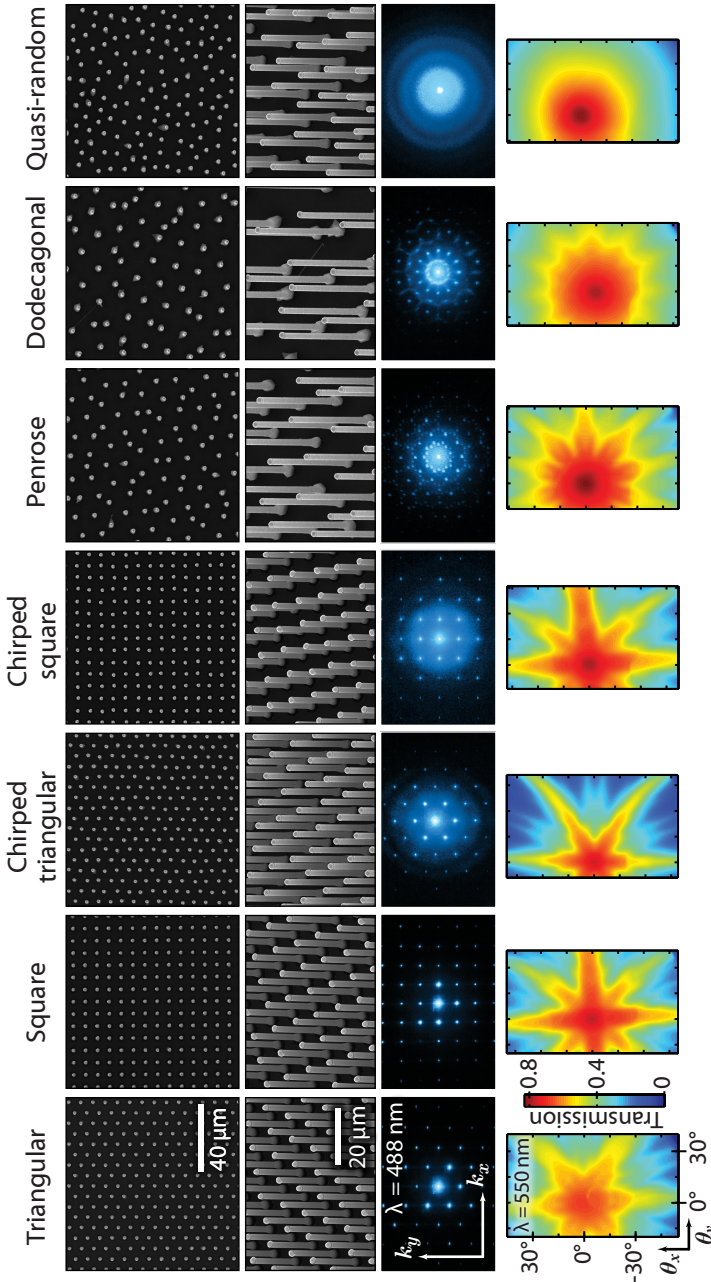


Figure 3.18. Representative composition and optical properties of each wire-array tiling pattern. The scale bars in the left column apply to all images across each row. Top row: SEM images of as-grown wire arrays viewed from a top-down perspective. Second row: SEM images viewed at a 20° angle. Third row: Transmitted diffraction patterns of polymer-embedded wire arrays on a quartz slide, observed at $\lambda = 488$ nm. The axes indicate $4,000 \text{ cm}^{-1}$ in the direction of k_x and k_y . Bottom row: Integrated transmission of each wire array observed at $\lambda = 550$ nm as a function of the beam incidence angle (θ_x, θ_y) .

would be particularly problematic for solar cells, which usually receive peak illumination intensity at near-normal incidence angles (when the sun is directly overhead). These observations suggest that, in order for Si wire arrays to achieve suitable absorption over the relevant wavelengths and incidence angles of solar illumination, the light incident upon them must be randomized to prevent it from simply passing between the wires. For this reason, the absorption of each wire array was also measured with a Lambertian back-reflector (BaSO_4 on Al) placed beneath the wires to randomize the light reaching the back of the array.

Figure 3.19 plots the figures of merit (A_{avg}) for each wire array's measured absorption both with (b) and without (a) the Lambertian back-reflector; as a function of areal packing fraction (η_f), wire dimensions, and array lattice pattern. The use of the back-reflector dramatically improved the absorption of each wire array, particularly those with lower packing fractions. Although the low-packing-fraction arrays ($\eta_f < 7\%$) exhibited lower overall absorption, their A_{avg} values were often many times (10–25 \times) their areal packing fractions, with the greatest $A_{\text{avg}} : \eta_f$ ratios corresponding to the arrays with the longest wire length (nearly 100 μm). This enhancement likely arose from the inherent scattering and diffraction of light passing between the wires. Surprisingly, the wire arrays with the highest packing fractions ($\eta_f = 12\text{--}16\%$) did not exhibit the largest values of A_{avg} . This was partially because these arrays were composed of shorter wires ($\sim 25 \mu\text{m}$ in length) as a result of the slower VLS growth rate obtained for high-packing-fraction arrays. The shorter wire length limited the absorption of infrared light in these arrays. Additionally, the densely packed arrays exhibited greater reflectivity than moderately packed arrays, presumably due to the increasing surface area of the reflective top surfaces of the wires. Thus, it was found that arrays with moderate wire packing fractions ($\eta_f = 8\text{--}10\%$) and longer wire lengths (40–60 μm) provided the optimal tradeoff between optical opacity and low reflectivity.

The highest absorption figure of merit, $A_{\text{avg}} = 78\%$, was obtained by a square-tiled array of 65 μm -long wires having $\eta_f = 8.8\%$. (Note that this array's absorption was featured in Figs. 3.8 and 3.10.) This absorption would produce $J_{\text{abs}} = 33.0 \text{ mA}\cdot\text{cm}^{-2}$ under the AM 1.5G reference spectrum, and falls only slightly short of the absorption of the commercial wafer-based solar cell that we measured for comparison ($A_{\text{avg}} = 87\%$). Based on this study, it was determined that reasonable absorption could be obtained by wire arrays with relatively low areal packing fractions ($\eta_f < 10\%$) and wire lengths of $> 60 \mu\text{m}$, but that further absorption enhancements would be required in order to compete with the optical absorption of wafer-based Si solar cells. Despite being able to fabricate wire arrays with tiling patterns ranging from triangular to quasi-random lattices, it was found that external light-scattering sources (e.g. Lambertian back-reflectors) were required to sufficiently randomize light for absorption, particularly at normal incidence. The increased reflectance of the more-densely packed arrays also suggested that higher absorption might be possible by reducing the reflectivity of the wire surfaces. These observations guided the development of a novel light-trapping geometry to further improve the optical absorption of Si microwire arrays.

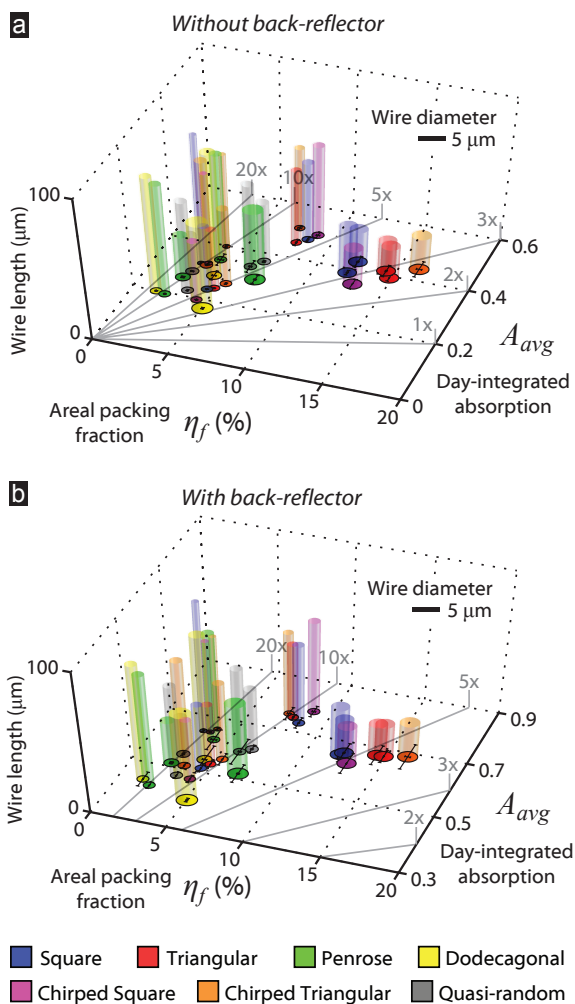


Figure 3.19. Absorption figures of merit vs. array geometry. Plots show A_{avg} values for each wire array of this study: **a**, measured with no back-reflector (quartz slide), and **b**, measured with a Lambertian (BaSO_4) back-reflector. The A_{avg} values are plotted on the y -axis as a function of the areal packing fraction, η_f (x -axis), wire length (cylinder height on z -axis), wire diameter (cylinder width vs. scale bar), and array lattice pattern (by color: red, triangular; blue, square; orange, chirped-triangular; purple, chirped-square; green, Penrose; yellow, dodecagonal; gray, quasi-random). The gray lines indicate $A_{avg} : \eta_f$ ratios of 1, 2, 3, 5, 10, and 20, as labeled. A_{avg} error bars indicate the extent of any sub-bandgap absorption factor; η_f error bars originate from the variance the diameters of the wires in each array.

3.4 Light-trapping in Si wire arrays

To enhance the optical absorption of Si microwire arrays, a novel light-trapping geometry was developed, depicted in Figure 3.20. This geometry enabled our wire arrays to achieve absorption on par with wafer-based Si solar cells, despite using only 1/100th as much Si, and also provided provisions for two key challenges facing the future development of Si wire-array solar cells: Surface passivation and electrical contacting. The effectiveness of these light-trapping measures was immediately evident from visual appearance of the wire arrays, as illustrated in Figure 3.21.

The light-trapping efforts began by applying a SiN_x antireflective (AR) coating to the Si wires. SiN_x is commonly used for this purpose on crystalline wafer-based Si solar cells—not only does it have a well-suited refractive index for an impedance-matching layer, but it can also serve as an effective front-surface passivation layer. A single ~ 80 nm thick SiN_x layer can reduce the front-surface reflectance losses from 35% to 9% in planar Si solar cells, [119, 118] and furthermore, SiN_x coatings can yield front surface recombination velocities below $10 \text{ cm}\cdot\text{s}^{-1}$. [120, 121] In fact, in Chapter 5, we will employ the very same SiN_x deposition procedure to passivate the surfaces of single-wire Si solar cells, enabling them to achieve record efficiencies for VLS-grown photovoltaic materials.

The key element that distinguished our light-trapping microwire-array geometry from other nanowire-array or planar light-trapping schemes was the use of dielectric particles between the wires. These particles served to scatter light that would normally miss the wires, instead redirecting it into the Si for absorption. While conceptually simple, the redirection of light rays that would otherwise miss a solar cell is the fundamental operating principal of geometric optical concentration, and has profound implications on the limiting efficiency of solar cells: Under ideal optical concentration, the limiting efficiency of crystalline Si solar cells is increased from $\sim 30\%$ to 36–37%. [20] High concentration factors can be achieved using conventional optical concentrators (e.g. focusing lenses or mirrors)—but only at the cost of reduced acceptance angle for sunlight, thus requiring these systems to employ tracking mechanisms to follow the path of the

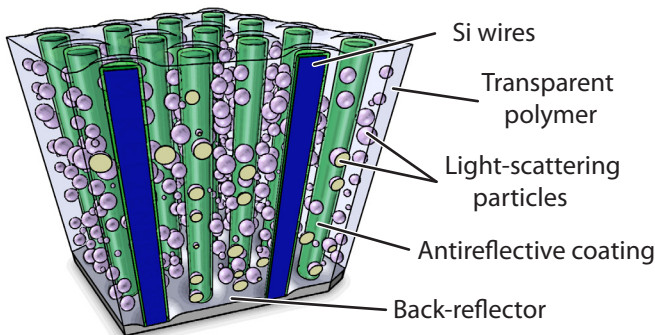


Figure 3.20. Schematic diagram of light-trapping elements in a Si wire array.

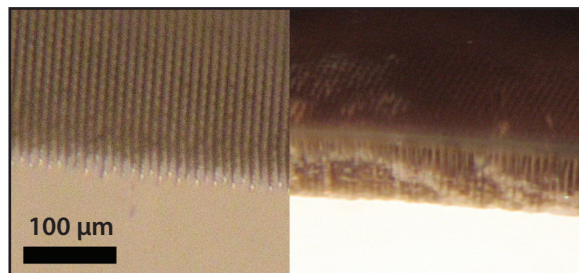


Figure 3.21. Optical micrograph of light-trapping wire array. The image shows peeled-off wire arrays without (left) and with (right) Al_2O_3 light-trapping particles and a-SiN_x:H antireflective coating.

sun across the sky. The randomized light-scattering scheme of our dielectric-particle-infilled wire arrays offers nowhere near these concentration factors, but also presents no restriction of acceptance angle for sunlight—an important requirement for low-cost photovoltaic applications.

The use of random light-scattering materials to fill the voids between active photovoltaic devices is commonly employed at the macroscopic level: Nearly all commercial Si photovoltaic modules feature a diffuse, white backsheet to reflectively scatter the light that falls between the cells, whereupon a significant portion of it is internally reflected within the module to reach the cells. For an encapsulant of refractive index n , this effect can concentrate the light incident upon each cell by up to n^2 ($\sim 2.25\times$ for common encapsulants) if the cells are spaced infinitely far apart. Even modern photovoltaic modules with relatively tightly packed cells benefit slightly (2–3%) from this effect. [122] Similar behavior has also been described at the microscopic level: Yablonovitch et al. demonstrated that films of PMMA-embedded Si granules can achieve high absorption ($\sim 90\%$) despite low packing ($\sim 50\%$) of the optical plane, [85] and it has also been shown that infilling nanowire arrays with a material of higher refractive index can substantially decrease reflectance losses. [73]

Our previous measurements (section 3.3) showed that Lambertian back-reflectors, made from BaSO_4 integrating-sphere paint, were most effective in improving the optical absorption of Si microwire arrays (particularly for normal-incidence illumination). Lambertian back-reflectors lead to ergodic light-trapping in planar structures, [84] and it has been shown that commercial white paint is a better back-reflector material for thin-film photovoltaics than any deposited (or even detached) metallic back-reflector. [123] However, one must also consider that polymer-embedded Si microwire-array solar cells will require electrical contacts to each wire, likely necessitating that the back-reflector material double as a rear electrode (e.g., as envisioned in Figure 5.17). Thus as a pragmatic concession, our light-trapping geometry employed a simple metallic back-reflector, relying instead on the dielectric light-scattering particles to provide the necessary randomization of incident light.

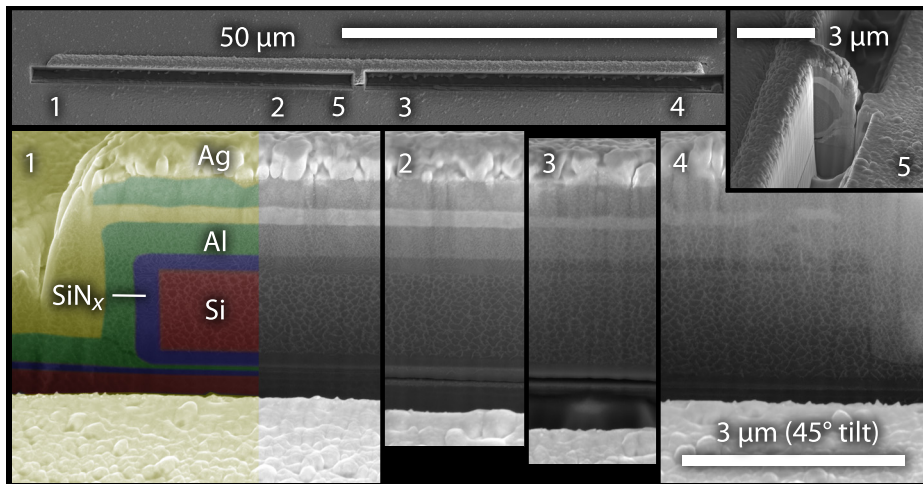


Figure 3.22. Determination of nitride thickness. Lower panels show cross-sectional SEM images taken along the length of a SiN_x -coated wire. The upper panel shows the extent of the wire and indicates the approximate location of each cross-sectional image. Partial false-coloring added for clarity.

3.4.1 Fabrication of light-trapping structures

Antireflective coating. The silicon nitride antireflective coatings were deposited onto Si wire arrays using an Oxford Instruments Plasmalab System100 plasma-enhanced chemical vapor deposition (PECVD) tool. SiH_4 and NH_3 gas chemistry was used at 350°C and 1 torr, at a ratio that had been chosen to yield films with a refractive index near 2.0. The PECVD process was performed with in-situ stress control by alternately pulsing a 13.56 MHz radio-frequency generator and a 50 kHz low-frequency generator, both with 20 W forward power. Due to the large surface area and aspect ratio of the arrays, the coating required a 3–5 \times longer deposition time than would be required for a planar film of the same thickness.

The thickness of the SiN_x coating was measured by SEM, using focused-ion beam (FIB) milling to produce wire cross-sections (Fig. 3.22). Individual wires were removed from the growth substrate and deposited (horizontally) onto a Si wafer that was coated with 80 nm Si_3N_3 (for contrast reference). This was coated with various layers of metal (Ag, Al) to facilitate milling and imaging. The deposited SiN_x thickness was observed to increase gradually along the length of the wires, reaching $\sim 2\times$ the base thickness at the top sidewall of the wire, and $\sim 2.5\times$ the base thickness on the top surface of the wires. The SiN_x thickness appeared uniform around the diameter of the wires.

Multiple-angle spectroscopic ellipsometry was also performed to characterize the optical properties of the PECVD SiN_x , as described in Appendix A.1. Based on these measurements, it was determined that the absorption of an 80 nm nitride film should be negligible ($<2\%$) throughout most of the measurement range in this study ($\lambda > 500$ nm).

Light-scattering particles. Alumina particles were embedded within the PDMS infill of the light-trapping wire arrays, to scatter the light that might otherwise pass between the wires without being absorbed. Al_2O_3 particles ($< 0.9 \mu\text{m}$ nominal particle size) were hydrophobicized via surface functionalization ($> 1 \text{ hr}$ in $10 \mu\text{l/ml}$ trimethylchlorosilane in CH_2Cl_2). After being washed several times to remove excess trimethylchlorosilane, the particles were suspended in CH_2Cl_2 by sonication. This suspension was mixed with uncured PDMS to yield an approximate ratio of 1:10:10 Al_2O_3 : CH_2Cl_2 :PDMS by weight. The suspension was drop cast onto the wire arrays and spun at speeds of 1500–3000 RPM (depending on device area). Prior to curing, the arrays were centrifuged for several minutes to drive the Al_2O_3 particles towards the bottom of the PDMS layer.

To characterize the distribution of the Al_2O_3 particles within the wire arrays, they were sliced in half with a razor blade for cross-sectional SEM imaging. Due to the insulating nature of the PDMS, an environmental SEM was employed, using H_2O vapor at 2–4 mbar to mitigate charging effects. As shown in Figure 3.23, the Al_2O_3 particles were visible between the wires, generally distributed within the lower half of the PDMS film.

The optical properties of the PDMS-embedded Al_2O_3 particles were also measured, to ensure that they did not contribute to parasitic absorption within the Si wire arrays. A drop of PDMS with suspended Al_2O_3 particles was cured on a quartz slide without spinning or centrifuging, to yield a film of thickness comparable to that of the wire arrays ($\sim 300 \mu\text{m}$). As shown in Figure 3.24, the measured absorption was less than 2% throughout the spectral range of this study.

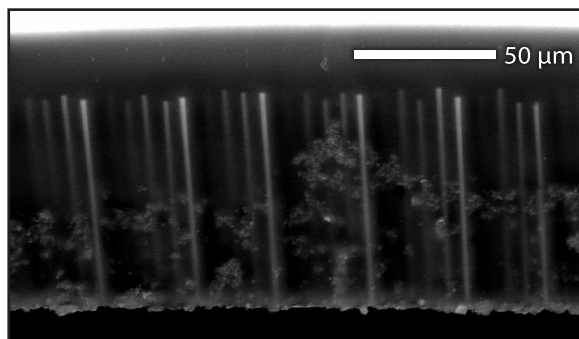


Figure 3.23. SEM image of a wire array infilled with Al_2O_3 particles

Back-reflector. The back-reflector for the light-trapping studies consisted of an optically thick ($> 100 \text{ nm}$) layer of evaporated Ag. To enable the wire arrays to be characterized both with and without the back-reflector, the Ag was evaporated onto quartz slides upon which the devices could be placed, rather than directly onto the back surfaces of the devices. The reflectivity of a Ag back-reflector was plotted in Figure 3.12.

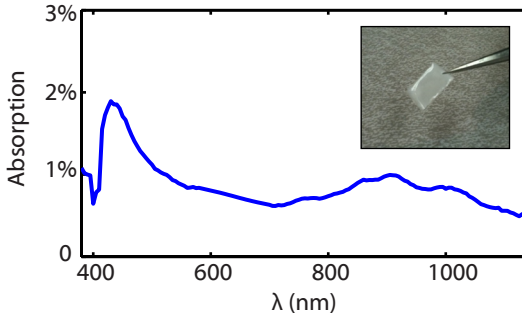


Figure 3.24. Measured optical absorption of PDMS-embedded Al_2O_3 particles. Determined from hemispherical transmission and reflection measurements of a $\sim 300\ \mu\text{m}$ thick film of Al_2O_3 particles embedded within PDMS. Inset: Digital photograph of this specimen.

3.4.2 Optical absorption enhancement

Figure 3.25a shows the measured absorption of a square-tiled array of $67\ \mu\text{m}$ long Si wires with no light-trapping elements. This array had an areal packing fraction of $\eta_f = 4.2\%$, and thus contained the same volume of Si as a $2.8\ \mu\text{m}$ thick planar sheet of Si. As expected, its peak absorption was relatively low at normal incidence (< 0.5), and increased at steeper angles of incidence. The wire array was then placed on a specular Ag back-reflector (Fig. 3.25b), which substantially increased the absorption of the array (approaching peak normal-incidence values of 0.8). However, the normal-incidence absorption remained significantly weaker than that at off-normal-incidence angles. A different portion of this wire array was prepared with the antireflective coating and light-scattering particles described above. As shown in Figure 3.25c, the addition of the light-trapping elements virtually eliminated the angular sensitivity of the wire array's absorption, and increased the peak normal-incidence absorption to 0.92. When placed upon the Ag back-reflector, the array's peak absorption increased to 0.96 (Fig. 3.25d), which is nearly the maximal absorption achievable by any material fully embedded within PDMS (due to the $\sim 3\%$ reflectivity of the PDMS-air dielectric interface).

The figure of merit calculations corresponding to these absorption measurements are plotted in Figure 3.26. Also shown, for comparison, is the A_{avg} calculation that corresponds to the measured absorption of the commercial, $280\ \mu\text{m}$ thick polycrystalline Si solar cell with a dielectric AR-coating. The optimal Si wire array exhibited $A_{\text{avg}} = 0.85$, which although slightly below that of the commercial Si solar cell ($A_{\text{avg}} = 0.87$), is remarkable considering that this wire array film contained $\sim 1\%$ as much Si (per specimen area) as the commercial solar cell. This volume reduction implies substantial optical concentration within the Si wires.

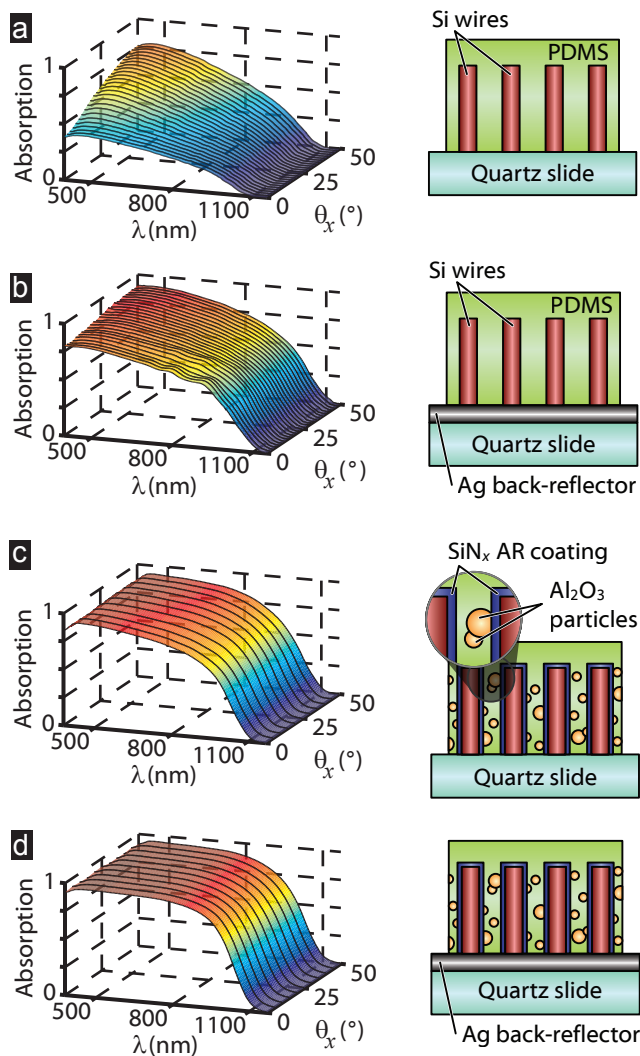


Figure 3.25. Effects of light-trapping elements on optical absorption. Each panel shows the schematic diagram and the measured absorption of a $\eta_f = 4.2\%$ square-tiled wire array; measured without light-trapping elements on (a) a quartz slide and (b) a Ag back-reflector, and with light-trapping elements on (c) a quartz slide and (d) a Ag back-reflector.

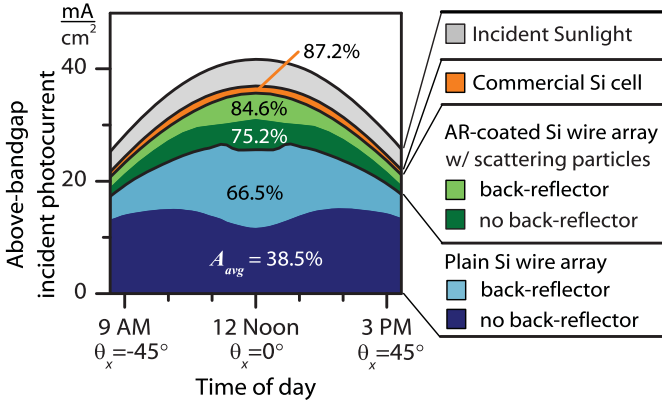


Figure 3.26. A_{avg} of light-trapping Si microwire arrays, corresponding to the absorption measurements shown in Figure 3.25. Also shown is the A_{avg} corresponding to the commercial Si solar cell measured in Figure 3.11.

3.4.3 Comparison to planar absorbers

To further gauge the absorption enhancement of the wire-array geometry, the absorption of the optimal array from Figure 3.25d (A_{WA}) was compared to the theoretical absorption limits of a $2.8 \mu\text{m}$ thick planar Si absorber (which represents the same average volume of Si, per unit area, as the wire array). Following the approaches of section 3.1.3 (ignoring coherence effects) and using tabulated optical properties of Si, [92], two theoretical absorption limits were calculated for the equivalently thick Si slab with an ideal back-reflector: *i*) A_{Si} , corresponding to specular surfaces (black); and *ii*) A_{LT} , corresponding to textured surfaces with ideal (zero) front-surface reflectance (blue). The latter case, the “ergodic limit,” represents the maximally achievable absorption (in the ray optics limit) of a planar-sheet absorber that utilizes ideally random light trapping. [18, 85]

As shown in Figure 3.27 (top), the wire array’s absorption exceeded the planar light-trapping limit for infrared wavelengths ($\lambda > 800 \text{ nm}$). This behavior exemplifies a useful property of micro-structured, non-planar absorber geometries (including wire arrays), in that they can achieve greater absorption per material volume than achievable by a randomly textured, planar-sheet absorber geometry—as described by Yablonovitch, through use of a statistical ray optics model, for idealized films of polymer-embedded Si granules. [85] Similar behavior has also recently been simulated [53] and measured [124] in Si nanowire arrays. Figure 3.27 (lower) illustrates, using the AM 1.5D spectrum [15] at normal incidence, that the enhanced infrared absorption of the Si wire array yielded a greater overall absorption of above-bandgap photons than the equivalently thick, ideally light-trapping planar absorber. In fact, taking all measured incidence angles into account, the day-integrated absorption of the wire array ($A_{\text{avg}} = 0.85$) slightly exceeded that of the planar light-trapping case ($A_{\text{avg}} = 0.82$). Thus, the Si wire array geometry can enable solar cells that reach, and potentially even exceed, the theoretical absorption limit, per volume of Si, of ideal light-trapping within a conventional planar geometry.

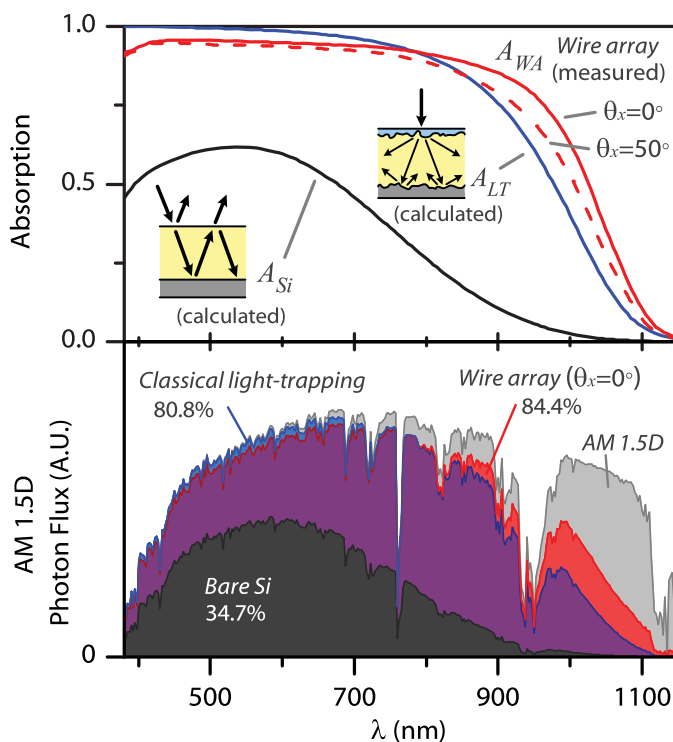


Figure 3.27. Measured absorption of a light-trapping Si wire array vs. the theoretical absorption limits for an equivalently thick planar Si absorber Top: measured absorption (A_{WA} , red) of the Si wire array from Figure 3.25 (which had an equivalent planar Si thickness of $2.8 \mu\text{m}$), at normal (solid) and 50° (dashed) incidence; vs. the calculated normal-incidence absorption of a $2.8 \mu\text{m}$ thick planar Si absorber, with an ideal back-reflector, assuming: *i*) bare, non-texturized surfaces (A_{Si} , black), and *ii*) ideal, randomly textured surfaces (A_{LT} , blue). Bottom: Illustration of normal-incidence, spectrally weighted absorption of the AM 1.5D reference spectrum, [15] corresponding to each of the three absorption cases plotted above.

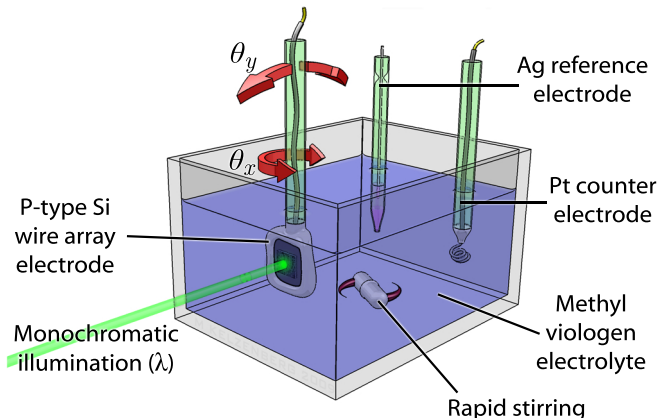


Figure 3.28. Schematic diagram of the photoelectrochemical cell configuration.

3.5 Photoelectrochemical characterization

The enhanced optical absorption properties of Si wire arrays enable high quantum efficiencies for photovoltaic applications. To demonstrate this, we used a photoelectrochemical cell to measure the external quantum efficiency (E.Q.E.) of Si wire-array photoelectrodes, which consisted of p-type wires grown on degenerately doped (and thus photovoltaically inactive [79]) Si wafers. The cell's transparent electrolyte formed a rectifying junction to the top and sides of each wire (analogous to a radial p-n junction), enabling photoelectrochemical characterization of the angle- and wavelength-dependent absorption and charge-carrier collection efficiency of the wire-array electrodes. This enabled the first experimental verification of two key virtues of the Si microwire-array solar cell geometry: (i), that it can operate with nearly 100% internal quantum efficiency, and (ii), that light-trapping can effect dramatic improvements in the performance of a charge-collecting device.

Figure 3.28 depicts the photoelectrochemical cell configuration that was used to measure the angle- and wavelength- dependent E.Q.E. of Si microwire-array electrodes. The electrolyte solution contained 0.5 M KCl(aq) and 0.01 M aqueous methyl viologen redox couple at pH 1 (adjusted with HCl). A detailed account of the operation of this cell and the energy-conversion properties of the p-Si wire-array electrodes has been published elsewhere [125], and the technique has also recently been used to study flexible polymer-embedded wire arrays. [126] The Si microwire-array electrodes were prepared for measurement as follows:

Wire-array growth. Square-tiled, 7 μm -pitch arrays of Si microwires were grown via Cu-catalyzed VLS, in a similar manner as those prepared for optical measurements, with the exception that BCl_3 was present during the VLS growth to produce wires with an estimated p-type doping of $\sim 5 \times 10^{17} \text{ cm}^{-3}$. The arrays were grown by Shannon Boettcher and Daniel Turner-Evans.

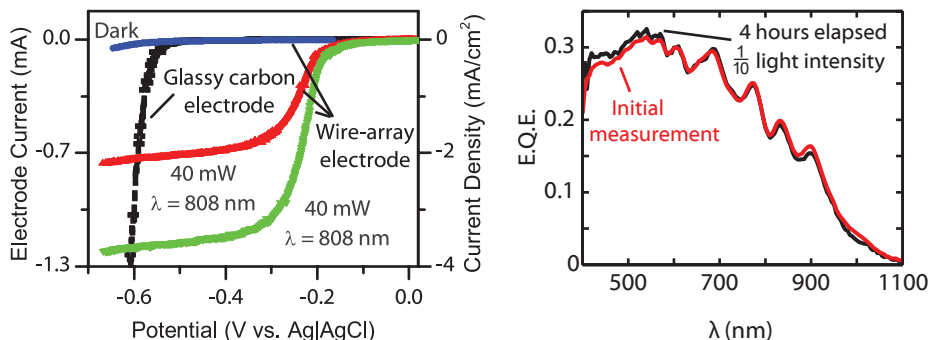


Figure 3.29. Photoelectrochemical J - V (left) and spectral response (right) characteristics of a typical p-Si wire-array electrode.

Catalyst removal. Following growth, the arrays were etched in 10% HF(aq) for 10 s, then in 30% FeCl₃(aq) for 30 min, and finally in 20% KOH(aq) for 1 min at room temperature.

Electrode fabrication. Electrodes were fabricated from ~ 5 mm square portions of the wire arrays, which were affixed to a Cu wire lead using a Ga/In eutectic to make ohmic contact to the back side of the growth wafer, and an epoxy to seal the sides and back of the device. The electrodes were fabricated by Shannon Boettcher and Emily Warren.

Native oxide removal. Immediately prior to measurement, each electrode was etched in 5% HF(aq) for ~ 10 s, then rinsed and placed into the photoelectrochemical cell electrolyte.

Figure 3.29 (left) compares the electrochemical J - V behavior of a p-Si wire-array electrode to that of a photo-inactive conducting glassy carbon electrode. The measurements were performed under illumination from an 808 nm laser diode. For the glassy carbon electrode, the onset of reduction current occurred at approx. -0.55 V vs. the Ag|AgCl reference electrode. Under illumination, the photocurrent onset for the p-Si wire arrays occurred at a significantly more oxidizing potential, approx. -0.15 V vs. Ag|AgCl, implying a photovoltage of ~ 0.4 V for this particular wire array under the test conditions. The spectral response and E.Q.E. of each wire-array electrode were measured at a fixed potential of -0.4 to -0.5 V vs. Ag|AgCl, so as to bias the liquid junction near short-circuit conditions. In this potential regime, the dark current measured at the glassy carbon electrode was negligible while the photocurrent response from the wire array was relatively flat and scaled linearly with incident light intensity. The E.Q.E. measurements were repeated under varying light intensities and chop rates, over a course of several hours, with negligible difference in the recorded data; as shown in Figure 3.29 (right).

The integrating sphere stage motors and illumination source (described in section 3.2.1) were used to provide referenced, monochromatic illumination as

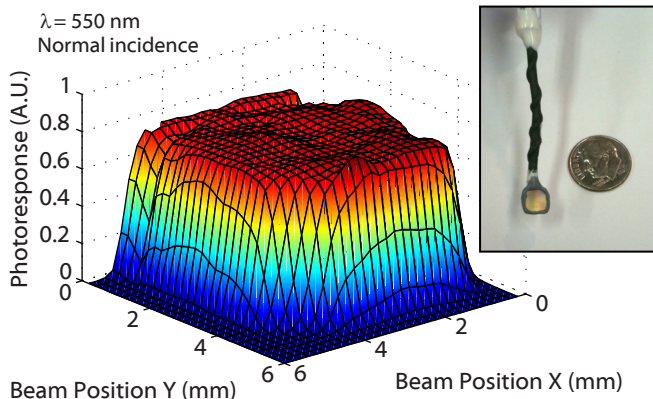


Figure 3.30. Spatial uniformity of the E.Q.E. of a wire-array electrode (pictured, inset).

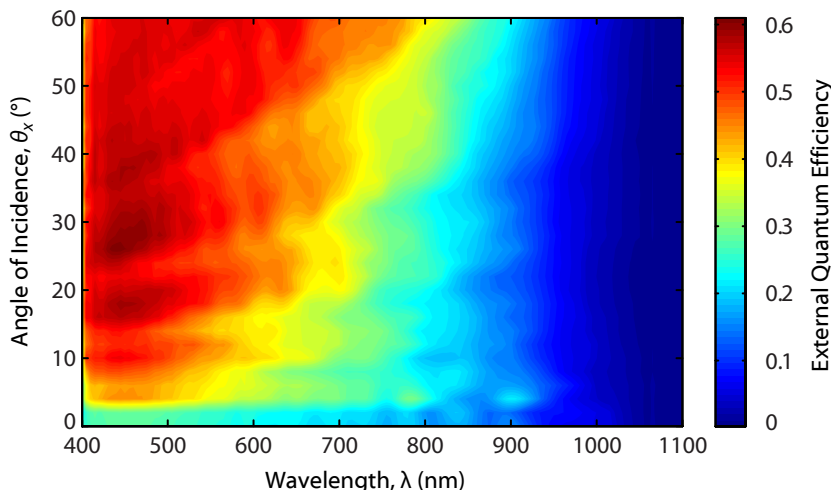


Figure 3.31. Angle- and wavelength-resolved photoresponse of a Si wire-array electrode.

well as motorized articulation of the electrode within the cell. E.Q.E. measurements were performed under chopped ($f = 30$ Hz) illumination using lock-in detection to record the photocurrent from the wire-array electrode (and reject any contribution of dark current) under otherwise dark conditions. The light source provided relatively low illumination levels ($< 10 \mu\text{A}$ beam photocurrent), which avoided mass transport issues within the cell. To determine E.Q.E., the photoresponse of each electrode was normalized to that of a calibrated Si photodiode that had been measured at the same position within the cell, using the approach of equation 3.12.

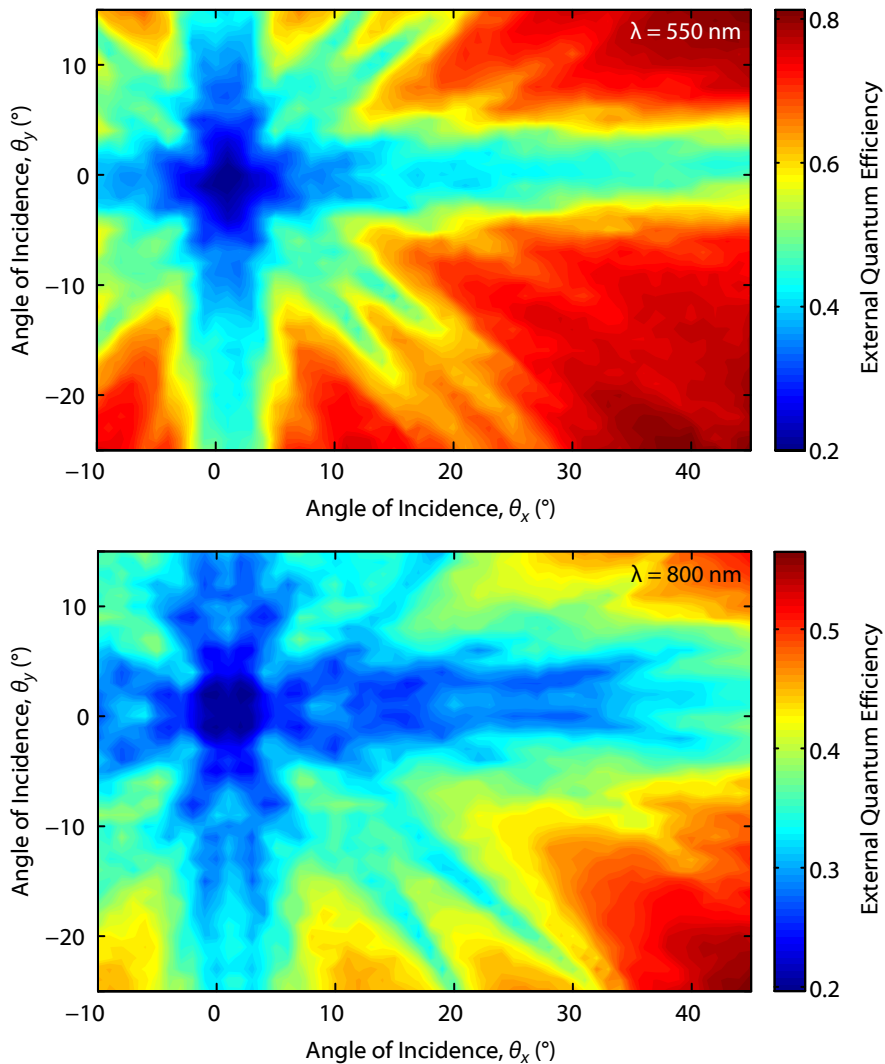


Figure 3.32. Angle-resolved photoresponse of a Si wire-array electrode as a function of incidence angle, measured at $\lambda = 550 \text{ nm}$ (top) and $\lambda = 800 \text{ nm}$ (bottom).

Figure 3.30 demonstrates the spatial uniformity of the E.Q.E. of a Si wire-array electrode. The electrode was rastered across a $\lambda = 550$ nm beam (with a ~ 1 mm² spot size) at normal incidence. No more than $\pm 10\%$ variation in E.Q.E. was observed across the entire device area, indicating excellent uniformity of array geometry and electrical properties. Figure 3.31 plots the E.Q.E. of this same electrode as a function of incident wavelength and angle θ_x . Figure 3.32 shows the two-dimensional, angle-resolved (θ_x, θ_y) E.Q.E. of this electrode at $\lambda = 550$ nm and $\lambda = 800$ nm. The high pattern fidelity of this wire array gave rise to an E.Q.E. profile which was highly dependent on incidence angle, resembling the transmission patterns observed for polymer-embedded, square-tiled wire arrays (Fig. 3.18). The E.Q.E. was substantially lower at illumination angles parallel to the rows or columns of wires within the array. By convention, most of the absorption/E.Q.E. measurements in this study were performed by varying θ_x with $\theta_y \doteq 0^\circ$, which traversed the angles where periodic arrays exhibit minimal absorption/E.Q.E. Thus, many of the wire arrays would exhibit increased absorption/E.Q.E. if they were simply oriented differently within the measurement plane.

3.5.1 Determination of internal quantum efficiency

A particular concern for photovoltaic applications of VLS-grown wire arrays is the possibility of parasitic absorption, which could be caused by the presence of surface states, impurities, or residual VLS catalyst metal deposits. [52] To determine the extent of useful (i.e., non-parasitic) absorption, the internal quantum efficiency (I.Q.E.) of the Si wire-array electrodes was determined by normalizing their measured E.Q.E. to their measured absorption.

Figure 3.33 compares the measured normal-incidence E.Q.E. of a square-tiled, $\eta_f = 3.0\%$ wire-array electrode (blue) to the measured normal-incidence absorption of the wires after being embedded in PDMS and peeled from the growth substrate (black). Due to the similarity between these illumination conditions (e.g. the similar refractive indices of the surrounding PDMS/electrolyte solution), this comparison was used to determine the approximate I.Q.E. of the wire-array electrode (red). The I.Q.E. exceeded 0.9 for most above-bandgap photon energies ($\lambda = 400$ – 900 nm), in good agreement with radial junction theory, which predicts a near-unity I.Q.E. for any wire having a radius less than the minority-carrier diffusion length. Although the reported I.Q.E. declined for $\lambda > 900$ nm, the measured absorption nevertheless differed from the measured E.Q.E. by no more than 0.05 throughout the entire measurement range, confirming that the observed absorption was predominately non-parasitic, while also providing a compelling demonstration of the broadband, near-unity I.Q.E. expected for a radial-junction, Si wire-array photovoltaic device.

To confirm the validity of this experimental method, two control measurements were performed to verify the assumptions that were made in reporting the I.Q.E. After the E.Q.E. of each wire-array electrode had been measured, the wires were embedded in PDMS and peeled-off for optical absorption measurements (to determine I.Q.E.). This exposed the underlying growth substrate,

which was partially covered with layer of residual PDMS and wire stumps from the original wire-array electrode, as shown in Figure 3.34 (inset). This enabled the E.Q.E. of the recovered growth-substrate to be measured under identical conditions in the photoelectrochemical cell, to determine the extent to which it contributed to the apparent E.Q.E. of the wire array. As shown in Figure 3.34, the E.Q.E. of the growth substrate was very low (≤ 0.04) throughout the measurement range, as expected for degenerately doped, p^+ -Si contaminated with VLS-growth catalyst metals. [79] The actual contribution of the growth substrate to the measured E.Q.E. of the wire-array electrodes was likely even less than this, because the wire array would have partially shaded this underlying substrate. Furthermore, a portion of the observed growth-substrate electrode response was likely due to the wire stubs remaining on the growth substrate. This confirmed that the measured E.Q.E. of the wire array electrode corresponded closely to the photoresponse of the wires themselves. As a second control measurement, the reflectivity of the recovered growth substrate was measured in the integrating sphere. As shown in Figure 3.34, the substrate exhibited relatively low reflectivity (0.04–0.16), suggesting that the growth wafer beneath the wire array electrode did not contribute significantly as an optical back-reflector.

These control experiments largely validated our primary assumptions in approximating the I.Q.E. of the wire array electrode by comparing its E.Q.E. (measured on the growth substrate) to the optical absorption of the peeled-off wire array (measured on a quartz slide). Because the optical and electrical prop-

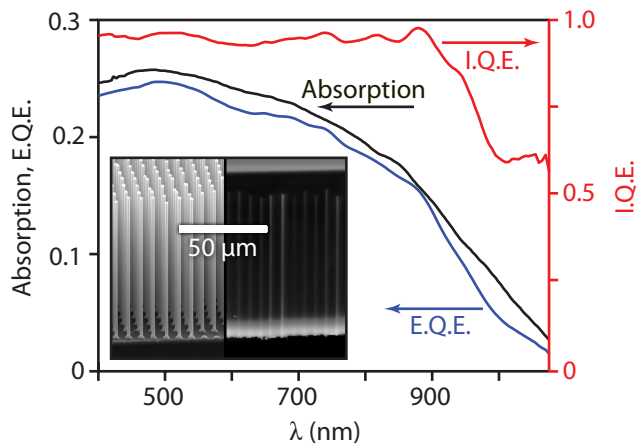


Figure 3.33. Internal quantum efficiency of a Si wire-array electrode, comparing the normal-incidence absorption measurement of the polymer-embedded wire array (black) and the normal-incidence E.Q.E. of the wire-array electrode (blue). The resulting internal quantum efficiency (I.Q.E.) is plotted in red. A 50-nm running average was applied to reduce interference fringes in the experimental data. Inset: SEM images of the wire-array electrode (left) and the polymer-embedded wire array (right).

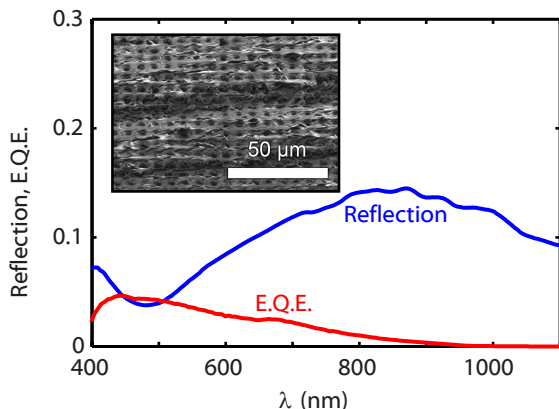


Figure 3.34. Control measurements performed on a recovered growth-substrate electrode, showing the hemispherical reflection (blue), the photoelectrochemical E.Q.E. (red), and a SEM image (inset, 45° tilt) of the device.

erties were ultimately measured in different configurations, it was impossible to account for (or avoid) all sources of experimental error (e.g., if the wires were sheered from vertical during peel-off). We suspect that the reported drop in I.Q.E. at infrared wavelengths ($\lambda > 900$ nm) was due to the experimental differences between the absorption and E.Q.E. measurement configurations, rather than a reduced collection efficiency within the wires at these wavelengths. To help ensure that the wires were oriented at the same angle with respect to the incidence beam, prior to each optical or photoelectrochemical measurement, the illumination incidence angles (θ_x, θ_y) were adjusted to yield the maximum transmission or minimum E.Q.E., respectively. This occurred when the wires were exactly parallel to the incident beam, and provided a reproducible normal-incidence reference point for both measurements.

3.5.2 Enhanced E.Q.E. via light-trapping

The photoelectrochemical characterization technique described above enabled the benefits of light-trapping to be directly observed as an increase in the photoresponse of the Si wire-array electrodes. However, because the wires were immersed in an electrolyte and attached to their growth substrate, the technique did not permit the use of a polymer infill, a dielectric AR-coating, and/or a metal back-reflector—which were integral to the design of the highly absorbing Si wire arrays. Thus, relatively long (130 μm) and sparse ($\eta_f = 6.2\%$) square-tiled wire arrays were grown, to minimize the transmission of light into the photovoltaically inactive growth substrate, while also minimizing the area of the reflective top surfaces of the Si wires. Electrodes were fabricated from these wire arrays, as shown in Figure 3.35 (upper left). This geometry yielded up to 0.85 peak E.Q.E. (lower left), but suffered from substantially reduced E.Q.E. at

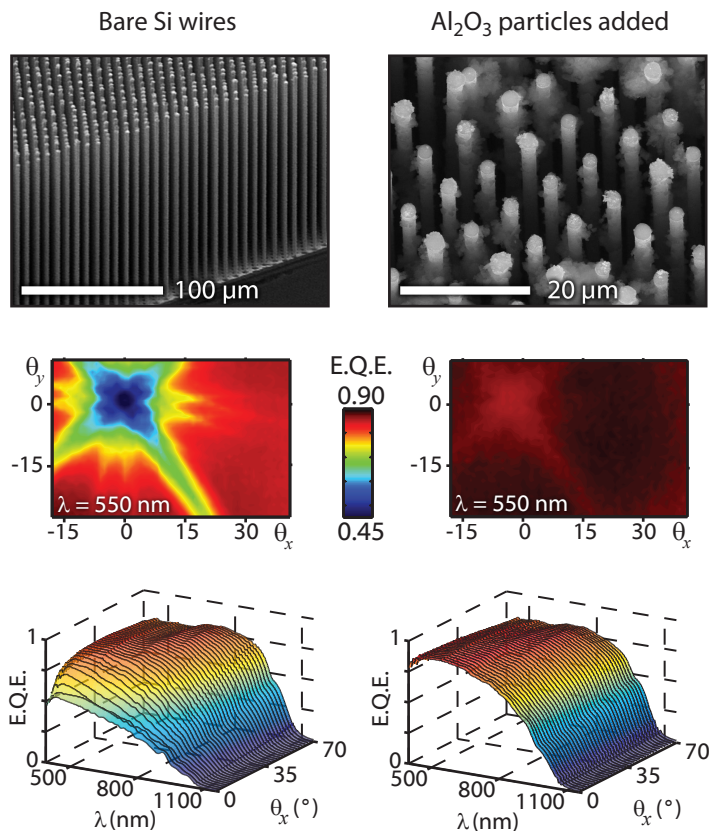


Figure 3.35. Effect of light-scattering particles on wire array electrode E.Q.E. Top: SEM image; center: 2D angle-resolved E.Q.E. at $\lambda = 550$ nm; and bottom: Wavelength-angle-resolved E.Q.E. at $\theta_y = 0^\circ$, of a Si wire-array electrode without (left) and with (right) Al_2O_3 light-scattering particles.

normal incidence (center left). To enhance the E.Q.E. of the wire-array electrode, light-scattering particles were inserted between the wires by dispersing $0.08 \mu\text{m}$ nominal-diameter Al_2O_3 particles into ethanol, placing the wire array electrode at the bottom of this solution, and centrifuging until sufficient particle density was observed at the base of the wire array (Fig. 3.35, upper right). The electrodes were lightly rinsed with isopropanol and water, then returned to the photoelectrochemical cell for E.Q.E. measurements. (No substantial loss of the Al_2O_3 particles was observed during the course of these measurements.)

As shown in Figure 3.35 (center right), the addition of the Al_2O_3 light-scattering particles virtually eliminated the normal-incidence “dead spot” in the wire array’s photoresponse, and increased the peak E.Q.E. to 0.89 (lower right). Figure 3.36 plots these E.Q.E. measurements weighted across the day-integrated solar spectrum (following the calculation of A_{avg} above). The effectiveness of

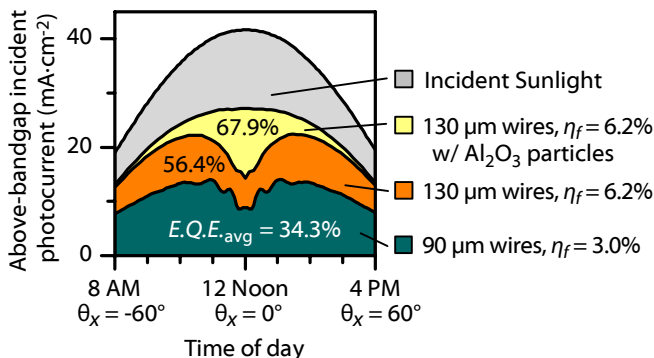


Figure 3.36. E.Q.E. figures of merit for Si wire-array electrodes.

the light-scattering particles is evident in the dramatic improvement of the photoresponse near normal incidence, and increased the $E.Q.E._{avg}$ of this wire array from 0.56 to 0.68. This value is significant, considering that the photoelectrochemical cell configuration precluded the use of a metal back-reflector or an antireflective coating, both of which were shown to substantially improve the optical absorption (Fig. 3.25), and both of which could be employed within a solid-state, radial p-n junction wire array solar cell. Thus, the results presented here represent lower bounds, rather than upper limits, on the E.Q.E. that could be achieved by use of the Si wire-array geometry.

3.6 Discussion and outlook

In this chapter, we have experimentally demonstrated that Si microwire arrays have advantageous optical properties for photovoltaic applications, including reasonable absorption of sunlight despite low areal packing fractions, extended near-infrared absorption compared to planar-sheet absorbers, and effective optical concentration over a wide range of incidence angles. By placing dielectric light-scattering particles between the wires, combined with antireflective layers and back-reflectors, we demonstrated a wire array with nearly 96% peak absorption of visible light, as well as 85% overall absorption of above-bandgap sunlight—even though the wires only occupied about 4% of the specimen plane (or approximately 1/100th as much Si as a conventional wafer-based solar cell). Our photoelectrochemical characterization of Si microwire-array electrodes validated that the observed absorption enhancements led to performance gains in a charge-collecting device, while also providing a novel experimental demonstration of the near-unity internal quantum efficiency predicted for the radial-junction geometry.

The observed absorption enhancement and collection efficiency suggest that Si wire array solar cells can benefit from the well-known improvements in open-circuit voltage (and thus photovoltaic efficiency) that are achievable under effective optical concentration. When sunlight illuminates a wire array, the absorption is laterally confined within the relatively small cross-sectional area of

the wires. In this regard, the $\eta_f = 4.2\%$ wire array that exhibited $A_{\text{avg}} = 0.85$ (Fig. 3.26) can be considered, to first order, as a $24\times$ lateral geometric concentrator that achieved a $20\times$ average intensity concentration without the use of conventional focusing optics.

Perhaps the most surprising result of these studies was that three-dimensional structure of the Si microwire arrays allowed them to absorb slightly more sunlight, per volume of Si, than would be possible with conventional light trapping in a planar geometry. This behavior suggests a potentially tremendous opportunity to increase optical concentration within micro- or nano-structured photovoltaics well beyond the limits of classical isotropic light-trapping. Several theoretical studies have discussed the enhanced photogeneration rates in nanowire array absorbers, [53, 127] and a recent study by Garnett et al. has experimentally confirmed that Si nanowire arrays can exceed the $2n^2$ ergodic light-trapping limit. [124] These and other promising achievements represent a compelling and rapidly growing area of photovoltaics research.

Finally, we note the observations reported herein are not limited to Si microwire-array solar cells: wire-array geometries, along with other micro-structured, non-planar absorber geometries (e.g., the sliver cell, [28] Si microcells, [29] or nanopillar-array cells [128]), offer unique opportunities to manipulate the ratio of illumination area to absorption volume, and may be useful in improving the efficiency or reducing the materials consumption of many photovoltaic technologies.

Bulk electrical properties of Si microwires

Although silicon is the most abundant solid element in Earth’s crust, producing crystalline Si material of suitable quality and purity for photovoltaic applications remains one of the most challenging and costly aspects of solar cell manufacturing. [12, 9] Certain impurities, namely dopants, are required to form the p-n junctions to which solar cells owe their photovoltaic behavior. However, most impurities will hinder the performance of Si solar cells—many at concentrations well below one part per billion, [129, 130] and some defects and impurities can further lead to light-induced degradation of solar cell performance. [131, 132, 133]

The proposed Si microwire-array solar cell seeks to reduce the cost of photovoltaics by exploiting the potentially inexpensive vapor-liquid-solid (VLS) method of crystal growth for the production of Si material. Thus, the key requirement of the VLS growth process is that it be capable of producing high-quality Si with well-controlled electrical properties. In this chapter, we present techniques that were used to characterize and optimize the electrical properties of VLS-grown Si microwires, thereby enabling high photovoltaic performance.

4.1 Introduction

The most important bulk property of crystalline Si for photovoltaic applications is the *minority-carrier lifetime*, τ . This parameter determines the rate of minority-carrier recombination and generation that gives rise to the dark current in p-n junctions, which limits the open-circuit voltage and fill factor of p-n junction solar cells. Furthermore, the lifetime of minority carriers determines how far they can diffuse before recombining, and thus whether or not they can reach the p-n junction of the solar cell to be collected as current. This characteristic length is the *minority-carrier diffusion length*, L :

$$L = \sqrt{\tau D} \quad (4.1)$$

where D is the diffusion coefficient for the minority carriers. Because semiconductors can exhibit a great range of minority-carrier lifetimes and mobilities (and thus D), L provides a useful metric by which to gauge the relative quality of these materials for photovoltaic applications.* Even within crystalline Si, electrons and holes have slightly different mobilities, and impurities mildly affect the mobility of both carrier types. Thus the relationship between L and τ

*An equivalent, frequently-cited metric of material quality is the *mobility-lifetime product*, $\mu\tau$, from which L can be calculated as: $L = \sqrt{\mu\tau \frac{kT}{q}}$.

Table 4.1. Typical minority carrier diffusion lengths for silicon.

Technology	Silicon material	L
Wafered	Research-grade monocrystalline (FZ)	0.5–3 mm [134, 135]
	Production-grade monocrystalline (CZ)	100–300 μm [9, 135]
	Multicrystalline Si (cast)	30–100 μm [9, 135]
Thin-film	Polycrystalline	1–10 μm [14]
	Micro-, nano-crystalline	0.5–2 μm [136, 137]
	Amorphous (hydrogenated)	100–300 nm [138, 139]

FZ: Float-zone refining. CZ: Chochralski pulling.

varies slightly depending on the carrier type and doping density. Nonetheless, for crystalline Si photovoltaics, these two quantities are interchangeably used as ubiquitous descriptors of material quality: the longer the lifetime or diffusion length, the better the material (and typically, the more expensive it is to produce). Typical values of L for Si solar cells are shown in Table 4.1.

Crystalline silicon for wafer-based photovoltaics is traditionally produced in two steps: the decomposition of highly purified chlorosilanes (HSiCl_3 , SiCl_4) to form polysilicon feedstock (e.g., the Siemens process), followed by the melting and recrystallization the Si feedstock either as cast multicrystalline ingots, or as monocrystalline boules by Czochralski pulling (CZ) or float zone (FZ) refining. [9, 48] The recrystallization step plays a critical role in the purification of the Si: Because impurities are more soluble in the liquid melt than in the crystal, they become preferentially segregated from the crystal at its growth front. [140] The purification achieved through recrystallization is determined by the *segregation coefficient* of each impurity species, which specifies the ratio of its concentration within the crystal to that within the melt. Metals are a common class of impurities that plague crystalline Si for photovoltaics and microelectronics, but conveniently, many of the most deleterious metal species have segregation coefficients below 10^{-4} . [130, 141] In addition to the segregation of undesired impurities, the recrystallization step also provides the opportunity to introduce the desired impurities to dope the Si crystal by adding them directly to the melt (typical for casting or CZ pulling).

The production of crystalline Si wires via the VLS growth technique bypasses the traditional two-step decomposition/recrystallization process, and is thus a promising route to reduce the cost of Si production. In a single chemical vapor deposition (CVD) step, the SiCl_4 feedstock is both decomposed at the metal catalyst tip, and subsequently crystallized into the growing wire. This presents a major challenge from the standpoint of material purity: Whereas traditional crystal growth begins with a melt of highly purified polysilicon, VLS growth begins with a melt composed entirely of catalyst metal. During growth, the metal impurity concentration within the catalyst eutectic melt inherently remains several orders of magnitude larger than that within a traditional polysilicon melt. Thus, the incorporation of catalyst metal impurities may be so great

that its concentration is effectively limited by the metal's solid solubility limit in Si rather than by its segregation coefficient, or by other dynamics unique to VLS growth. [142] This fact necessitates careful selection of catalyst metals and growth conditions to obtain high-quality Si.

The introduction of the dopants can also present a challenge for VLS growth. In traditional casting or CZ pulling, the crystal is grown from a fixed volume of feedstock melt, which allows uniform doping to be achieved by mixing a calculated amount of the dopant species into the melt prior to growth. In VLS growth, the crystalline Si material is produced by a much smaller volume of catalyst eutectic melt that is continuously replenished with Si. Achieving uniform doping thus requires either a gas-phase dopant source that is also replenished during growth, or a solid/liquid-phase dopant source within the initial catalyst melt that has sufficient segregation properties so as to effect the desired doping density throughout the duration of crystal growth without replenishment. The latter may be achieved by explicitly adding dopants to the catalyst metal material, or by simply using a catalyst species which itself acts as a dopant in Si (such as Al). [143, 144]

Regardless of the method used to synthesize photovoltaic materials, the quality and impurity content of the resultant material is of utmost importance to any solar cell technology. This chapter is devoted to characterizing these properties of our VLS-grown Si microwires. As with most crystalline Si photovoltaics, subsequent processing will further improve the material quality, impurity content, and doping profiles of our wires; including bulk/surface defect passivation, impurity gettering, and diffusion doping—these topics will be discussed in Chapter 5.

4.2 Fabrication of single-wire test structures

Numerous characterization techniques have been used to directly study the crystal quality and impurity content of VLS-grown Si wires, including transmission electron microscopy (TEM), [35, 39, 145, 146] secondary-ion mass spectrometry (SIMS), [80] and local electrode atom probe (LEAP) tomography. [147, 148] However, it is the favorable electrical properties resulting from good crystal quality and purity that are ultimately desired for photovoltaic devices. These properties can be observed using electrical measurement techniques that necessitate means of contacting the wire(s) with electrodes. Early work on macroscopic, VLS-grown crystals (typically referred to as *whiskers* or *filamentary crystals*) employed fairly conventional techniques to obtain electrical contacts, such as soldering wire leads to either end of a wire. [142] Forming contacts to individual Si nano- or microwires, due to their small size, requires more advanced fabrication techniques to produce single-wire measurements. The following techniques were investigated:

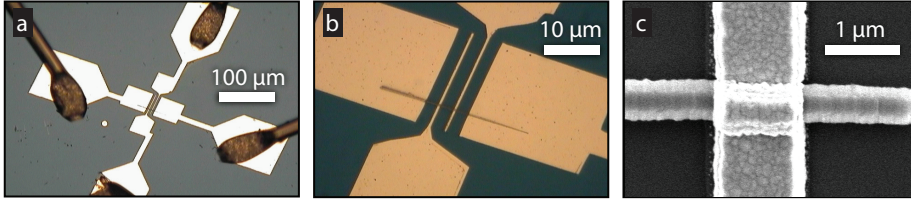


Figure 4.1. Typical single-wire device fabricated by e-beam lithography. **a**, **b**, Optical micrographs of a packaged, wire-bonded single-wire device with four-point contacts. **c**, SEM image of a single contact. *Images taken with permission from [39, §3.5].*

4.2.1 Electron-beam lithography

The challenge of defining sub-micron features such as nanowire electrodes is easily overcome by the high-resolution patterning capability of electron-beam (e-beam) lithography. Single-wire devices can be fabricated by removing wires from the growth wafer, placing them (horizontally) on insulating substrates, and then covering them with a uniform layer of electron-sensitive resist to allow patterning. In the surge of semiconductor nanowire research throughout the past decade, e-beam lithography has remained the most widely used method of fabricating single-wire devices, and was used in the vast majority of single-wire work cited elsewhere in this thesis. [149, 150, 151, 152, 153, 154, 155, 156, 157, 147, 158, 159, 160, 161, 162, 163, 164, 165] These studies include numerous examples of e-beam lithography: It has been used to fabricate various types of self- and manually aligned nanowire electrodes, as well as to mask portions of individual nanowires for etching, surface modification, deposition, and ion-implantation procedures.

Given the well-established practice of using of e-beam lithography to fabricate single Si nanowire devices, we selected this technique for our initial studies of Si nanowires grown from SiH_4 . This work was described in greater detail in Brendan Kayes' PhD thesis. [39, §3.5] The nanowires were first removed from the growth substrate by sonication in isopropyl alcohol (IPA), and were dispersed onto degenerately doped (n^+) Si wafers coated with 100 nm Si_3N_3 . The wafers were then coated with a double layer of poly(methyl methacrylate) (PMMA) e-beam resist, and patterned using a SEM instrument outfitted with e-beam lithography capabilities. The patterned wafers were developed in solutions of methyl isobutyl ketone (MIBK) and IPA, opening contact windows over each nanowire for metallization. The electrodes were formed by thermal evaporation of Cr (5 nm) and Ag ($\sim 1 \mu\text{m}$) followed by lift-off, resulting in electrically contacted single-wire devices like that shown in Figure 4.1.

Aligning the electrode patterns to individual nanowires by e-beam lithography presented several challenges. The devices required relatively thick Ag contacts ($\geq 1 \mu\text{m}$) to ensure electrical continuity around the sides of each wire, as well as to hold the wires to the substrate during lift-off. This in turn necessitated the use of a thick PMMA layer ($\geq 2 \mu\text{m}$), which led to extended write times with

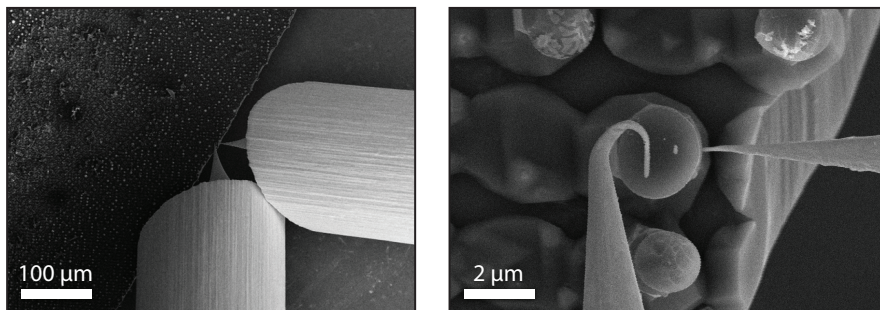


Figure 4.2. Single Si wire contacted using nanoprobe instrument. SEM images show the use of two W nanoprobe tips to characterize the I - V behavior of a single, $\sim 10\ \mu\text{m}$ tall Si microwire, viewed from above. The probe at the bottom of the image sourced current through the catalyst tip of the wire, and the probe to the right sensed voltage $\sim 2\ \mu\text{m}$ below the wire tip. The substrate wafer was grounded and served as both the current sink and the voltage reference.

our instrument (up to several hours per device). The wires also proved to be difficult to locate, because they were barely visible beneath the thick PMMA layer during SEM imaging. To compound matters, while searching for wires the imaging beam simultaneously exposed the PMMA, providing only a brief window of opportunity in which to successfully locate and pattern each device. To partially alleviate this dilemma, a low beam current ($\sim 20\ \text{pA}$) was used for imaging, and a higher beam current ($\sim 200\ \text{pA}$) was used for exposure. However, as our research interests tended toward larger-diameter Si wires, the anticipated requirements of thicker PMMA layers, greater imaging difficulty, and longer exposure times led us to investigate alternative higher-throughput means of contacting single Si microwires.

4.2.2 Nanoprobe

A nanoprobe instrument equipped with a SEM (Omicron) enabled us to directly contact our Si wires with tungsten probe tips in an ultrahigh vacuum environment. An example of this procedure is shown in Figure 4.2. This instrument featured up to 4 etched W probe tips with sub-micron positioning capability, in theory, allowing four-point current-voltage (I - V) measurements to be performed on individual wires in virtually any configuration—including as grown (oriented vertically) on the growth wafer, which was not possible with lithographic contacting strategies. [166] This instrument also permitted qualitative observations of the mechanical properties of the wires: typical Si microwires of 1 – $2\ \mu\text{m}$ diameter and 50 – $100\ \mu\text{m}$ length appeared to be elastically deformed by the application of force by the probe tip. In fact, these wires could be bent to form a complete arch (the wire tip contacting the growth substrate) without fracturing, and appeared to return to their original vertical orientation when released.

Despite this seemingly straightforward approach to single-wire electrical measurements, we encountered several practical limitations that precluded its use as our primary means of performing single-wire measurements. The greatest impediment to our use of the instrument was low throughput: loading new specimen or probe tips into the instrument required a ~ 12 -hour pump-down cycle, and positioning the probe tips became increasingly difficult, if not impossible, with more than two of our etched W probe tips. The reason for this can be seen in Figure 4.2: although each probe tapered to a sharp point, the large-diameter W wires from which they were etched would often collide with one another, or with the substrate wafer, before the tip reached the Si wire of interest. In shuffling the tips between the four positioning stages to find non-interfering probe/specimen combinations, they were frequently damaged by inadvertent collisions during the exchange or approach sequences, requiring an additional load/unload pump-down cycle to be replaced. Furthermore, the I - V behavior of the wires and contacts was observed to vary depending on how much force was applied by the probe, and it was not clear whether this was due to a changing contact surface area, or changing electrical properties due to strain. While the nanoprobe provides a robust environment in which to investigate these phenomena, such was not the goal of our study.

4.2.3 Photolithography

Photolithography has been less-frequently employed than e-beam lithography amongst the single-wire device studies cited elsewhere in this thesis, [167, 168, 169] but quickly emerged as our preferred technique for the fabrication of single-wire test structures. Photolithography offered two key advantages over the e-beam-lithography technique described above: Photoresist is sensitive only to ultraviolet light, allowing the use of the mask aligner's optical microscope to locate individual wires without the risk of unintentional exposure, and with much greater ease due to the transparency of the resist at visible wavelengths and the large view field of the microscope. Furthermore, using photolithography, the entire pattern is exposed at the same time using masked flood-illumination (vs. serialized e-beam-scanning), reducing the duration of each exposure from hours to seconds. By using a positive photoresist, we were still able to pattern multiple (in fact, up to ~ 30) single-wire devices on each wafer fragment loaded into the mask aligner. And despite the lower resolution of photolithographic patterning and optical microscopy (vs. e-beam lithography and SEM), we were nonetheless able to contact single-nanowire devices with diameters as low as ~ 200 nm. For these reasons, photolithography proved to be an invaluable tool for high-yield, high-throughput production of single-wire test structures, and was used to fabricate the remainder of single-wire devices presented in this thesis. The general procedure used to fabricate single-wire devices using photolithography was as follows:

Removal from growth substrate. Following VLS growth, the Si wire arrays were removed from the growth substrate and suspended in IPA using sonication or, if necessary, a razor blade.

Transferal to device substrate. The solution of suspended wires was deposited onto degenerately doped, n-type Si wafers coated with 100 nm of Si_3N_3 ($\rho < 0.01 \text{ } \Omega\text{-cm}$, 3" Si(100), International Wafer Service), and was allowed to air dry while spinning at 100–300 rpm to distribute the wires. This process was repeated as necessary (1–5 times) to yield the desired density of randomly oriented wires lying flat on the substrate surface.

Application of photoresist. The device substrates were then coated with a double-layer photoresist film, consisting of a lift-off resist (LOR3A or LOR10A, Microchem; spun at ~ 1500 rpm for 1 min, then baked at 185°C for 5 min) covered by a positive imaging resist (S1813, Microchem; spun at 3000 rpm for 1 min, then baked at 115°C for 2 min). The lift-off resist produced an undercut profile when developed, which was required for successful lift-off of metal films exceeding ~ 500 nm thickness. The resist-coated device wafers divided into smaller samples ($\sim 1''$ square) for patterning.

Alignment, exposure, and development. The electrode patterns were aligned to individual wires and exposed using a conventional optical mask aligner (MA6, Karl Suss; 15 s exposure at $15 \text{ mW}\cdot\text{cm}^{-2}$ I-line intensity or equivalent). Numerous devices were patterned on each sample, after which the resist was developed (MF-319, Microchem; 90–300 s as needed), then rinsed in H_2O .

Contact metallization. Immediately prior to metallization, the samples were immersed in aqueous buffered HF for 5–20 s to remove the native oxide from the exposed portions of the wires. The contact metals were then deposited by thermal evaporation of ≥ 300 nm Al (chosen for its ability to form ohmic contact to Si), followed by as much Ag as needed (≥ 200 nm) to bring the total metal thickness to 1200–1500 nm, which was necessary to fully cover the larger-diameter wires and to provide a more favorable metal surface for wire bonding.

Lift-off. Lift-off was performed by immersion in photoresist remover (Remover PG, Microchem) for 30 min to 12 h (as necessary) at 60°C . The devices were sequentially rinsed with acetone, IPA, ethanol, and then H_2O .

Two primary factors limited the range of wires that could be contacted with this technique. Wires smaller than ~ 200 nm in diameter could not be seen in the optical mask aligner, and wires larger than $\sim 2.2 \text{ } \mu\text{m}$ were typically lost to adhesion failure during lift-off. Single-wire devices that were fabricated using this technique are featured in Figures 4.3, 4.7, and 5.3; and appear throughout Chapter 5.

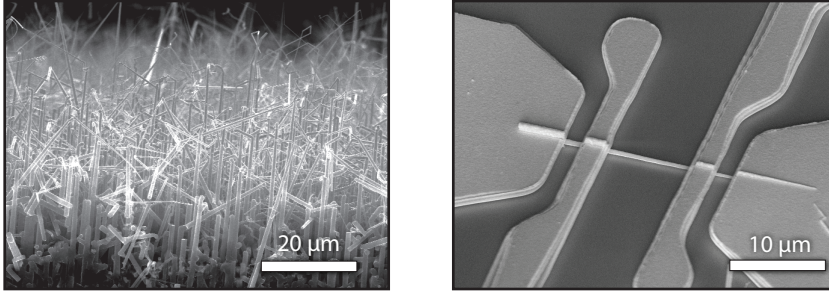


Figure 4.3. SiH₄-grown wires and single-wire devices. **Left:** SEM image of the wires produced by VLS growth from SiH₄ using evaporated (non-patterned) Au catalyst (taken at 90° substrate tilt). **Right:** SEM image of a four-probe contacted single-wire device (taken at 45° substrate tilt).

4.3 Properties of Si wires grown from SiH₄

Silicon nanowires were grown for single-wire characterization using a gold-catalyzed VLS process in a low-pressure CVD (LPCVD) reactor with SiH₄ gas chemistry. The growths were performed by Brendan Kayes; further details can be found in his PhD thesis. [39, §3.4] Si(111) growth wafers were prepared by cleaning for 10 min in a 5:1:1 solution of H₂O:H₂O₂:NH₄OH, at ~80 °C, then for 10 min in a 6:1:1 solution of H₂O:H₂O₂:HCl, and then for 20 min in buffered HF before being transferred to a thermal evaporator, in which 5 nm Au was deposited to provide the catalyst particles for VLS growth. Three batches of Si wires were grown to produce wires of different doping types and densities using phosphine (PH₃) or trimethyl boron (TMB; B[CH₃]₃) as in-situ n- or p-type dopant sources, respectively. CVD was performed using SiH₄ (5% in Ar) at 1 Torr; under the flow rates (F), growth temperatures (T), growth times (t_g), and dopant species gas concentrations listed in Table 4.2.

Figure 4.3 (left) shows a SEM image of the p-type wires that were grown by this procedure. Four-probe Al/Ag electrodes were patterned to individual wires using the procedures for photolithography, metallization, and lift-off described in section 4.2.3, using a photomask pattern with 10 μm spacing between the

Table 4.2. Growth conditions for SiH₄-grown Si wires.

Doping	F (sccm)	T (°C)	t_g (h)	Impurity	P_{base} (Torr)
Unintentional	100	550	6	—	5.4×10^{-6}
p-type	100	500	12	141 ppm B(CH ₃) ₃	2×10^{-7}
n-type	50	500	12	5 ppm PH ₃	3×10^{-7}

P_{base} : Reactor base pressure prior to growth.

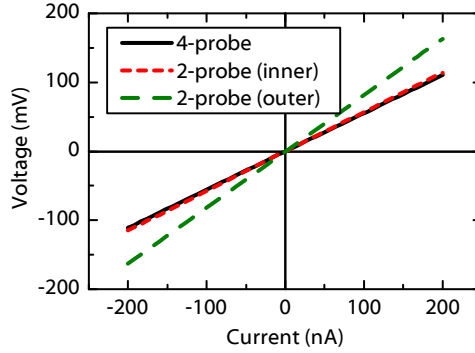


Figure 4.4. I - V characteristics of the SiH_4 -grown wire device shown in Fig. 4.3.

inner electrodes. A typical p-type single-wire device is shown in Figure 4.3 (right), exemplifying the visible taper in wire diameter that was typical of SiH_4 -grown wires.

The four-probe electrode configuration allowed the current-voltage (I - V) behavior of the central wire segment to be measured independently of any resistance of the contacts. [47, p. 30] A source meter unit (KI236, Keithley) was used to source electrical current (I) between the outer contacts to the wire while recording the voltage (V) between the inner contacts. The high input impedance ($> 10^{14} \Omega$) of the voltage-sense circuitry ensured that virtually no current flowed from the inner contacts, allowing the true voltage of the wire to be measured even if the contact resistance was large. By combining two-, three-, and four-probe I - V measurements, we were able to characterize the behavior of the wire and both inner contacts for each fabricated device.

Figure 4.4 plots the measured I - V characteristics of a p-type single-wire device. The similarity between the two-probe (inner) and four-probe I - V characteristics confirms that the contacts were ohmic (i.e., low-resistance and non-rectifying). Ohmic contact behavior was typically observed for the n-type and p-type wires, whereas the unintentionally doped wires exhibited non-linear contact I - V behavior (which necessitated four-probe measurements to determine the wire resistance). To determine the carrier type of each wire, the underlying n^+ Si wafer was used as a gate electrode to induce field-effect modulation of the wire resistance (see, for example, [149]). Using four-probe I - V measurements, the wire resistance was determined as a function of gate bias voltage ranging from -50 V to $+50$ V. Depending on the carrier type of the Si wires, the gate field effect induces either accumulation or depletion of carriers along the bottom of the wire, which manifests as an increasing (p-type) or decreasing (n-type) wire resistance at positive gate voltages.* Back-gated measurements confirmed the expected carrier types of our n-type and p-type wires (Fig. 4.5), and revealed that the unintentionally doped wires were p-type.

*Traditional field-effect transistor behavior (i.e., inversion) was not observed in our wires, possibly due to the thick gate oxide (100 nm Si_3N_3), the combination of a back-side gate with top-side wrap-around electrodes, or the particular electrostatics of nanowire transistors. [170]

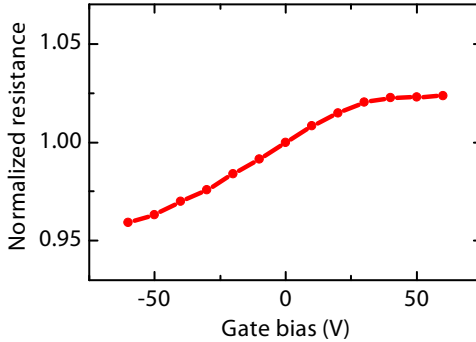


Figure 4.5. Field-effect resistance modulation in a SiH_4 -grown single-wire device. The device exhibits p-type behavior.

Combining the measured resistance (R) and the dimensions of each wire allowed us to calculate the effective bulk resistivity of the Si (assuming that resistivity was homogeneous throughout the wire):

$$\rho_{\text{eff}} = \frac{\pi d^2 R}{4l} \quad (4.2)$$

where d is the wire diameter and l is the length of the wire enclosed by the inner contacts, both observed by SEM. In the case of wires that exhibited substantial tapering in diameter, the geometric mean of the diameter at each end of the wire was used for d in (4.2). The resistivity of each wire was used to determine the effective doping concentration, $N_{D,\text{eff}}$ or $N_{A,\text{eff}}$, for n-type and p-type wires, respectively, using the well-known relationship between doping concentration and resistivity for Si. [47, p. 32] The effective doping concentrations of our SiH_4 -grown single-wire devices is plotted in Figure 4.6. The effectiveness of the in situ doping procedure is evident in the distribution of N_{eff} : the measured values spanned over six orders of magnitude, but typically varied by less than two orders of magnitude within each doping type.

There are several potential reasons why the carrier concentration in Si nano- or microwires may not be homogeneous as was assumed in calculating the effective doping concentrations of Figure 4.6. Several studies have found evidence of radial variation in dopant incorporation within VLS-grown Si nanowires. [164, 165, 171] Furthermore, the presence of trapped surface-state charge can induce accumulation or depletion of free carriers near the wire surfaces, effectively altering the radial carrier profile (but not the doping profile) of the wires. [151, 168] Either of these effects could manifest as an increasing or decreasing N_{eff} as a function of wire radius. However, this was not observed (within the degree of measurement variation) in our wires, leading us to conclude that the carrier profiles were likely reasonably homogeneous in our wires (i.e., within 1–2 orders of magnitude). Axial variations in dopant concentration have also been observed in VLS-grown Si nanowires, [162] which could be indicated by the observed vari-

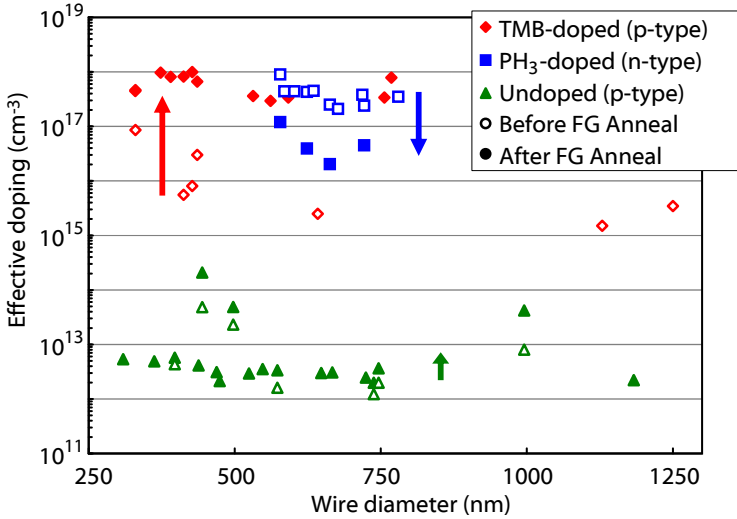


Figure 4.6. Effective electrically active doping concentration and carrier type observed in SiH_4 -grown wires, as a function of wire diameter and in situ dopant source. The arrows indicate the approximate change in behavior observed following a 300°C anneal in forming gas.

ations in N_{eff} for each wire type. Because our SiH_4 -grown wires were highly disordered as grown, it was not possible to determine whether each single-wire device comprised a wire segment representative of the base or the tip region of the original wires.

To further investigate the electrical properties of our SiH_4 -grown Si wires, we annealed the single-wire devices in forming gas (5% H_2 in N_2) for 1 h at 300°C . The electrical resistance of each type of wire was observed to change in a consistent manner, leading to different values of N_{eff} as shown in Figure 4.6. Because our I - V measurements employed a four-probe technique, this behavior could not be attributed to a change in contact resistance brought about by annealing. It was also unlikely that the change in N_{eff} was caused by activation of previously inactive dopants: this would not explain the apparent decrease in N_{eff} for n-type (P) wires, and furthermore, high dopant activation fractions have been reported for similar VLS-grown Si wires with in situ B doping. [171] Rather, the observed change in N_{eff} of our intentionally doped wires was consistent with the presence of a trapped positive surface charge on the wires that was (at least partially) neutralized upon annealing. Positive surface charge would induce carrier depletion or accumulation in p-type or n-type Si, respectively; thus the neutralization of such a charge would increase or decrease, respectively, the N_{eff} of the wires—as we observed upon annealing. The N_{eff} of our unintentionally doped (p-type) wires also increased, but only slightly so, indicating that full surface-induced depletion still dominated the electrical resistivity of

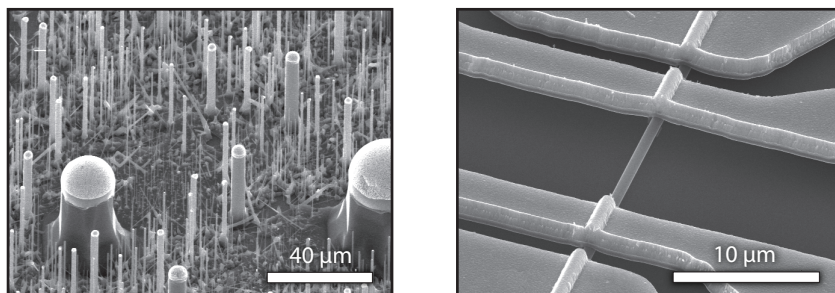


Figure 4.7. SiCl₄-grown wires and single-wire devices. **Left:** SEM image of the wires produced by VLS growth from SiCl₄ using evaporated (non-patterned) Au catalyst. **Right:** SEM image of a four-probe contacted single-wire device. Both images were taken at a 45° substrate tilt.

these devices. Others have also reported evidence of positive surface charge for VLS-grown Si nanowires. [168]

4.4 Properties of Si wires grown from SiCl₄

The addition of a high-temperature ($T \sim 1000^\circ\text{C}$) SiCl₄-based CVD reactor to our labs in 2007 brought about dramatic improvements in our ability to synthesize high-quality Si microwires for photovoltaic applications using the VLS growth process. Despite the prevalence of SiH₄-based VLS growth techniques in recent literature, the initial reports of VLS Si growth were in fact achieved using a similar high-temperature SiCl₄ chemistry. [33] Compared to SiH₄-based VLS growth, we observed dramatically higher crystal growth rates ($\sim 5 \mu\text{m}\cdot\text{min}^{-1}$) and markedly improved wire morphology using SiCl₄-based VLS growth. Transmission electron microscopy studies confirmed that the SiCl₄-grown Si wires were monocrystalline and grew epitaxially from the growth substrate. [39, p. 83] Furthermore, the high temperature of SiCl₄ CVD enabled the use of two VLS catalyst metals in addition to Au: Ni and Cu—both of which were predicted to yield higher-quality material for photovoltaic devices. [130] Finally, a photolithographic templating technique was developed which enabled the growth of high-fidelity Si wire arrays over large areas ($>1 \text{ cm}^2$) with precise control over wire diameter, length, and position within the array, as described in section 1.5.1. [37] Despite these achievements, little was known about the electrical properties of the SiCl₄-grown Si microwires, and their viability as photovoltaic materials hinged upon our abilities to characterize and optimize these properties.

Silicon nano- and microwires were grown for single-wire characterization using a high-temperature SiCl₄-based VLS growth process. [39, Ch. 4] To obtain a wide range of wire diameters from each growth, no photolithographic patterning was employed: The catalyst metal was thermally evaporated directly onto bare,

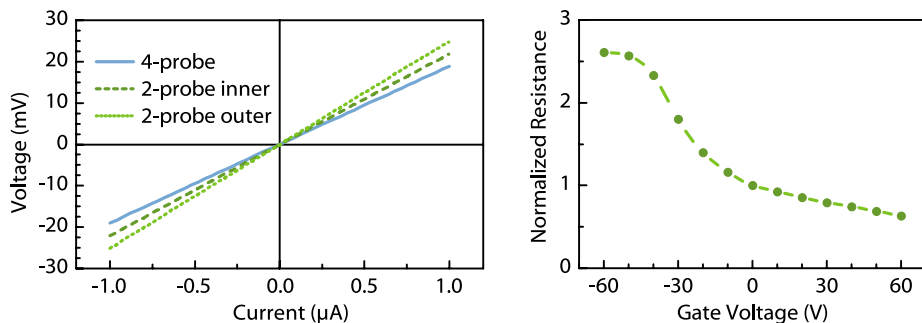


Figure 4.8. Electrical characteristics of a single SiCl₄-grown wire device. Left: Two- and four-probe I - V characteristics of the single-wire device shown in Fig. 4.7. **Right:** Normalized resistance of a single-wire device as a function of back-gate bias, exhibiting n-type behavior.

intrinsic Si(111) growth substrates, and was annealed at 1050 °C* for 20 min in the reactor prior to growth, under 1 atm H₂ flowed at 1000 sccm, to produce the metal droplets necessary for wire growth. The Si wires were then grown at this temperature and pressure by introducing SiCl₄ gas (Strem, 6N purity)[†] for 20 min at a flowrate of 20 sccm, while continuing the flow of H₂. The wires were unintentionally doped, i.e., no in situ dopant source gases were present.

Figure 4.7 (left) shows an image of the wires that were grown using a 100 nm thick Au film to provide the catalyst droplets in this procedure. The growth conditions produced hexagonally faceted Si wires, with diameters ranging from 30 nm to 30 μm and lengths of over 50 μm. Mild sawtooth faceting [172] was also observed on the sidewalls of the Au-catalyzed wires. Four-probe Al/Ag electrodes were patterned to individual wires using the procedures for photolithography, metallization, and lift-off described for SiH₄-grown wires above. A typical Au-catalyzed single-wire device is shown in Figure 4.7 (right).

Two-, three-, and four-probe I - V measurements were performed to characterize the behavior of each contact and wire device, following the procedures described for SiH₄-grown wires above. Figure 4.8 shows the I - V behavior and back-gated resistance modulation of a typical single-wire device. As observed for SiH₄-grown wires, the as-deposited contacts generally showed ohmic behavior with contact resistances on the order of wire resistance or less. However, whereas the unintentionally doped SiH₄-grown wires exhibited highly resistive, p-type behavior ($N_{A,\text{eff}} < 10^{14} \text{ cm}^{-3}$), the unintentionally doped SiCl₄-grown wires exhibited n-type behavior of widely varying resistivity—particularly for Au-catalyzed wires, whose effective doping concentration ranged from 10^{14} – 10^{20} cm^{-3} . Figure 4.9 plots the measured effective doping levels of single-wire devices originating from numerous growth runs performed over several months.

*This was the setpoint for the temperature controller. The substrate was estimated to be ~50 °C cooler.

[†]The term *6N purity* means *six nines* pure, or 99.9999% pure.

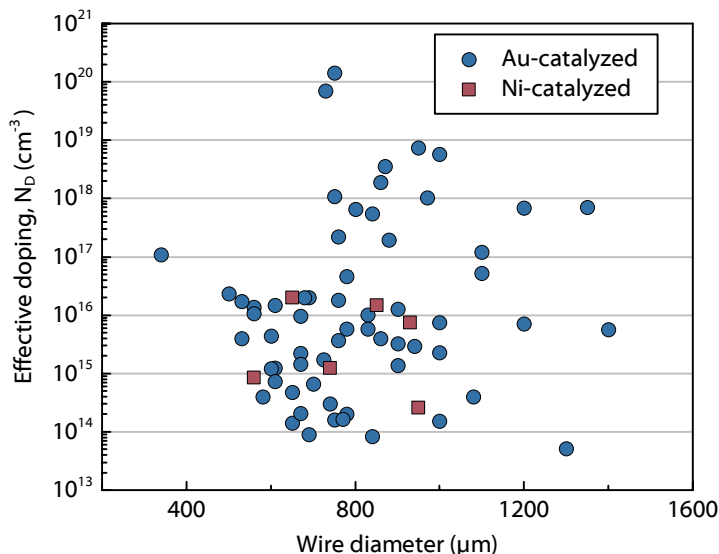


Figure 4.9. Effective doping concentration and carrier type observed in unintentionally doped, SiCl_4 -grown single-wire devices as a function of wire diameter and VLS catalyst metal.

To determine the cause of the unpredictable n-type behavior observed in the SiCl_4 -grown wires, they were subject to Auger electron spectroscopy (AES) and energy-dispersive X-ray spectroscopy (EDAX) for qualitative elemental analysis. These measurements revealed substantial catalyst metal cross-contamination between all wire types (e.g., Ni detected in Cu-catalyzed wires), suggesting that the CVD reactor tube and/or boat were harboring significant amounts of catalyst metal (and possibly other contaminants) between growth runs. For this reason, the reactor was outfitted with interchangeable tube liners and sample boats, each of which was devoted solely for use with a specific catalyst metal and substrate doping type. The reactor was also upgraded to permit in situ p-type (B) doping of wires by flowing BCl_3 gas during growth. Finally, to reduce potential impurities in the catalyst metal, only high-purity ($\geq 5\text{N}$) sources were used for evaporation. These changes resulted in the ability to reproducibly grow Si microwires with well-controlled p-type doping levels ranging from below 10^{14} cm^{-3} to above 10^{19} cm^{-3} , depending on the relative concentration of BCl_3 during growth. Figure 4.10 plots the effective doping concentrations, N_A , measured in six batches of Cu-catalyzed wires grown under different BCl_3 concentrations, demonstrating the excellent control of wire doping achieved by these reactor modifications.

Ultimately, the cause of the effective n-type behavior observed in the unintentionally doped wires was not determined. The AES and EDAX studies, although pivotal in our discovery of the cross-contamination problem in the reactor, lacked the chemical sensitivity necessary to identify potential n-type dopant species at even the highest electrically measured concentrations. None of the primary cata-

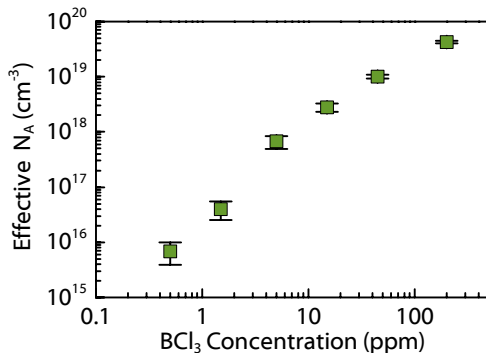


Figure 4.10. Effective doping concentration of Cu-catalyzed, B-doped wires grown from SiCl_4 , as a function of BCl_3 concentration during growth. Each data point represents the mean measured value of at least five single-wire devices; error bars report the standard error. *Wire growth and measurements performed by Morgan Putnam.*

lyst metals (Au, Ni, or Cu) are known to cause effective carrier concentrations as high as were observed in some of the wires ($N_{A,\text{eff}} > 10^{19} \text{ cm}^{-3}$), and in fact tend to compensate common dopants in Si. [173, 174, 175] However it is possible that the catalyst metals contained trace amounts of n-type dopant species, either as supplied (due to the initial use of 3N-purity source materials) or as deposited (due to potential cross-contamination in the evaporator system, which was frequently used with a wide variety of materials). It is also possible that the dopant species originated from the growth-substrate wafers: Although the wires for this study were grown on intrinsic Si, other users of the reactor frequently grew wires on degenerately doped wafers of both carrier types, which may have transmitted dopant species to subsequent wire growths via contamination of the reactor tube or boat. Finally, we note that numerous other potential contaminants had been intentionally introduced into the reactor in the course of other research concurrent to this study, including Al, Mg, In, Zn, [39, §4.6] and perhaps most suspect, metallurgical-grade Si.

Nonetheless, prior to the reactor retrofit, a large number of high-quality n-type Si microwire arrays were grown and studied, leading to the fabrication of high-aspect-ratio wire-array photoelectrochemical cells, [176] single-wire solar cells (introduced below), and the first measurements of minority-carrier diffusion lengths in VLS-grown Si (section 4.5.1). The decontamination of the growth reactor and addition of in situ p-type doping capabilities would later lead to the synthesis of Si wires with remarkable diffusion lengths, and the realization of high-performance Si microwire photovoltaics (Chapter 5).

4.4.1 Induced rectifying-contact devices

In SiCl_4 -grown single-wire devices with effective n-type doping concentrations ranging from approximately 5×10^{17} to $5 \times 10^{18} \text{ cm}^{-3}$, it was found that rectify-

ing junctions could be selectively formed beneath the inner electrode at one end of the device by electrically heating a segment of the wire. This was achieved by sourcing a slowly increasing current between the adjacent contacts at one of the wire until the enclosed wire segment was destroyed due to the extreme current density (typically $>10 \text{ kA}\cdot\text{cm}^{-2}$).^{*} Similar nano-scale joule heating has also been employed for selective surface functionalization of Si nanowires. [177] In our case, this procedure produced a rectifying junction beneath the inner contact to the remaining portion of the nanowire, as shown in Figure 4.11. While the nature of the induced junction is not explicitly understood, the observed rectifying behavior was likely due to the formation of a Schottky barrier, a p-n alloy junction, or a combination of these effects. There are several possible explanations for how such junctions could be formed: Al contacts to planar Si have been used previously to fabricate photovoltaic devices, either as Schottky junctions [178, 179] or as aluminum alloy p-n junction diodes. [180] Schottky photovoltaic devices are possible because annealed Al-Si contacts can exhibit Schottky barrier heights of up to 0.8 V with increasing heat treatment temperatures. [181, 182] And, at temperatures above the Al-Si eutectic point (577 °C), a p-n aluminum alloy junction solar cell can be formed in n-type silicon, because after cooling, Al acts as a p-type dopant in the recrystallized Si. [183] Regardless of the nature of the junction, excellent rectification behavior was obtained, with typical devices exhibiting diode ideality factors, n , ranging from 2.0 to 3.6. Most devices showed an ideality factor of ~ 3.5 for biases from 0.15 to 0.3 V, and ideality factors of ~ 2.5 for biases from 0.4 to 0.6 V. These values were consistent with the ideality factors reported for Al-Si photovoltaic Schottky junctions. [178] The series resistance observed at high forward biases ($>1 \text{ V}$) was approximately equal to the wire resistance plus the contact resistance measured prior to junction formation. Reverse breakdown occurred between -5 and -10 V , which was also near the

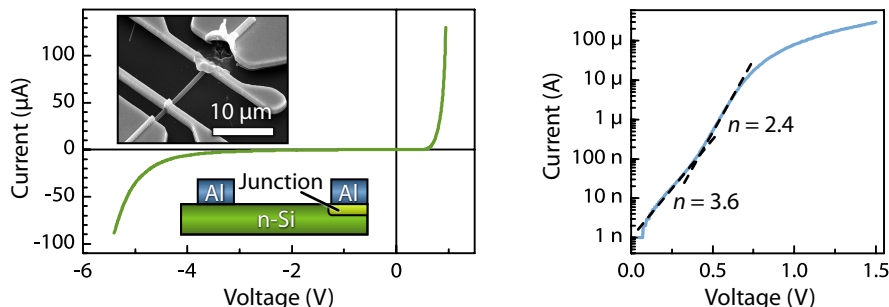


Figure 4.11. I–V behavior of an induced-rectifying-contact device. Left: The I – V behavior observed between the two inner contacts to the wire (linear scale); with simplified schematic (inset below) and 45°-tilt SEM image of the device (inset above). **Right:** Log-scale I – V plot, showing fits for the diode ideality factor, n .

^{*}This technique would become known as the “splat” method.

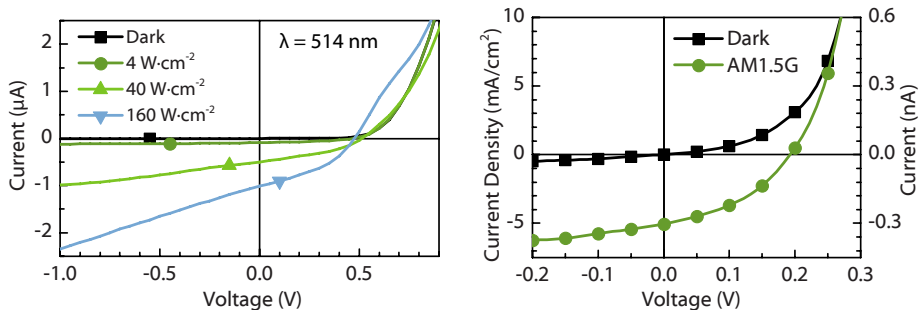


Figure 4.12. I - V characteristics of the single-wire device from Fig. 4.11, observed under varying intensities of $\lambda = 514$ nm laser illumination (left) and under simulated AM 1.5G ($100 \text{ mW}\cdot\text{cm}^{-2}$) illumination (right). In the latter panel, the current density (J) was determined by normalizing the response to the total exposed area (top-down) of the wire.

expected threshold for avalanche or tunnel breakdown for a one-sided abrupt junction at the estimated doping levels of our devices. [47, p. 108]

When illuminated, the induced-rectifying-contact single-wire devices exhibited photovoltaic behavior, as shown in Figure 4.12. Open-circuit photovoltages of up to ~ 500 mV were observed under concentrated laser illumination. The devices were also characterized as single-wire solar cells under simulated AM 1.5G illumination. To determine the current density and photovoltaic efficiency of these cells, the measured current was normalized to the exposed (non-shaded) light-collection area of the wire as determined by SEM imaging (rather than the circular cross-sectional area of the wire).^{*} The champion cell exhibited an open-circuit voltage, V_{oc} , of 190 mV; a short-circuit current density, J_{sc} , of $5.0 \text{ mA}\cdot\text{cm}^{-2}$; and a fill factor, FF , of 0.40; which corresponds to an overall solar energy conversion efficiency of $\eta = 0.46\%$.

The spectral response of the single-wire solar cells was also measured, as shown in Figure 4.13. These data were measured under chopped illumination from a supercontinuum laser source (Fianium) coupled to a $1/4$ m monochromator, which provided ~ 1 nm spectral resolution. This source produced a spot ($> 1 \text{ mm}^2$) of uniform illumination, whose spectral power density [$\text{W}\cdot\text{cm}^{-2}\cdot\text{nm}^{-1}$] ranged from approximately 1 to 5 suns (AM0) throughout the measurement range. A calibrated, apertured ($50 \mu\text{m}$ -diameter) Si photodiode was used to measure the light intensity incident upon the device, from which external quantum efficiency (E.Q.E.) was calculated.

^{*}The practice of excluding the area shaded by contacts is not generally accepted in reporting the efficiencies of macroscopic solar cells. Nonetheless, the convention applied here has been followed throughout the field of single-microwire and single-nanowire photovoltaics [160] and is thus appropriate for the presentation and comparison of the results. A more fundamental problem is that single-nanowire solar cells lack a well-defined area upon which to normalize photovoltaic efficiency in the traditional sense: their photonic dimensions enable them to interact with (and potentially absorb) more optical energy than, from a classical (ray-optics) perspective, should be incident on their physical area (see section 5.4.1).

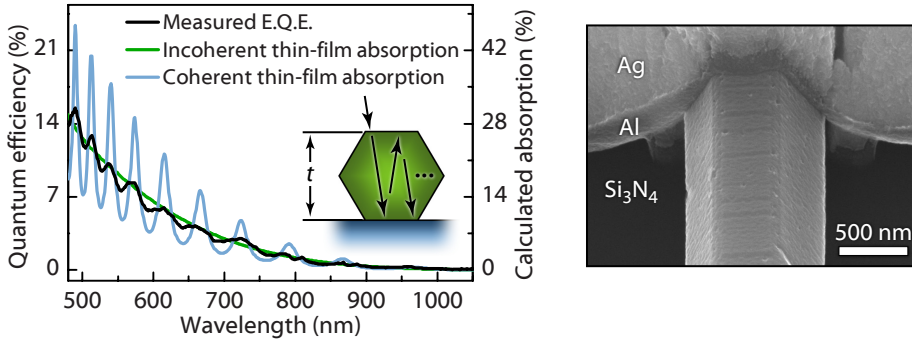


Figure 4.13. Spectral response of the single-wire solar cell from Fig. 4.11 showing the measured external quantum efficiency vs. the calculated absorption for a thin Si film of the same thickness (t) as the wire, under assumptions of incoherent and coherent interference at the front and back surfaces. SEM imaging (right) revealed that the wire was hexagonally faceted with a 900 nm diameter ($t = 780$ nm).

The observed E.Q.E. of the single-wire solar cells can be explained by thin-film absorption with mild coherent interference effects (see section 3.1.3). SEM imaging (also shown in Fig. 4.13) confirmed that the wires were hexagonally faceted, with the front (top) and back (bottom) facets oriented normal to the direction of illumination. Each wire thus formed a thin-film absorber layer with a well-defined thickness equal to the minor chord of the hexagonal cross section of the wire, defined as dimension t in Figure 4.13 (inset). Based on published values of the absorption and refractive index of Si, [75] we calculated the expected absorption of a thin film of thickness t for the cases of coherent or incoherent specular interference at the front and back surfaces, as described in section 3.1.3. The excellent agreement between the peak locations for coherent thin-film absorption and the measured E.Q.E. confirmed that interference at the front and back surfaces of the wires played a role in the observed spectral response. However, the observed interference fringes were much milder in magnitude than the calculated coherent absorption, indicating that interference effects were potentially limited by the wire surface roughness and diameter taper (which were mild but easily observed in SEM images) or by the effects of the other wire facets, which were ignored in the calculation.

The overall agreement between the expected thin-film absorption and the measured E.Q.E. also indicated that the internal quantum efficiency (I.Q.E.) was fairly constant across all measured wavelengths. This was expected, because carriers must diffuse roughly the same horizontal distance to reach the junction regardless of whether they were excited nearer the top or bottom of the wire. Such wavelength-independent I.Q.E. is characteristic of solar cells that orthogonalize the directions of light absorption and carrier collection, such as radial-junction wire-arrays or vertical multijunction devices. [41, 22] Here, the horizontal orientation and axial junction-geometry of the single-wire solar cells proved to particularly disadvantages for their photovoltaic performance—ensuring poor

absorption and low carrier-collection efficiency, respectively. Despite this, these structures would emerge as tremendously useful research platforms for studying carrier transport within VLS-grown Si wires, enabling our first measurements of minority-carrier diffusion length.

4.5 Measurement of minority-carrier recombination rates

The induced-rectifying-contact devices fabricated from SiCl_4 -grown Si microwires enabled the measurement of minority-carrier collection lengths using *scanning photocurrent microscopy* (SPCM).^{*} This technique produces images of spatially resolved carrier collection within a photovoltaic (or photoconductive) device by recording the photocurrent induced as a localized optical excitation beam is scanned over the device. SPCM has been used by others to study the band structure, [152] contact effects, [155] doping profiles [162], and carrier transport [156, 150, 154, 161] of semiconductor nanowires; as well as to determine the minority-carrier diffusion length in CdS nanowires [153] and to study single-nanowire GaAs solar cells. [169]

The SPCM measurements were performed using a confocal microscope with near-field scanning optical microscopy (NSOM) capabilities (WITec AlphaS-NOM). Figure 4.14 depicts the SPCM measurement configuration for confocal (left) and near-field (right) excitation. The single-wire devices were prepared by flush-mounting them in ceramic packages (DIP16) and contacting them with low-profile Al wire bonds to permit the use of short-working-distance microscope objectives as well as cantilevered NSOM tips. A low-profile microscope stage was built to accommodate the packaged devices and provide terminal access to each pin. Optical excitation was provided by a $\lambda = 650$ nm semiconductor diode laser chopped at a frequency of 2 kHz.[†] The beam was then focused through the microscope to produce a diffraction-limited spot size at the sample. The minimum beam waist (full-width half-max) of this excitation source, d_{beam} , was determined by the numerical aperture (N.A.) of the objective:

$$d_{\text{beam}} \approx \frac{0.6 \cdot \lambda}{\text{N.A.}} \quad (4.3)$$

In this study, the smallest achieved beam waist ($\sim 0.5 \mu\text{m}$) resulted from the use of a 50 \times objective with a N.A. of 0.95. To further improve the resolution of the excitation source, the focused beam could be sent through the tip of a

^{*}The SPCM technique described here is perhaps more commonly known within the photovoltaics community as a *light-, photon-, or optical-beam-induced current* (LBIC, PBIC, or OBIC) technique. There seems to be little consensus regarding the choice of terminology. To our knowledge, the term *SPCM* dates back to 1978, where it was used with a sub-bandgap excitation source to probe inhomogeneously distributed impurities in semiconductors. [184] More recently, several timely publications from the research group of L. Lauhon [154, 150] had established SPCM as a robust technique for probing carrier transport in semiconductor nanowires, and helped inspire the use of this technique in our present work.

[†]Recently we have determined that a slower (200 Hz) chop rate enables faster system response speed because it allows the use of synchronous filtering on the lock-in amplifier.

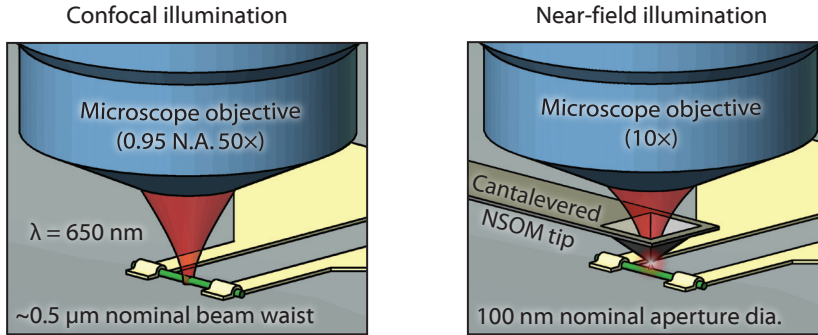


Figure 4.14. Schematic diagram of SPCM measurements, depicting confocal excitation (left) and near-field excitation (right). *Images are not to scale.*

cantilevered contact-mode NSOM probe with optical apertures ranging in diameter (d_{tip}) from ~ 100 nm (as supplied) to ~ 500 nm (intentionally enlarged using FIB milling). For either excitation mode, the SPCM images were formed by rastering the specimen beneath the excitation source while recording the device photocurrent, which was measured using a custom-built current preamplifier and lock-in detection (SR830, Stanford Research Systems). Details of the SPCM instrumentation and procedures are provided in Appendix C.

Scanning photocurrent microscopy was used to study the values of minority-carrier diffusion length and surface recombination velocity for Si microwires grown from SiCl_4 using three different VLS catalyst metals: Au, Ni, and Cu. The choice of catalyst metal for VLS growth is expected to strongly influence the quality of the resulting Si, because each metal differs greatly in its solubility, mobility, and electrical activity as a recombination center in Si. The presence of residual catalyst metals in the bulk and at the surfaces of VLS-grown Si wires is not only predicted based on the solubility of these metals at growth temperatures, but has also been experimentally observed using secondary ion mass spectrometry [80] and local-electrode atom-probe tomography. [147] Although the properties of these metals as bulk impurities in crystalline Si are well known, [129, 173, 174, 175] their recombination activity in VLS-grown materials had received little quantitative attention until the following studies were performed.

4.5.1 Au-catalyzed Si wires

Figure 4.16 shows the SEM and SPCM images of the Au-catalyzed single-wire device from Figure 4.11. This device was measured using both confocal ($d_{\text{beam}} \approx 1 \mu\text{m}$) and near-field ($d_{\text{tip}} \approx 500 \text{nm}$) excitation sources. The use of the NSOM tip permitted greater spatial resolution than confocal excitation, and also provided atomic force microscopy (AFM) topography maps of the wire device. However, the near-field SPCM images were influenced by the presence of small

metal particles on the wire surface, presumably originating from the melting the Al/Ag contact during junction formation, which led to optical (rather than electrical) artifacts in the SPCM profiles. The overall agreement between the photocurrent profiles obtained with near-field and confocal SPCM methods indicated that confocal excitation was adequate to study the carrier collection in our wires, despite the lower spatial resolution of this technique.

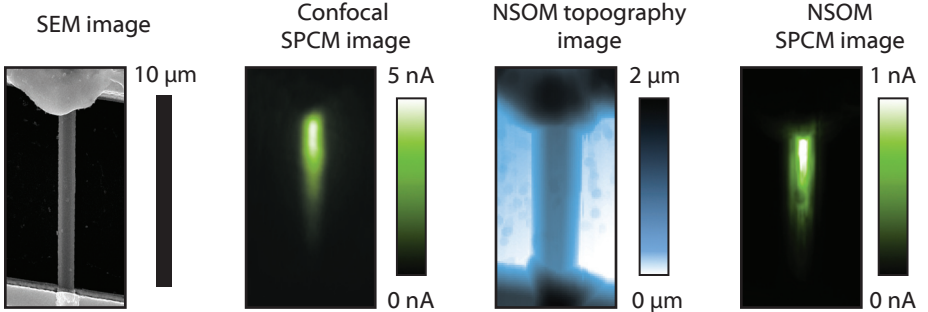


Figure 4.15. SPCM characterization of the Au-catalyzed wire from Fig. 4.11. From left to right: SEM image; SPCM image acquired using confocal excitation through a 60 \times , 0.6 N.A. objective ($\sim 1 \mu\text{m}$ beam waist); AFM topography image recorded by the NSOM tip; and SPCM image acquired using near-field excitation through a tip having $\sim 500 \text{ nm}$ aperture diameter. All image panels appear at the same magnification and orientation.

The axial SPCM profiles were analyzed to determine the charge collection properties of the induced-rectifying-contact Si wire devices. As plotted in Figure 4.16, photovoltaic (negative) photocarrier collection was observed with a peak nearest the rectifying junction. The collected current decayed exponentially away from the junction at both reverse and forward biases; however, the exponential decay rate of the photocurrent did not change with the bias. This behavior is consistent with minority carrier diffusion-limited carrier transport within the quasi-neutral region of the microwire solar cells, with negligible drift current contribution. In this situation, exponential fits to the axial SPCM profiles (i.e., evaluated along the length of the wire) allow the direct extraction of the minority carrier collection length within the n-type base of the microwire solar cells. [48, p. 95] Hole collection lengths, $L_{p,\text{eff}}$, ranged from 1–4 μm for the devices measured, which remain the largest measured values of room-temperature L_{eff} reported to date for Au-catalyzed VLS-grown Si wires.

The observed minority-carrier collection lengths indicate the effective minority carrier lifetime within the Si microwires, according to the relationship:

$$\tau_{\text{eff}} = \frac{L_{\text{eff}}^2}{D} \quad (4.4)$$

where D is the minority-carrier diffusion coefficient. Using values for D identical to that of bulk Si [47] at the measured doping concentration of these devices

($N_D \approx 10^{18} \text{ cm}^{-3}$), we calculated effective hole lifetimes of $\tau_{p,\text{eff}} \approx 15 \text{ ns}$. This calculation provides a lower limit of the bulk minority-carrier lifetime in our Si microwires (τ_p), and would be equal to this value if the carrier transport were limited solely by bulk (rather than surface) recombination. This minimum value of τ_p is larger than expected, but not unreasonable in comparison with the predicted bulk carrier lifetimes for Si doped with Au at the concentration corresponding to its solid solubility limit at our VLS growth temperature of $1050 \text{ }^\circ\text{C}$. At this temperature, Au can diffuse into Si at concentrations of up to 10^{16} cm^{-3} [173] and SIMS measurements on our microwires placed an upper limit on Au concentration of $1.7 \times 10^{16} \text{ cm}^{-3}$. [80] This Au concentration would produce an expected minority hole lifetime of 2–4 ns based on accepted literature values for the energy levels and capture cross-sections of Au traps in Si. [173] It is possible that slightly lower Au concentrations were present in our wires as, for example, rapid Au-catalyzed VLS growth has been suggested to yield Au incorporation concentrations well below that predicted by its solid solubility limit or segregation coefficient. [142] It is also possible that some of the elemental Au observed in our wires by SIMS had formed metallic precipitates rather than homogeneously distributed defects within the Si, [35] or that the effective carrier capture cross-sections for Au in our VLS-grown material simply differed slightly from the selected literature values. A moderate range of values have been reported for these parameters. [185, 186, 187, 188, 173]

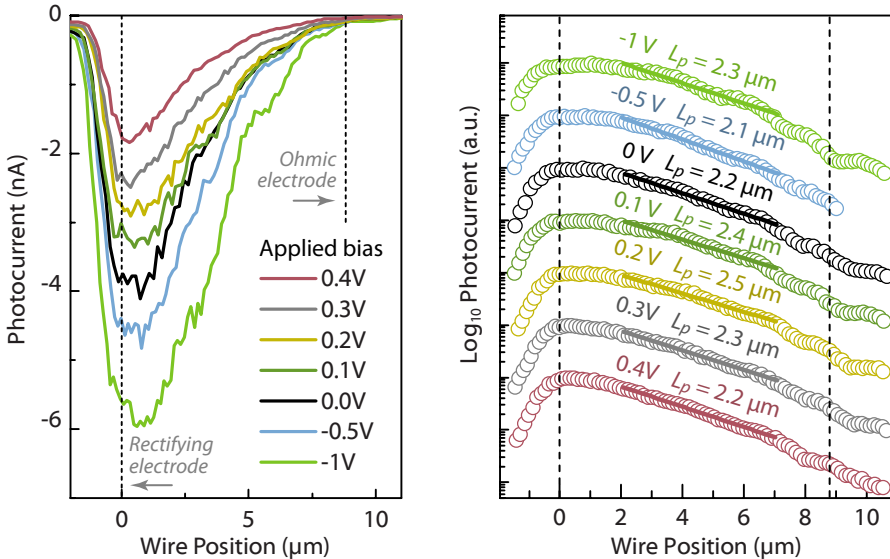


Figure 4.16. SPCM profiles and extracted minority-collection length. Linear-scale (left) and log-scale (right) cross-sectional SPCM profiles taken along the axis of the wire device from Fig. 4.15 at several applied biases. The exponential fits to the SPCM profiles reveal effective minority-hole collection length values ($L_{p,\text{eff}}$) as noted.

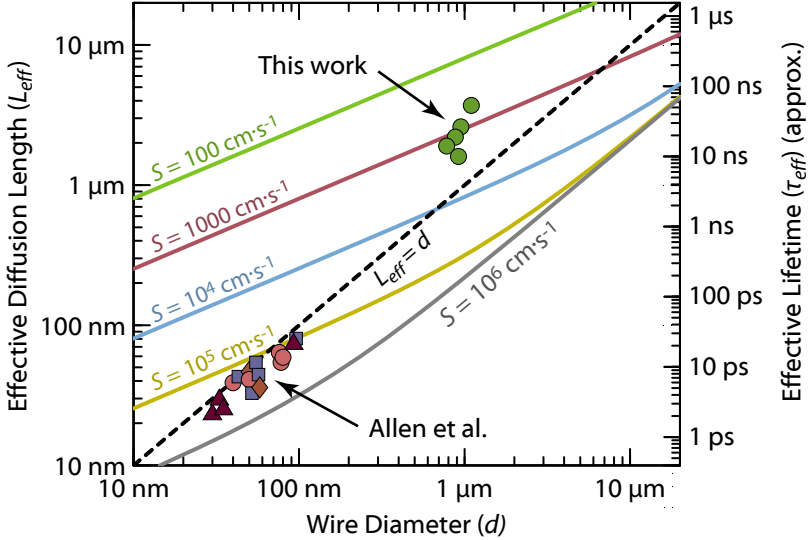


Figure 4.17. Effective carrier lifetime and collection length vs. bulk lifetime and surface recombination velocity, for heavily doped ($N_D \approx 10^{18} \text{ cm}^{-3}$) n-type Si wires. The solid contours indicate the effective lifetime due to surface recombination velocities, S , ranging from 100 to $10^6 \text{ cm}\cdot\text{s}^{-1}$. Upper data points correspond to present measurements, lower data points correspond to measurements reported by Allen et al. [147]

The SPCM profiles also enabled us to calculate an upper limit on the surface recombination velocity (S) of the Si microwires, by assuming that the observed minority-carrier collection length was limited solely by surface recombination. For a cylindrical wire of diameter d , with bulk minority-carrier lifetime τ_b and surface recombination velocity S , the charge-carrier continuity equation can be solved to determine the effective minority-carrier lifetime, τ_{eff} , as: [147]

$$\frac{1}{\tau_{\text{eff}}} = \frac{4\beta^2 D}{d^2} + \frac{1}{\tau_b} \quad (4.5)$$

where β is the solution to the equation:

$$\beta J_1(\beta) - \frac{dS}{2D} J_0(\beta) = 0 \quad (4.6)$$

By solving this equation in the absence of bulk recombination ($\tau_b \rightarrow \infty$), we calculated that the measured values of τ_{eff} correspond to a maximum surface recombination velocity of $S \approx 1000 \text{ cm}\cdot\text{s}^{-1}$, which is reasonable for a native oxide on (111)-oriented n-type Si. [189]

Figure 4.17 plots the measured carrier collection lengths (L_{eff}) and lifetimes (τ_{eff}) of our wires as a function of diameter, and also shows contours corresponding to surface-recombination-limited lifetimes for values of S ranging from 100 to

$10^5 \text{ cm}\cdot\text{s}^{-1}$. Due to the variation in measured values of τ_{eff} and the limited range of wire diameters studied, we were unable to conclude whether the observed behavior was limited by bulk or surface recombination. However, our measurements can be compared to those reported by Allen et al., who performed a similar study on Au-catalyzed, SiH_4 -grown VLS Si nanowires, employing electron-beam-induced current (EBIC) measurements to ascertain the effective diffusion lengths within single-nanowire devices. [147] Because Allen's nanowires were of similar doping concentration and carrier type as our microwires, his measurements can be plotted for approximate comparison on Figure 4.16.* Although his SiH_4 -grown nanowires were synthesized at lower temperatures ($460 \text{ }^\circ\text{C}$) and would thus be expected to have lower incorporation of Au, Allen observed relatively short ($< 100 \text{ nm}$) collection lengths, which were attributed to a high surface recombination velocity ($S > 10^5 \text{ cm}\cdot\text{s}^{-1}$). Because neither study placed an upper limit on the bulk diffusion length within Au-catalyzed, VLS-grown Si, it is not known which source gas chemistry and growth temperature (low-temperature SiH_4 or high-temperature SiCl_4) yielded higher-quality material in terms of bulk minority-carrier lifetime. However from a practical standpoint, efficient Si wire solar cells will require both long minority-carrier lifetimes as well as low surface recombination velocities, making L_{eff} a reasonable indicator of photovoltaic potential. The comparison made in Figure 4.17 demonstrates not only the importance of reducing surface recombination in Si wires for photovoltaic applications, but also illustrates why larger-diameter wires are favored (all other things equal) for mitigating the lifetime suppression associated with a given surface recombination velocity.

4.5.2 Ni-catalyzed Si wires

Induced-rectifying-contact devices were fabricated from unintentionally doped (n-type), SiCl_4 -grown, Ni-catalyzed wires, which had notably lower effective carrier concentrations than the Au-catalyzed single-wire solar cells characterized above ($N_D = 10^{15} - 10^{16} \text{ cm}^{-3}$). The higher resistivity of these wires presented additional challenges to the measurement of minority carrier collection length via SPCM. First, the repeatable formation of ohmic and rectifying contacts proved to be more troublesome: the junction formation procedure via resistive heating was rarely successful in creating sufficiently rectifying behavior, appearing instead to only slightly modify the barrier height or interface charge density of the original quasi-ohmic contacts. The few rectifying devices that were successfully fabricated showed markedly poorer photovoltaic performance ($V_{\text{oc}} < 100 \text{ mV}$) and higher leakage currents than the Au-catalyzed wire devices. Furthermore at these doping levels, the band-bending due to contacts, depletion regions, and surface charge extend further into the wires, potentially complicating the extraction of collection length from the SPCM profiles. Finally, the higher resistivity

*Measurements for wires of different carrier type or impurity concentration cannot be precisely compared as shown in Fig. 4.17, because the doping-dependent mobility values change the relation between L_{eff} and τ_{eff} (4.4) as well as the location of the surface-recombination-limited lifetime contours (4.5). Thus the values of S and τ inferred from Fig. 4.16 are approximate, as the measurements correspond to individual wires ranging from $N_D = 10^{17} - 10^{20} \text{ cm}^{-3}$.

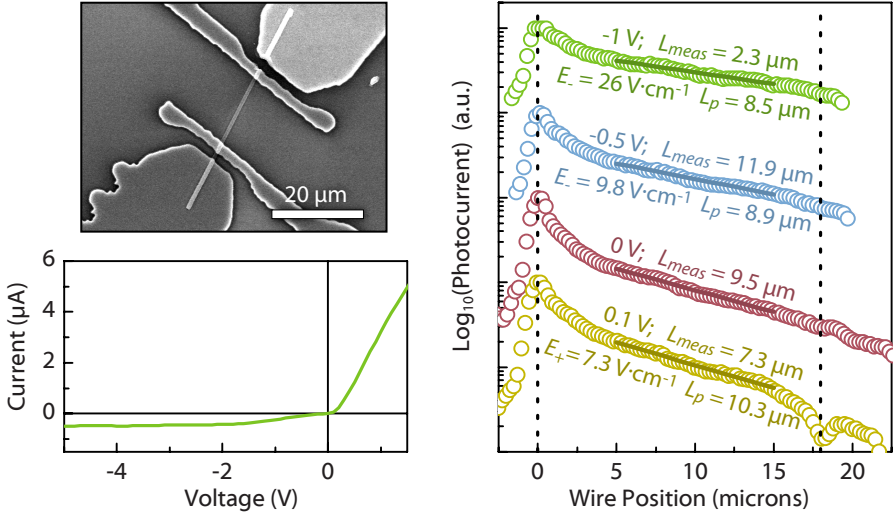


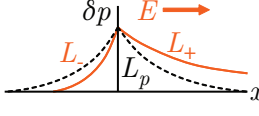
Figure 4.18. SPCM characterization of a Ni-catalyzed single-wire device. **Upper left:** SEM image of the induced-rectifying-contact device. **Lower left:** Linear-scale dark I - V behavior of this device. **Right:** Axial SPCM profiles of this device obtained at various applied biases, showing fits to obtain spatial decay lengths (L_{meas}) and the drift-assistance-corrected values of minority-carrier collection length (L_{eff}). Device fabricated by Daniel Turner-Evans.

of the Ni-catalyzed material, combined with the larger leakage currents of the induced rectifying contacts, caused non-negligible resistive voltage drops to violate the conditions for quasi-neutrality within the wires, exacting a correction to the collection lengths inferred from SPCM profiles. Despite these challenges, several Ni-catalyzed wire devices were successfully fabricated and characterized, revealing appreciably longer minority-carrier collection lengths than observed in Au-catalyzed wires.

Figure 4.18 shows a Ni-catalyzed single-wire device, its I - V characteristics, and its axial SPCM profiles at various applied biases. Prior to inducing rectifying behavior, the four-probe resistance of the wire had been measured to be $R_w = 230 \text{ k}\Omega$ (corresponding to an effective doping concentration of $N_D \approx 10^{16} \text{ cm}^{-3}$). After the rectifying junction was formed, the device exhibited series-resistance-limited I - V behavior under forward bias, and also passed a non-negligible leakage current in reverse bias. Knowledge of the wire resistance and the I - V behavior of the rectifying device allowed us to calculate, to first order, the magnitude of the electric field within the wire at each applied bias:

$$E = \frac{IR_w}{l} \quad (4.7)$$

where l is the length of the wire. The presence of a non-negligible electric field (i.e., non-quasi-neutrality) within the wire leads to drift-assisted diffusion of minority carriers; elongating the carrier collection length in the direction of the drift assistance, and contracting it in the opposite: [48, p. 83]



$$L_{\pm} = L_p \left(\frac{qL_p}{kT} E + 1 \right)^{\mp 1} \quad (4.8)$$

As shown in Figure 4.18, the exponential fits to the axial SPCM profiles indicated spatial decay lengths (L_{meas}) that varied significantly with applied bias. However, applying the above first-order correction for drift-assisted diffusion yielded reasonably consistent $L_{p,\text{eff}}$ values of $\sim 10 \mu\text{m}$ at all applied biases. This corresponds to an effective minority-carrier lifetime of $\tau_{p,\text{eff}} = 90 \text{ ns}$, and implies a maximum surface recombination velocity of $S \leq 300 \text{ cm}\cdot\text{s}^{-1}$. In comparing this result to that for the more heavily doped Au-catalyzed wires, it is important to remember that for n-type Si, a given minority-carrier lifetime will yield approximately 1.7 times the diffusion length at $N_D = 10^{16} \text{ cm}^{-3}$ than at $N_D = 10^{18} \text{ cm}^{-3}$.

4.5.3 Cu-catalyzed Si wires

The minority-carrier recombination rates for our Cu-catalyzed Si microwires were studied in an effort led by Morgan Putnam, using a variation on the above SPCM technique. [190] Whereas the rectifying contacts to the Au- and Ni-catalyzed single-wire devices were formed by selective resistive heating of originally ohmic contact electrodes, a two-step photolithography/metallization technique was employed to independently deposit ohmic (metal-semiconductor) and rectifying (metal-insular-semiconductor Schottky barrier) contacts to either end of the Cu-catalyzed devices. A similar two-step approach had been employed by Allen et al. (using different metals for either contact type) to study minority-carrier recombination rates in Au-catalyzed Si nanowires by EBIC. [147] Additionally, whereas the Au- and Ni-catalyzed wires described above were unintentionally doped (n-type) by unknown impurities in the catalyst metal, growth reactor, or source gas mixture; the Cu-catalyzed wires were intentionally doped p-type by flowing BCl_3 gas during the VLS growth, yielding well-controlled wire resistivity corresponding to an effective doping concentration of $N_A \approx 10^{17} \text{ cm}^{-3}$.

Initial SPCM measurements on these wires indicated very low minority-carrier collection lengths ($L_{\text{eff}} < 1 \mu\text{m}$). However, when the devices were re-measured under continuous, broad-area illumination from the microscope lamp, L_{eff} increased to $\sim 10 \mu\text{m}$. Because neither the broad-area nor the localized (laser) illumination sources were intense enough to cause high-level injection conditions in the wires, Putnam concluded that the observed increase in L_{eff} was caused by a reduced surface recombination velocity due to the filling of surface states by the photogenerated carriers. This behavior indicated an effective minority-carrier lifetime of $\tau_{n,\text{eff}} = 60 \text{ ns}$ and a maximum surface recombination velocity

of $S \leq 900 \text{ cm}^2\text{s}^{-1}$. This study confirmed that the bulk minority-carrier diffusion length within Cu-catalyzed Si microwires was at least $10 \text{ }\mu\text{m}$, while also demonstrating the importance of surface passivation for Si microwire photovoltaics.

More recently, the fabrication of diffused p-n junctions in our Cu-catalyzed Si microwires has led to observations of even longer minority-carrier collection lengths ($L_{\text{eff}} \gg 30 \text{ }\mu\text{m}$)—further confirming the surprising material quality of Si synthesized by Cu-catalyzed VLS growth. These wires were fabricated under the same conditions as the wires described above, but further benefited from the impurity-gettering effects of P diffusion [191] as well as advanced passivation techniques that yielded extremely low surface recombination velocities ($S \ll 70 \text{ cm}^2\text{s}^{-1}$). The full details of these efforts are presented in Chapter 5, but knowledge of the results adds an important insight to the following discussion on the quality of VLS-grown material.

4.6 Discussion

The methods described in this chapter have enabled the measurement of two key electrical properties of VLS-grown Si wires for photovoltaic applications: Minority-carrier lifetime and effective doping concentration. The fabrication of single-wire devices with photolithographically aligned, four-point contact electrodes provided a high-throughput research platform, allowing us to characterize the effects of growth chemistry (SiH_4 vs. SiCl_4), unintentional and intentional (in situ) doping, and catalyst metal choice (Au, Cu, and Ni). A simple method was developed for creating rectifying contacts that yielded promising photovoltaic behavior from single silicon wires. Most importantly, we have confirmed our ability to control the electrically active doping concentration during VLS growth, and have synthesized Si wires with remarkably long minority-carrier collection lengths—two paramount achievements towards the realization of high-performance Si wire solar cells. Table 4.3 summarizes the types of single-wire structures that were fabricated, and the electrical properties that were observed.

4.6.1 Catalyst choice for photovoltaic applications

The VLS growth process has been shown to produce Si wires using at least 12 different catalyst metals: Ag, Al, Au, Cd, Cu, Fe, Ga, In, Ni, Pd, Pt, and Zn. [36] The choice of catalyst metal determines not only the process window, source-gas compatibility, and growth kinetics of the VLS process; but can also have profound effects on the morphology, doping concentration, and minority-carrier lifetime of the resultant Si material. From the standpoint of photovoltaics manufacturing, these metals also vary greatly in their cost, availability, toxicity, and compatibility with existing industrial processes. Since the VLS growth process was first reported in 1964, [33] Au has remained by far the most-studied VLS catalyst metal, and offers an unparalleled range of growth system compatibility. However, the high cost and limited abundance of Au, combined with its

Table 4.3. Summary of minority-carrier lifetime measurements by catalyst type.

Catalyst	L_{eff} (μm)	τ_{min} (ns)	Measured device structure		
			Type ^a	N_{eff} (cm^{-3})	Dopant source
Au	2–4	8–20	IRC	10^{17} – 10^{18}	Unintentional (n-type)
Ni	10	90	IRC	10^{15} – 10^{16}	Unintentional (n-type)
Cu	10	60	SC	10^{17}	In situ BCl_3 (p-type)
Cu ^b	$\gg 30$	$\gg 500$	DJ	10^{17}	In situ BCl_3 (p-type)

^aIRC: Induced rectifying contact. SC: Schottky contact.

DJ: Diffused p-n junction.

^bThis device and measurement are presented in Chapter 5.

well-known status as a lifetime killer in crystalline Si, suggest it may be unfavorable as a VLS catalyst metal for large-scale production of Si photovoltaics. Here, we discuss the relative merits of the three catalyst metals used in this study, and comment on their potential suitability for photovoltaic applications. Table 4.4 lists the approximate solubility limit of each studied catalyst metal in Si at the growth temperature of our SiCl_4 reactor (1000 °C). For all three catalysts, solid-solubility (rather than impurity segregation) is expected to limit the incorporation of the metal within the wires at this temperature.* These concentrations can be compared to the degradation threshold for each species: the concentration above which their presence has been shown to degrade the photovoltaic efficiency of planar (p-base CZ) Si solar cells. Also shown are the approximate prices of each metal as of this writing.

The striking difference between the market price of Au vs. Cu or Ni may at first suggest that Au is prohibitively expensive for use in photovoltaic material production. Even when the costs of purified, research-grade metals are considered (which surpass the commodity price of Au by only $\sim 1.5\times$, vs. $\sim 75\times$ for Cu), the cost of Au remains ~ 200 -times greater than that of Cu or Ni, per volume of catalyst metal tip (which is the primary factor in determining the wire diameter in VLS growth). In fact, the cost of the Au used to grow Si wire arrays as described in this chapter, neglecting that lost during thermal evaporation, would amount to over $\$3/W_p$ for a 15%-efficient wire-array solar cell. However, the sub-ppm solubility limit of Au in Si indicates that the value of Au contained within the wires themselves—or even within a fully saturated growth wafer—would be negligible ($\ll \$0.01/W_p$). It is not unreasonable to surmise that, regardless of metal choice, a majority of the catalyst tip material could be recovered in an industrial process. Thus we might conclude that the *quality* of the VLS-grown material, rather than the cost of the catalyst metal, will ultimately determine the suitability of each catalyst type for VLS-growth of

*We calculate segregation-coefficient-limited concentrations of $2.4 \times 10^{17} \text{ cm}^{-3}$ (Au), $3.9 \times 10^{18} \text{ cm}^{-3}$ (Ni), and $4.4 \times 10^{18} \text{ cm}^{-3}$ (Cu). [130, 192, 193, 36]

Table 4.4. Selected properties of Au, Ni, and Cu as SiCl₄ VLS growth catalysts.

Catalyst	Solubility in Si [1000 °C] (cm ⁻³)	Degradation threshold (cm ⁻³) [129]	Commodity market price ^a (per kg)	Research-grade material price ^b (per cc)
Au	1×10 ¹⁶ [173]	2×10 ¹³	\$37,000	\$1000
Ni	2×10 ¹⁷ [194, 195]	6×10 ¹⁵	\$27	\$5
Cu	3×10 ¹⁷ [196]	4×10 ¹⁷	\$8	\$5

^aCommodity prices as of April 22, 2010 (Au, Cu: COMEX. Ni: LME).

^bFrom listed price of 1 kg 5N-purity material from our supplier, April 27, 2010.

photovoltaic materials.*

Fortuitously, the lower-cost catalysts Ni and Cu are also favored from the standpoint of material quality. As shown in Table 4.4, Au is poorly tolerated in Si solar cells, and its presence is expected to degrade efficiency at concentrations nearly three orders of magnitude below its solubility limit. As mentioned in section 4.5.1, the L_{eff} observed for our Au-catalyzed wires (2–4 μm) was already on par with the anticipated L_p for n-Si doped with Au at its solubility limit. Thus we would not expect surface passivation to effect significantly longer L_{eff} in these devices. We note that gettering (especially P-diffusion) may prove particularly effective in lowering Au concentrations, due to the radial surface proximity of the microwire geometry. [198, 191] Si microwire-array solar cells, grown by high-temperature (SiCl₄) Au-catalyzed VLS, have recently been shown to achieve $V_{\text{oc}} \sim 500$ mV after a thermal-oxidation and P-diffusion. [199] Au is also unique among the studied catalyst metals in that its relatively low eutectic temperature (363 °C) permits substantially lower-temperature VLS growth. Its solubility at a growth temperature of 450 °C is speculated to be $< 10^{14}$ cm⁻³—much nearer its degradation threshold—although thus far experiments have only placed an upper bound of $\sim 5 \times 10^{17}$ cm⁻³ on Au concentration within wires grown at this temperature. [147] Single-nanowire p-i-n Si solar cells grown by low-temperature Au-catalyzed SiH₄ VLS have also recently achieved $V_{\text{oc}} \sim 500$ mV, [200] and rapid growth rates have been demonstrated for low-temperature Si₂H₆-based processes. [201] However for our study, the deleterious nature of Au in Si, combined with the excellent morphology and growth rate of high-temperature SiCl₄ VLS-growth, led us away from the use of Au as a catalyst for producing high-efficiency Si microwire photovoltaics.

Ni and Cu differ greatly from Au as VLS growth catalysts: both are several orders of magnitude more soluble and mobile within crystalline Si, [196, 175] and

*Note however that catalyst metal choice can indirectly (but potentially profoundly) affect the cost of material production, for example, by enabling higher growth rates or lower growth temperatures. Our discussion pertains to the fixed growth conditions of this study (1000 °C SiCl₄ CVD), at which we observed (but did not quantify) approximately similar growth rates for all catalyst metals. Others have more-thoroughly studied the role of the catalyst metal in determining VLS growth rates. [197]

at 1000 °C, can diffuse through an entire Si wafer in a matter of seconds. [202] Both have particularly complex phase diagrams with Si [193, 192] which exhibit much higher liquid-eutectic temperatures than Au (802 °C for Cu; 993 °C for Ni) as well as numerous silicide phases, some of which can also catalyze VLS growth. [36] Neither Cu nor Ni will remain at interstitial sites in room-temperature crystalline Si, and rapidly precipitate upon cooling from high temperatures. Depending on cooling rate, this behavior can lead to a diverse range of recombination activity in Si, further complicated by the roles of other defects and impurities in initiating the precipitation. [114, 115, 116, 141, 174, 175, 202, 203, 204] Nonetheless, several studies suggest that these metals may be well tolerated in thin-film photovoltaics: Ni has been shown to effectively passivate other lifetime-limiting impurities in low-quality Si, and Si wafers diffused with Ni at 900 °C have exhibited $L_n \sim 20 \mu\text{m}$. [174] Even more promising, L values approaching $\sim 30 \mu\text{m}$ have been reported for Si saturated with $\sim 10^{17} \text{ cm}^{-3}$ Cu, [205] and 15%-efficient thin-film Si solar cells have been grown from a Cu melt at 950 °C. [206] Ultimately, as shown in Table 4.4, Cu was the only studied catalyst metal whose anticipated concentration within our VLS-grown wires fell below its efficiency degradation threshold. These factors led us to select Cu as the growth catalyst for producing high-performance radial-junction solar cells in the following chapter of this thesis. We note that the promising L_{eff} observed for the Ni-catalyzed wires may also warrant future investigation.

Radial p-n junction microwire solar cells

The principal functional element of the semiconductor solar cell is the p-n junction. The quality of the junction establishes the voltage at which photovoltaic power can be delivered to an external circuit. In terms of reaching the theoretical limits of photovoltaic energy conversion (following the principal of detailed balance), [16] the pursuit of the ideal p-n junction has arguably proven the most difficult for Si solar cells: whereas the world-record cell has achieved a short-circuit current density very near the theoretical maximum ($J_{sc} = 42.7 \text{ mA}\cdot\text{cm}^{-2}$), its open-circuit voltage ($V_{oc} = 706 \text{ mV}$) remains far below the theoretically possible 845 mV. [19, 17] A key challenge for the development of novel photovoltaic technologies including Si microwire solar cells is the demonstration of high-quality p-n junctions, which are required to achieve high open-circuit voltages and fill factors.

In this chapter, we describe a novel process that has been developed to produce high-quality radial p-n junctions in VLS-grown Si microwires. These techniques enable us to produce single-wire solar cells with record efficiencies and open-circuit voltages for VLS-grown Si photovoltaics. The results confirm that Si microwire-array solar cells have the potential to exceed 17% efficiency.

5.1 Formation of radial p-n junctions

The steps used to fabricate Si microwire arrays with radial p-n junctions are depicted in Figure 5.1. The technique made use of a polymer-infill etch-mask to define a SiO_2 diffusion-barrier over the lower portion of each wire, followed by conventional P diffusion, to selectively produce radial p-n junctions in the upper portion of each wire. SEM images of a microwire array following these procedures are shown in Figure 5.2.

Growth. Ordered arrays of Si microwires (1.2–1.8 μm diameter, square-tiled, 7 μm pitch) were grown from SiCl_4 by the photolithographically patterned VLS process described in section 1.5.1, using BCl_3 to provide in situ p-type doping, and 300 nm evaporated Cu as the catalyst. The wires were grown on p-type Si(111) wafers ($\rho < 0.001 \Omega\cdot\text{cm}$).

Catalyst removal. The Cu catalyst was removed by etching the wire arrays for 30 s in 5% HF(aq), for 20 min in an RCA-2 solution (6:1:1 by volume $\text{H}_2\text{O}:\text{H}_2\text{O}_2(30\% \text{ in } \text{H}_2\text{O}):\text{conc. HCl(aq)}$ at 75 °C) and for 60 s in 20 wt % KOH(aq) at 20 °C.

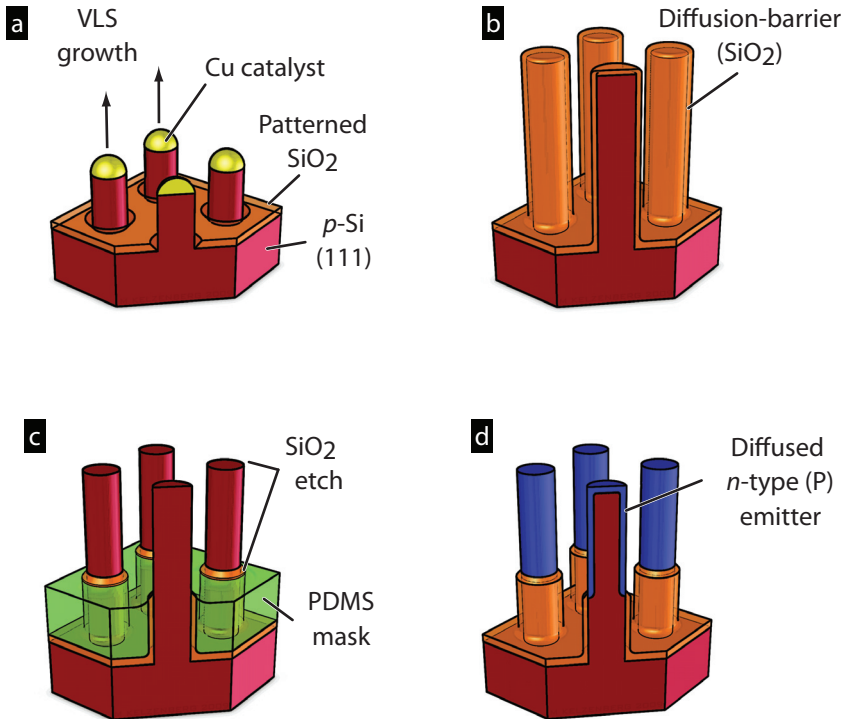


Figure 5.1. Fabrication procedure for radial p-n junction Si microwire arrays. Schematic diagrams depict: **a**, VLS-growth of p-type Si microwire arrays; **b**, catalyst removal and growth of a thermal-oxide diffusion-barrier; **c**, selective removal of the oxide barrier using a polymer-infill etch mask; and **d**, thermal diffusion of radial p-n junctions.

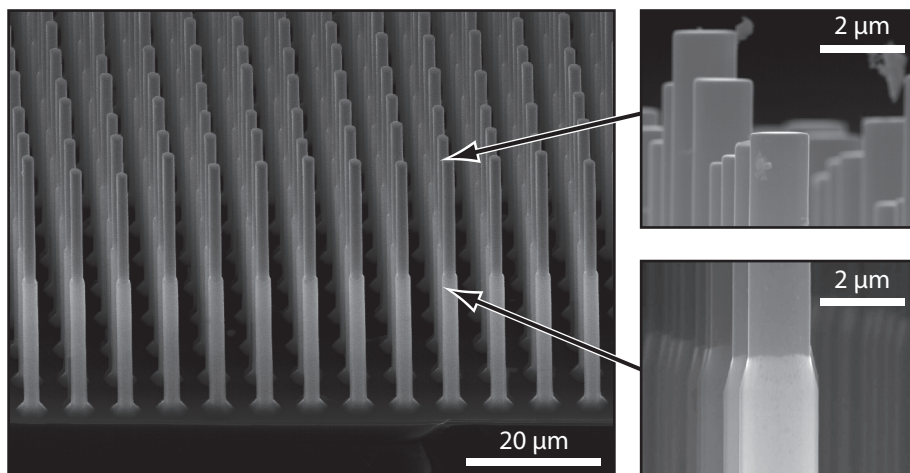


Figure 5.2. Si wire array following the radial junction formation procedure. SEM images provided by Shannon Boettcher.

Oxidation. A conformal SiO_2 diffusion-barrier (~ 200 nm thickness) was grown by dry thermal oxidation for 2 hr at 1100°C .

Polymer infill. The wire arrays were then partially infilled with polydimethylsiloxane (PDMS) using the method described by Plass et al. [42] Briefly, the wire array samples were coated with a solution that contained 4.4 g hexamethylcyclotrisiloxane (Sigma-Aldrich), 1 g PDMS (Sylgard 184, Dow Corning), and 0.10 g curing agent in 5 mL of dichloromethane; spun at 1000 rpm for 30 s; and cured for 30 min at 150°C ; producing a $10\text{--}15\ \mu\text{m}$ thick PDMS layer at the base of the wire array. Thicker infill layers were achieved by repeating this process (up to 4 times).

Masked oxide etch. The partially infilled arrays were etched for 5 min in buffered HF (BHF) to remove the exposed diffusion-barrier oxide.

Polymer removal. The PDMS was removed by etching for 30 min in a solution of 1.0 M tetra-*n*-butylammonium fluoride made using a 1:1 (vol) mixture of tetrahydrofuran and dimethylformamide. [207] A 10 min piranha etch (3:1 aq. conc. H_2SO_4 :30% H_2O_2) was also performed to remove any residual organic contamination.

Thermal diffusion. To form the radial p-n junctions, the wire arrays were etched for 5 s in 10% HF(aq), then thermal P diffusion was performed for 10 min at 850°C using solid-source $\text{CeP}_5\text{O}_{14}$ wafers (Saint-Gobain, PH-900), followed by a 30 s deglaze in BHF. Spreading resistance measurements (Solecon Laboratories) on planar Si control wafers indicated a junction depth of $x_j = 100$ nm and a surface dopant concentration of $N_D = 1 \times 10^{19}\ \text{cm}^{-3}$ (see Appendix A.2).

5.2 Fabrication of single-wire devices

Electrically contacted single-wire devices were fabricated using the photolithographic technique described in section 4.2.3. Briefly, the radial p-n junction wires were removed from the growth substrate using a razor blade, deposited onto transparent (sapphire) or reflective (SiN_x -coated Ag) insulating substrates,* and then patterned with Ag-capped Al contacts. Prior to contact metal evaporation, the patterned devices were etched for 3 min in BHF to remove the diffusion-barrier oxide beneath the base-region electrodes. Evaporation was performed from two tilt angles (approximately $\pm 45^\circ$ tilt) to ensure electrical continuity around the wires. Typical devices had a single contact to either end of the wire, however some devices were patterned with four or eight contacts to enable independent four-probe I - V characterization of the base, emitter, and p-n junctions. Figure 5.3 shows a single-wire device of each contact pattern type.

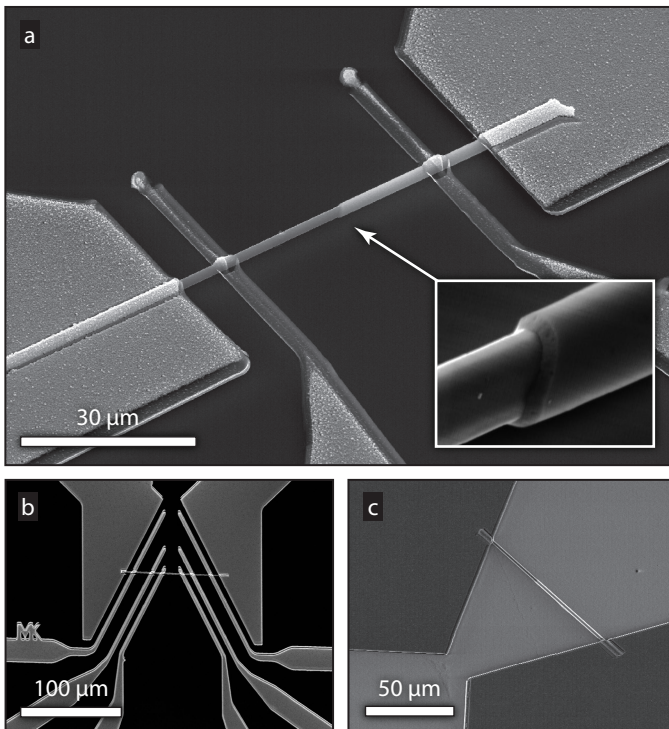


Figure 5.3. Single-wire, radial p-n junction devices. SEM images of of typical (a) four-probe, (b) eight-probe, and (c) two-probe single-wire devices. Panel (a) was taken at 45° tilt.

*Sapphire substrates: 2", ~ 350 μm thick, double side polished C-plane wafers. Ag substrates: 3" Si wafers, top side polished, coated with ~ 100 nm Ag by thermal evaporation, then ~ 300 nm SiN_x by PECVD.

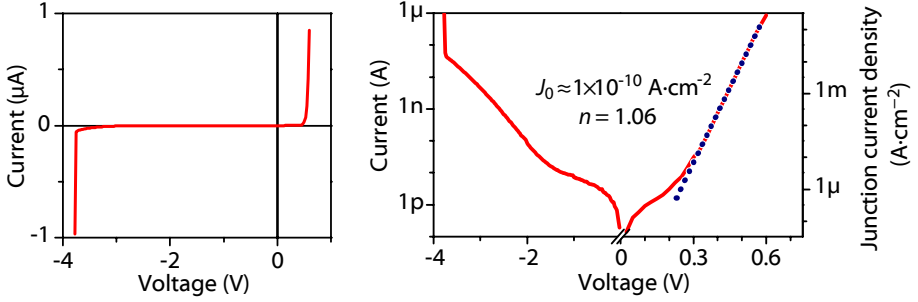


Figure 5.4. I - V characteristics of a typical single-wire radial p-n junction device, plotted on a linear (left) and log (right) scale. The junction current density and the dark saturation current density (J_0) were both normalized to the estimated cylindrical area of the radial p-n junction ($3 \times 10^{-6} \text{ cm}^2$).

5.2.1 Current-voltage behavior

The single-wire radial p-n junction devices exhibited dark I - V behavior characteristic of high-quality p-n junction diodes, as plotted in Figure 5.4. The as-grown devices often achieved ideality factors (n) of nearly 1.0, indicating that the dark saturation current (J_0) was dominated by bulk or surface recombination within the quasi-neutral regions (vs. within the junction depletion region). [176, p. 98] By normalizing the I - V behavior to the estimated cylindrical area of the radial p-n junction (calculated based on the observed device dimensions and an estimated junction depth of 100 nm), we calculated a planar-junction-equivalent dark saturation current of $J_0 \approx 10^{-10} \text{ A}\cdot\text{cm}^{-2}$. Four-probe I - V measurements were performed on devices with four or more contacts to characterize the effective base doping ($N_A \approx 10^{17} \text{ cm}^{-3}$) using equation (4.2), and two-probe I - V measurements were used to place an upper bound on the sheet resistance of the emitter ($R_S < 6 \text{ k}\Omega/\square$), using the equation:

$$R_S = R_{\text{meas}} \frac{\pi d}{l} \quad (5.1)$$

where R_{meas} is the measured wire resistance, d is the wire diameter, and l is the distance between the two electrodes (valid so long as the emitter is thin compared to the wire radius). The contacts to both regions were generally ohmic and low-resistance: series-resistance-limited I - V behavior was typically not observed until forward biases exceeded 0.8 V.

5.2.2 Scanning photocurrent microscopy

Due to the high surface area to volume ratio, Si wire solar cells are very sensitive to surface recombination, particularly within the bottom segment of each wire where no radial p-n junction is present (henceforth referred to as the axial region of the device). In this region, minority carriers must diffuse axially to reach the

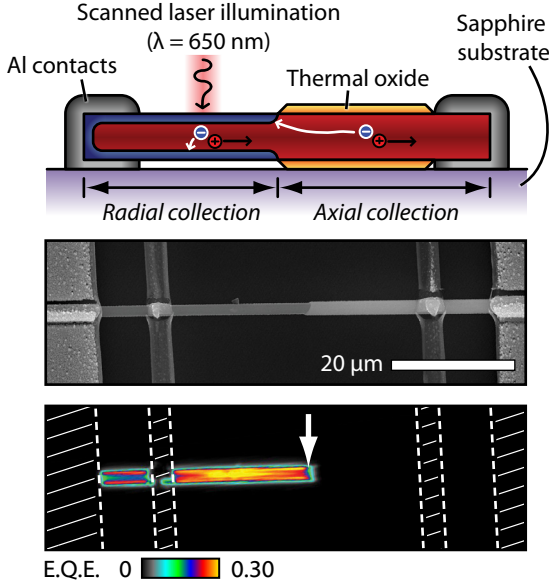


Figure 5.5. SPCM characterization of minority-carrier recombination in a radial p-n junction Si microwire device. **Top:** Schematic diagram of SPCM illumination and minority-carrier transport within radial p-n junction Si microwires indicating the regions of axial and radial transport. **Below:** SEM image (center) and SPCM image (bottom) of the single-wire device that was pictured in Figure 5.3. The SPCM data were normalized to the incident beam photocurrent and are reported in terms of the external quantum efficiency (E.Q.E.). The white arrow indicates the start of the radial p-n junction (which extends to the left), and the hashed white areas indicate the location of the metal contacts.

junction in order to be collected, as depicted in Figure 5.5 (left). The effective distance that carriers can travel before recombining, L_{eff} , can be greatly reduced by surface recombination: surface-limited values of L_{eff} as low as ~ 20 nm have been reported for VLS-grown Si nanowires, [147] whereas in the previous chapter, we observed L_{eff} as high as ~ 10 μm for our microwires (under light-induced surface passivation).

To determine the L_{eff} of our radial p-n junction Si microwires, we again performed scanning photocurrent microscopy (SPCM) to obtain spatially resolved maps of minority-carrier collection within the single-wire devices. To facilitate comparison between devices measured under different illumination conditions, the SPCM data were normalized by dividing the specimen current by the incident beam photocurrent (determined with a calibrated photodiode), and are thus reported in terms of absolute external quantum efficiency (E.Q.E.). Figure 5.5 shows the normalized SPCM image of a typical single-wire device. Relatively uniform carrier collection was observed throughout the radial portion of the wire, but no carrier collection was observed from the axial portion. In fact, the abrupt spatial transition between the two collection regimes could not be resolved by

the $\sim 0.5 \mu\text{m}$ diameter beam spot of the $\lambda = 650 \text{ nm}$ illumination source, indicating that the effective axial minority-carrier collection length, L_{eff} , was $\leq 0.5 \mu\text{m}$. As with our prior studies of p-type Cu-catalyzed Si microwires (described in section 4.5.3), the SPCM profiles of our radial p-n junction wires were found to be insensitive to specimen bias (ranging from -1 to 0.4 V). But unlike the prior devices, which had native-oxide-terminated surfaces whose recombination activity could be suppressed by applying broad-area illumination, the SPCM profiles of the radial p-n junction devices were not affected by application of broad-area illumination—making it difficult to determine whether the low L_{eff} was limited by rampant surface recombination, or by drastically reduced bulk diffusion lengths compared to the as-grown p-type microwires.

5.3 Passivation of wire surfaces

To determine whether the low minority-carrier collection lengths ($L_{\text{eff}} \leq 0.5 \mu\text{m}$) observed in the radial p-n junction wires were limited by bulk or surface recombination, we investigated three methods of surface passivation: hydrogen termination (via immersion in hydrofluoric acid), and deposited films of either silicon or silicon nitride. The details of each of these studies are presented in sections 5.3.1, 5.3.2, and 5.3.3, respectively. The effect of each passivation method on L_{eff} , as determined by SPCM, are tabulated in Figure 5.6.

As a first investigation into the effects of surface passivation on carrier recombination in Si microwires, we repeated the SPCM measurements on single-wire devices that were fully immersed in $\text{pH} = 5.0$ buffered hydrofluoric acid (BHF). Hydrofluoric acid removes oxides from crystalline Si surfaces and provides hydrogen-termination of dangling bonds, resulting in unusually low surface recombination velocities ($S < 1 \text{ cm}\cdot\text{s}^{-1}$). [208] After at least ~ 3 min of immersion in BHF (the approximate time required to remove the SiO_2 diffusion-barrier), SPCM measurements revealed uniform carrier collection from both the axial and the radial portions of the wire, as shown in Figure 5.6 (second row). Because no spatial decay in carrier-collection efficiency was observed throughout the $\sim 20 \mu\text{m}$ length of the axial wire segment, we were only able to place a lower bound on the value of L_{eff} ($\gg 20 \mu\text{m}$). This behavior confirms that the bulk minority-carrier diffusion length within the wires, L_n , was $\gg 20 \mu\text{m}$, and that the short L_{eff} observed prior to BHF immersion was therefore due to a high surface recombination velocity of $S \geq 4 \times 10^5 \text{ cm}\cdot\text{s}^{-1}$ (calculated using equations 4.4 and 4.5).

To effect passivation of the Si microwire devices with an air-stable solid-state surface termination, we used plasma-enhanced CVD (PECVD) to coat the wires with amorphous hydrogenated thin films of either Si (a-Si:H) or silicon nitride (a-SiN_x:H). PECVD a-Si:H and a-SiN_x:H coatings are commonly used in solar cell fabrication due their stability and ease of growth ($T < 400 \text{ }^\circ\text{C}$). Low surface recombination velocities ($S < 10 \text{ cm}\cdot\text{s}^{-1}$) have been reported for Si surfaces coated with either material, [121, 209] and each offers additional beneficial properties for photovoltaic applications: a-Si:H forms a heterojunction to crystalline

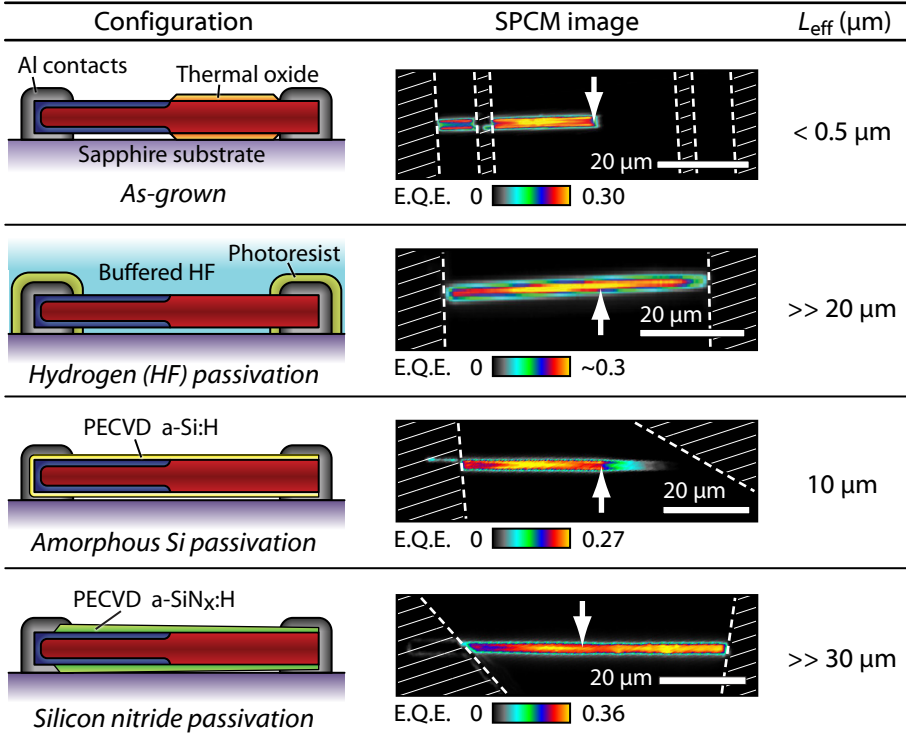


Figure 5.6. SPCM characterization of minority-carrier recombination in radial p-n junction Si microwire devices having various surface passivation treatments. Left: Schematic diagrams of single-wire device structures. Center: SPCM image of a typical device of each surface passivation type, with inferred values of L_{eff} indicated to the right. The SPCM data were normalized to the incident beam photocurrent and are reported in terms of the external quantum efficiency (E.Q.E.). The white arrow indicates the start of the radial p-n junction (which extends to the left), and the hashed white areas indicate the location of the metal contacts.

Si, enabling extremely high open-circuit voltages (up to 743 mV) for wafer-based crystalline Si solar cells; [210] while a-SiN_x:H functions as a versatile antireflective (AR) coating for crystalline Si, [211] and in this role, was instrumental to our realization of highly absorbing Si microwire arrays in Chapter 3.

After diffusing p-n junctions into a Si wire array, we removed the remaining surface oxide, performed a standard clean, and then split the array into several pieces. One array was coated with ~10 nm of undoped PECVD a-Si:H that was grown from SiH₄ at 240 °C. Another was coated with low-stress PECVD a-SiN_x:H that was grown from SiH₄/NH₃ at 350 °C, the thickness of the of which tapered from ~120 nm at the wire tips to ~60 nm at the wire bases (as shown in Fig. 3.22). Both PECVD films were also deposited onto planar p-type control wafers (400 μm thick float-zone Si, double-side polished, $\rho > 4 \text{ k}\Omega\cdot\text{cm}$) to enable optical characterization by spectroscopic ellipsometry (see Appendix A.1), as well as microwave-frequency photoconductivity decay measurements* which indicated $S < 20 \text{ cm}\cdot\text{s}^{-1}$ for a-Si:H passivation, and $S < 10 \text{ cm}\cdot\text{s}^{-1}$ for a-SiN_x:H passivation.

As shown in Figure 5.6, the SPCM profile of a typical a-Si:H-coated single-wire solar cell (third row) exhibited two prominent differences from the non-coated device (top row). Most notably, carrier collection was observed within the axial region of the a-Si:H-coated device, with a characteristic decay length of $L_{\text{eff}} \approx 10 \text{ }\mu\text{m}$, indicating a surface recombination velocity of $S \approx 450 \text{ cm}\cdot\text{s}^{-1}$. Also, the peak external quantum efficiency (E.Q.E.) of the a-Si:H-coated wire device was slightly less than that of the non-coated device. We suspect that this was largely due to the difference in wire diameter between each device (the imaged a-Si:H-coated device was slightly thinner than the non-coated wire). Some loss in E.Q.E. may also have been caused by parasitic optical absorption within the a-Si:H coating. But this layer is not necessarily electrically inactive: spectral response measurements on a-Si:H-coated single-wire solar cells (section 5.4.1) indicated high internal quantum yield even at blue wavelengths, suggesting that the a-Si:H layer was either largely electrically active or much thinner than expected based on deposition time.

In contrast, the SPCM profile of a typical a-SiN_x:H-coated single-wire device (Fig. 5.6, bottom row) exhibited markedly higher peak E.Q.E. than the non-coated device, due to the antireflective nature of the nitride coating. Furthermore, carrier collection was observed throughout the entire axial portion of the a-SiN_x:H-coated wire, with no apparent spatial decay ($L_{\text{eff}} \gg 30 \text{ }\mu\text{m}$). In fact, the E.Q.E. typically increased slightly in the axial portion of these wires, because the tapering thickness of the a-SiN_x:H in this region yielded a more-optimal antireflective coating at the excitation wavelength. These observations imply a low surface recombination velocity ($S \ll 70 \text{ cm}\cdot\text{s}^{-1}$) as well a substantially longer minority-carrier diffusion length than previously observed in VLS-grown Si wires ($L_n \gg 30 \text{ }\mu\text{m}$, $\tau_n \gg 500 \text{ ns}$). Because our observation of L_n was limited by the ~30 μm axial length of the a-SiN_x:H-coated single-wire devices, the uniform SPCM profiles suggest not only that L_n was many times this value,

*Measurements performed by Daniel Turner-Evans. See reference [212] or [208] for a description of this technique.

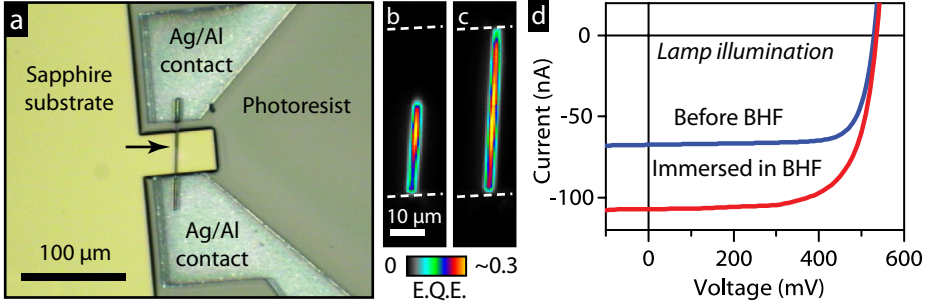


Figure 5.7. Characterization of single-wire devices passivated by immersion in hydrofluoric acid. **a**, Microscope image of the test structure. **b,c**, SPCM profiles of the exposed wire area before (b) and after (c) immersion in BHF. Dashed lines indicate the location of metal contacts. **d**, Light I - V behavior under microscope lamp illumination, measured before and during immersion in BHF. Note that the reduced spatial resolution of these SPCM profiles was due to the use of a $20\times$, $N.A. = 0.4$ objective to provide greater working distance.

but also indicate an extremely low effective surface recombination velocity at the Al:p-Si interface.

5.3.1 Passivation with buffered hydrofluoric acid

Immersion in buffered hydrofluoric acid provided a convenient means by which to modulate the surface recombination rates of already-fabricated single-wire devices. BHF is known to provide unusually low surface recombination velocities at Si surfaces ($S < 1 \text{ cm}\cdot\text{s}^{-1}$). [208] To enable SPCM measurements to be performed on the single-wire radial p-n junction devices while they were fully immersed in BHF, they were first covered with a positive photoresist layer (S1813, Microchem) to protect the metal contacts from corrosion. The photoresist was patterned and developed to open a well over the central portion of each wire (Fig. 5.7a), and to expose the contact pads for wire bonds (located several millimeters away). Initial I - V behavior and SPCM profiles were recorded to determine the properties and extent of the radial p-n junction within each device (Fig. 5.7b). A droplet of pH = 5.0 BHF (Buffer HF Improved, Transene) was then placed over the wire and covered by a small plastic coverslip to prevent evaporation and enable imaging through the liquid. During immersion in BHF (allowing 1–3 min to etch away the diffusion-barrier SiO_2), uniform carrier collection was observed from throughout the axial region of the wire (Fig. 5.7c), indicating an effective carrier collection length of $L_{\text{eff}} \gg 20 \text{ }\mu\text{m}$ (which was the longest axial wire length investigated in this study). Light I - V measurements, performed under broad-area illumination from the microscope’s halogen lamp, showed an increase in short-circuit current roughly commensurate with the increase in active area that was observed by SPCM (Fig. 5.7d). The SPCM be-

havior of the BHF-immersed devices remained stable for 10–30 min, after which time the contacts failed due to corrosion.

Some single-wire devices were also fabricated from wires that had been etched in BHF to fully remove the SiO_2 diffusion barrier from their surfaces prior to removal from the growth substrate. These wires also exhibited $L_{\text{eff}} \leq 0.5 \mu\text{m}$ behavior under SPCM, indicating that a high axial-region surface recombination velocity also existed at native-oxide-terminated surfaces, and that the passivation obtained by immersion in BHF was not air stable.

5.3.2 Passivation with PECVD a-Si:H

Our radial p-n junction Si microwires were coated with their a-Si:H surface-passivation layer prior to being removed from the growth substrate. The wire arrays were first chemically etched in BHF to remove any remaining surface oxide (including the diffusion-barrier oxide), and a standard clean was performed. The a-Si:H films were deposited by PECVD at 240 °C and 500 mTorr, using SiH_4 (5% in Ar) and a 13.56 MHz plasma at 3 W forward power. A 30 min deposition time was chosen to produce a ~ 10 nm thick (estimated) layer of undoped a-Si:H on the wire sidewalls. Single-wire devices were fabricated as described above, and after metallization, it was found that they required a 30 min anneal at 275 °C in forming gas (5% H_2 in N_2) to produce ohmic contacts through the nominally intrinsic a-Si:H layer.

SPCM measurements on a-Si:H-coated wires indicated exponentially decaying carrier collection along the axial length of each wire, as expected for transport limited by minority-carrier diffusion and recombination within the quasi-neutral region of a p-n junction device. Figure 5.8 plots linear- and log-scale cross sections of the SPCM profile of a typical a-Si:H-coated single-wire device. Roughly constant E.Q.E. was observed throughout the radial portion of

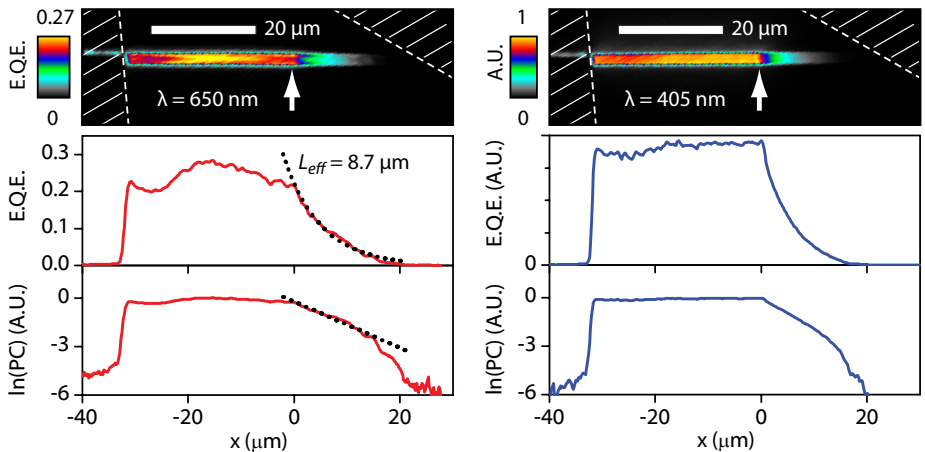


Figure 5.8. SPCM characterization of an a-Si:H-coated single-wire device, performed using $\lambda = 650$ nm (left) and $\lambda = 450$ nm (right) excitation sources.

the wire ($x < 0 \mu\text{m}$), while exponentially decaying E.Q.E. was observed in the axial portion of the wire ($x > 0 \mu\text{m}$). A fit to the exponential decay indicated $L_{\text{eff}} = 8.7 \mu\text{m}$ for this device. Six a-Si:H-coated single-wire devices were studied by SPCM, and L_{eff} values ranging from 5.4–9.8 μm were observed.

Because the SiO_2 diffusion-barrier had been removed from the a-Si:H-coated wires, the spatial extent of the axial region could not be directly observed by optical microscopy. Thus, the endpoint of the radial p-n junction was inferred from the SPCM profiles of each wire, assumed to occur at the onset of exponentially decaying E.Q.E. However, minor fluctuations in E.Q.E. were also observed throughout the entire wire, obfuscating the transition between radial and axial collection. We determined that these fluctuations arose from photonic effects rather than from variations in the carrier-collection efficiency along the wires. At the illumination wavelength ($\lambda = 650 \text{ nm}$), the optical absorption properties of Si microwires are dominated by scattering and dielectric resonance effects, which depend strongly on the wire diameter. [213] The diameters of our wires varied and generally decreased slightly from base to tip, with a typical taper of 10–20% observed by SEM (e.g., see Fig. 3.22). To demonstrate that the radial-region carrier-collection efficiency was approximately uniform, we performed SPCM measurements with a $\lambda = 405 \text{ nm}$ illumination source, at which wavelength the Si microwires were optically opaque and thus less affected by dielectric resonances. The $\lambda = 405 \text{ nm}$ SPCM images revealed a more-uniform carrier-collection efficiency within the radial region of the wire, as well as a more pronounced transition to exponentially decaying behavior within the axial region of the wire.

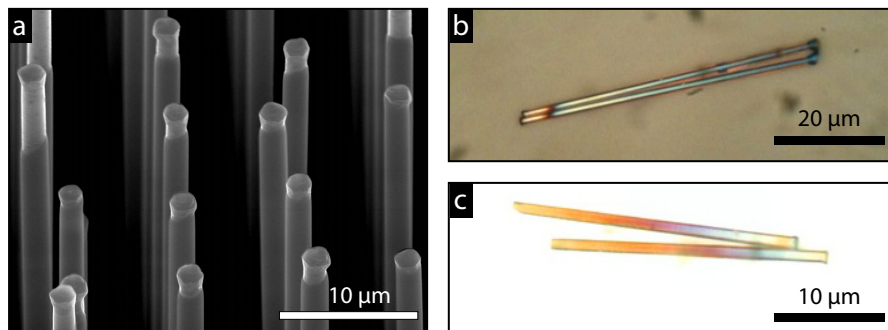


Figure 5.9. Images of an a-SiN_x:H-coated wire array and individual wires. a, SEM image of an a-SiN_x:H-coated wire array, taken after the tip of each Si wire had been exposed using a wax-infill-masked chemical etch. **b, c,** Optical micrographs of individual a-SiN_x:H-coated wires as dispersed for electrical contacting. *Image (a) provided by Daniel Turner-Evans.*

5.3.3 Passivation with PECVD a-SiN_x:H

The a-SiN_x:H surface-passivation layers were deposited by the same PECVD process that was used to deposit the antireflective coatings on our light-trapping structures (see section 3.4.1), and the wire arrays were prepared similarly to those that were coated with a-Si:H. Prior to removing a-SiN_x:H-coated wires from the growth substrate for single-wire contacting, the arrays were partially infilled with wax (Quickstick 135, South Bay Tech.) and then etched for 10 s in 49% HF(aq) to remove the a-SiN_x:H from the uppermost 1–10 μm of each wire, enabling electrical contact to the tips of each single-wire device. Figure 5.9 shows an a-SiN_x:H-coated wire array following the masked nitride-etch and wax removal. A gradual taper in the nitride thickness (ranging from ~60 nm thick at the wire base to ~120 nm thick at the wire tip, see Fig. 3.22) also gave rise to vivid coloration along the length of each wire under optical microscopy.

The SPCM measurements on a-SiN_x:H-coated wires indicated relatively constant E.Q.E. throughout the entire non-shaded extent of each wire, indicative of large values of L_{eff} . This behavior, combined with the absence of the SiO₂ diffusion-barrier as a visual aid, presented a challenge to the determination of the junction position within the a-SiN_x:H-coated wires. SPCM measurements performed at $\lambda = 405$ nm and $\lambda = 650$ nm both showed mild variations in E.Q.E. along the length of the a-SiN_x:H-coated wires, as shown in Figure 5.10. However, the two measurements showed no common trends that might identify the start of the radial junction, suggesting that the variations were due to optical (rather than electrical) phenomena. In addition to the effects of wire-diameter taper encountered with a-Si:H-coated single-wire devices (which were evident only in the $\lambda = 650$ nm SPCM images), the a-SiN_x:H-coated wires exhibited additional optical artifacts due to the varying nitride thickness (evident at both SPCM wavelengths, and in the varying apparent coloration of the wires under optical microscopy).

To determine the location of the radial p-n junctions within the a-SiN_x:H-coated wires, it was found that irradiating them with 30 keV electrons in the course of scanning electron microscopy resulted in $L_{\text{eff}} < 0.5$ μm behavior within their axial regions. Thus, immediately following SEM imaging of the single-wire

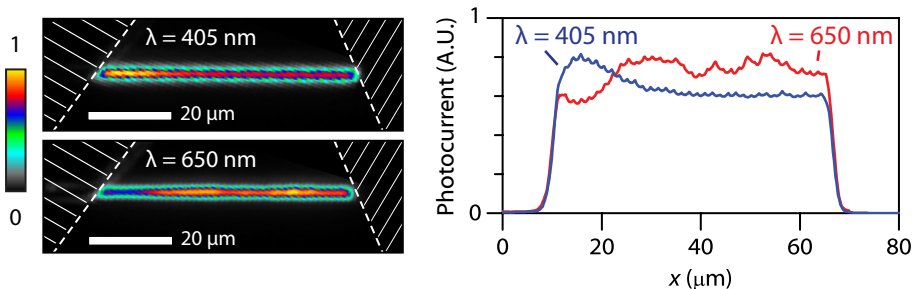


Figure 5.10. SPCM characterization of an a-SiN_x:H-coated single-wire device performed using $\lambda = 650$ nm and $\lambda = 450$ nm excitation sources.

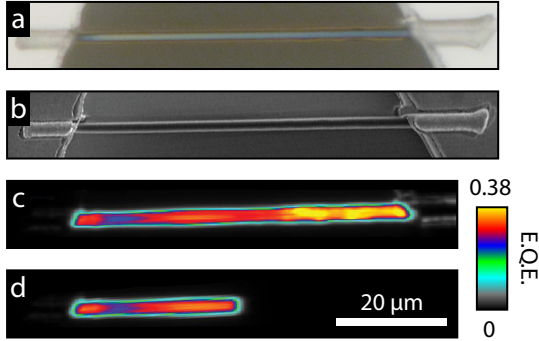


Figure 5.11. Determining the junction position within the a-SiN_x:H-coated single-wire devices. **a**, Optical microscope image, **b**, SEM image, and **c–d**, $\lambda = 650$ nm SPCM images of an a-SiN_x:H-coated single-wire device. The SPCM images were recorded before (**c**) and after (**d**) exposure to 30 keV electrons in the course of SEM imaging.

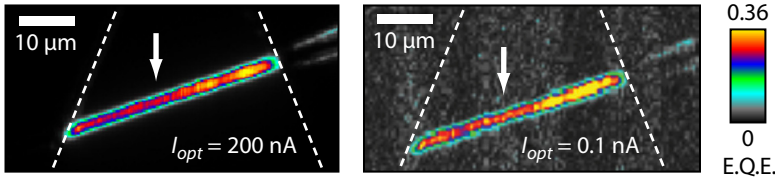


Figure 5.12. Invariance of L_{eff} at reduced carrier injection levels. SPCM profiles of an a-SiN_x:H-coated device measured under typical ($I_{\text{opt}} = 200$ nA) and reduced ($I_{\text{opt}} = 0.1$ nA) excitation intensity. The dashed white lines indicate the location of the contacts, and the arrows indicate the start of radial p-n junction.

devices, the junction position could be observed by SPCM. Figure 5.11 shows the SPCM profiles for an a-SiN_x:H-coated device observed before (above) and after (below) SEM imaging, revealing an axial wire length of ~ 30 μm .

The long minority-carrier collection lengths observed in a-SiN_x:H-coated wires appeared to be unaffected by carrier injection levels (within the available range of excitation power).^{*} A typical beam photocurrent of ~ 20 – 200 nA was used, which induced peak specimen photocurrent values of the same approximate magnitude as each device's one-sun I_{sc} . However, all devices exhibited nominally identical SPCM profiles under $\sim 2000\times$ lower illumination levels (Fig. 5.12), indicating that the observed recombination rates were not an effect of higher injection levels than would be present within each wire under one-sun illumination.

^{*}Higher-power excitation was available, but our detection instrumentation saturated at specimen currents exceeding ~ 100 nA.

5.4 Photovoltaic performance of single-wire test structures

The long minority-carrier collection lengths ($L_{\text{eff}} \gg 30 \mu\text{m}$) observed for the a-SiN_x:H-coated single-wire devices confirmed that, although the growth of the Si microwires was catalyzed by Cu (one of the most soluble, mobile, and prevalent impurities in Si microelectronics fabrication), [175] it was nonetheless possible to synthesize long-diffusion-length material with well-passivated surfaces. These achievements enabled the single-wire radial p-n junction devices to operate as remarkably efficient single-wire solar cells—exhibiting the highest open-circuit voltages (V_{oc}), fill factors (FF), and photovoltaic efficiencies (η) reported to date for VLS-grown Si wire solar cells (summarized in Table 5.1). Figure 5.13 plots the current-density vs. voltage (J - V) behavior of the most efficient devices of each surface coating type. To improve the performance of the single-wire cells, they were fabricated on reflective substrates (SiN_x-coated Ag) to improve the absorption of incident light. Following the convention of prior single-wire solar cell studies, the current density was determined by normalizing the device current by the total exposed (non-shaded) area of each wire. [157, 159, 169, 163] The data were measured at 25 °C using a 1000 W Xe arc lamp with air mass filters (Oriel), calibrated to one-sun intensity with an NREL-traceable Si reference cell (PV Measurements).

Comparing the surface coatings, the long collection length and reduced reflectivity of the a-SiN_x:H-coated devices consistently yielded the highest short-circuit current densities (up to 26 mA·cm⁻²), and resulted in the device with the greatest overall photovoltaic efficiency ($\eta = 9.0\%$). Interestingly, the a-Si:H-coated devices consistently produced the highest open-circuit voltages (up to

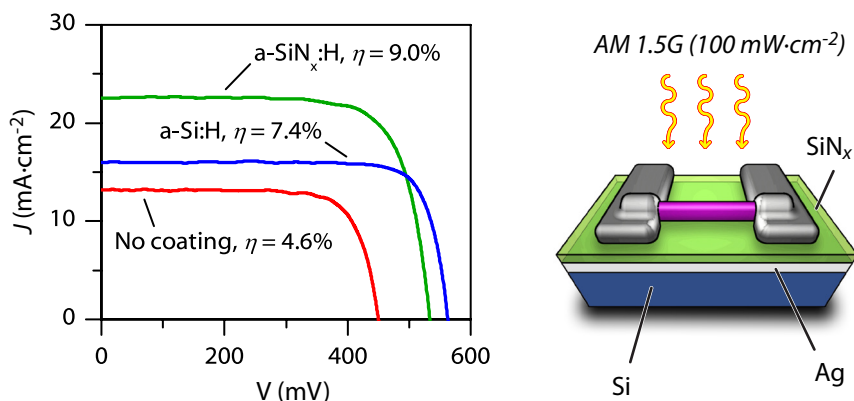


Figure 5.13. Photovoltaic J - V characteristics of the champion single-wire solar cells of each surface passivation type (left) and a schematic diagram of the illumination configuration (right). The current density of each device was normalized to the non-shaded wire area (determined by SEM).

Table 5.1. Measured properties of single-microwire solar-cell test structures. Table indicates the observed minority-carrier collection lengths (L_{eff}), inferred axial-region surface recombination velocities (S), and measured photovoltaic performance (AM 1.5G, 100 mW·cm⁻²). Upper values (bold) represent the champion cell, and lower values show the range of measured values (n denotes number of samples).

Wire coating	L_{eff} (μm)	S (cm·s ⁻¹)	η (%)	V_{oc} (mV)	J_{sc} (mA·cm ⁻²)	FF (%)
No coating ($n = 12$)	< 0.5	> 4×10 ⁵	4.6 1.5 – 4.6	451 390 – 496	13 6.9 – 16	77 58 – 81
a-Si:H ($n = 20$)	5 – 10	450 – 600	7.4 3.6 – 7.4	564 561 – 595	16 7.8 – 17	81 77 – 82
a-SiN _x :H ($n = 13$)	>> 30	<< 70	9.0 4.8 – 9.0	535 462 – 543	23 17 – 26	75 56 – 78

595 mV), despite having many times greater S within the axial region. This behavior may indicate that, although the a-SiN_x:H coating provided the best passivation of the p-type (base) surfaces, the a-Si:H provided superior passivation of the n-type (emitter) surfaces or the Al-Si interfaces, and that the latter recombination sources were more detrimental to the V_{oc} of these devices. Further work is needed to elucidate these recombination sources, and to develop passivation strategies that combine the high V_{oc} of a-Si:H coatings with the high J_{sc} of a-SiN_x:H coatings.

5.4.1 Spectral response

Spectral response measurements were performed on the champion single-wire test structures of each surface-coating type (whose J – V characteristics are shown in Fig. 5.13). The photoresponse of each device was measured at short circuit (0 V) under uniform, collimated, monochromatic illumination ($\lambda = 300$ –1100 nm) using lock-in detection. The illumination was provided by a 300 W Xe arc lamp coupled to a 1/4 m monochromator (Oriel) configured to provide a ~5 nm passband. Because the optical absorption of horizontally oriented wires depends on the polarization of the incident light, [213, 152] and because the polarization state of our illumination source was not known, the spectral response of each device was measured twice, rotating the specimen 90° between measurements, and then averaged to determine the response of each wire to unpolarized light (such as sunlight). The photoresponse of each device was normalized (by area) to that of a 3 mm diameter calibrated photodiode to determine the absolute external quantum efficiency (E.Q.E.) at each wavelength, plotted in Figure 5.14a.

Following the convention of prior single-wire solar cell studies, [157, 159, 163, 169] the exposed physical area of each wire (observed by SEM; excluding

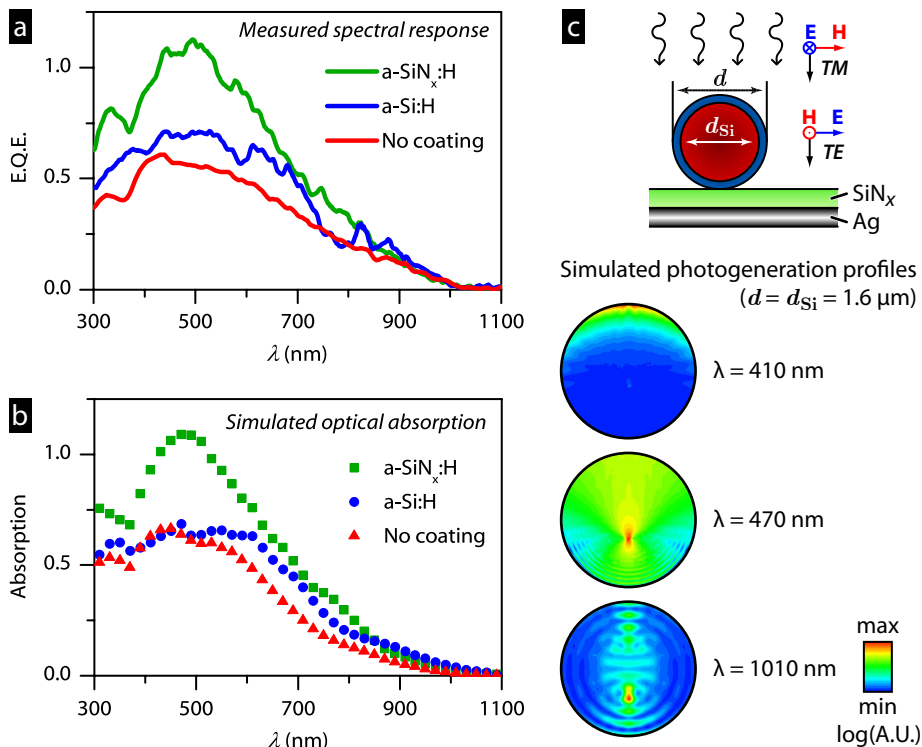


Figure 5.14. **a**, Measured spectral response of the champion single-wire solar cell of each passivation type. External quantum efficiency (E.Q.E.) was determined based on the non-shaded physical area of each wire. **b**, Simulated optical absorption of each of the three devices plotted in (a). **c**, Schematic of illumination configuration and simulation structure (top), and simulated photogeneration profiles within the non-coated Si wire device at three selected illumination wavelengths (below).

that covered by the metal contacts) was used to calculate the E.Q.E.* Interestingly, this normalization resulted in an apparent peak E.Q.E. of $\sim 110\%$ (near $\lambda = 500$ nm) for the a-SiN_x:H-coated single-wire device, warranting further investigation of the optical absorption and the effective area of these microstructures.

The observation of E.Q.E. $> 100\%$ can be explained by the photonic dimensions of the Si microwires (which were 1.2–1.8 μm in diameter). At this size regime, scattering theory predicts that particles can exhibit effective absorption cross-sections which exceed their physical cross-sections. [214] This enables microwires (and nanowires) to interact with (and potentially absorb) more sunlight than predicted by physical area and conventional ray optics. [213, 56, 124]

*For wires coated with SiO₂, a-Si:H, or a-SiN_x:H, the outer diameter of the wire structure (d), rather than the diameter of the crystalline Si wire (d_{Si}), was used to calculate device area (see diagram in Fig. 5.14c). For tapered wires, the mean diameter was used.

Combined with the antireflectivity a-SiN_x:H coatings, the opacity of the Si wires ($L_{\text{abs}} < d$ at $\lambda \sim 500$ nm), and the use of a back-reflecting (Ag) substrate, this can lead to an apparent E.Q.E. in excess of 100% when the measured photocurrent is normalized to the optical power incident on the physical area of the wire.

To further investigate the interaction of light with horizontal Si microwires, we simulated the optical absorption of each of the studied single-wire structures under the experimental configuration of Figure 5.14c. Two-dimensional electromagnetic simulations were performed at 40 discrete wavelengths spanning the measurement range ($\lambda = 310, 330, \dots, 1090$ nm) using finite-difference time-domain software (FDTD Solutions, Lumerical). At each wavelength, the results of independent transverse-electric (TE) and transverse-magnetic (TM) simulations were averaged, and partial spectral averaging was applied,* to emulate unpolarized plane-wave illumination at normal incidence.† Each simulation took into account the measured wire diameter (d), the estimated surface-coating thickness, and the measured PECVD film optical properties (see Figs. A.1 and A.2), using tabulated optical constants for Si [75] and approximating the Ag substrate as an ideal metal boundary condition.

Figure 5.14c (below) shows the simulated absorption profiles for the non-coated, 1.61 μm diameter Si wire device at three selected wavelengths. At short wavelengths ($\lambda < 450$ nm), the absorption was concentrated near the wire surface, whereas at longer wavelengths ($\lambda > 500$ nm), the absorption was concentrated near the center of the wire. Following each simulation, the absolute absorption was calculated by dividing the total energy dissipated within the Si by the total energy of the plane wave incident above the cross-sectional width of the wire structure (d in Fig. 5.14c). For comparison with experimental E.Q.E. measurements, the simulated absorption of the non-coated wire was reduced by 23% to account for the inactive (axial) portion of the champion cell, which had been determined by SPCM. (The exposed length of the wire was 51.1 μm , but the radial junction extended through only 39.5 μm .) The other devices were essentially active throughout their entire exposed area, due to the long L_{eff} of the a-SiN_x:H-coated wire, and due to the close proximity of the radial junction to the opposite contact in the champion a-Si:H-coated device.

As shown in Figure 5.14, the simulated absorption of the horizontal wire structures exhibited marked qualitative and quantitative agreement with the experimentally observed E.Q.E. of the single-wire solar cells. This suggests that the internal quantum efficiency (I.Q.E.) of the single-wire solar cells was close to 100% at all wavelengths, as expected for radial-junction devices of diameter less than the minority carrier diffusion length. Both the measured E.Q.E. and simulated absorption of each device also predicted similar J_{sc} values (weighted across the AM 1.5G spectrum) to those measured under calibrated solar illumination (Table 5.2), indicating good agreement between simulations and measurement

*The partial spectral averaging suppressed coherent interference (i.e., dielectric resonance) effects that were not experimentally observed due to the mild taper in wire diameter and film thickness along each device. The PSA width (Δf) was calculated based on simulation frequency (f) and Si refractive index (n_{Si}), as $\Delta f = f \left(1 + \frac{d_{\text{Si}} n_{\text{Si}}}{\lambda} \right)^{-1}$.

†Implemented as a “Total Field Scattered Field” (TFSF) source in Lumerical.

Table 5.2. Measured vs. calculated J_{sc} of champion single-wire solar cells. Table shows the outer diameter (d); the estimated surface-coating film thickness (t_{film}); and the short-circuit current density (J_{sc}) of the champion cell of each surface-coating type measured under one-sun illumination, calculated from spectral response measurements, and calculated from optical absorption simulations.

Surface coating	d (μm)	t_{film} (nm)	Short-circuit current density ($\text{mA}\cdot\text{cm}^{-2}$)		
			1-sun AM 1.5G (measured)	$\int_{\text{AM1.5G}} \text{E.Q.E. (meas.)}$	$\int_{\text{AM1.5G}} \text{Absorption (sim.)}$
None (SiO_2)	1.61	—	13.2	13.3	13.0
a-Si:H	1.45	8	16.2	16.9	15.7
a-SiN _x :H	1.47	70	22.5	22.7	21.1

techniques. We note that the high apparent I.Q.E. inferred for ultraviolet wavelengths is indicative of a low emitter-region surface recombination velocity [215] as well as a relatively long emitter-region minority-carrier lifetime. [216] This was not unexpected given our choice of a shallow ($x_j < 100$ nm), lightly doped ($N_{D,\text{surf}} \sim 10^{19} \text{ cm}^{-3}$) diffused junction profile.

The optical simulations also predicted a peak apparent absorption of 109% for the a-SiN_x:H-coated wire, confirming that the this structure’s effective absorption area exceeded its physical cross-sectional area.* Thus E.Q.E. values exceeding 100% do not indicate nonconventional absorption processes (i.e., multiple exciton generation), nor do they reflect inaccurate measurement of physical area; rather, this illustrates the challenge in defining the active area of solar cells whose dimensions do not significantly exceed the free-space wavelength of the incident illumination. Normalizing the performance of such solar cells to their physical area, although consistent with the conventions applied to macroscopic solar cells, could lead to apparent efficiencies which cannot be achieved over macroscopic areas. This property is beneficial for the use of single-wire solar cells as nanoelectronic power sources (as suggested by Tian, Kempa, et al.), and allows them to achieve enhanced power output compared to planar devices. [157, 159] However, for macroscopic solar cell considerations, the photovoltaic performance of each wire must be normalized to the effective per-wire absorption area (within the optical plane), regardless of the physical cross-sectional area of the wire. This motivated us to measure our single-wire solar cells in a manner consistent with the illumination conditions of a wire-array solar cell, thereby enabling us to predict the efficiency attainable by macroscopic Si microwire-array solar cells.

5.5 Predicted efficiency of large-area solar cells

Our single-wire test structures allowed us to consider the potential performance of large-area solar cells made from VLS-grown Si wires. Two proposed wire-array

*Note that this result did not indicate a violation of energy conservation in the simulations: the width of the plane wave excitation source was several microns wider than the width (d) of the wire.

solar cell geometries are discussed here: a device consisting of tightly packed, horizontally aligned wires (Fig. 5.15), and a device consisting of sparsely packed, vertically aligned wires (Fig. 5.17).

5.5.1 Horizontally aligned wires

Within the proposed horizontal-microwire-array solar cell of Figure 5.15, the configuration of each individual wire closely resembles that of our single-wire test structures. The use of interdigitated back-side contacts would provide a metallic back-reflector beneath each wire (analogous to the SiN_x -coated Ag substrates used for our single-wire devices), and would also eliminate any contact shading losses (which were neglected in our calculation of single-wire efficiency). Thus it seems reasonable to conclude that if such a device could be fabricated, it could attain efficiencies on par with our single-wire solar cells (i.e., up to 9%).

However, as discussed in the previous section, the photonic dimensions of Si microwires enable them to interact with (and potentially absorb) more light than predicted by their physical cross-sectional area (from a classical ray-optics perspective). Thus it is possible, for tightly packed arrays of horizontal microwires, that adjacent microwires could effectively “shade” one another without physically overlapping—which would result in lower large-area cell efficiencies than the apparent single-wire efficiencies. To investigate this effect, we compared the simulated optical absorption of an “isolated” wire to that of an “arrayed” wire, as depicted in Figure 5.16. The simulated wires were of similar dimensions as our champion $\text{a-SiN}_x\text{:H}$ -coated single-wire solar cell, and we employed the same modeling approach as was presented in our discussion regarding the spectral response of isolated single-wire solar cells (see Fig. 5.14). To extend our analysis

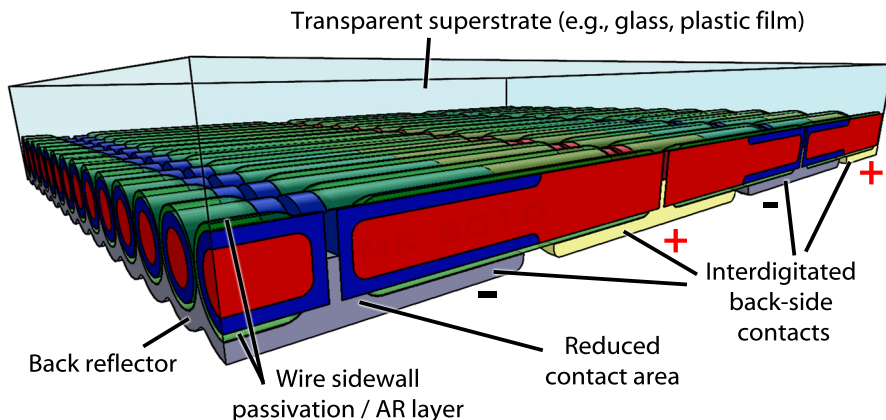


Figure 5.15. Proposed large-area wire-array solar cell consisting of aligned, tightly packed, horizontally oriented Si microwires with radial p-n junctions.

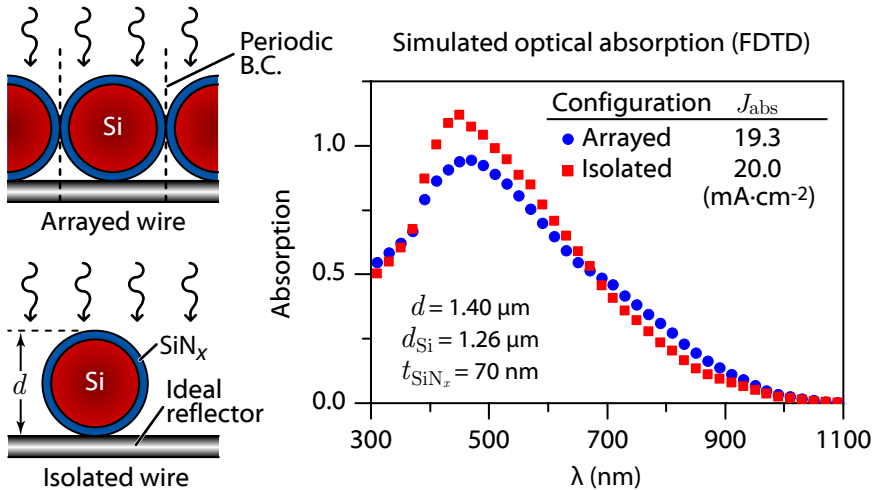


Figure 5.16. Simulated optical absorption of horizontally oriented Si microwires, in a tightly packed array configuration (depicted above), and isolated as single-wire devices (below).

to the arrayed configuration, we simply modified the simulation to apply periodic boundary conditions at either side of the wire.* The simulation results are plotted in Figure 5.16.

As expected, the presence of neighboring wires affected the simulated absorption of each wire. In particular, the phenomena of $>100\%$ apparent per-wire absorption became impossible for the arrayed wires, as this would violate the conservation of energy. Indeed, the peak apparent absorption decreased from 112% for the isolated wire to 94% for the arrayed wire. However, the arrayed configuration was beneficial to absorption at other wavelengths (e.g., 800 nm), which can be conceptualized as light scattering between adjacent wires. Weighting the two simulated absorption spectra by the solar spectrum (AM 1.5G), we found that the photoabsorption current density (J_{abs}) differed by only 3.6% between the isolated horizontal wire ($20.0 \text{ mA}\cdot\text{cm}^{-2}$) and the arrayed horizontal wires ($19.3 \text{ mA}\cdot\text{cm}^{-2}$).

Thus, our single-wire measurements provided a reasonable indicator of the performance potential of solar cells made from densely packed, horizontally aligned Si microwires (i.e., their efficiency could approach $\sim 9\%$). There also remain numerous unexplored and promising routes to significantly enhance the efficiencies of such solar cells: their performance could be improved, for example, by engineering the diameter and pitch of the wires so as to maximize dielectric resonance absorption enhancements, as proposed for nanowire solar cells. [213, 56]

*Isolated wire simulations employed a TFSF source (wider than the wire) with perfectly matched layer (PML) boundary conditions (BCs) located several microns to either side of the wire. Arrayed wire simulations employed a plane-wave source with periodic BCs immediately to either side of the wire.

Furthermore, the geometry seems particularly well-suited for the use of aligned, lenticular-lens micro-optical concentrators like those demonstrated on Si micro-cells. [29] At present, however, the efficiencies of even our best single-microwire solar cells were greatly limited by incomplete optical absorption, as evidenced by their low J_{sc} and poor infrared spectral response despite our use of back-reflecting substrates and antireflective coatings. Thus we conclude that solar cells comprising arrays of horizontally oriented, crystalline Si microwires (such as that proposed in Figure 5.15), will require the use of larger-diameter wires than studied herein, or other breakthroughs in absorption engineering, in order to obtain photovoltaic efficiencies that rival wafer-based Si photovoltaics.

5.5.2 Vertically aligned wires

Alternatively, the optical absorption studies in Chapter 3 showed that light-trapping arrays of vertically oriented, polymer-embedded Si microwires can absorb up to 85% of above-bandgap sunlight, and thus offer a high photovoltaic performance potential for wires of the dimensions studied herein. Accordingly, we can performed single-wire measurements to predict the efficiency of the three-dimensional photovoltaic structure shown in Figure 5.17. Conveniently, our light-trapping absorption measurements were performed on square-tiled wire arrays of the same approximate pitch and wire dimensions as the radial p-n junction wire array from which our single-wire devices were fabricated (Fig. 5.1). Based on the measured optical absorption of the light-trapping array, we calculate that it could produce up to $J_{sc} = 35.9 \text{ mA}\cdot\text{cm}^{-2}$ as a solar cell (under normal-incidence one-sun AM 1.5G illumination), assuming that all absorbed photons were collected as electrical current. This value corresponds to $I_{sc} = 17.6 \text{ nA}$ per each $7 \times 7 \text{ }\mu\text{m}$ wire-array unit cell. To emulate these wire excitation conditions, we measured the I - V behavior of our champion a-Si:H-coated single-wire solar

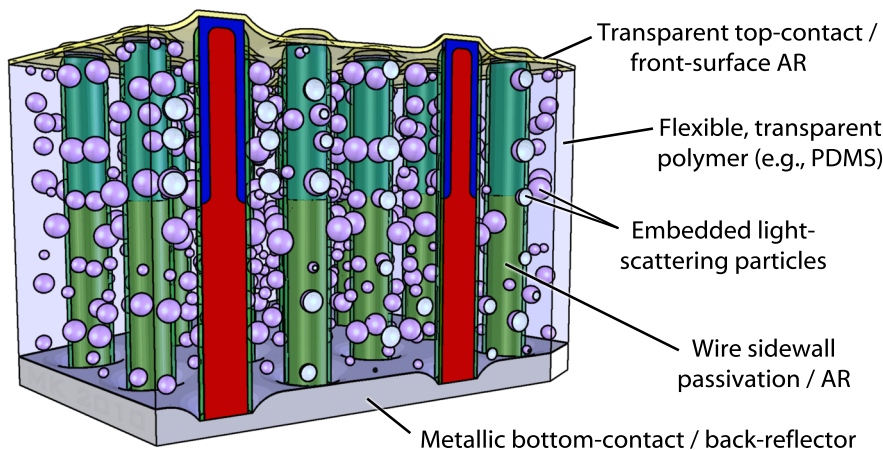


Figure 5.17. Proposed large-area wire-array solar cell consisting of sparsely packed, vertically oriented Si microwires with radial p-n junctions.

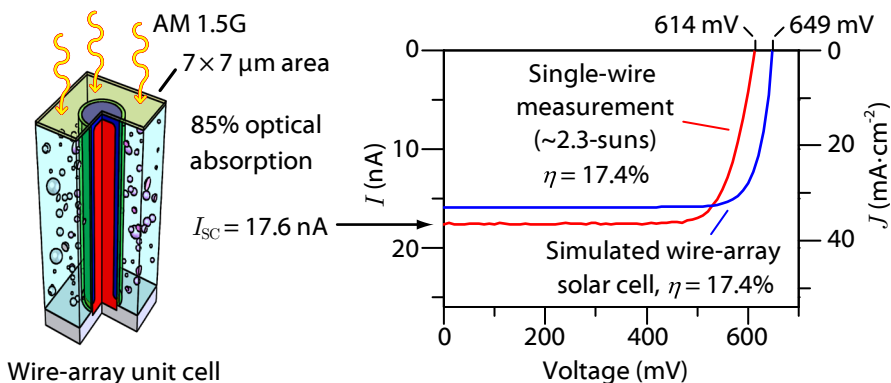


Figure 5.18. Projected efficiency of large-area wire-array solar cell. Measured I - V of champion single-wire solar cell under emulated wire-array illumination conditions vs. simulated efficiency of wire-array solar cell from section 2.3.

cell, oriented horizontally, under ~ 2.3 -suns illumination intensity, which produced the desired $I_{sc} = 17.6$ nA. As shown in Figure 5.18, the elevated injection levels of this illumination configuration also increased the open-circuit voltage to $V_{oc} = 614$ mV. If each wire within the proposed vertical-wire-array solar cell exhibited this identical I - V behavior, neglecting contact resistance or shading effects, the large-area device would have a photovoltaic efficiency of 17.4%. Table 5.3 compares the performance of this single-wire device under horizontal one-sun illumination and projected one-sun wire-array illumination levels.

The experimental efficiency projection for the large-area microwire-array solar cells of Figure 5.17 is in good agreement with the 17.4% efficiency predicted by our optoelectronic simulations of this structure in Chapter 2 (section 2.3). For comparison, the simulated I - V behavior is also shown in Figure 5.18. The simulations, which also considered the optical losses due to the front-surface reflection and free-carrier absorption of an ITO top contact, predicted lower J_{sc} (32.4 mA·cm $^{-2}$) than we calculated based on our experimental absorption measurements (35.9 mA·cm $^{-2}$). However, the simulations also predicted that the reduced contact area of the proposed wire-array device (i.e., when only the top and bottom surfaces of each wire are contacted) enable a higher V_{oc} (649 mV), yielding similar overall efficiency as predicted by experimental projections. Although

Table 5.3. Performance of single-wire solar cell under horizontal one-sun illumination vs. projected wire-array illumination

	V_{oc} (mV)	I_{sc} (nA)	J_{sc} (mA·cm $^{-2}$)	FF (%)	η (%)
Horizontal single-wire	594	7.6	8.3	81	4.0
Vertical wire-array	614	17.9	35.9	79	17.4

our measurements and simulations have not accounted for many challenges facing large-area wire-array solar cells (such as contact-grid shading, resistive losses, or variations in wire properties), the results nonetheless demonstrate the potential of VLS-grown Si wire-array solar cells to compete, on an efficiency basis, with commercial multicrystalline wafer-based Si technology—an important and fundamental milestone for the development of Si microwire photovoltaics.

Conclusion and outlook

This thesis has presented further evidence that Si microwire solar cells may offer a compelling route toward cost-effective crystalline Si photovoltaics. Specifically, we have experimentally verified that these devices satisfy the three fundamental requirements for high energy-conversion efficiency:

1. They effectively absorb sunlight—in fact, wire arrays made from as much Si as a ~ 3 μm thick wafer can absorb about 85% of the above-bandgap, day-integrated sunlight.
2. They efficiently collect carriers. We observed near-unity internal quantum efficiency in a wire-array photoelectrode, and even witnessed carriers diffusing the entire length of single-wire devices ($L_n \gg 30$ μm).
3. They can achieve high operating voltages, as evidenced by single-wire measurements ($V_{oc} \approx 600$ mV) and as predicted by numerical modeling ($V_{oc} \approx 650$ mV).

Combined, these observations suggest that Si microwire-array solar cells will be able to exceed 17% efficiency.

Many challenges remain in the pathway toward realizing high-efficiency, large-area, Si microwire-array solar cells. We have only observed such high performance on a handful of single-wire devices, and our simulations have neglected such important factors as contact resistance, shading loss, and variation in wire quality. Nonetheless, our theoretical and experimental approaches have produced the most thorough, as well as the most encouraging, understanding of the potential efficiencies of Si microwire photovoltaics to date.

6.1 Advantages of Si microwire photovoltaics

Although the concept of producing solar cells from VLS-grown Si wires is not new one, [31, 32] its true promise has only recently become clear. Researchers around the world are now pioneering countless novel micro- and nanowire-based photovoltaic technologies. Our study began as an effort to exploit radial p-n junctions to produce moderate-efficiency solar cells from low-quality Si. [39] Through fruitful collaborations, this has fostered a novel and innovative approach to high-efficiency thin-film Si photovoltaics. The result is a microstructured solar cell that combines the electrical qualities of multicrystalline Si wafers, the material consumption of thin-film technologies, and the mechanical properties of a window decal.

A survey of the achievements in the field of Si microwire photovoltaics suggests that these technologies will benefit from the following:

High-speed, high-fidelity growth technique. Using the VLS process, crystalline Si microwires can be synthesized directly from SiCl_4 feedstock—entirely bypassing the decomposition and recrystallization steps of contemporary polysilicon production (i.e., the Siemens process), while simultaneously utilizing one of its unwanted by-products. [9, 38] The SiCl_4 -based VLS growth process employed in our study routinely produced high-quality material at growth rates in excess of $5 \mu\text{m}\cdot\text{min}^{-1}$ (enabling deposition times of 20 minutes or less), and much higher growth rates ($\sim\mu\text{m}\cdot\text{s}^{-1}$) have been reported for similar growth chemistries [197] as well as for lower-temperature Si_2H_6 -based VLS processes. [201] High-fidelity wire arrays were grown over areas limited only by the size of our reactor ($\sim\text{cm}^2$). [37]

Alternate VLS catalyst metals. Numerous catalyst metals are compatible with VLS growth. [36] Our work has confirmed the promise of Cu (vs. Au) as a catalyst metal, which is not only less expensive, but more importantly, is better tolerated in Si photovoltaics. [129] The use of other catalysts such as Ni or Al may also prove beneficial.

Demonstrated layer-transfer and substrate re-use. Using polymer infill materials, a surprisingly simple layer-transfer technique has been developed for Si wire arrays. [42] Not only does this produce mechanically flexible films with relatively clean crystal fracture, but it also permits the crystalline Si growth wafer to be reused multiple times—producing additional wire arrays without requiring further patterning or vacuum-based processing. [43]

Mechanical flexibility. The flexibility of polymer-embedded wire arrays may lend itself to roll-to-roll processing techniques, and suggests potential applications as conformal (e.g., building-integrated) photovoltaics or as portable high-performance solar energy sources. [128, 29]

Enhanced optical absorption. The effectiveness of light-trapping in Si wire arrays leads to enhanced optical absorption compared to conventional planar geometries, and enables a solar cell geometry that utilizes 1/100th as much Si as traditional wafer-based devices. Nanowires may offer even greater enhancements. [53, 124]

Long minority-carrier diffusion length. Si microwire solar cells have exhibited diffusion lengths of $\gg 30 \mu\text{m}$, suggesting that their material quality is on par with that typical of multicrystalline Si wafer-based solar cells.

Well-passivated surfaces. PECVD a- $\text{SiN}_x\text{:H}$ can yield surface recombination velocities of $S \ll 30 \text{ cm}\cdot\text{s}^{-1}$ in VLS-grown Si microwires, while also acting as an effective antireflective coating.

Promising single-wire performance. Si microwires with diffused radial p-n junctions have exhibited V_{oc} as high as 595 mV with FF above 80%. Their apparent photovoltaic efficiency (up to 9.0%) was limited simply by optical transparency due to their horizontal orientation. When measured

under illumination conditions commensurate with one-sun illumination of vertically oriented wire arrays, these devices have yielded V_{oc} as high as 614 mV, and suggest that large-area devices would exceed 17% efficiency.

High efficiency potential. Comprehensive optoelectronic modeling, based on experimentally observed minority-carrier diffusion lengths for VLS-grown Si microwires, has predicted efficiencies of over 17%, and V_{oc} of ~ 650 mV.

6.2 Toward efficient Si microwire-array solar cells

Despite the promise of Si wire-array photovoltaics, the reported efficiencies of VLS-grown Si wire-array solar cells have thus far remained low. But this is quickly changing: the field has experienced rapid growth and is routinely producing new breakthroughs in the fabrication and understanding of these devices. Just a few short years ago, record efficiencies were well below 1% for large-area solar cells (<4% for single-wire devices), and open-circuit voltages had not exceeded ~ 300 mV. However recently, V_{oc} of ~ 500 mV have been reported for both large-area and single-wire devices, [199, 200] and we have demonstrated single-wire devices with $\eta \sim 9\%$ and $V_{oc} \sim 600$ mV. The exceptional material quality and favorable properties of VLS-grown Si wires suggest that these numbers will soon be surpassed.

Recently, efforts led by Morgan Putnam have produced Si microwire-array solar cells with efficiencies approaching 8%. [217, 218] Depicted in Figure 6.1, these devices were fabricated using the crystalline Si growth-wafer to provide the back-side electrical contact and support for the structure. The same radial p-n junction fabrication process (presented in section 5.2) was employed to make these devices, using a transparent wax as the infill material and ITO as the top-side contact. The initial devices achieved energy conversion efficiencies of $\sim 4\%$. However, by incorporating the light-trapping techniques presented in section 3.4 (and in doing so, effecting a-SiN_x:H surface passivation as described in section 5.3.3), the efficiencies improved dramatically—nearing doubling the J_{sc} for the champion cells.

Due to the relatively small size of these research cells, the determination of active area was critical in order to accurately report their efficiencies. This can be challenging for research prototype cells—for example, physically implausible values of J_{sc} have been reported in recent literature. [219] To measure the active area of his devices (~ 0.1 mm²), Putnam employed the same SPCM technique that was used to characterize our single-wire devices (see sections 4.5 and 5.2.2), stitching together ~ 25 individual 90×90 μm SPCM images to outline the perimeter of each individual cell (not shown). In doing so, he was also able to directly visualize the effectiveness of the light-trapping elements, as shown in Figure 6.1. Examining these SPCM images, it can be seen that the devices without light-trapping elements exhibited dramatically lower response when the laser excitation was incident between the wires (dropping to $\sim 20\%$ of the peak value). The devices with light-trapping elements exhibited much more uniform response across the array.

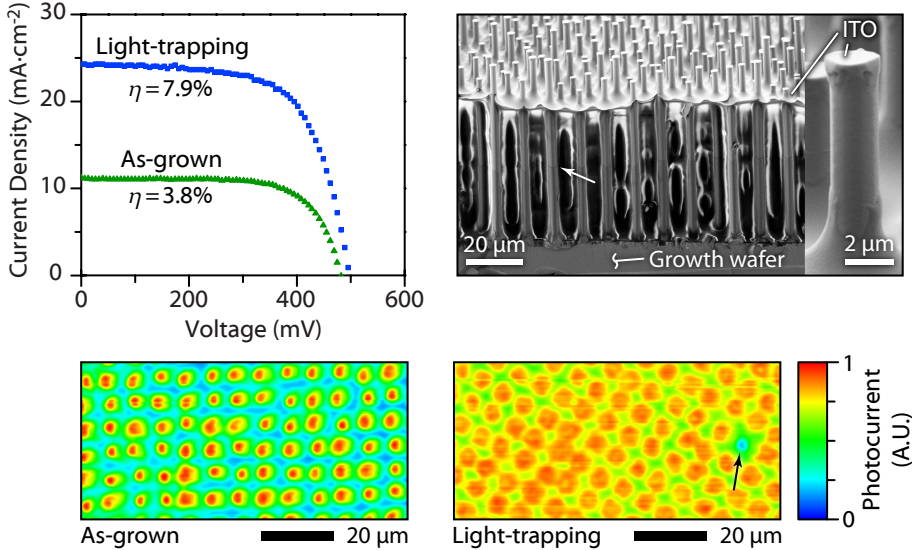


Figure 6.1. Si microwire-array solar cell. **Upper right:** Cross-sectional SEM image of Si microwire-array solar cell. The arrow indicates the extent of the radial p-n junctions. **Upper left:** Photovoltaic J - V behavior of champion ~ 0.1 mm² devices under simulated AM 1.5G illumination (100 mW·cm⁻²). **Bottom:** SPCM images of microwire-array solar cells without (left) and with (right) light-trapping elements. The black arrow indicates a wire with a failed contact. *Images provided by Morgan Putnam. [217, 218]*

6.3 Outlook

The remarkable achievements made in the field of Si nano- and microwire photovoltaics promote their continued development for renewable energy technologies. The following topics highlight areas of active and potential future research.

Advanced surface passivation. The use of a-SiN_x:H surface passivation led to the highest observed efficiencies in our single-wire devices. This material produced the lowest-observed surface recombination velocity on the wire sidewalls ($S < 70$ cm·s⁻¹) and also served as an effective antireflective coating. However, notably higher V_{oc} (~ 600 mV) was obtained with a-Si:H surface passivation. a-Si:H is known to provide highly effective passivation of the contact electrodes to Si solar cells. [210, 17] Future efforts should seek to combine these or other materials to produce a surface treatment that yields well-passivated contacted and non-contacted regions of the wire, while also providing anti-reflective properties.

Absorption enhancement. Our optical measurements revealed that Si microwire arrays can absorb slightly more sunlight, per volume of Si, than

planar absorbers with classical (isotropic) light trapping. Practical efficiency gains could be realized by understanding and maximizing this effect. Future studies should further investigate the effects of array dimensions, infill materials, light-scattering geometry, and other advanced light-trapping concepts.

Axial junction geometry. Our investigation of Si microwire solar cells was initially motivated in large part by the concept of the radial p-n junction. This geometry was thought necessary to accommodate the low L expected for VLS-grown material. However, our observations of surprisingly long L ($\gg 30 \mu\text{m}$) now suggest that other junction geometries are possible. For example, the axial junction geometry is particularly promising because it would further reduce the junction area (and thus dark current) of wire-array solar cells, enabling higher V_{oc} (cf. point-contact solar cells). [26] Furthermore, axial junctions can be produced by in situ modulation of dopant source gases (e.g., [159]) during VLS growth, potentially bypassing the processing steps used to produce diffused radial p-n junctions.

Other materials. Although the work in this thesis has focused solely on crystalline Si, we note that the radial junction geometry and VLS growth techniques have been widely investigated for the production of other photovoltaic materials, including GaAs, [169] GaN, [163], and CdS. [128] Heterogeneous tandem-junction single-nanowire devices have also been fabricated with axial tunnel junctions, suggesting that multi-junction geometries might also be possible. [159] Furthermore, the tendency of VLS growth to produce defect-free crystals, [33] combined with the radial junction's tolerance of low minority-carrier diffusion lengths, [41] yields a promising synthesis route for investigating new photovoltaic materials—including those which may have been overlooked for lack of adequate diffusion lengths or viable synthesis routes.

Sub-bandgap absorption. Although we suspected that the sub-bandgap absorption observed in VLS-grown Si wire arrays was likely indicative of parasitic processes (see section 3.2.4), this behavior may also hint at an opportunity to engineer useful sub-bandgap absorption in Si wire-array solar cells. Prior studies on impurity photovoltaic effect (IPV) solar cells have suggested that In impurities in crystalline Si solar cells could improve their efficiency, so long as the cell provided a short minority-carrier collection path. [106] Si microwire photovoltaics are well-suited for this concept, providing not only a suitable junction geometry, but also offering a viable fabrication route through the use of In as a VLS catalyst. [39, §3.4]

Computer-aided design. The numerical methods presented in Chapter 2 provide a powerful tool to not only simulate the behavior of Si microwire-array solar cells, but also to optimize their design. That our simulations have already predicted efficiencies above 17% is particularly encouraging considering that the parameter space has been largely unexplored at this

point. Numerical optimization and sensitivity analysis have a tremendous potential to produce modest improvements in these estimates, and more importantly, to guide the design of future wire-array devices.

Supplementary information

A.1 Optical properties of PECVD films

In these studies, amorphous hydrogenated films of silicon (a-Si:H) and silicon nitride (a-SiN_x:H) were deposited by plasma-enhanced chemical vapor deposition (PECVD) onto Si microwire-arrays to serve as antireflective and/or surface-passivation layers. The optical properties of both film types were measured by depositing them onto planar Si wafers and performing multiple-angle spectroscopic ellipsometry. Ψ and Δ spectra, ranging from 350–2200 nm, were measured at angles of 60°, 65°, and 70° (as shown in Figure A.1 for an a-SiN_x:H film). The spectra were then fit to a Forouhi-Bloomer model for amorphous dielectric materials. [220] The real and imaginary parts of the refractive index produced by the fit are tabulated in Table A.1, and are plotted in Figures A.1 and A.2 for a-SiN_x:H and a-Si:H, respectively. These values were used for the optical modeling of Si wire solar cells presented throughout in this study.

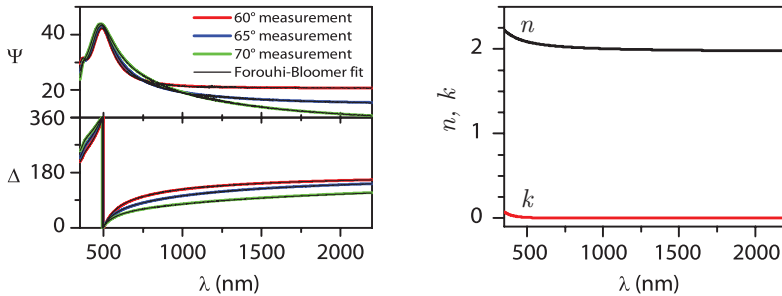


Figure A.1. Optical properties of PECVD SiN_x as determined by ellipsometry.

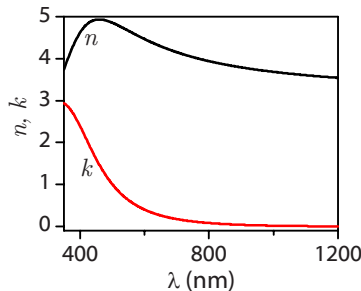


Figure A.2. Optical properties of PECVD a-Si:H as determined by ellipsometry.

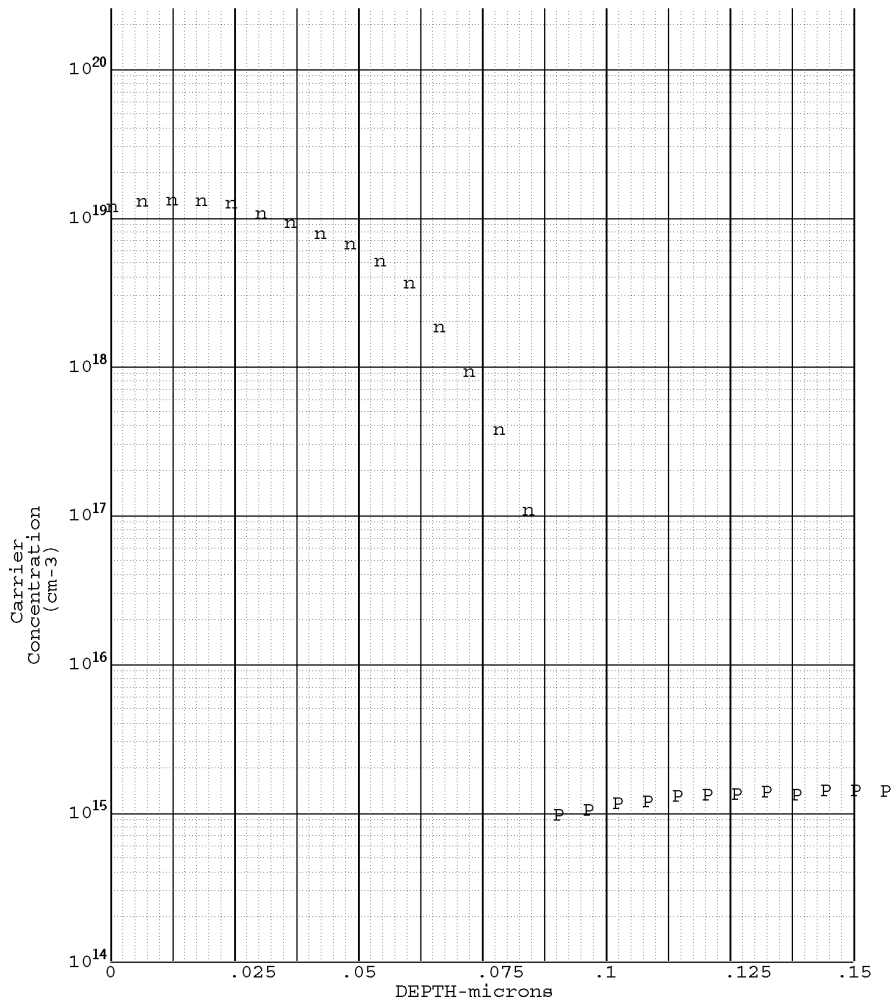
Table A.1. Optical properties of PECVD films

λ (nm)	a-Si:H		a-SiN _x :H	
	n	k	n	k
350	3.74	2.93	2.23	7.5×10^{-2}
400	4.62	2.39	2.16	3.3×10^{-2}
450	4.93	1.61	2.12	1.6×10^{-2}
500	4.86	1.01	2.09	8.5×10^{-3}
550	4.66	0.63	2.07	4.6×10^{-3}
600	4.47	0.40	2.05	2.6×10^{-3}
650	4.30	0.26	2.04	1.4×10^{-3}
700	4.15	0.18	2.03	7.2×10^{-4}
750	4.04	0.12	2.03	3.3×10^{-4}
800	3.94	8.2×10^{-2}	2.02	1.3×10^{-4}
850	3.86	5.7×10^{-2}	2.02	2.9×10^{-5}
900	3.79	3.4×10^{-2}	2.01	1.7×10^{-7}
950	3.73	2.7×10^{-2}	2.01	1.5×10^{-5}
1000	3.68	1.8×10^{-2}	2.01	5.8×10^{-5}
1050	3.64	1.2×10^{-2}	2.00	1.2×10^{-4}
1100	3.60	7.8×10^{-3}	2.00	1.9×10^{-4}
1150	3.57	4.8×10^{-3}	2.00	2.7×10^{-4}
1200	3.54	2.8×10^{-3}	2.00	3.5×10^{-4}

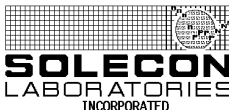
Note: All ellipsometry measurements and a-SiN_x:H depositions were performed by Ryan Briggs. The a-Si:H depositions were performed by Daniel Turner-Evans.

A.2 Spreading resistance analysis of diffused p-n junction profiles in planar control wafers

Thermal P diffusions were performed on planar Si control wafers (p-type CZ, $N_A \approx 10^{15} \text{ cm}^{-3}$), following the same procedure used to produce radial p-n junctions in Chapter 5. All specimen were fabricated by Daniel Turner-Evans, and spreading resistance measurements were performed by Solecon Laboratories. The following figures plot the junction profiles obtained for 5 min and 10 min diffusions at $T = 850 \text{ }^\circ\text{C}$.

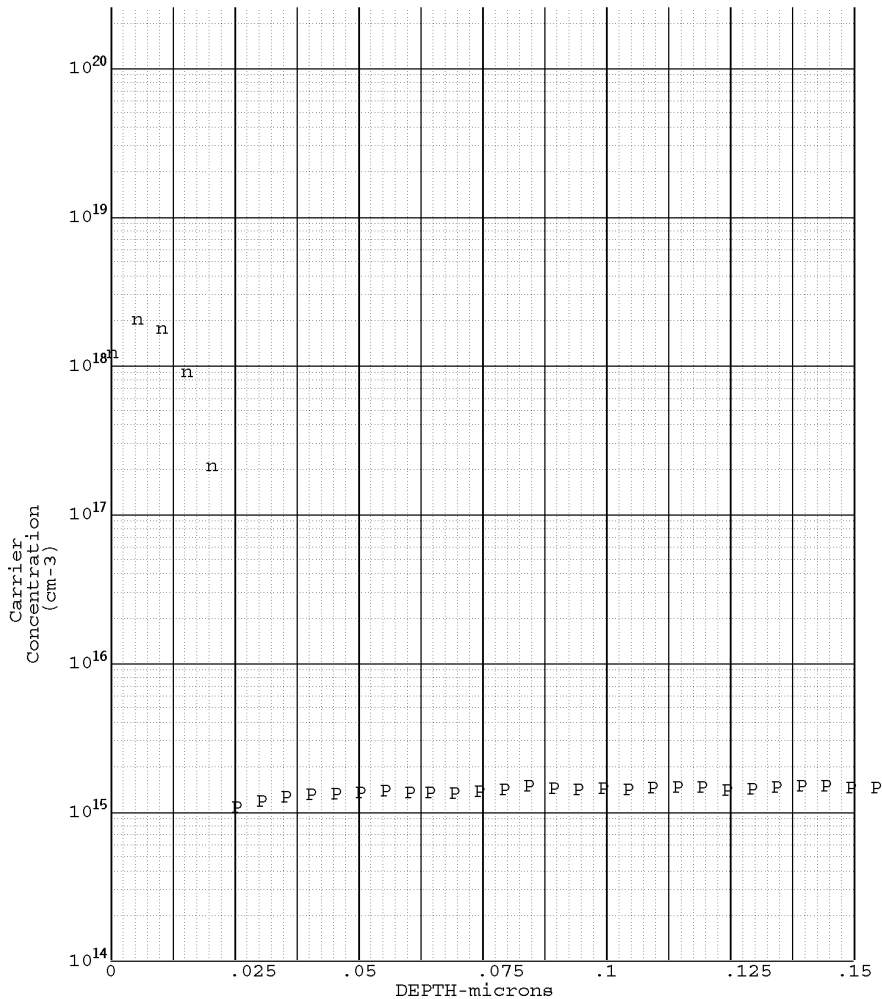


Date	07/20/09	Probe Load	2.5 grams	Orientation	<100> Si
File #	RNBUI400	Bevel Angle	.00299	Step Increm	2 um
Source	CALTECH			Sample #	#16 A
Job #	907029			1-N Dose=	6.6E+13 cm-2
Profile by	Mike			Sheet=	840 ohms/sq

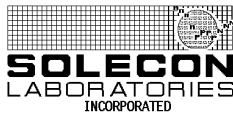


770 Trademark Drive Reno, NV 89521-5926 (775) 853-5900 www.solecon.com

Figure A.3. Junction profile, 10 min P diffusion, $T = 850^{\circ}\text{C}$



Date	07/20/09	Probe Load	2.5 grams	Orientation	<100> Si
File #	RNBU1412	Bevel Angle	.00248	Step Increment	2 um
Source	CALTECH			Sample #	#14 B
Job #	907029			1-N Dose=	3.1E+12 cm-2 Sheet= 8.4 Kohms/sq
Profile by	Mike				



770 Trademark Drive Reno, NV 89521-5926 (775) 853-5900 www.solecon.com

Figure A.4. Junction profile, 5 min P diffusion, T = 850 °C

A.3 Selected *Sentaurus* command files

The following command files provide a subset of those used to perform the studies on the effect of core depletion in radial p-n junction Si solar cells.

A.3.1 *Sentaurus Structure Editor* command file

This SDE command script produces a radial p-n junction structure for cylindrical device physics simulations using `mesh` with various refinement boxes. A mesh generated by this script is shown in Figure A.5

Listing A.1. SDE command file for two-dimensional cylindrical simulation of radial-junction solar cells. *Note: some lines have been broken for typesetting.*

```
#####
# Radial p-n junction solar cell structure for core depletion studies
# Sentaurus Structure Editor command file (abridged for inclusion in PhD thesis)
#
# Michael Kelzenberg, California Institute of Technology, 2010
#####
#
#Global settings (project variables):
# @R@ wire radius, microns
# @WireLength@ length of "above substrate" wire (note that the actual structure is 1 um longer)
#
#Local settings:
#
#define EmitterDoping 5e+18
# [cm^-3]
#define BaseDoping 1E+17
# [cm^-3]
#define tox 0.01
# [microns] (oxide shell used to set sidewall SRV value)
#define tEmitter 0.2
# [microns] (thickness of emitter) 05
#define EMinGrid 0.01
# [um] min. refinement mesh size in emitter region
#define EMaxGrid 0.1
# [um] max. refinement mesh size in emitter region
#define ERatio 1.5
# grid relaxation ratio for emitter region
#define BMinGrid 0.05
# [um] min. refinement mesh size in base region
#define BMaxGrid 0.2
# [um] max. refinement mesh size in base region
#define BRatio 1.2
# grid relaxation ratio for base region
#
#####
# Cross section of radial-junction wire device for cylindrical device physics simulations:
#
# =====# This diagram shows the name and location
# | E_UPPER ^# of the multibox refinements and contacts
# +-----+ v#
# | E_LOWER v# The symbols ^ and v indicate which corner
# | ^ ^ ^# of each multibox is meshed most densely
# | ^ ^ ! ^#
# | # E ! E # The upper left hand corner of the structure
# | # _ ! _ # is placed at (0,0)
# | B_UPPER # U ! U #
# | # L ! R #
# | # ! #
# +-----+
# | # ! #
# | # E ! E #
# | B_LOWER # _ ! _ # <- L-(2*tEmitter)
# | # L ! L # } top contact
# | # L ! R # <- L-tEmitter
# | v#v ! v#
# +-----+ <- L
# | S_D ^# DL#DR ^#
# +-----+
# | SUBS v#
# +-----+ <- L+lum
# ^bottom^contact^ (R/2)
#
#####
```

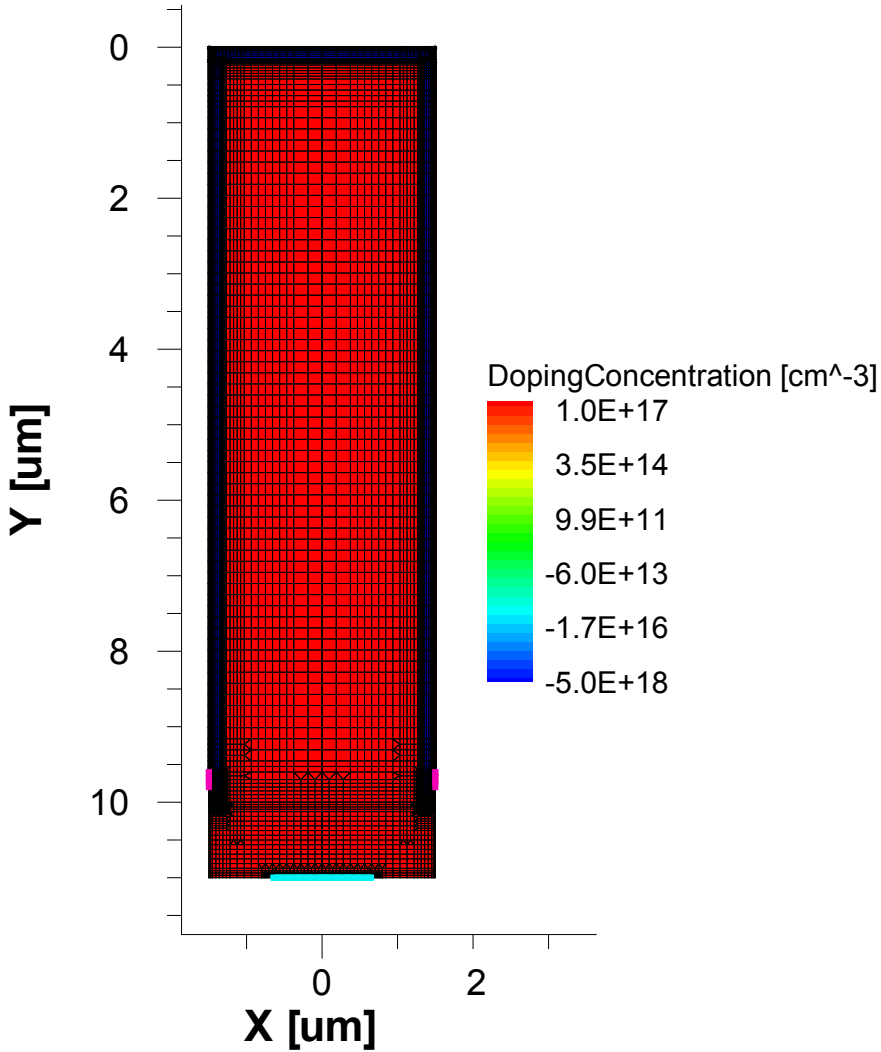


Figure A.5. Radial p-n junction structure for two-dimensional cylindrical simulations. The structure has been mirrored about $x=0$ to illustrate the entire wire cross section. The structure was generated with $R = 1.5 \mu\text{m}$ and $\text{WireLength} = 10 \mu\text{m}$.


```

#MATERIAL
(sdego:create-rectangle (position 0 0 0) (position @R@ (+ @WireLength@ 1.0) 0) "Silicon" "Emitter_region")
(sdego:create-rectangle (position 0 tEmitter 0) (position (- @R@ tEmitter) @WireLength@ 0) "Silicon" "Base_region")
(sdego:create-rectangle (position 0 @WireLength@ 0) (position @R@ (+ @WireLength@ 1.0) 0) "Silicon" "Subs_region")

#PROFILES
(sedr:define-constant-profile "ConstantProfileDefinition_forEmitter" "BoronActiveConcentration" EmitterDoping)
(sedr:define-constant-profile-region "ConstantProfilePlacement_forEmitter" "ConstantProfileDefinition_forEmitter" "Emitter_region")
(sedr:define-constant-profile "ConstantProfileDefinition_forBase" "PhosphorusActiveConcentration" BaseDoping)
(sedr:define-constant-profile-region "ConstantProfilePlacement_forBase" "ConstantProfileDefinition_forBase" "Base_region")
(sedr:define-constant-profile "ConstantProfileDefinition_forSubs" "PhosphorusActiveConcentration" BaseDoping)
(sedr:define-constant-profile-region "ConstantProfilePlacement_forSubs" "ConstantProfileDefinition_forSubs" "Subs_region")

#CONTACTS
(sdego:insert-vertex (position (+ (- @R@ tEmitter) 0.5) (+ @WireLength@ 1) 0))
(sdego:insert-vertex (position @R@ (- @WireLength@ tEmitter) 0))
(sdego:insert-vertex (position @R@ (- @WireLength@ (+ tEmitter 2) 0))

(sdego:define-contact-set "Top_contact" 4 (color:rgb 1 0 0) "##")
(sdego:define-contact-set "Bottom_contact" 4 (color:rgb 0 1 0) "###")

(sdego:set-current-contact-set "Top_contact")
(sdego:define-2d-contact (list (car (find-edge-id (position @R@ (- @WireLength@ (+ tEmitter 1.5) 0)))) "Top_contact")
(sdego:set-current-contact-set "Bottom_contact")
(sdego:define-2d-contact (list (car (find-edge-id (position (+ (- @R@ tEmitter) 0.25) (+ @WireLength@ 1.0) 0)))) "Bottom_contact")

#REFINEMENTS FOR CONTACTS
(sedr:define-refeval-window "RefEvalWin_forBaseContact" "Rectangle"
  (position 0 (- (+ @WireLength@ 1.0) (+ EMinGrid 2) 0)
    (position (+ (* @R@ 0.5) (+ EMinGrid 2) (+ @WireLength@ 1.0) 0) )
)
(sedr:define-refinement-size "RefSizeDefinition_forContact" EMinGrid EMinGrid EMinGrid EMinGrid )
(sedr:define-refinement-placement "RefinementPlacement_forBaseContact" "RefSizeDefinition_forContact" "RefEvalWin_forBaseContact" )

(sedr:define-refeval-window "RefEvalWin_forShellContact" "Rectangle"
  (position (- @R@ (+ EMinGrid 2) ) (- (- @WireLength@ (+ tEmitter 2.0) )
    (+ EMinGrid 2) 0)
    (position @R@ (+ (- @WireLength@ tEmitter) (+ EMinGrid 2) )
    0) )
)
(sedr:define-refinement-size "RefSizeDefinition_forShellContact" EMinGrid EMinGrid EMinGrid EMinGrid )
(sedr:define-refinement-placement "RefinementPlacement_forShellContact" "RefSizeDefinition_forShellContact" "RefEvalWin_forShellContact" )

#REFINEMENTS FOR MATERIAL
(sedr:define-refinement-size "RefinementDefinition_forSilicon" BMaxGrid BMaxGrid EMinGrid EMinGrid )
(sedr:define-refinement-material "RefinementPlacement_forSilicon" "RefinementDefinition_forSilicon" "Silicon" )
(sedr:define-refinement-function "RefinementDefinition_forSilicon" "DopingConcentration" "MaxTransDiff" 0.5)

#REMAINING REFINEMENTS

#POSITION
(sedr:define-refeval-window "RefEvalWin_E_Upper" "Rectangle" (position 0 0 0)
  (position @R@ (+ tEmitter 0.5) 0) )
(sedr:define-refeval-window "RefEvalWin_E_Lower" "Rectangle"
  (position 0 (+ tEmitter 0.5) 0) (position @R@ tEmitter 0) )
(sedr:define-refeval-window "RefEvalWin_B_Upper" "Rectangle"
  (position 0 tEmitter 0) (position (- @R@ tEmitter) (- (+ @WireLength@ 0.5) (+ tEmitter 0.5) 0) )
)
(sedr:define-refeval-window "RefEvalWin_B_Lower" "Rectangle" (position 0 @WireLength@ 0)
  (position (- @R@ tEmitter) (- (+ @WireLength@ 0.5) (+ tEmitter 0.5) 0) )
)
(sedr:define-refeval-window "RefEvalWin_E_UL" "Rectangle" (position (- @R@ tEmitter) tEmitter 0)
  (position (- @R@ (+ tEmitter 0.5) ) (- (+ @WireLength@ 0.5) (+ tEmitter 0.5) 0) )
)
(sedr:define-refeval-window "RefEvalWin_E_LL" "Rectangle" (position (- @R@ tEmitter) @WireLength@ 0)
  (position (- @R@ (+ tEmitter 0.5) ) (- (+ @WireLength@ 0.5) (+ tEmitter 0.5) 0) )
)
(sedr:define-refeval-window "RefEvalWin_E_UR" "Rectangle" (position @R@ tEmitter 0)
  (position (- @R@ (+ tEmitter 0.5) ) (- (+ @WireLength@ 0.5) (+ tEmitter 0.5) 0) )
)
(sedr:define-refeval-window "RefEvalWin_E_LR" "Rectangle" (position @R@ @WireLength@ 0)
  (position (- @R@ (+ tEmitter 0.5) ) (- (+ @WireLength@ 0.5) (+ tEmitter 0.5) 0) )
)
(sedr:define-refeval-window "RefEvalWin_E_LR" "Rectangle" (position @R@ @WireLength@ 0)
  (position (- @R@ (+ tEmitter 0.5) ) (- (+ @WireLength@ 0.5) (+ tEmitter 0.5) 0) )
)
(sedr:define-refeval-window "RefEvalWin_S_D" "Rectangle" (position 0 @WireLength@ 0)
  (position (- @R@ tEmitter) (+ @WireLength@ 0.5) 0) )
(sedr:define-refeval-window "RefEvalWin_S_DR" "Rectangle" (position @R@ @WireLength@ 0)
  (position (- @R@ (+ tEmitter 0.5) ) (+ @WireLength@ 0.5) 0) )
(sedr:define-refeval-window "RefEvalWin_S_DL" "Rectangle" (position (- @R@ tEmitter) @WireLength@ 0)
  (position (- @R@ (+ tEmitter 0.5) ) (+ @WireLength@ 0.5) 0) )
(sedr:define-refeval-window "RefEvalWin_SUBS" "Rectangle" (position 0 (+ @WireLength@ 0.5) 0)
  (position @R@ (+ @WireLength@ 1.0) 0) )

#REFINEMENT PITCH
(sedr:define-multibox-size "MultiboxDefinition_E_Upper" BMaxGrid EMaxGrid EMinGrid EMinGrid -ERatio ERatio )
(sedr:define-multibox-size "MultiboxDefinition_E_Lower" BMaxGrid EMaxGrid EMinGrid EMinGrid -ERatio -ERatio )
(sedr:define-multibox-size "MultiboxDefinition_B_Upper" BMaxGrid BMaxGrid BMinGrid BMinGrid -BRatio BRatio )
(sedr:define-multibox-size "MultiboxDefinition_B_Lower" BMaxGrid BMaxGrid BMinGrid BMinGrid -BRatio -BRatio )
(sedr:define-multibox-size "MultiboxDefinition_E_UL" EMaxGrid BMaxGrid EMinGrid BMinGrid ERatio BRatio )
(sedr:define-multibox-size "MultiboxDefinition_E_UR" EMaxGrid BMaxGrid EMinGrid BMinGrid -ERatio BRatio )
(sedr:define-multibox-size "MultiboxDefinition_E_LL" EMaxGrid BMaxGrid EMinGrid EMinGrid ERatio -BRatio )
(sedr:define-multibox-size "MultiboxDefinition_E_LR" EMaxGrid BMaxGrid EMinGrid EMinGrid -ERatio -BRatio )
(sedr:define-multibox-size "MultiboxDefinition_S_D" BMaxGrid BMaxGrid BMinGrid BMinGrid -BRatio BRatio )

```

```

(scdcr:define-multibox-size "MultiboxDefinition_S_DR" BMaxGrid BMaxGrid BMinGrid EMinGrid -BRatio BRatio )
(scdcr:define-multibox-size "MultiboxDefinition_S_DL" BMaxGrid BMaxGrid BMinGrid EMinGrid BRatio BRatio )
(scdcr:define-multibox-size "MultiboxDefinition_SUBS" BMaxGrid BMaxGrid BMinGrid BMinGrid -BRatio -BRatio )
#PLACEMENTS
(scdcr:define-multibox-placement "MultiboxPlacement_E_Upper" "MultiboxDefinition_E_Upper" "RefEvalWin_E_Upper" )
(scdcr:define-multibox-placement "MultiboxPlacement_E_Lower" "MultiboxDefinition_E_Lower" "RefEvalWin_E_Lower" )
(scdcr:define-multibox-placement "MultiboxPlacement_B_Upper" "MultiboxDefinition_B_Upper" "RefEvalWin_B_Upper" )
(scdcr:define-multibox-placement "MultiboxPlacement_B_Lower" "MultiboxDefinition_B_Lower" "RefEvalWin_B_Lower" )
(scdcr:define-multibox-placement "MultiboxPlacement_E_UR" "MultiboxDefinition_E_UR" "RefEvalWin_E_UR" )
(scdcr:define-multibox-placement "MultiboxPlacement_E_UL" "MultiboxDefinition_E_UL" "RefEvalWin_E_UL" )
(scdcr:define-multibox-placement "MultiboxPlacement_E_LR" "MultiboxDefinition_E_LR" "RefEvalWin_E_LR" )
(scdcr:define-multibox-placement "MultiboxPlacement_E_LL" "MultiboxDefinition_E_LL" "RefEvalWin_E_LL" )
(scdcr:define-multibox-placement "MultiboxPlacement_S_D" "MultiboxDefinition_S_D" "RefEvalWin_S_D" )
(scdcr:define-multibox-placement "MultiboxPlacement_S_DR" "MultiboxDefinition_S_DR" "RefEvalWin_S_DR" )
(scdcr:define-multibox-placement "MultiboxPlacement_S_DL" "MultiboxDefinition_S_DL" "RefEvalWin_S_DL" )
(scdcr:define-multibox-placement "MultiboxPlacement_SUBS" "MultiboxDefinition_SUBS" "RefEvalWin_SUBS" )

# OXIDE SIDEWALL
(sdgeo:create-rectangle (position @R@ 0 0) (position (+ @R@ tox) (- @WireLength@ (* tEmitter 2.0) 0) "Oxide"
"OxideShell_region" )
(scdcr:define-refeval-window "RefEvalWin_Oxide" "Rectangle" (position @R@ 0 0)
(position (+ @R@ tox) (- @WireLength@ 1.0) 0) )
(scdcr:define-multibox-size "MultiboxDefinition_forOxide" BMaxGrid BMaxGrid EMinGrid ERatio 0 )
(scdcr:define-multibox-placement "MultiboxPlacement_forOxide" "MultiboxDefinition_forOxide" "RefEvalWin_Oxide" )

# OXIDE OXIDE TOP
(sdgeo:create-rectangle (position 0 0 0) (position (+ @R@ tox) -tox 0) "Oxide" "OxideShell_region" )
(scdcr:define-refeval-window "RefEvalWin_TopOxide" "Rectangle" (position 0 0 0) (position (+ @R@ tox) -tox 0) )
(scdcr:define-multibox-size "MultiboxDefinition_forTopOxide" BMaxGrid BMaxGrid EMinGrid ERatio 0 )
(scdcr:define-multibox-placement "MultiboxPlacement_forTopOxide" "MultiboxDefinition_forTopOxide"
"RefEvalWin_TopOxide" )

# DONE. GENERATE MESH.
(sde:save-model "n@node@")
(sde:build-mesh "mesh" "-s -F tdr " "n@node@")

```

A.3.2 *Sentaurus Device* command file

This `sdevice` command file performs light J - V simulations as well as other types of simulations that have been developed but were not discussed in this thesis. For example, the full electrostatics of Au impurities were modeled based on the Au trap parameters provided by Fairfield and Gokhale. [173] These considerations are particularly important when simulating devices in which the Au concentration approaches or exceeds the doping concentration. The code also demonstrates several useful capabilities of Sentaurus Workbench and Sentaurus Device, such as inline calculation of the device normalization area, and automatic termination criteria to stop photovoltaic simulations when the device reaches V_{oc} . Note that some simulation parameters (e.g., surface recombination velocities) are specified in the parameter file (not shown).

Light J - V is simulated using `OptBeam` generation with several illumination beams that approximate the AM 1.5G spectrum. A set of five such illumination beams is included below as listing A.3; tables and scripts for producing other discretizations of solar spectra are provided in section B.11. The `Area` value is calculated so that the simulation output (in the current plot file) is reported in units of current density ($\text{A}\cdot\text{cm}^{-2}$), as normalized to the top (circular) surface of the cylindrical device.

Dark J - V is simulated much like light J - V , but without optical generation or break criteria during the voltage the sweep.

Spectral response is simulated using `OptBeam` generation with a single beam whose wavelength is varied during the sweep. Illumination intensity and

normalization area are calculated so that the simulation output is reported in units of external quantum efficiency (E.Q.E.).

Scanning photocurrent microscopy (SPCM) profiles are simulated using monochromatic `OptBeam` generation with a spatially varying plane of beam incidence. As the incidence plane is swept along the axis of the wire, exponentially decaying absorption profiles are produced both above and below the plane. The back-to-back exponential profiles approximate the Gaussian illumination beam encountered in SPCM measurements, the “width” of which is determined by the absorption coefficient. The illumination intensity and normalization area are calculated so that the simulation output is reported in units of E.Q.E.

Listing A.2. `sdevice` command file for simulating dark and light J - V behavior as well as spectral response and SPCM profiles.

```
#####
# Radial p-n junction solar cell structure for core depletion studies
# Sentaurus Device command file (abridged for inclusion in PhD thesis)
#
# Michael Kelzenberg, California Institute of Technology, 2010
#####

# EXPTYPE determines the type of measurement to be simulated:
# 0 - dark I/V 0 to 2 V
# 1 - AM1.5G light J-V from "spectrum" file
# 2 - spectral response
# 3 - SPCM-like experiment
#
#set EXPTYPE 0

# Electrostatic modeling of Au traps - specify concentration [cm^-3]
#set AuConc 0

# Contact surface recombination velocities [cm s^-1]
#set STopContact 1000
#set SBottomContact 1000

# Sidewall surface recombination velocity
#set SRV 1350
# NOTE: Sidewall SRV value is set in the parameter file. Changing the value here will
# have no effect unless "SRV" is also referenced in the parameter file. My parameter
# file is not included in this listing.

*****
* FILE
*****
File
{
  Grid           = "n@node|-1@msh.tdr"
  Parameters     = "@parameter@"
  plot           = "@tdrdat@"
  current        = "@plot@"
}

*****
* ELECTRODES
*****
Electrode
{
  { name="Bottom_contact" voltage=0.0 hRecVelocity=@SBottomContact}
  { name="Top_contact"    voltage=0.0 eRecVelocity=@STopContact}
}

*****
```

```

* PLOT
*****
Plot
{
  eCurrent/Vector    hCurrent/Vector      current/Vector      CurrentPotential
  SpaceCharge        eDensity             hDensity            DopingConcentration
  Potential          ConductionBandEnergy ValenceBandEnergy   ElectricField/Vector
  SRH                Auger                               TotalRecombination
  BeamGeneration    OptBeam
}

#if @AuConc@ != 0
  eTrappedCharge hTrappedCharge
  eGapStatesRecombination hGapStatesRecombination
#endif

#if @SRV@ != 0
  SurfaceRecombination
#endif
}

#if @EXPTYPE@ == 2
CurrentPlot
{
  * Record wavelength for x-axis of spectral response plots
  Region="NW_region" Model="OptBeam(0)" Parameter="WaveLength"
}
#endif

#if @EXPTYPE@ == 3
CurrentPlot
{
  * Record illumination position for x-axis of SPCM plot
  Model="OptBeam(0)" Parameter="SemSurf"
}
#endif

*****
* PHYSICS
*****
Physics
{
  Mobility(DopingDep)

#if @SRHLifeTime@ != 0
  Recombination( SRH Auger )
#else
  Recombination( Auger )
#endif

#if @AuConc@ != 0
  * GOLD TRAPS
  * Parameters based on Bullis, W. M. Solid-State Electron. 1966, 9, 143-168.
  * Using 300K data for capture cross sections from FAIRFIELD and GOCKHALE
  Traps
  (
    * Trap 1 - acceptor trap located 0.54 eV from conduction band
    (
      Acceptor Level Add2TotalDoping
      Conc = @AuConc@ * [cm^-3]
      EnergyMid = 0.54 fromCondBand * [eV]
      eGfactor = 2
      eXsection = 1.7e-16 * [cm^2]
      hXsection = 1.1e-14 * [cm^2]
    )
    * Trap 2 - donor trap located 0.35 eV from valence band
    (
      Donor Level Add2TotalDoping
      Conc = @AuConc@ * [cm^-3]
      EnergyMid = 0.35 fromValBand * [eV]
      eGfactor = 0.5
      eXsection = 6.3e-15 * [cm^2]
      hXsection = 2.4e-15 * [cm^2]
    )
  )
}

```

```

    )
  )
#endif

#if @EXPTYPE@ == 1
  * Light I-V
  * Load command file containing 5-point AML5G approximation:
#include "../spectra/Si_Regular_Solar_5.cmd.sub"
#endif

#if @EXPTYPE@ == 2
  *Spectral response (using optical beam illumination)
  *Here we use an area 1000 times larger than reality, so that the 1mA/cm2
  *input light beam would fall at 1.0 [A/cm2] on the output graph.

Area!=( puts [format %.4e [expr 1000/(@R@*@R@*1E-8*3.1415) ] ] )!
OptBeam(
  ( WaveLength = 2.00e-05 * [cm]
    WaveInt = 6.24151e+15 * [photons*cm^-2*sec^-1] (this corresponds to 1mA/cm2)
    SemAbs (material="Silicon")
    Semsurf = 0.0
    SemWindow = (0,!( puts -nonewline [format %.8e [expr (@R@*1E-4) ] ] )! )
  )
)
#elif @EXPTYPE@ == 3
  *Pseudo-SPCM response illumination optical beam
  *Here we use an area 500 times larger than reality, so that the 1mA/cm2
  *input light beam would fall at 1.0 [A/cm2] on the output graph (beam is doubled
  *because of up- and downwards propagation.

Area!=( puts [format %.4e [expr 500/(@R@*@R@*1E-8*3.1415) ] ] )!
OptBeam(
  ( WaveInt = 6.24151e+15 * [photons*cm^-2*sec^-1] (this corresponds to 1mA/cm2)
    SemAbs (value=1e+06)
    SemSurf = 0.0
    SemWindow = (0,!( puts -nonewline [format %.8e [expr (@R@*1E-4) ] ] )! )
  )
)
#else
  *This is the area of the wire (circle)
  *using this for the contact 'area' in sentaurus causes the electrode
  *currents to be reported in terms of the current density (A/cm2)
Area!=( puts [format %.4e [expr 1/(@R@*@R@*1E-8*3.1415) ] ] )!
#endif
}

#if @SRV@ != 0
* SURFACE RECOMBINATION
Physics (MaterialInterface="Oxide/Silicon")
{
  Recombination( surfaceSRH )
}
#endif

*****
* MATH
*****
Math
{
  Number_of_Threads=2
  RelErrControl
  Digits=18
  RhsMin=1E-15
  ExtendedPrecision
  ExitOnFailure
  Method=Pardiso * This seems to give best multi-processor performance
  Cylindrical (0.0)
}

#if @EXPTYPE@ == 1 || @EXPTYPE@ == 2 || @EXPTYPE@ == 3
  * This performs better absorption calculations in areas of grid variation
  * Note: OptBeam calculations with RecBoxInteger are very slow. Synopsys seems
  * to recommend other generation methods (i.e., raytrace, transfer matrix...)

```

```

RecBoxInteger (5e-2 3 30)
#endif

#if @EXPTYPE@ == 1
* This terminates the simulation once the current becomes negative
* ( i.e. after VOC is reached )
* Note this would have to be changed for p-n vs n-p junctions....
BreakCriteria
{ Current (Contact = "Bottom_contact" minval = -1E-20) }
#endif

#if @AuConc@ != 0
Traps(Damping=2) * This helps things converge
#endif
}

*****
* SOLVE
*****
Solve
{
*--First solve the V=0 case (short cicuit condition)
Coupled { poisson }
Coupled { poisson electron hole }

#if @EXPTYPE@ == 0

*--DARK I-V:
Plot( FilePrefix = "n@node@_EQ_" )
NewCurrentPrefix="DarkIV_"
Quasistationary( InitialStep=0.02 MinStep=1E-4 MaxStep=0.02 Increment=1.4 Goal
{ Name=Top_contact Voltage=2.0 })
{ Coupled { poisson electron hole } }

#elif @EXPTYPE@ == 1

*-- Light I-V
Plot( FilePrefix = "n@node@_ISC_" )
NewCurrentPrefix="SolarIV_"

Quasistationary( InitialStep=0.01 MinStep=1E-4 MaxStep=0.01 Increment=2
Goal { Name=Top_contact Voltage=1.0 })
{
Coupled ( Digits=10 ) { poisson electron hole }
}
Plot( FilePrefix = "n@node@_nearVOC_" )

#elif @EXPTYPE@ == 2

*-- Spec. Response
NewCurrentPrefix="SpecResp_"
Quasistationary( InitialStep=0.02 MinStep=1E-4 MaxStep=0.02
Goal { Model="OptBeam(0)" Parameter="WaveLength" Value=1.2e-4 })
{
Coupled ( Digits=10 ) { poisson electron hole }
Plot ( FilePrefix="n@node@_Illum500nm_" Time=(0.3) )
}

#elif @EXPTYPE@ == 3

*-- Pseudo-SPCM
NewCurrentPrefix="SPCM_"
Quasistationary( InitialStep=0.02 MinStep=1E-4 MaxStep=0.02
Goal { Model="OptBeam(0)" Parameter="SemSurf"
Value=! ( puts -nonewline [format %.4e [expr @WireLength@*1e-04 ] ] ) ! )
{
Coupled ( Digits=18 ) { poisson electron hole }
Plot ( FilePrefix="n@node@_middleSPCM_" Time=(0.5) )
}
#endif
}

```

Listing A.3. sdevice include file for five-point AM 1.5G illumination approximation with OptBeam generation.

```
* AM1.5G 5-Point Spectral Approximation
* Calculated by Michael Kelzenberg / Matlab Script

OptBeam
(
  * Point 1
  ( WaveLength = 4.517463e-005 * [cm]
    WavePower = 2.429340e-002 * [W/cm^2]
    SemAbs (material="Silicon")
    Semsurf = 0.0
    SemWindow = (0,!( puts -nonewline [format %.8e [expr (@R@*1E-4)] ] )! )
  )
  * Point 2
  ( WaveLength = 5.988427e-005 * [cm]
    WavePower = 1.828469e-002 * [W/cm^2]
    SemAbs (material="Silicon")
    Semsurf = 0.0
    SemWindow = (0,!( puts -nonewline [format %.8e [expr (@R@*1E-4)] ] )! )
  )
  * Point 3
  ( WaveLength = 7.227098e-005 * [cm]
    WavePower = 1.518556e-002 * [W/cm^2]
    SemAbs (material="Silicon")
    Semsurf = 0.0
    SemWindow = (0,!( puts -nonewline [format %.8e [expr (@R@*1E-4)] ] )! )
  )
  * Point 4
  ( WaveLength = 8.554730e-005 * [cm]
    WavePower = 1.281337e-002 * [W/cm^2]
    SemAbs (material="Silicon")
    Semsurf = 0.0
    SemWindow = (0,!( puts -nonewline [format %.8e [expr (@R@*1E-4)] ] )! )
  )
  * Point 5
  ( WaveLength = 1.027769e-004 * [cm]
    WavePower = 1.059251e-002 * [W/cm^2]
    SemAbs (material="Silicon")
    Semsurf = 0.0
    SemWindow = (0,!( puts -nonewline [format %.8e [expr (@R@*1E-4)] ] )! )
  )
)
#set incidentCurrent 4.415081e-002
#set incidentPower 8.116953e-002
```

A.3.3 *Inspect* command file

This `inspect` command file loads and plots the terminal behavior of the simulated device, extracts the simulated photovoltaic performance (V_{oc} , J_{sc} , FF , and η), and exports these values to the SWB workspace.

Listing A.4. `inspect` command script.

```
#####
# Radial p-n junction solar cell structure for core depletion studies
# Inspect script for extracting light I-V performance
#
# Michael Kelzenberg, California Institute of Technology, 2010
#####
cv_setCurveAttr LogI_n@previous@ LogI0_n@previous@ #00ff00 solid 3 none 5 black 1 black

proj_load ./SolarIV_n@previous@_des.plt CELL_n@previous@
cv_createDS CURRENT_n@previous@ {CELL_n@previous@ Top_contact InnerVoltage}
                                     {CELL_n@previous@ Bottom_contact TotalCurrent} y
cv_createDS VOLTAGE_n@previous@ {CELL_n@previous@ Top_contact InnerVoltage}
                                     {CELL_n@previous@ Top_contact InnerVoltage} y2
cv_createWithFormula POWER_n@previous@ "<CURRENT_n@previous@>*<VOLTAGE_n@previous@>" A A
cv_display POWER_n@previous@ y

cv_setCurveAttr
      CURRENT_n@previous@ CURRENT_n@previous@ #ff0000 solid 3 none 5 black 1 black
cv_setCurveAttr POWER_n@previous@ POWER_n@previous@ #00ff00 solid 3 none 5 black 1 black

set PMAX [cv_compute "vecmax(<POWER_n@previous@>)" A A A A]
set VOC [cv_getZero "CURRENT_n@previous@" 0 1 -1 1]

set XY [cv_getVals "CURRENT_n@previous@" ]
set X [lindex $XY 0]
set Y [lindex $XY 1]

set ISC [lindex $Y 0]

set PIDEAL [expr $ISC*$VOC]

set FF [expr abs($PMAX/$PIDEAL)]

set IQE [expr $ISC/.0690312]
set EFF [expr $PMAX/0.100865]

puts -nonewline "DOE: EFF "
puts [format %.3f [expr 100*$EFF] ]

puts -nonewline "DOE: ISC "
puts [format %.2f [expr 1000*$ISC] ]

puts -nonewline "DOE: VOC "
puts [format %.3f $VOC]

puts -nonewline "DOE: FF "
puts [format %.1f [expr 100*$FF] ]

gr_mappedAxis Y 1
gr_setAxisAttr Y {} {helvetica -12} 0.0 {} black 1 {helvetica -12} 0 5 0 black
```


Method of integrating *Lumerical FDTD* within *Sentaurus TCAD*

Sentaurus Device, part of the Synopsys *Sentaurus TCAD* software suite, is a robust semiconductor device physics simulation tool that is well-suited for simulating the performance of three-dimensional solar cell geometries such as Si microwire photovoltaics. It includes models for most of the device physics phenomena relevant to photovoltaics, which combined with its use of modern numerical methods, make it one of the most capable device-physics-based solar cell simulators available today. It can simulate arbitrary semiconductor geometries in two or three dimensions using a finite-element mesh (grid). This permits simulation of novel, nonplanar solar cell geometries, but can introduce several challenges in defining the device structure for simulations. In particular, for a typical Si solar cell, the following spatially varying quantities must be specified throughout the simulation volume:

- Optical generation rate
- Impurity concentration (e.g., dopants or traps)
- Carrier lifetime

These profiles can be easily specified or calculated for one-dimensional structures (e.g., Gaussian emitter doping profiles or exponential Beer's-law optical absorption profiles), but can become more complicated for arbitrary three-dimensional structures. For these reasons, the TCAD software includes numerous capabilities to specify analytical profiles, to simulate processing steps (e.g., diffusion doping), and to calculate optical absorption (e.g., ray-tracing, FDTD) in 3D structures. However, in certain situations we have found it useful to manually specify these profiles, based on external calculations, assumptions, or simulations. This appendix presents a method that has been developed to map arbitrary external profiles onto the numerical mesh used for *Sentaurus Device* simulations.

B.1 Introduction

In this thesis work, techniques were developed to import optical generation profiles calculated by FDTD simulations (*Lumerical FDTD Solutions*)* into device physics simulations (*Sentaurus Device*). This enabled comprehensive optoelectronic modeling of Si microwire-array solar cells, as presented in Chapter 2.

*Our choice of Lumerical FDTD software over the *Sentaurus* (internal) FDTD methods simply because of the expertise base for the former within our group.

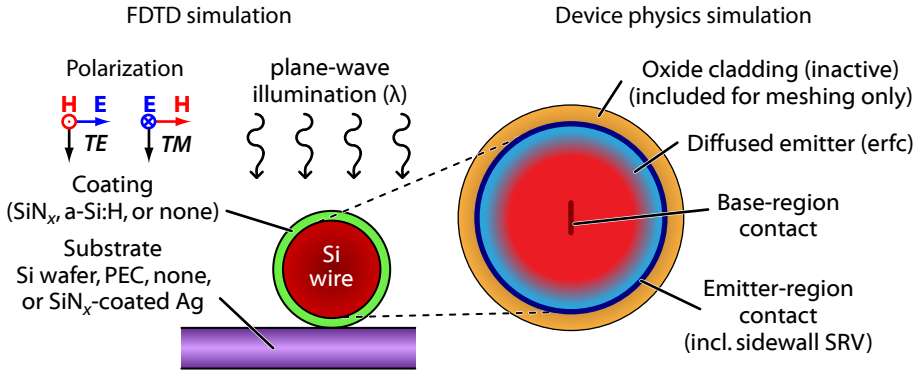


Figure B.1. Schematic diagram of simulation geometries for modeling optical (left) and electrical (right) behavior of horizontally oriented single-microwire Si solar cells.

This process was implemented within the *Sentaurus Workbench* (SWB) environment, extending its tool database to include the Lumerical CAD/FDTD programs as well as *MATLAB* scripts. *MATLAB* provides a convenient programming environment well-suited to the task of processing and storing the photo-generation profiles for device-physics simulations. Integrating these programs within SWB enabled us to automate the entire simulation process (structure generation, FDTD simulations, device physics simulations, and variable extraction), making use of the software’s preprocessor to generalize the configuration of each simulation step. This allowed us to employ SWB’s automated design features (such as parametric sweeps and numerical optimization), and also to take advantage of its project interface for generating, executing, and keeping track of a large number of simulations and parameters. For example, the FDTD simulations presented in section 5.4.1 were implemented as a project within SWB, and can be run from start to finish with virtually no user interaction.

In this appendix, we describe the major steps of this simulation approach, and show how it has been integrated into the SWB environment. Source code is included for each key step, including a *MATLAB* script that generates mesh files containing arbitrary input profiles for Sentaurus simulations. To illustrate the use of these techniques, we describe a project that simulates the spectral response and solar $J-V$ behavior of a single-wire solar cell structure like those fabricated in Chapter 5. The general structure of the simulated device is shown in Figure B.1. Both the optical (FDTD) and electrical (device physics) simulations are performed in two-dimensional coordinates. The particular details of the FDTD and device physics simulations are not discussed here; they closely follow those presented elsewhere in this thesis. Our discussion focuses instead on the procedures and tools required to import the optical generation profiles into Sentaurus Device utilizing the automation features of the SWB platform.

B.1.1 Requirements

This work made use of the following software under an x86_64 Linux environment:

- TCAD Sentaurus C-2009.06-SP2
- MATLAB R2009b
- Lumerical FDTD/CAD v6.5.5

The computational requirements vary depending on the size and complexity of the simulated structure. The two-dimensional structures discussed in this appendix can be easily simulated on modern personal computers having a few GB of RAM. The larger three-dimensional structures (i.e., the Si microwire-array solar cells presented in Chapter 2) were simulated on individual workstations in our lab, the most powerful of which were SunFire x2270 servers (Sun Microsystems) having 48 GB RAM (1300 MHz DDR3) and dual 64-bit processors (Intel Xeon 5500-series, 3 GHz).

Use of these techniques requires a moderate understanding of the TCAD software suite, including Sentaurus Device, the mesh generation tools, and the SWB preprocessor and project environment. These instructions also assume familiarity with Linux environments, MATLAB, and the Lumerical FDTD software.

B.2 Understanding the mesh files

Sentaurus operates on a finite element mesh, which consists of vertices, edges, and elements that store the discretized state of a device during simulations (e.g., doping, carrier concentration, or electric field). Information describing the layout of the mesh is known as the *grid*, which defines the physical position (coordinates) of each mesh element. Information describing the physical state of the device is known as the *data*, which provides the numerical value of each simulated quantity at each mesh element. Combined, the grid and data specify the device structure for Sentaurus simulation.

There are two file formats for storing grid and data information. The first and default type is “TDR”—a binary file format which combines both the grid and data information into a single `.tdr` file. This results in a smaller file size and eliminates any confusion about which grid belongs with which data. However it has proven difficult to read or write to these binary files without knowledge of their format. Our scripts do not presently support `.tdr` files. The other file format, “DF-ISE”, is a text-based format which can be deciphered and written by relatively simple parsing scripts. A DF-ISE mesh consists of a grid (`.grd`) file and one or more data (`.dat`) files. For typical simulations, there is a single `.dat` file corresponding the `.grd` file, which contains data values for all simulation input profiles. However, the simulation input profiles can be divided amongst

multiple `.dat` files, each of which corresponds to the same `.grd` file but contains different physical quantities. For example, in the project highlighted herein, a Sentaurus mesh generation program generates the original `.grd` file as well as the `.dat` file describing the device doping profiles, while our MATLAB script generates a separate `.dat` file describing the optical generation profile. DF-ISE and TDR files can be merged, separated, and converted using the *Sentaurus Data Explorer* (TDX) program as described in the TCAD users manuals.

When using DF-ISE files, Sentaurus Device requires a grid file and a data file to specify the device structure (i.e., dimensions and doping profiles). Optionally, additional data files can be used to specify optical generation, SRH lifetime, or possibly other physical quantities (see the *File* section of the Sentaurus Device manual). Each `.dat` file must correspond to the same `.grd` file. During the simulation, Sentaurus will also save one or more new `.dat` files (depending on the command file settings), specifying the state of the mesh quantities (e.g., electric field) within the evolving simulation. A corresponding `.grd` file does not need to be saved (except, possibly, if mesh is modified by adaptive meshing which I have not explored).

Simulation meshes can be viewed using the program *Tecplot SV*. Tecplot can directly load and display TDR files since they contain both the grid and data components of the mesh. To view DF-ISE files in Tecplot, however, both a `.grd` and one (or more) `.dat` files must be specified. To simplify this, the primary `.dat` file is typically always given the same base filename as the `.grd` file. For a combined Lumerical/Sentaurus simulation, the typical set of mesh files for each experiment will include:

<code>n1_pof.grd</code>	the grid generated by the mesh generation tool
<code>n1_pof.dat</code>	the corresponding device data profiles (doping, etc.)
<code>n2_optgen.dat</code>	a data file generated by our MATLAB script (specifying the optical generation profile)
<code>n3_des.dat</code>	a data file automatically produced after the final iteration of Sentaurus Device, containing all physical quantities requested within the <i>Plot</i> section of the command file
<code>n3_ISC_des.dat</code>	a data file recorded at 0 V bias, produced by a instruction within the <i>Solve</i> section of the command file
<code>n3_nearVOC_des.dat</code>	a data file recorded when the simulated device current crosses 0 A (i.e., near V_{oc}), also produced by an instruction within the <i>Solve</i> section of the command file

In the above file names, the numbers 1, 2, and 3 would correspond to the node numbers (in SWB) of the mesh generation step, our MATLAB script step, and the Sentaurus Device simulation step, respectively. To visualize these mesh

files—for example, that of the MATLAB step, the following command can be used to invoke Tecplot SV at the shell prompt:*

```
tecplot_sv nA_pof.grd nB_optgen.dat &
```

B.2.1 Generating custom data files

The grid file contains all the information one needs to generate a new data file containing a user-specified (external) profile. The grid file maps each mesh element to a physical point in space (x,y) , and it is usually straightforward to calculate the value of the external profile $P(x,y)$ for each mesh element. For our earlier work (PVSC 2009), I wrote a program that parsed each `.grd` file, constructing a map of the mesh in memory; then calculated the profile values for each mesh element and generated a properly formatted `.dat` file from scratch.

More recently, however, I have found an easier approach in which we instruct the Sentaurus mesh generation program to store the spatial coordinates of each mesh element within the initial `.dat` file (which normally only contains the doping data). This saves us the trouble of parsing the `.grd` file and building the mesh in memory. Reading the `.dat` file provides both the spatial coordinates (x,y) of each mesh element, as well as the correct order in which to write the desired profile values $P(x,y)$ in the new `.dat` file. This conceptually simpler approach is presented here.

B.3 Step 1: Generating the mesh

Structure generation for Sentaurus TCAD tools is typically accomplished using *Sentaurus Structure Editor* (also referred to as SDE). This provides a scriptable, graphical environment for specifying material shapes, doping, meshing parameters, etc. However, the mesh itself is not generated by SDE, rather, it is produced by a command-line meshing program that is invoked by SDE. When the mesh is requested, SDE converts its model into a command file for the meshing program, runs the program, and then displays the resulting mesh in its GUI. Although this generally simplifies the process of mesh generation, it is important to understand the behavior of the underlying mesh program and the format of the mesh command file prepared by SDE. Most importantly, to instruct the mesh program to store the x - and y - coordinates of each mesh element within the data file, the following commands must be appended to the mesh command file:

```
Definitions {
  AnalyticalProfile "XPosition" {
    Species = "PMIUserField0"
    Function = General(init="", function = "x", value = 10)
  }
  AnalyticalProfile "YPosition" {
```

*The `-mesa` rendering option is also required for compatibility with some remote X11 clients, such as *Cygwin-X* or *Xming*, which we often use for remote access from Windows-based machines.

```

    Species = "PMIUserField1"
    Function = General(init="", function = "y", value = 10)
  }
}
Placements {
  AnalyticalProfile "XPosition" {
    Reference = "XPosition"
    EvaluateWindow {
      Element = material ["Silicon"]
    }
  }
  AnalyticalProfile "YPosition" {
    Reference = "YPosition"
    EvaluateWindow {
      Element = material ["Silicon"]
    }
  }
}
}

```

These commands instruct the mesh program to store the value of the functions x and y as `PMIUserField0` and `PMIUserField1` in the mesh data file. The species names “`PMUserField N` ” must be used (rather than “`XPosition`” or “`ArbitraryName`”) because they are valid *DATEX* fields. (See Sentaurus user’s manuals for a list of valid *DATEX* fields.) Note that the above syntax could also be used to specify arbitrary analytical profiles, such as doping (`Species = "BoronActiveConcentration"`) or even optical absorption (`Species = "OpticalGeneration"`).

To issue the above commands to the meshing program, they must be saved as a text file within the project directory (for example, `mk_store_xy.cmd`) and then appended to the meshing command file prepared by SDE, using the following command syntax:

```
(sdr:append-cmd-file "mk_store_xy.cmd")
```

This command should immediately precede the command to invoke the meshing program, (`sde:build-mesh`), within the SDE command file.

B.3.1 Meshing strategy

Obtaining an optimal mesh is generally the most time-consuming step for a new Sentaurus project. TCAD Sentaurus includes three different mesh generators: *mesh*, *snmesh*, and *noffset3d*. Each offers its own benefits and drawbacks, and users should consult the manuals to understand and select the appropriate mesh tool for the desired structure. My basic understanding of the mesh options, based on my limited experience with 2D simulations, is as follows:

Mesh: Produces axis-aligned (rectangular) meshes with minimal triangulation.

As the most basic meshing program, it offers fewer options for “intuitive” grid refinement, and usually requires a great deal of manual refinement instructions (i.e., multiboxes) to produce a suitable grid. Most of the simulations presented in this thesis were meshed using *mesh* with numerous multiboxes placed over the entire device extent. *Mesh* also supports offset mesh generation using the `-noffset` option, which I have not explored.

SNMesh: A more advanced axis-aligned mesher, `smesh` offers more convenient refinement options (e.g., specifying finer meshing at surfaces or region boundaries), and tends to produce more smoothly varying grids with greater overall connectivity. **However, `smesh` cannot produce DF-ISE meshes**, and is thus not directly compatible with our profile conversion scripts at this point. It may be possible to convert its `.tdr` meshes to DF-ISE format, but this has not been investigated.

Offset3D: Produces meshes by “offsetting” material surfaces and boundaries based on specified grid densities and offset distances (i.e., an “onion peel” approach). After offsetting boundaries, it fills the remaining areas/volumes with triangular or tetrahedral meshes. It can produce very efficient grids for non-axis-aligned or 3D structures, but in my experience with the single-wire radial-junction structure shown in Figure B.1, has suffered from perplexing and erratic behavior that has requires fine-tuning of its input parameters as well as careful scrutiny of each grid it produces. I suspect that this is due to the presence of a closed circular boundary in the structure, which seems to causes gaps or overlaps in the grid of the concentric offset layers. I have nonetheless been able to produce a variety of efficient simulation grids for modeling these devices, and the method has worked reliably for other structures.

Figure B.2 is a screenshot illustrating the meshes produced by each of the three mesh generation programs (for the same radial p-n junction geometry). The oxide region (red) surrounding the wire provides a boundary at which grid refinement parameters can be specified (for `smesh` and `noffset3d` only), but does not serve any other purpose in our simulations. `SNMesh` and `noffset3d` both produced suitable grids, whereas the `mesh`-generated grid would likely require further refinement near the oxide/Si interface. For this structure, `noffset3d` was ultimately favored for its efficient handling of the curved p-n junction interface and compatibility with DF-ISE-format mesh files. Within the project, SDE was employed to specify the device structure and invoke `noffset3d` to generate the mesh. However, `noffset3d` required that several additional offsetting parameters be specified in its command file (which were added using `append-cmd-file` in SDE), in order to generate a suitable mesh. Furthermore, following a careful inspection of the resulting grid, several refinement boxes were added (manually) to patch inadequately meshed areas that appeared to be caused by mismatches between the circumference of the innermost vs. outermost offset layers.

B.4 Step 2: Simulating optical generation profiles using *Lumerical FDTD*

Lumerical calculates the steady-state electromagnetic field phasor vectors \vec{E} and \vec{H} throughout the simulation volume. Assuming that all absorption is due to band-to-band absorption within the semiconductor material, the optical generation rate is determined by the energy loss per unit volume, or divergence of

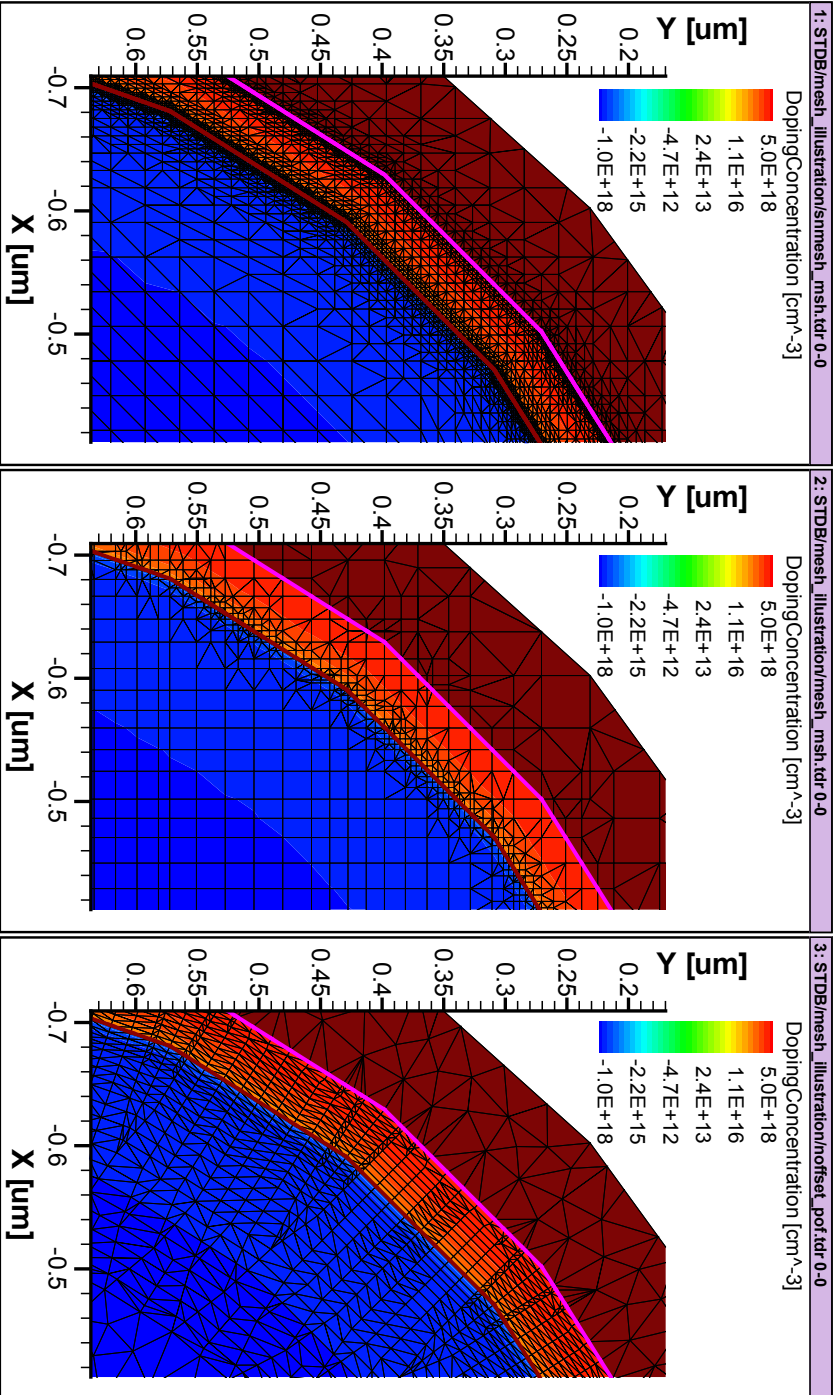


Figure B.2. Screenshot of simulation meshes produced by each tool. Left: SNMesh. Center: Mesh. Right: NOffset3d. Each mesh was generated for the same single-wire structure. The screenshot shows an area near the edge of the wire (viewed in Tecplot).

the Poynting vector. The equations work out such that G_{opt} can be determined directly from the electric field magnitude $|\vec{E}|$ and the imaginary part of the material's permittivity, ϵ'' , as:

$$G_{\text{opt}} = \frac{\Re\{\nabla \cdot \vec{P}\}}{2E_{\text{ph}}} = \frac{\pi\epsilon'' |\vec{E}|^2}{h} \quad (\text{B.1})$$

These calculations can be performed within Lumerical, making use of its MATLAB-like programming environment and built-in function library. First, however, each simulation must be configured to record the quantities ϵ'' and $|\vec{E}|$. This is accomplished by adding an index monitor ("**indexMonitor**" in our example code) and a frequency-domain power monitor ("**fldMonitor**") throughout the simulation volume, and configuring them to record the appropriate quantities (e.g., E_x , E_y , E_z , etc.) After the simulation has been run, the following commands can be used to calculate G_{opt} throughout the simulation volume (note that this example is for two-dimensional simulations):

```
load("simulation_filename.fsp");

freq = getdata("fldMonitor", "f");
x = getdata("fldMonitor", "x");
y = getdata("fldMonitor", "y");

E2 = getelectric("fldMonitor");
n = getdata("indexMonitor", "index_x");

omega = 2 * pi * freq;
epsilon = eps0 * n^2;
Pabs = 0.5 * omega * E2 * imag(epsilon);
Ngen = Pabs * 1e-6 / (6.626e-34 * freq); # cm^-3 s^-1
Current = 1.61e-19 * integrate(Ngen, 1:2, x, y);

matlabsave("output_filename.mat", x, y, Pabs, Ngen);
write("Absorbed photocurrent: " + num2str(Current) + " A per um");
```

The above code also uses the `integrate()` function to calculate the overall absorbed photocurrent of the structure (i.e., the maximally obtainable short circuit current of a solar cell). The resulting photogeneration profile variables are written to a MATLAB `.mat` file for further processing in the next step.

In addition to the direct calculation of photogeneration profiles (G_{opt}), it is also useful to determine the overall absorption of the structure using appropriately placed* field monitors. The total absorbed photocurrent calculated by volume integration above (`Current`) should always concur with the absorption calculated based on how much energy passes through the monitors surrounding the device (the latter calculation is aided by the `transmission()` function in Lumerical).

*By *appropriately placed*, we mean that the monitors should form a closed (Gaussian) surface around the absorption volume.

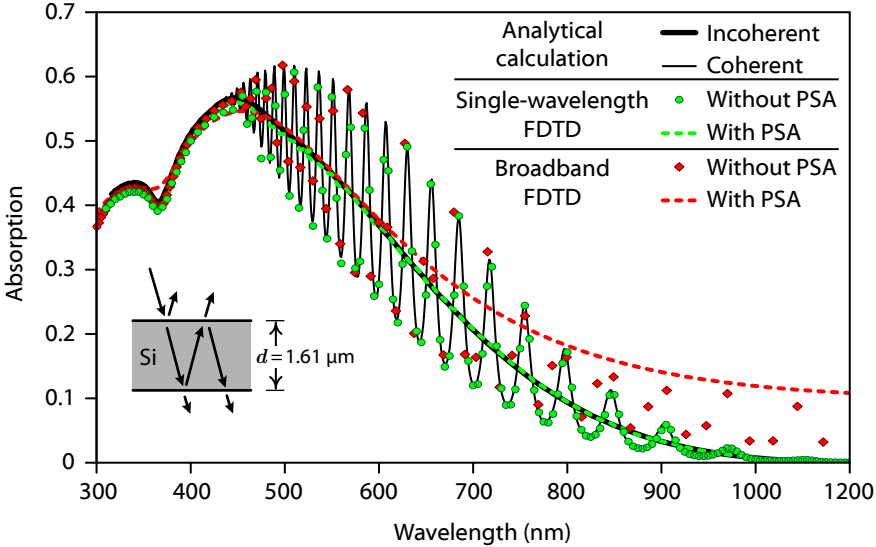


Figure B.3. Effect of partial spectral averaging (PSA) on Lumerical FDTD simulations. The absorption of a 1.61 μm thick planar Si slab (in air) is plotted, as calculated by single-wavelength (green) and broadband (red) FDTD simulations, with and without PSA using Δf values calculated by equation B.2 ($k = 1$). All simulations used Lumerical’s most-dense automatic grid setting. The broadband simulation represents the best material fit we were able to obtain for Si, using up to 18 fit parameters and trying a variety of tolerance and bandwidth settings for the fit. The black lines plot the absorption calculated by analytical means, with and without interference considerations.

B.4.1 Partial spectral averaging

Thin, partially transparent structures can exhibit large fluctuations in their reflection and transmission as the illumination wavelength is varied, due to interference (the phenomena responsible for Newton’s rings). Similar effects are also observed in FDTD, and can result in apparently “noisy” absorption calculations as the wavelength is varied (unless the simulation wavelengths are very closely spaced). To circumvent this problem, Lumerical offers *partial spectral averaging* (PSA), which averages simulation results over a small frequency range (via Lorentzian weighting) surrounding the principal simulation frequency. Given a device structure of thickness d , refractive index n , and a simulation wavelength of λ (and frequency f), the spectral half-width (Δf) of k interference fringes is given by the equation:

$$\Delta f = \frac{f}{1 + \frac{kd_{\text{Si}}n}{\lambda}} \quad [\text{Hz}] \quad (\text{B.2})$$

I have found that using the value of Δf corresponding to $k = 1$ gives good results when using Lumerical’s partial spectral averaging. This concept is illustrated in Figure B.3, in which FDTD simulations have been performed to calculate

the absorption of a simple planar Si slab of thickness $d = 1.61 \mu\text{m}$. The results of the FDTD simulations can be compared to the analytical solution for the absorption of this structure, calculated as described in section 3.1.3. The absorption calculated by FDTD simulations with vs. without PSA nearly exactly agrees with the analytical solutions for incoherent vs. coherent absorption, respectively. The figure also illustrates the difficulties we encountered attempting to perform broadband simulations of Si structures in Lumerical. For these reasons, all FDTD modeling presented in this thesis was performed using single-wavelength simulations, with partial spectral averaging where appropriate. The syntax to employ PSA in the single-microwire Si solar cell structures discussed herein is shown in the source code listings of section B.10.

B.5 Step 3: Generating the external-profile data file

The external-profile data file is generated using a MATLAB script (included in the source code listings of section B.10). This script first opens the `.dat` file produced in the initial mesh generation step, reading the values of `PMIUserField0` and `PMIUserField1` for each mesh element. Then, it produces a new `.dat` file containing the values of the external profile. A user-definable function determines the profile value at each spatial position. The script can be modified in several locations to specify the names of the input and output files, the names of the regions to process, the name of the output field, and most importantly, the function that determines the external profile value as a function of spatial coordinates. Comments within the script file provide details of how these modifications are made. The results of the script can be verified in Tecplot SV, as illustrated in Figure B.4.

To map profile values from the fixed-pitch (rectangular) FDTD grid to the varying element dimensions of the finite-element mesh, it is most conceptually simple to employ bilinear interpolation (the method used in the provided source code listing).^{*} However, this method could potentially introduce aliasing artifacts if the absorption profiles vary on a shorter length scale than the finite element mesh. For example, mild distortion of the sinusoidal profile is visible in the center of the wire shown in Figure B.4, where the finite-element grid is most coarsely spaced.

One solution to this problem might be to apply an antialiasing (averaging) filter to the FDTD dataset that conserves the total optical generation within the simulation volume (assuming that such “blurring” of G_{opt} is insignificant in terms of the electrical behavior of the device). A better solution is to use MATLAB’s built-in library of Delaunay triangulation functions to average the FDTD grid cells over the Voronoi region corresponding to each mesh element. An implementation of this approach is depicted in Figure B.5. We start by constructing the Delaunay triangulation corresponding to the finite-element mesh.

^{*}Because the FDTD grid pitch must always be smaller than length scales of absorption or resonant field profiles, it is usually suitable to employ nearest-neighbor interpolation, which is considerably faster for large simulation volumes. We use bilinear interpolation here because it does not add significant processing time for the example 2D structures.

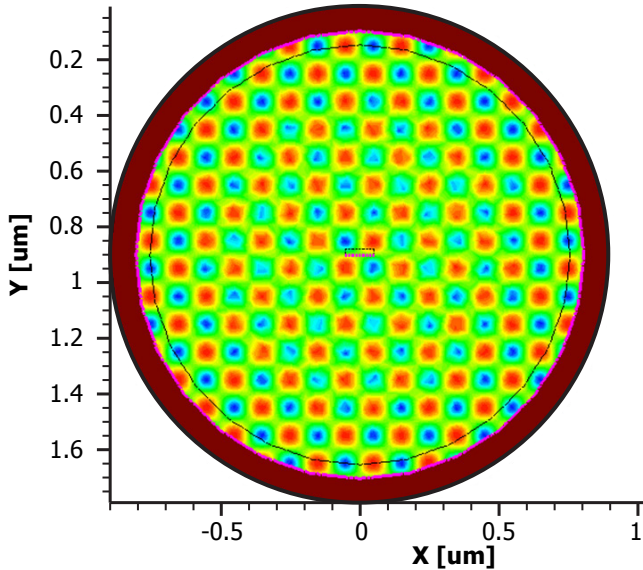


Figure B.4. Result of running the MATLAB script on the `noffset3d`-generated mesh from Figure B.2, using a sinusoid profile function to test the mapping (visualized in Tecplot SV).

We then iterate across the FDTD grid, assigning each grid cell (or “pixel”) to the nearest finite-element vertex. We can finally iterate through each element of the finite-element mesh and calculate the profile value to store in the resulting `.dat` file: elements to which one or more FDTD cells were mapped are assigned the average value of these cells, whereas elements to which zero cells were mapped are assigned the value of the nearest FDTD cell (or an interpolated value). This approach is not strictly conservative, but is certainly more so than linear interpolation. In our implementation, we utilized a script that parsed the `.grd` file so that a constrained Delaunay mesh could be constructed for each region. However, it might also be feasible to implement this approach with only the knowledge of the mesh coordinates and physical extent of each region, masking the FDTD grid-mapping by region instead of confining the Delaunay triangulation by region.

In most cases, simple interpolation has proven suitable for importing FDTD generation profiles onto Sentauros Device simulation meshes. For example, this approach yields accurate results for the simulation grid shown in Figure B.5 for $\lambda \gtrsim 400$ nm, below which wavelengths the shallow excitation profile is not conservatively mapped to the finite-element mesh. It is important to remember that, even if perfectly conservative optical generation mapping is performed, the finite-element mesh must still be dense enough to accurately represent the actual optical generation profile for device physics simulations. Thus, the most straightforward way to ensure accuracy in the grid conversion process is to simply increase the density of the device-physics mesh (if computationally feasible) until the largest mesh cells are of similar size as the FDTD cells, at which point

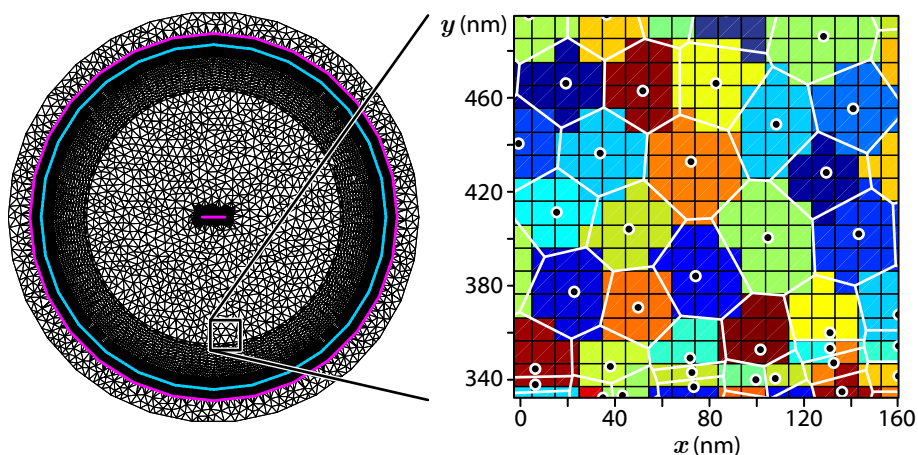


Figure B.5. Use of Delaunay triangulation to improve the accuracy of profile conversion. **Left:** finite-element simulation mesh for a $d = 1.61$ μm single-wire solar cell structure. The magenta lines indicate the contact electrodes, and the blue line indicates the p-n junction. **Right:** profile conversion algorithm applied to a central region of the wire. The orthogonal grid lines delimit the FDTD grid cells (“pixels”), and the black markers indicate the vertices of the finite-element mesh. The white lines show the Voronoi polygons for each mesh region. Each FDTD cell is colored based on which mesh element to which it is mapped (the colors are randomly chosen to illustrate the mapping).

aliasing is not a concern. As a test, numerical integration over the FDTD grid (as calculated in Lumerical or MATLAB) should produce the same approximate result as numerical integration over the device-physics mesh in Tecplot SV.*

B.6 Step 4: Loading the external profile in Sentaurus.

Sentaurus Device is invoked using the following `File` section syntax to specify the external optical generation file that was generated generated in the previous step.

```
File
{
  Grid           = "n|node|sde@_pof.grd"
  Doping         = "n|node|sde@_pof.dat"
  OpticalGenerationFile = "n|node|matlab@_optgen.dat"
  ...
}
```

The `File` section can also include directives that cause Sentaurus Device to load external profile values for several other fields, including carrier lifetime, emission rate, or trapped charge density.

B.7 Integrating these steps into SWB

The above steps, as well as additional steps to run and process the Lumerical FDTD simulations, can be integrated into Sentaurus Workbench (SWB) as user-configured tools. User-configured tools are specified in the user's `tooldb` (tool database) file, which is located in the STDB directory, and can be edited from within SWB by selecting `Edit→Tool DB→User`. To add the features of this appendix to SWB, one can copy the Tcl code provided in section B.10 into his or her `tooldb` file (creating a new file if it does not exist).

The provided `tooldb` file allows SWB projects to script and invoke Lumerical FDTD/CAD and MATLAB steps as part of the simulation process flow. A screenshot of a project that simulates a single-microwire Si solar cell structure (like that depicted in Figure B.1) is shown in Figure B.6. The process steps employed by this project are:

1. **Sentaurus Structure Editor**—builds the finite-element mesh. Parameters for this step could include device dimensions or doping levels.

*Tecplot SV is unaware of whether two-dimensional simulation data correspond to planar or cylindrical devices. For cylindrical devices, the simulation-plane density profiles (e.g., `OpticalGeneration`) must be (manually) multiplied by the circumferential depth ($2\pi x$, assuming cylindrical symmetry about $x=0$) to yield physically meaningful values when integrated. This can be accomplished by specifying a new data set in Tecplot SV (via "alter data"), such as the following:

```
{CylOptGen [umz^-1 umr^-1 s^-1]} = 6.2832*1E-4*{OpticalGeneration
[cm^-3*s^-1]}*{X [um]}
```

Scenario	Polarization	Wavelength	ShellSRV	SRH Lifetime	ShellSRV	Inspect	Abs_pavg	FF	VOC	ISC	IOE	EFF
25		790	1e-6	1e-5	--	--	0.13612	77.6	0.462	1.369012e-12	0.364	
26		810	1e-6	1e-5	--	--	0.124357	77.5	0.461	1.280693e-12	0.363	
27		830	1e-6	1e-5	--	--	0.11115	77.5	0.458	1.171053e-12	0.361	
28		850	1e-6	1e-5	--	--	0.0969028	77.5	0.454	1.041495e-12	0.360	
29		870	1e-6	1e-5	--	--	0.0760507	77.1	0.447	8.371018e-13	0.379	
30		890	1e-6	1e-5	--	--	0.0628994	76.5	0.443	7.070629e-13	0.379	
31		910	1e-6	1e-5	--	--	0.0514043	76.2	0.439	5.898282e-13	0.378	
32		930	1e-6	1e-5	--	--	0.0413627	76.2	0.432	4.863385e-13	0.377	
33		950	1e-6	1e-5	--	--	0.0304037	75.2	0.424	3.650770e-13	0.378	
34		970	1e-6	1e-5	--	--	0.0233158	74.8	0.418	2.836891e-13	0.376	
35		990	1e-6	1e-5	--	--	0.0178442	74.5	0.410	2.210197e-13	0.376	
36		1010	1e-6	1e-5	--	--	0.0121224	73.3	0.400	1.535384e-13	0.376	
37		1030	1e-6	1e-5	--	--	0.0077692	72.4	0.386	1.004792e-13	0.376	
38		1050	1e-6	1e-5	--	--	0.00497042	71.3	0.373	6.497083e-14	0.378	
39		1070	1e-6	1e-5	--	--	0.00304151	69.5	0.359	4.018285e-14	0.378	
40		1090	1e-6	1e-5	--	--	0.00184559	67.8	0.342	2.399631e-14	0.378	
41				1e-2				82.3	0.725	1.078671e+01		6.38
42				1e-3				82.8	0.698	1.078639e+01		6.18
43				1e-4				83.3	0.645	1.078327e+01		5.74
44		AM15		1e-6				82.3	0.589	1.075446e+01		5.17
45				1e-6				81.2	0.544	1.059755e+01		4.64
46				1e-7				80.9	0.527	1.041848e+01		4.40

Figure B.6. Screenshot of SWB project that integrates Lumerical and MATLAB processing steps.

2. **Lumerical CAD**—prepares the Lumerical FDTD simulation structure. Parameters could include wavelength and polarization.
3. **Shell**—executes the Lumerical FDTD simulation using a `csh` script.
4. **Lumerical CAD**—loads the completed FDTD simulation, processes the results, and saves the optical generation profile and the FDTD grid in a MATLAB-format (`.mat`) data file.
5. **MATLAB**—loads the finite-element mesh from step 1 and the optical generation profiles from step 4. Generates the `.dat` file specifying the optical generation profile on the finite-element mesh.
6. **Sentaurus Device**—simulates the I - V characteristics of the solar cell using the optical generation profile data produced in step 5. Typical parameters could include carrier lifetimes and surface recombination velocities.
7. **Inspect**—extracts the operating parameters of the device (e.g., I_{sc} , V_{oc} , FF , η , E.Q.E., or I.Q.E.) and exports them as project variables in the SWB table.

This framework provides means to automate all of the simulation steps presented in this appendix, allowing each experiment to vary the device and simulation parameters such as geometry, material quality, and illumination wavelength. This platform has proven remarkably useful in my work, not only for performing elaborate optoelectronic simulations, but also for automating simple parametric sweeps in FDTD simulations. The SWB environment is particularly advantageous from an organizational and archival standpoint: SWB projects not only provide a tabulated record of the simulation parameters and results for each experiment, but also retain the input and output files for each simulation step in their directories, all of which are easily referenced by node number.

B.8 Simulating solar illumination

In the project shown in Figure B.6, each experiment corresponds to a single illumination wavelength (and polarization state). This allows the polarization-dependent spectral response of the device to be simulated in a straightforward manner. To simulate broadband, unpolarized illumination such as sunlight (i.e., the AM 1.5G spectrum), several general approaches are possible:

Single-experiment, broadband illumination: A single Lumerical simulation can utilize a broadband light source which spans the solar spectrum. During post-processing, the data can be normalized and weighted to yield the simulated response under solar illumination. Further details of this method are provided in the Lumerical reference guide. (□)

Although this approach may be the simplest, I have thus far been unable to adequately model the dispersion of Si across the solar spectrum in

Lumerical (see Figure B.3). Aside from the stark inaccuracy of my broadband simulation attempts, they have required manyfold greater memory and CPU time than the combined requirements of single-wavelength simulations spanning $\lambda = 300$ to 1100 nm in 20 nm increments.

Multi-experiment, summed monochromatic illumination: For each device geometry, numerous single-wavelength simulations are run to span the solar spectrum (each as a separate experiment, stemming from a common SDE node). To simulate solar illumination, an additional experiment is configured with a special keyword or value in place of a normal numerical value for the parameter *wavelength* (such as "AM15" or 15). This experiment's CAD/FDTD steps are skipped; instead, the combined and weighted FDTD results from the preceding single-wavelength simulations provide the **OpticalGeneration** profile for its Sentaurus Device step. The special *wavelength* keyword triggers the MATLAB script to load the single-wavelength results, then sum and weight them appropriately for the desired solar spectrum, and store this composite photogeneration profile in a `.dat` file for the Sentaurus simulation.

Using this approach, both the 1-sun efficiency and the spectral response of the cell can be easily recorded in the project table within SWB. However, this method is somewhat cumbersome as it requires diligence in experimental layout and execution order, since all the single-wavelength FDTD simulations must be run before the broadband illumination profile can be calculated. For this reason it is not amenable to optimization within SWB. Nonetheless this is the technique I employ for most applications. By separating experiments by scenario, and by careful naming of the optical generation files, I am able to complete this process in two steps: the first, to specify and run all single-wavelength simulations; and the second, to run the broadband simulations.

Single-experiment, summed monochromatic illumination: The single-wavelength approach above can be condensed into a single experiment within SWB. The first Lumerical CAD step is scripted to prepare multiple single-wavelength simulation files to span the solar spectrum (under a single project node prefix). The FDTD execution step is scripted to run all of these simulations. Similarly, the second Lumerical and the MATLAB steps are altered to sequentially process a multitude of individual simulations. Finally, after processing all single-wavelength simulations, the MATLAB script can then weight and sum them appropriately to produce a single **OpticalGeneration** profile representing broadband solar illumination.

With this approach, wavelength and polarization would no longer appear as experiment parameters, and thus spectral response data would not be tabulated within the SWB project view. However, the scripts could easily be modified to record spectrally resolved simulation results as separate output files (just as Sentaurus Device produces `.plt` files recording the results of its internal $I-V$ sweeps). This approach is also compatible with numerical optimization in SWB.

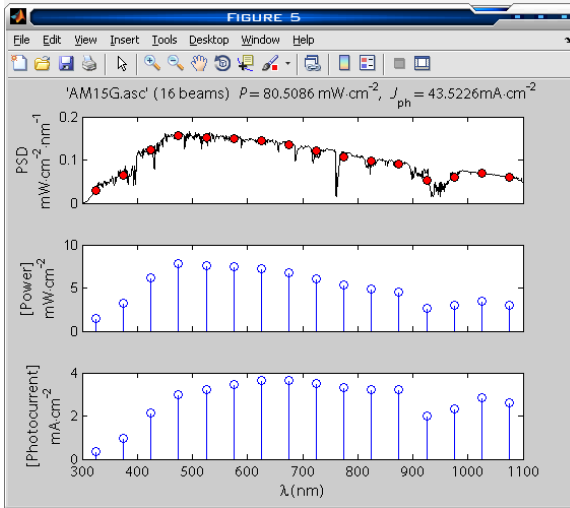


Figure B.7. Discrete solar spectrum script output.

A tabulation of weighting factors for discrete single-wavelength simulations to approximate solar illumination (corresponding to AM 1.5 global and direct reference spectra) [15] is provided in section B.11 at the end of this appendix. Also included is a general-purpose MATLAB script for integrating or binning solar spectra. A screenshot of a discrete solar spectrum produced by this script is shown in Figure B.7.

B.8.1 Tips

- A single-wavelength source magnitude of 86.6 in Lumerical corresponds to $1 \text{ mW}\cdot\text{cm}^{-2}$ illumination intensity. This simplifies the weighting of each profile, as each can be directly multiplied by the desired illumination intensity (in $\text{mW}\cdot\text{cm}^{-2}$) of the discrete (“binned”) solar spectrum. The source magnitude (E_0) is specified in units of $\text{V}\cdot\text{m}^{-1}$, thus the following equation determines illumination intensity:

$$\langle S \rangle = \frac{1}{2\mu_0 c} E_0^2 = \frac{\epsilon_0 c}{2} E_0^2 \quad [\text{W}\cdot\text{m}^{-2}] \quad (\text{B.3})$$

- If polarization-dependent simulation data are not needed, each single-wavelength FDTD simulation can be run (simultaneously or consecutively) for both TE and TM polarization and then averaged in a single project node.

B.9 Tool information

B.9.1 Lumerical CAD (`lumcad`)



Lumerical CAD is used twice in our method of SWB integration. The first CAD step prepares and saves (but does not execute) the simulation structure. An intermediate shell step executes the FDTD simulation. The second CAD step then loads the simulation results, extracts the optical generation profiles, and saves this information to a MATLAB `.mat` file for subsequent processing.*

Input files :

- **Script file** (`lumcad_lcs.lsf`): The Lumerical script file, which will be pre-processed prior to invoking CAD. Scripts should call `exit(2)` at the end of their routine, otherwise the CAD window will remain open.
- **Template structure** (`lumcad_template.fsp`): Instead of using a script to generate the entire Lumerical simulation from scratch, it is often convenient to manually generate the structure beforehand as a “template” file. This way, a simple script can load the template structure, make only changes pertaining to the experiment’s parameters, and then save the resulting structure under the appropriate filename for the current node.

Output files :

- **Lumerical structure** (`n@node@lumstr.fsp`): The simulation structure, saved and ready for simulation.
- **Lumerical shell script** (`n@node@lumstr.sh`): This is the shell script that Lumerical automatically generates when the above structure is saved. Executing it invokes the MPI FDTD program to run the simulation. It is configured within CAD under the menu `Simulation`→`Set parallel options` menu.
- **Lumerical log file** (`n@node@lumstr_p0.log`): This is the log file produced by Lumerical FDTD as it runs the simulation.
- **MATLAB MAT file** (`n@node@lummat.mat`): The optical generation profile information extracted from a completed simulation, saved for subsequent MATLAB processing.

*Lumerical CAD does not have a “batch mode.” It will briefly open the GUI window while each script is executed.

B.9.2 Shell



The shell tool is a standard part of TCAD Sentaurus, and is not modified by the provided `tooldb` file. We utilize a C-shell (`cs`) script to launch the Lumerical FDTD simulations, and to examine their output files to make sure they ran to completion. The shell script command file is listed in section [B.10](#).

Note: My FDTD simulations rely on Lumerical’s *auto-shutoff* feature to determine when to terminate a simulation. If a simulation reaches the end of its allotted duration (“100% completion”) before encountering the auto-shutoff criteria, I generally consider the results to be invalid. Thus the provided shell script will mark the FDTD nodes as *failed* unless auto-stop is reached.

B.9.3 MATLAB



Batch-mode MATLAB scripts are run in a nongraphical instance of MATLAB, and can make use of the full library of nongraphical MATLAB functions—including the parallelization toolkit, which is particularly useful for dealing with large simulation structures.

Input files :

- **MATLAB m-file** (`matlab_mat.m`): When MATLAB nodes are executed, this script file is pre-processed and then piped to the MATLAB command prompt. Note that a new instance of MATLAB will be invoked for each MATLAB step; thus each node will not have access to workspace variables in other MATLAB sessions. Upon completion, the script should call `exit(0)` to quit the MATLAB session, otherwise SWB will wait indefinitely for the program to terminate. For this reason, it is also best to enclose all code in a `try` block, so that `exit(1)` can be called in the event of any error.
- **Other input files:** One or more `.mat` files containing optical generation profiles from previous Lumerical CAD steps, and the DF-ISE `.dat` file from the mesh generation step.

Output files :

- **DF-ISE mesh data** (`n@node@optgen.dat`): The optical generation profile mapped to the simulation grid.

- **Other output files:** The provided script will also store the mapped photogeneration data as a MATLAB `.mat` format, using the naming convention:

```
n@node|sde@_OptGen@Wavelen@@Polarization@.mat
```

This facilitates loading, weighting, and summing the numerous single-wavelength profiles when the special wavelength value of “15” is specified (see above).

B.10 Selected source code

This section provides the `toolpdb` file used to integrate Lumerical and MATLAB as tools in Sentaurus Workbench. Source code is also provided for the following simulation steps of the single-microwire Si solar cell model highlighted above:

- The Lumerical structure generation script
- The shell script for launching Lumerical FDTD simulations from SWB
- The Lumerical data extraction script
- The MATLAB grid conversion script

Although each file is somewhat specific to the single-microwire Si solar cell structure shown here, they have been prepared in hopes of providing a clear example of the approach we have developed for importing arbitrary input profiles for simulations with Sentaurus Device. A MATLAB script for binning the solar spectrum for discrete single-wavelength simulations is also provided.

B.10.1 toolpdb file

Listing B.1. User `toolpdb` file (Tcl).

```
#BEGIN FILE
# Lumerical / MATLAB integration for Sentaurus Workbench
# Michael Kelzenberg, 2010
# California Institute of Technology

#SPECIAL_SETTINGS BEGIN
global tcl_platform
global env
#SPECIAL_SETTINGS END

#FILE-TYPES BEGIN
lappend WB_tool(file_types) lumscript
set WB_tool(lumscript,ext) lsf
lappend WB_tool(file_types) lumstructure
set WB_tool(lumstructure,ext) fsp
lappend WB_tool(file_types) lumbat
set WB_tool(lumbat,ext) sh
lappend WB_tool(file_types) lumlog
set WB_tool(lumlog,ext) log
```

```

lappend WB_tool(file_types) matlabm
set WB_tool(matlabm,ext) m
lappend WB_tool(file_types) matlabmat
set WB_tool(matlabmat,ext) mat
#FILE-TYPES END

#TOOL BEGIN lumcad
set WB_tool(lumcad,category) device
set WB_tool(lumcad,visual_category) device_old
set WB_tool(lumcad,acronym) lcs
set WB_tool(lumcad,after) all
set WB_manual(lumcad) /usr/lumerical/docs/FDTD_reference_guide.pdf
set Icon(lumcad) $env(STDB)/ico/cad.gif
set WB_tool(lumcad,exec_mode) batch ; # (interactive | batch)
set WB_tool(lumcad,setup) { os_ln_rel @lumscript@ n@node@_lcs.lsf "@pwd@" }
set WB_tool(lumcad,epilogue) \
    { make_sh_executable "$wdir" @node@; extract_vars "$wdir" @stdout@ @node@ }
set WB_binaries(tool,lumcad) CAD-noaccel
set WB_tool(lumcad,cmd_line) "n@node@_lcs.lsf"
set WB_tool(lumcad,input) [list lumscript lumstructure]
set WB_tool(lumcad,input,lumscript,file) @toolname@_lcs.lsf
set WB_tool(lumcad,input,lumscript,newfile) @toolname@_lcs.lsf
set WB_tool(lumcad,input,lumscript,label) "Script file..."
set WB_tool(lumcad,input,lumscript,editor) text
set WB_tool(lumcad,input,lumscript,parametrized) 1
set WB_tool(lumcad,input,lumstructure,file) @toolname@_template.fsp
set WB_tool(lumcad,input,lumstructure,newfile) @toolname@_template.fsp
set WB_tool(lumcad,input,lumstructure,label) "Template structure..."
set WB_tool(lumcad,input,lumstructure,editor) lumstructure
set WB_tool(lumcad,input,lumstructure,parametrized) 0
set WB_tool(lumcad,output) [list lumstructure lumbar lumlog matlabmat]
set WB_tool(lumcad,output,lumstructure,file) n@node@_lumstr.fsp
set WB_tool(lumcad,output,lumbar,file) n@node@_lumstr.sh
set WB_tool(lumcad,output,lumlog,file) n@node@_lumstr_p0.log
set WB_tool(lumcad,output,matlabmat,file) n@node@_lummat.mat
set WB_tool(lumcad,output,files) "n@node@_* pp@node@_*"
set WB_tool(lumcad,interactive,option) "-edit"
set WB_tool(lumcad,batch,option) "-run"
lappend WB_tool(all) lumcad
#TOOL END

#TOOL BEGIN matlab
set WB_tool(matlab,category) gridgen
set WB_tool(matlab,visual_category) gridgen
set WB_tool(matlab,acronym) mat
set WB_tool(matlab,after) all
set WB_manual(matlab) /usr/matlab/help/begin_here.html
set Icon(matlab) $env(STDB)/ico/matlab.gif
set WB_tool(matlab,exec_mode) batch ; # (interactive | batch)
set WB_tool(matlab,setup) { os_ln_rel @matlabm@ n@node@_mat.m "@pwd@" }
set WB_tool(matlab,epilogue) { extract_vars "$wdir" @stdout@ @node@ }
set WB_binaries(tool,matlab) "matlab"
set WB_tool(matlab,cmd_line) "< n@node@_mat.m"
set WB_tool(matlab,input) [list matlabm]
set WB_tool(matlab,input,matlabm,file) @toolname@_mat.m
set WB_tool(matlab,input,matlabm,newfile) @toolname@_mat.m
set WB_tool(matlab,input,matlabm,label) "Matlab m-file..."
set WB_tool(matlab,input,matlabm,editor) text
set WB_tool(matlab,input,matlabm,parametrized) 1
set WB_tool(matlab,output) [list doping grid]
set WB_tool(matlab,output,doping,file) n@node@_optgen.dat
set WB_tool(matlab,output,grid,file) n@node@_optgen.grd
set WB_tool(matlab,output,files) "n@node@_* pp@node@_*"
set WB_tool(matlab,interactive,option) ""
set WB_tool(matlab,batch,option) "-nojvm -nodisplay"

```

```

lappend WB_tool(all) matlab
#TOOL END

#INPUT-EDITORS BEGIN
set WB_binaries(editor,text) gedit
lappend WB_editor(all) text
set WB_binaries(editor,lumstructure) CAD
lappend WB_editor(all) lumstructure
#INPUT-EDITORS END

#OUTPUT-VIEWERS BEGIN
set WB_viewer(lumstructure,files) "\{*n@node@_*.fsp\}"
set WB_viewer(lumstructure,label) ".fsp Files (Lumerical CAD)"
set WB_viewer(lumstructure,nbfiles) 3
set WB_viewer(lumstructure,cmd_line) @files@
set WB_viewer(lumstructure,exec_dir) @pwd@
set WB_binaries(viewer,lumstructure) CAD-noaccel
lappend WB_viewer(all) lumstructure

set WB_viewer(lumbat,files) "\{*n@node@_*.sh\}"
set WB_viewer(lumbat,label) "Shell file (for MPI-Lumerical)"
set WB_viewer(lumbat,nbfiles) 3
set WB_viewer(lumbat,cmd_line) @files@
set WB_viewer(lumbat,exec_dir) @pwd@
set WB_binaries(viewer,lumbat) gedit
lappend WB_viewer(all) lumbat

set WB_viewer(lumlog,files) "\{*n@node@_lumstr_p0.log\}"
set WB_viewer(lumlog,label) "Lumerical log file"
set WB_viewer(lumlog,nbfiles) 5
set WB_viewer(lumlog,cmd_line) @files@
set WB_viewer(lumlog,exec_dir) @pwd@
set WB_binaries(viewer,lumlog) "gnome-terminal -x tail -f -n +1"
lappend WB_viewer(all) lumlog

set WB_viewer(matlabmat,files) "\{*n@node@_matlabmat.mat\}"
set WB_viewer(matlabmat,label) "Matlab MAT file"
set WB_viewer(matlabmat,nbfiles) 3
set WB_viewer(matlabmat,cmd_line) @files@
set WB_viewer(matlabmat,exec_dir) @pwd@
set WB_binaries(viewer,matlabmat) matlab
lappend WB_viewer(all) matlabmat
#OUTPUT-VIEWERS END

#RunLimits
#accepted values for restriction_model:
#none,per_project,per_user,per_swb
set WB_limits(restriction_model) "per_user"
set WB_limits(lumcad,run_limit) 4
set WB_limits(matlab,run_limit) 4
#Run Limits end

#TCL-SOURCE BEGIN
# MK 2009
proc make_sh_executable { wdir node } {
    foreach file [glob -nocomplain -directory $wdir n${node}*.sh] {
        file attributes $file -permissions 00755
    }
}
#TCL-SOURCE END

```

B.10.2 Lumerical structure generation script

Listing B.2. Lumerical script for preparing FDTD simulation structures (lumcad_lcs.lsf).

```
#####
#
# Lumerical structure-generating script
# (c) 2009 Michael Kelzenberg
# California Institute of Technology
#
# This script loads a "template" file and modifies it according to the paramters
# set for this node in SWB (i.e., wavelength and polarization). The input/
# output files are defined below.
#
# Tip: Be carefule using "#" to comment out lines. This can confuse the
# sentaurus pre-processor. As a rule, always put a space after "#" if you are
# writing comments.
#
#####

clear;

template_file = "lumcad_template.fsp";
lumstr_file = "n@node@_lumstr.fsp";

Polarization = "@Polarization@";
Lambda = @Wavelen@ * 1e-9; # (m)

WireDiameter = 1.61e-6;
BoxWidth = 1.8e-6; #This is the width of the monitors surrounding the wire
IllumWidth = 4e-6; #This is the width of the illumination source

write("Single-wire solar cell FDTD structure generator script for LUMERICAL");
write("Michael Kelzenberg, 2010");
write("Settings: "+Polarization+"-polarization, "+num2str(Lambda*1e+9)+" nm.");
write("Loading template file: " + template_file);

load(template_file);

switchtolayout;

setparallel("Shell/batch file type","Linux multi-processors");
setparallel("Create parallel shell/batch file when saving fsp file",1);
setparallel("Number of processors per node",2);

simulation;
select("FDTD");

# Select a reasonable simulation duration (longer than will be required)
set("simulation time",1e-12);
if( Lambda > 800e-9 ) {
    set("simulation time",5e-12);
}
if( Lambda > 950e-9 ) {
    set("simulation time",10e-12);
}
if( Lambda > 1070e-9 ) {
    set("simulation time",20e-12);
}

# Set correct boundary conditions depending on polarization
if( Polarization == "TE" ) {
    set("x min bc","Anti-Symmetric");
}
```



```

} else {
    set ("x min bc", "Symmetric");
}

# Set wavelength and polarization of the source
sources;
select ("singleSource");
set ("amplitude", 86.8); #86.8 V/m is a illum. intensity of 1 mW/cm2
set ("polarization", Polarization);
set ("wavelength start", Lambda);
set ("wavelength stop", Lambda);

# Set the bandwidth for partial spectral averaging
monitors;
freq = 2.998e+8/Lambda;
n = real(getindex("SiAspnes", freq));
waveFract = 1; # 2 is for half-wave, 1 for full-wave
deltaF = freq / (1 + (waveFract*WireDiameter*n/Lambda) );

write("Partial spectral averaging deltaF = " + num2str( deltaF/1e12 ) + " THz");

select("topMonitor");
set ("delta", deltaF);
select("bottomMonitor");
set ("delta", deltaF);
select("leftMonitor");
set ("delta", deltaF);
select("rightMonitor");
set ("delta", deltaF);
select("wireMonitor");
set ("delta", deltaF);

write("Saving modified structure: " + lumstr_file);

save(lumstr_file);

write("Completed successfully");

exit(2);

```

B.10.3 FDTD execution shell script

Listing B.3. Shell script (csh) for launching MPI FDTD simulations from SWB (cshell_csh.cmd).

```

# Shell script for invoking FDTD simulations
# Michael Kelzenberg, 2010 (c)
# California Institute of Technology

# This script executes the .sh file generated by the prior Lumerical CAD step
# then parses the output to ensure that the simulation ran to completion.

#setdep @previous@

# TCL code in our tooldb file now takes care of setting the execut bit for
# Lumerical's MPI shell scripts, so the following is not needed here:
# chmod 755 *.sh

echo "*****"
echo "Shell script for running Lumerical FDTD simulations"
echo "Michael Kelzenberg, 2010"
echo ""
echo "Warning! Using 'Abort' in SWB will NOT terminate MPI FDTD simulations."

```



```

%This should be a valid DF-ISE .dat file (i.e. generated by mesh or
%noffset3d. The meshing program must be scripted to store the x- and y-
%position of each vertex of the grid as "PMIUserField0" and
%"PMIUserField1", respectively.
%%%%%%%%%%%%%%%%%%%%%%%%%%%%%%%%%%%%%%%%%%%%%%%%%%%%%%%%%%%%%%%%%%%%%%%%
datFile = 'n@node|sde@msh.dat';
grdFile = 'n@node|sde@msh.grd';

%FDTD MAT file %%%%%%%%%%%%%%%%%%%%%%%%%%%%%%%%%%%%%%%%%%%%%%%%%%%%%%%%%%%%%%%%%%%%%%%%%
%This should be the Matlab MAT file generated by the Lumerical CAD script
%including:
% Pabs_x,Pabs_y      X and Y specification of grid (m)
% freq              Freq. of simulation (Hz)
% Pabs *            Matrix of power absorption (W/m3)
% Ngen *            Matrix of optical generation rate (per cm3 per s)
% IntgPwr *         Total power absorption (W/m)
% Current *         Total photocurrent (A per um device length)
% Absfrac *         Fraction of absorbed light, i.e. Absorption Quantum Efficiency
% *these variables followed by '_pavg' corespond to partial spectral averaging
%
% Note: presently, only Pabs_x, Pabs_y, and Ngen_pavg are used by this script.
%%%%%%%%%%%%%%%%%%%%%%%%%%%%%%%%%%%%%%%%%%%%%%%%%%%%%%%%%%%%%%%%%%%%%%%%

FDTDFile = 'n@node|lumcad1@_lummat.mat';

%Regions to process %%%%%%%%%%%%%%%%%%%%%%%%%%%%%%%%%%%%%%%%%%%%%%%%%%%%%%%%%%%%%%%%%%%%%%%%%
%These are the regions to perform the optical generation mesh conversion.
%This must be a cell array of region names, including double-quotes (")
%around each region name!!!
% Example syntax: regionsToProcess = {"Base_region", "Emitter_region" };
%%%%%%%%%%%%%%%%%%%%%%%%%%%%%%%%%%%%%%%%%%%%%%%%%%%%%%%%%%%%%%%%%%%%%%%%
regionsToProcess = {"InnerContact_region" "Emitter_region" "Base_region"};

%The output dat and grd files are used for monochromatic-illumination device
% physics simulations (the next step in this experiment).
outputFile = ['n@node@_optgen.dat'];
outputGrid = ['n@node@_optgen.grd'];

%The export data file (.mat) is saved so that a MATLAB script can sum together
% multiple single-wavelength simulations to approximate solar illumination.
% We chose a file name that is unique to the wavelength, polarization, and
% the device physics simulation grid:
exportFile = 'n@node|sde@_OptGen@Wavelen@Polarization@.mat';

%Number of data values to output per line in output DAT file
numperline = 10;

try

disp('');
disp('-----');
disp(['OptGenConverter Version 2']);
disp(['(c) 2010 Michael Kelzenberg']);
disp(['California Institute of Technology']);
disp('-----');
disp(' ');

% A wavelength value of '15' is the signal to assemble 1-sun AM1.5G illumination
if (@Wavelen@ == 15)
    nodenum = @node@; nodenum_sde = @node|sde@;
    disp(['Invoking am15proc.m script to generate combined-wavelength OptGen' ...
        ' profile...']);
    disp(' ');
    disp('This will fail if the prerequisite single-wavelength FDTD profiles');

```

```

    disp(' have not been generated for this device physics simulation grid,');
    disp(' (n@node|sde@)');
    disp(' ');
    aml5proc;
    exit(0);
end

disp(['Opening DAT file ' datFile ]);

grd = fopen(datFile);
if (grd < 1)
    error(['Error opening file ' datFile ' for reading.']);
    %exit
end

if ( ~isequal( fgetl(grd), 'DF-ISE text'))
    disp('Error with grid file format: It might not be a DF-ISE text file. ');
    disp('Please double-check input file. The first line should read:');
    disp(' DF-ISE text');
    error('File parse error');
end

fln = 1;

verts = [];
regions = {};

nl = fgetl(grd); fln=fln+1;
while( isempty( regexp(nl, 'nb_vertices *= *[0-9]+') ) && ~feof(grd) )
    nl = fgetl(grd); fln=fln+1;
end
tmp=regexp(nl, '[0-9]+','match');
numverts = str2num(tmp{1});
disp([' File reports ' num2str(numverts) ' vertices']);

nl = fgetl(grd); fln=fln+1;
while( isempty( regexp(nl, 'nb_edges *= *[0-9]+') ) && ~feof(grd) )
    nl = fgetl(grd); fln=fln+1;
end
tmp=regexp(nl, '[0-9]+','match');
numedges = str2num(tmp{1});
disp([' File reports ' num2str(numedges) ' edges']);

nl = fgetl(grd); fln=fln+1;
while( isempty( regexp(nl, 'nb_elements *= *[0-9]+') ) && ~feof(grd) )
    nl = fgetl(grd); fln=fln+1;
end
tmp=regexp(nl, '[0-9]+','match');
numelems = str2num(tmp{1});
disp([' File reports ' num2str(numelems) ' elements']);

nl = fgetl(grd); fln=fln+1;
while( isempty( regexp(nl, 'nb_regions *= *[0-9]+') ) && ~feof(grd) )
    nl = fgetl(grd); fln=fln+1;
end
tmp = regexp(nl, '[0-9]+','match');
numregions = str2num(tmp{1});
disp([' File reports ' num2str(numregions) ' regions']);

%Advance to data section of file...
nl = fgetl(grd); fln=fln+1;
while( isempty( regexp(nl, 'Data.*\{', 'once') ) && ~feof(grd) )
    nl = fgetl(grd); fln=fln+1;
end

```

```

if ( feof(grd) )
    disp('Unexpected end-of-file, no data processed. ');
    disp(['Line: ' num2str(fln)]);
    error('File parse error. ');
end

regionArray = [];
disp(' ');
disp('Reading data points...');
%Main reading loop. Look for PMIUserField 0 or 1 data sets...
while ~feof(grd)

    nl = fgetl(grd); fln=fln+1;
    while ( isempty( regexpi(nl, '\s+function\s+=\s+PMIUserField[01]', 'once'))...
        && ~feof(grd) )
        nl = fgetl(grd); fln=fln+1;
    end
    if (feof(grd))
        break
    end

    tmp = regexp(nl, '[01]', 'match');
    axisNumber = str2num(tmp{1});

    nl = fgetl(grd); fln=fln+1;
    while ( isempty( regexpi(nl, '\s*validity\s*=\s*\{ \s*" .*" \s*\}', 'once'))...
        && ~feof(grd) )
        nl = fgetl(grd); fln=fln+1;
    end

    if (feof(grd))
        error(['File Parse Error near line ' num2str(fln)]);
        break
    end
    tmp = regexp(nl, '" .*"', 'match');
    regionName = tmp{1};

    nl = fgetl(grd); fln=fln+1;
    while ( isempty( regexpi(nl, '\s*Values\s*\(\s*[0-9]+\s*\)', 'once') )...
        && ~feof(grd) )
        nl = fgetl(grd); fln=fln+1;
    end

    if (feof(grd))
        disp(['File Parse Error near line ' num2str(fln)]);
        break
    end
    tmp = regexp(nl, '[0-9]+', 'match');
    numElems = str2num(tmp{1});

    dataPoints = [];
    while (1)
        nl = fgetl(grd); fln = fln+1;
        if(isempty(regexp(nl, '[0-9]+')) )
            break
        else
            thisline = regexp(nl, '[\.\-|e|E|+0-9][\s\.\-|e|E|+0-9]*', 'match');
            thisline = thisline{1};
            dataPoints = [dataPoints str2num(thisline)];
        end
        if ( ~isempty(regexp(nl, ',', 'once') ) )
            break
        end
    end
end

```

```

disp([' Region ' regionName ' read ' num2str(length(dataPoints)) '/' ...
      num2str(numElems) ' elements for axis ' num2str(axisNumber) ]);

%Error if data points disagree with number stated in header
if ( numElems ~= length(dataPoints) )
    disp(['Error: number of data points does not match file header']);
    disp(['Parse error near line ' num2str(flN)]);
    error(['File structure error in region ' regionName]);
end

existingRegion = 0;
for n=1:length(regionArray)
    canRegion = regionArray{n};
    if (isequal(regionName,canRegion.name))
        existingRegion = n;
    end
end

if (existingRegion)
    if (axisNumber == 0)
        regionArray{existingRegion}.xdata = dataPoints;
    else
        regionArray{existingRegion}.ydata = dataPoints;
    end

    if ~isequal( length(regionArray{existingRegion}.xdata), ...
                length(regionArray{existingRegion}.ydata) )
        disp(['Error: number of x data points does not match number of ' ...
              'y data points']);
        error(['File structure error in region ' regionName ]);
    end
else
    newRegion.name = regionName;
    if (axisNumber == 0)
        newRegion.xdata = dataPoints;
        newRegion.ydata = [];
    else
        newRegion.ydata = dataPoints;
        newRegion.xdata = [];
    end
    newRegion.gdata = zeros(size(dataPoints));
    regionArray{end+1} = newRegion;
end

end

for n=1:length(regionArray)
    if ~isequal( length(regionArray{n}.xdata), length(regionArray{n}.ydata) )
        disp(['Error: number of x data points does not match number of ' ...
              'y data points']);
        error(['File structure error in region ' regionArray{n}.name ]);
    end
end

disp(' ');
disp('Completed reading DAT file');
disp([' Read ' num2str(length(regionArray)) ' region(s)']);
disp(' ');
fclose(grd);

%Now ensure that data was successfully read for all requested regions
regionsToProcess = unique(regionsToProcess);
for n=1:length(regionsToProcess)

```

```

reqName = regionsToProcess{n};
hasRegion = 0;
for m=1:length(regionArray)
    if isequal( reqName, regionArray{m}.name )
        hasRegion=1;
        break;
    end
end
if ~hasRegion
    disp(['Error: Vertex position information for requested region ' ...
        reqName ' not contained within this grid.']);
    error(['Unable to process region: ' reqName ]);
end
end

% We're done parsing grid file -- Now we load FDTD results and define the
% mapping function. Note that the spatial translation applied to the x- and
% y-coordinates in the mapping function is specific to the project geometry:
disp(' ');
disp(['Loading MAT file ' FDTDFile ]);
load(FDTDFile);
optGenMatrix = OptGen';
%%%%%%%%%%%%%%%%%%%%%%%%%%%%%%%%%%%%%%%%%%%%%%%%%%%%%%%%%%%%%%%%%%%%%%%%
%Mapping function:
newoptgen = @(xi, yi) interp2(Pabs_x,Pabs_y, optGenMatrix, xi*1e-6,yi*1e-6 );
%%%%%%%%%%%%%%%%%%%%%%%%%%%%%%%%%%%%%%%%%%%%%%%%%%%%%%%%%%%%%%%%%%%%%%%%

% Now ready to write the output data file...
disp(['Opening output file ' outputFile ]);

ogo = fopen(outputFile,'w');
if (ogo < 1)
    error(['Error opening file ' outputFile ' for writing.']);
end

fprintf(ogo, 'DF-ISE text\n\n');
fprintf(ogo, ...
    'Info {\n version      = 1.0\n type          = dataset\n dimension    = 2\n');
fprintf(ogo, ' nb_vertices = %d\n nb_edges    = %d\n nb_faces    = 0\n', ...
    numverts, numedges);
fprintf(ogo, ' nb_elements = %d\n nb_regions = %d\n datasets   = [ ', ...
    numelems, numregions);
for n=1:length(regionsToProcess)
    fprintf(ogo, "OpticalGeneration" ');
end
fprintf(ogo, ']\n functions = [ ');
for n=1:length(regionsToProcess)
    fprintf(ogo, 'OpticalGeneration' ');
end
fprintf(ogo, ']\n)\n\nData {\n\n');

for n=1:length(regionsToProcess)
    reqName = regionsToProcess{n};
    hasRegion = 0;
    for m=1:length(regionArray)
        if isequal( reqName, regionArray{m}.name )
            hasRegion=m;
            break;
        end
    end
    if (hasRegion)
        reg = regionArray{hasRegion};

        disp( ['Proessing Optical Generation for region ' reg.name '...' ] );
    end
end

```

```

    fprintf(ogo, ['Dataset ("OpticalGeneration") {\n function = '...
                'OpticalGeneration\n type           = scalar\n dimension = 1\n'...
                'location = vertex\n validity   = [ ' reg.name ' ]\n' ] );
    fprintf(ogo, ' Values (%d) {\n', length(reg.xdata) );

gdata = zeros(size(reg.xdata));
nl = 1;
for nv=1:length(reg.xdata)

    ogi = newoptgen(reg.xdata(nv), reg.ydata(nv));
    fprintf(ogo, ' %22e', ogi);
    gdata(nv) = ogi;
    nl = nl + 1;
    if (nl > 10)
        fprintf(ogo, '\n');
        nl = 1;
    end
end
if (nl > 1)
    fprintf(ogo, '\n');
end
fprintf(ogo, ' }\n}\n\n');

disp( [' ' num2str(length(reg.xdata)) ' processed' ] );
regionArray{hasRegion}.gdata = gdata;
end
end

fprintf(ogo, '\n\n');
fclose(ogo);
disp(['Finished writing output file ' outputFile ]);

disp(' ');
disp(['Copying from grid file: ' grdFile]);
copyfile(grdFile, outputGrid);
disp(['To grid file: ' outputGrid]);

disp(' ');
disp(['Exporting generation profile: ' exportFile ]);
save( exportFile , 'regionArray', 'numverts', 'numedges', 'numelems', 'numregions');

disp(' ');
disp('Processing complete!');

exit(0);

catch ME
    disp(ME);
    exit(1); %This will mark the node as 'failed' in SWB.
end

```


B.11 Solar spectrum weightings for discrete simulations

Table B.1. Discrete solar spectrum, 100 nm bins.

Wavelength		AM 1.5G		AM 1.5D	
Beam (nm)	Bin (nm)	P $\text{mW}\cdot\text{cm}^{-2}$	J_{ph} $\text{mA}\cdot\text{cm}^{-2}$	P $\text{mW}\cdot\text{cm}^{-2}$	J_{ph} $\text{mA}\cdot\text{cm}^{-2}$
350	(300–400)	4.792	1.353	3.193	0.901
450	(400–500)	14.059	5.103	11.625	4.219
550	(500–600)	15.093	6.695	13.374	5.933
650	(600–700)	13.898	7.286	12.572	6.591
750	(700–800)	11.302	6.837	10.331	6.249
850	(800–900)	9.440	6.472	8.758	6.004
950	(900–1000)	5.637	4.320	5.298	4.060
1050	(1000–1100)	6.444	5.457	6.084	5.153
1150	(1100–1200)	3.168	2.939	3.022	2.803
1250	(1200–1300)	4.300	4.335	4.111	4.145
1350	(1300–1400)	1.167	1.270	1.121	1.220
1450	(1400–1500)	0.701	0.820	0.682	0.797
1550	(1500–1600)	2.554	3.193	2.481	3.102
1650	(1600–1700)	2.209	2.940	2.149	2.860
1750	(1700–1800)	1.444	2.038	1.407	1.987
1850	(1800–1900)	0.023	0.034	0.022	0.033
1950	(1900–2000)	0.283	0.446	0.279	0.438
2050	(2000–2100)	0.688	1.138	0.678	1.120
2150	(2100–2200)	0.848	1.470	0.835	1.448
2250	(2200–2300)	0.699	1.268	0.690	1.252
2350	(2300–2400)	0.483	0.915	0.478	0.906

Table B.2. Discrete solar spectrum, 50 nm bins.

Wavelength		AM 1.5G		AM 1.5D	
Beam (nm)	Bin (nm)	P $\text{mW}\cdot\text{cm}^{-2}$	J_{ph} $\text{mA}\cdot\text{cm}^{-2}$	P $\text{mW}\cdot\text{cm}^{-2}$	J_{ph} $\text{mA}\cdot\text{cm}^{-2}$
325	(300–350)	1.416	0.371	0.817	0.214
375	(350–400)	3.246	0.982	2.272	0.687
425	(400–450)	6.192	2.123	4.925	1.688
475	(450–500)	7.779	2.980	6.606	2.531

Discrete solar spectrum, 50 nm bins

Wavelength		AM 1.5G		AM 1.5D	
Beam (nm)	Bin (nm)	P $\text{mW}\cdot\text{cm}^{-2}$	J_{ph} $\text{mA}\cdot\text{cm}^{-2}$	P $\text{mW}\cdot\text{cm}^{-2}$	J_{ph} $\text{mA}\cdot\text{cm}^{-2}$
525	(500–550)	7.642	3.236	6.708	2.841
575	(550–600)	7.460	3.460	6.667	3.092
625	(600–650)	7.198	3.628	6.500	3.277
675	(650–700)	6.719	3.658	6.087	3.314
725	(700–750)	6.006	3.512	5.467	3.197
775	(750–800)	5.318	3.324	4.884	3.053
825	(800–850)	4.874	3.243	4.510	3.001
875	(850–900)	4.575	3.228	4.256	3.003
925	(900–950)	2.652	1.978	2.488	1.856
975	(950–1000)	2.977	2.341	2.802	2.203
1025	(1000–1050)	3.470	2.868	3.269	2.703
1075	(1050–1100)	2.986	2.589	2.825	2.449
1125	(1100–1150)	1.190	1.080	1.134	1.029
1175	(1150–1200)	1.961	1.858	1.871	1.774
1225	(1200–1250)	2.259	2.232	2.157	2.131
1275	(1250–1300)	2.046	2.104	1.958	2.014
1325	(1300–1350)	1.186	1.268	1.140	1.218
1375	(1350–1400)	0.002	0.002	0.002	0.002
1425	(1400–1450)	0.123	0.141	0.119	0.137
1475	(1450–1500)	0.570	0.678	0.555	0.660
1525	(1500–1550)	1.289	1.586	1.252	1.540
1575	(1550–1600)	1.265	1.607	1.229	1.562
1625	(1600–1650)	1.154	1.513	1.121	1.470
1675	(1650–1700)	1.057	1.428	1.029	1.390
1725	(1700–1750)	0.892	1.241	0.870	1.210
1775	(1750–1800)	0.556	0.796	0.542	0.776
1825	(1800–1850)	0.023	0.033	0.022	0.033
1875	(1850–1900)	0.000	0.000	0.000	0.000
1925	(1900–1950)	0.014	0.022	0.014	0.022
1975	(1950–2000)	0.266	0.424	0.261	0.416
2025	(2000–2050)	0.309	0.504	0.304	0.496
2075	(2050–2100)	0.379	0.634	0.373	0.625
2125	(2100–2150)	0.448	0.768	0.441	0.756
2175	(2150–2200)	0.400	0.702	0.394	0.691

Discrete solar spectrum, 50 nm bins

Wavelength		AM 1.5G		AM 1.5D	
Beam (nm)	Bin (nm)	P $\text{mW}\cdot\text{cm}^{-2}$	J_{ph} $\text{mA}\cdot\text{cm}^{-2}$	P $\text{mW}\cdot\text{cm}^{-2}$	J_{ph} $\text{mA}\cdot\text{cm}^{-2}$
2225	(2200–2250)	0.374	0.671	0.369	0.662
2275	(2250–2300)	0.325	0.597	0.322	0.590
2325	(2300–2350)	0.276	0.517	0.273	0.512
2375	(2350–2400)	0.208	0.398	0.206	0.394

Listing B.5. MATLAB script for integrating/binning the solar spectrum.

```

function [totalinputcurrent totalinputpower centerpts beampwr specpwr ...
    beamphot warnstring] = spectralCalculator(bins, centerpts)
% spectralCalculator(bins, centerpts) Calculates the discrete weightings
% for optical simulations based on
% 'binning' a continuous reference
% spectrum (e.g. the solar spectrum)
% into individual 'beams'.
%
% Arguments:
% centerpts - (n) discrete wavelengths for simulations ('beams')
% Note: centerpts can be left empty to have the 'beam' wavelengths
% chosen automatically, in a manner which conserves energy as well
% as photon flux. (Arbitrarily chosen beam energies will not
% generally conserve power.)
% bins - a list of (n+1) wavelengths, specifying the wavelength range
% over which to sum photons for each 'beam'. The power of the nth
% beam is calculated by summing the photons from bins(n) to bins(n+1).
%
% Environment:
% The workspace must contain the global variable SPECADATA:
% (first column) - reference spectrum wavelengths (nm)
% (second column) - power spectral density (mW/cm2/nm)
% (third column) - photon flux spectral density (per cm2 per nm)
% See also: loadSpectrum.m
%
% Outputs
% totalinputcurrent - Photocurrent of reference spectrum within bin
% range (mA/cm2)
% totalinputpower - Power within binned range of reference spectrum
% (mW/cm2)
% centerpts - The wavelength of each 'beam' (nm)
% beampwr - The power of each 'beam' (mW/cm2)
% specpwr - The spectral power density of each beam
% (mW/cm2/nm)
% beamphot - The photon flux of each beam (per cm2 per s)
% warnstring - Diagnostic error message
%
% Example use:
% spectralCalculator([280 1100],800)
% ans =
% 43.7352
%%%%%%%%%%%%%%%%%%%%%%%%%%%%%%%%%%%%%%%%%%%%%%%%%%%%%%%%%%%%%%%%%%%%%%%%
global SPECADATA;

wl_ = SPECADATA(:,1);
phot_ = SPECADATA(:,3);

```



```
[FileName,PathName] = uigetfile('*.asc','Select spectrum data file');  
SPECDATA = load([PathName FileName]);  
  
%convert to mW/cm2/nm  
SPECDATA(:,2) = SPECDATA(:,2)*1000/100/100;  
  
%add col. for photons/cm2/nm  
energies = 1.24 ./ (SPECDATA(:,1)./1000) * 1.61E-19; %energy/photon (J)  
  
SPECDATA(:,3) = SPECDATA(:,2)./1000./energies;  
  
%add col. for photocurrent/cm2/nm  
SPECDATA(:,4) = SPECDATA(:,3).*1.61E-19;
```


SPCM instrument

In this thesis work, instrumentation and procedures were developed for performing *scanning photocurrent microscopy* (SPCM) measurements on single Si microwire devices. This characterization technique was employed in sections 4.5 and 5.3, and was also used to characterize carrier collection in wire-array devices by Brendan Kayes and Morgan Putnam in their thesis work. [39, 217] This appendix provides details on the operation of the SPCM instrumentation.

C.1 System description

In scanning photocurrent microscopy, a localized optical excitation source is scanned (rastered) along a photovoltaic or photoconductive device. The specimen current is recorded as a function of excitation position, producing spatially resolved maps of absorption and/or carrier collection within the device. Examples of SPCM can be found in nanowire research literature. [152, 155, 162, 156, 150, 154, 161, 153, 169] This technique is also widely used in photovoltaics research (typically with lower spatial resolution), where it is often referred as a *light-beam induced current* (LBIC) technique.

Our SPCM measurements were performed using a confocal microscope with near-field scanning optical microscopy (NSOM) capabilities (WITec AlphaS-NOM), located in the Molecular Materials Research Center of the Beckman Institute at Caltech. A simplified diagram of the instrument configuration and electrical connections is shown in Figure C.1.

Optical excitation source. A variety of excitation sources can be used for SPCM, however, most measurements are performed with a $\lambda \approx 650$ nm semiconductor diode laser (<5 mW continuous) that is dedicated for use with this instrument. The laser source is mounted on a kinematic stage with micrometer adjustments for pitch and yaw. The free-space beam path consists of an optical chopper system, turning mirrors, iris diaphragms, a variable neutral density filter (NDF) wheel, and a fiber coupler. A single-mode fiber is used to couple the laser source to the microscope. The fiber coupler uses a 10 \times objective with a numerical aperture (N.A.) of 0.2 to focus the collimated laser source onto the optical fiber. In our work, this provided low but adequate coupling efficiencies. The free-space optics are enclosed to prevent inadvertent disruption of (or exposure to) the laser source.

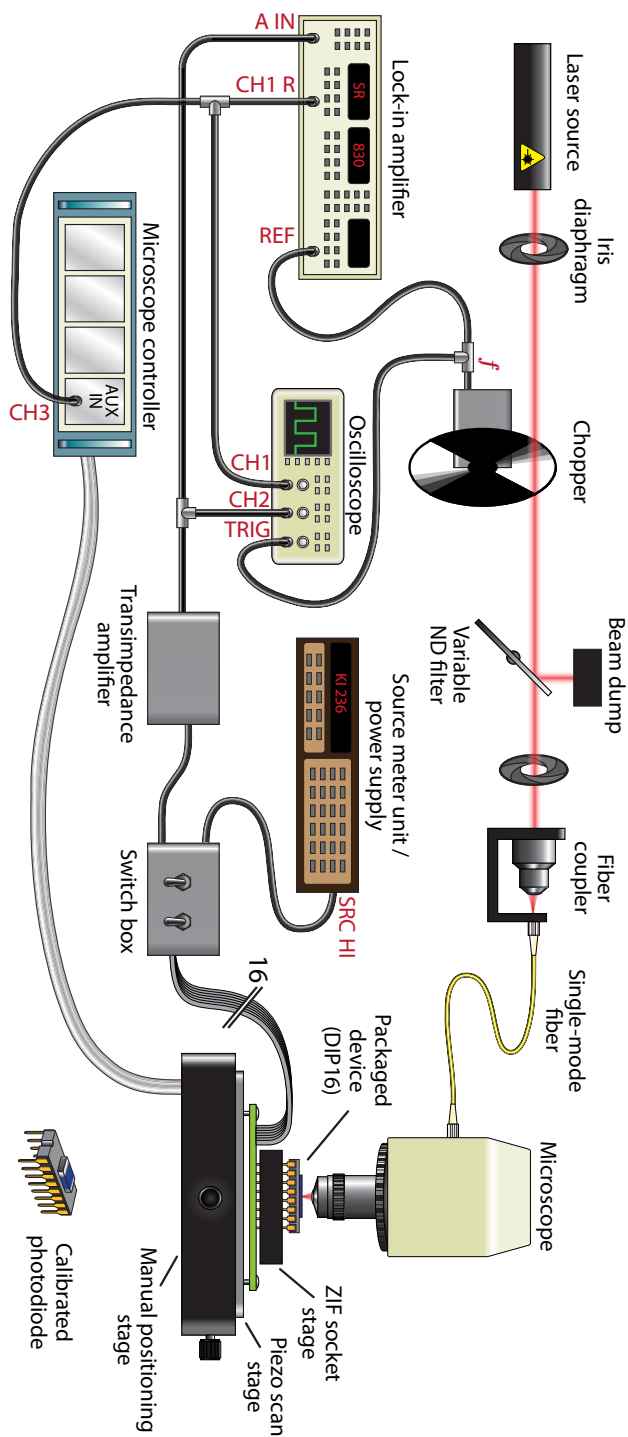


Figure C.1. Schematic illustration of SPCM instrumentation.

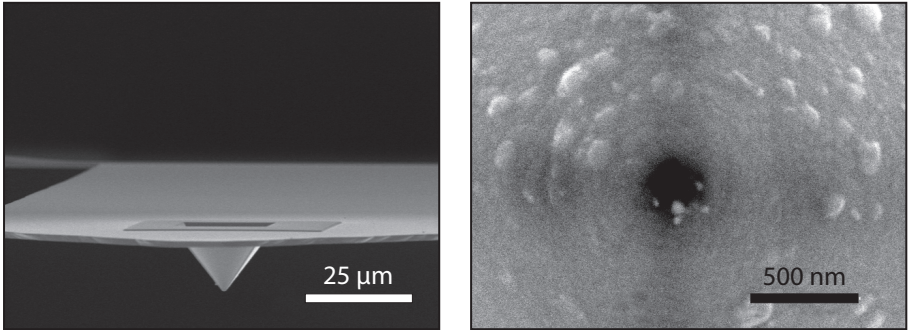


Figure C.2. Cantilevered NSOM tips. Left: side profile view. Right: aperture, enlarged to ~ 200 nm.

Microscope. The WITec alphaSNOM microscope system includes the microscope assembly as well as various controller modules, a support PC, and the software used to perform the experiments. Only the upper microscope optics are employed for our SPCM measurements. Broad-area illumination is provided by a variable-power halogen lamp, with condenser and field aperture diaphragms located in the upper microscope arm. Localized laser illumination is provided through an FC fiber port with an integrated focal adjustment micrometer. A 3-position beamsplitter assembly permits various combinations of broad-area and localized illumination. Reflection-mode imaging is provided by a color video camera located within the left eyepiece.

The microscope offers two excitation modes for SPCM (depicted in Fig. 4.14). For *confocal* excitation, the beam is focused to a diffraction-limited spot through the microscope objective. The minimum achievable beam waist is:

$$d_{\text{beam}} \approx \frac{0.6 \cdot \lambda}{\text{N.A.}} \quad (\text{C.1})$$

where λ is the free-space wavelength of the light source. The highest-resolution objective available for free-space SPCM measurements in our system is presently a 50 \times , N.A. = 0.95 lens (larger N.A. values are possible with oil immersion).

Higher resolution can be obtained using *near-field* excitation. In this mode, a cantilevered NSOM tip is mounted at the focal point of a 10 \times objective, with a small aperture aligned to the excitation beam. The NSOM tip is brought into contact with the specimen and scanned using a feedback loop (similar to atomic force microscopy). New NSOM tips have nominal aperture diameters of ~ 90 nm. To improve the transmission of light through the tips, the apertures can be intentionally enlarged using FIB milling. Figure C.2 shows an NSOM tip whose aperture was enlarged to ~ 200 nm in the course of this thesis work.

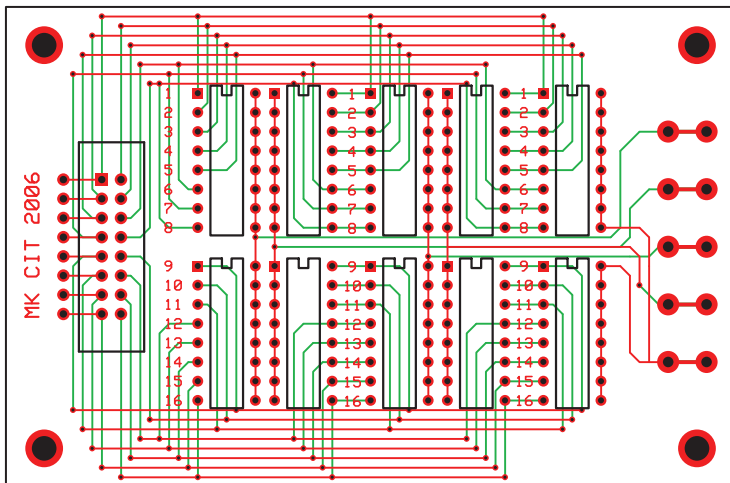


Figure C.3. Printed circuit board layout for SPCM switch box. The circuit connects a 16-pin ribbon-cable header or DIP socket (left) to five terminals (right) using ten 8-position DIP switches (center).

Specimen stage. The microscope system includes a manual x - y translation with $> 1''$ travel, as well as a piezo scan stage with $100\ \mu\text{m}$ of x - y travel. Bolted to the piezo scan stage is a low-profile sample holder that was built to enable microscopy on electrically contacted devices. The sample holder consists of an aluminum back-plate, a printed circuit board, and a 16-pin, zero-insertion-force (ZIF), dual-inline-pin (DIP) socket (3M, P/N 216-6278-00-3303). A 16-conductor ribbon cable connects the sample holder to the switch box located immediately beside the microscope stage.

Switch box. The switch box permits up to five terminals to be connected to the packaged device pins. For each terminal, a bank of DIP switches addresses which pin(s) are connected. A ‘grounding’ toggle switch is also provided for each terminal, which when closed, shorts the terminal to chassis ground. This provides some protection for loading/unloading of static-sensitive devices, and also provides a convenient way to ground one terminal of the device for short-circuit SPCM measurements. The printed circuit board for the switch box is shown in Figure C.3.

Transimpedance amplifier. The current preamplifier, or *transimpedance amplifier* (TIA), amplifies the specimen current by $10^7\ \Omega$ ($140\ \text{dB}\Omega$) to produce a detectable voltage signal for the lock-in amplifier (LIA). An active TIA enables much faster system response than a shunt resistor alone, and also provides a virtual ground for straightforward device biasing.

A schematic of the TIA is shown in Figure C.4. A low-noise, JFET-input-stage operational amplifier (OPA657, Texas Instruments) was chosen for its high gain-bandwidth product ($1.6\ \text{GHz}$) and low input bias current

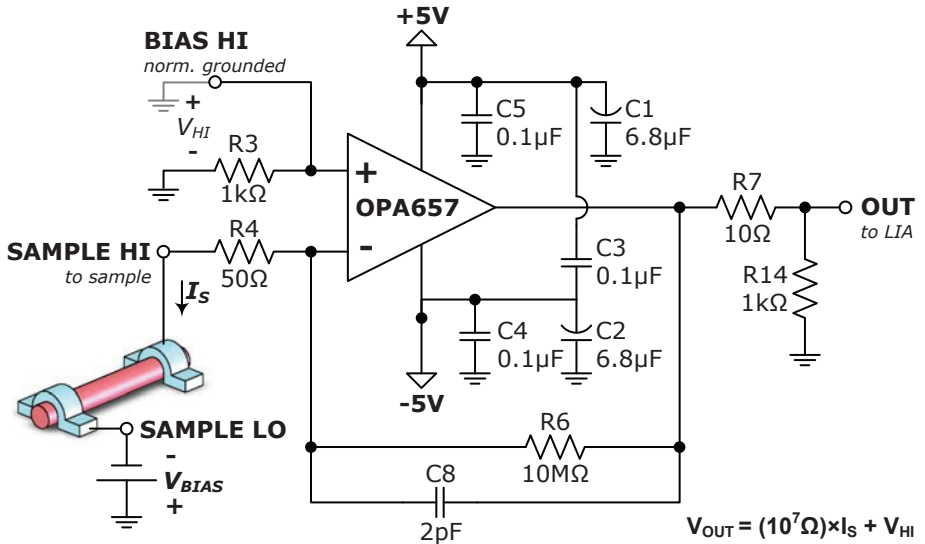


Figure C.4. Transimpedance amplifier circuit schematic.

(<2 pA). To reduce stray capacitance, the circuit was assembled on a high-speed evaluation board (DEM-OPA-SO-1A, Texas Instruments) using surface-mount components (SO-8 amplifier, 1206 SMD passive components), and was placed in a shielded enclosure. The chosen feedback capacitor value yields good response for single-wire devices and short cable lengths (linear response is observed up to 5 kHz, the maximum chop rate). This is suitable for smaller devices (e.g., 0.1 mm² solar cells) but becomes unstable for excessively high input capacitance or cable lengths. Our experience indicates that the practical noise floor for this TIA and specimen configuration (unshielded at room temperature) is ~0.1 pA of specimen photocurrent (using a 1 s time constant for lock-in detection). The TIA approaches saturation for specimen currents in excess of ~0.4 μA (including any dark current or non-chopped photocurrent), although the input stage of our LIA saturates shortly before this point.

Device biasing. The TIA input terminal serves as a virtual ground for the device under test (so long as the amplifier is not saturated). Most SPCM measurements are performed at short circuit (0 V bias) using the switch box to ground the opposite device terminal. If it is desired to bias the device while performing SPCM measurements (e.g., as required for photoconductive devices), the opposite device terminal can instead be connected to a suitable power supply (as shown in Fig. C.4). We typically used a source meter unit (236, Keithley Instruments) to provide specimen bias, which also enabled in situ I - V characterization for specimen currents below ~400 nA.

Lock-in detection and SPCM image formation. A digital lock-in amplifier (SR830, Stanford Research Systems) provides phase-sensitive detection and filtering of the specimen photocurrent. The analog output channel of the LIA (0–10 V full scale) is connected to an auxiliary input channel on the microscope controller.* During confocal (or near-field) microscopy scans, the microscope software is then configured to record the voltage on this input channel to form the SPCM image. A scaling factor can be specified within the software so that SPCM images are reported in terms of specimen photocurrent magnitude (i_D) rather than the LIA output voltage (V_{LIA}). The scaling factor can be calculated from the expression for the system gain:

$$V_{\text{LIA}} = 4.5 \frac{R_{\text{TIA}}}{V_{\text{sens}}} i_D \quad (\text{C.2})$$

where R_{TIA} is the gain of the transimpedance amplifier ($10^7 \Omega$) and V_{sens} is the sensitivity range of the LIA.

Calibrated photodiode. An encapsulated Si photodiode (Advanced Photonix, P/N PDB-C160SM), mounted in a DIP16 package, can be placed in the specimen stage to determine the incident beam photocurrent (i_{ph}) prior to each confocal SPCM session. The responsivity of the photodiode has been calibrated using our spectral response equipment (its external quantum efficiency is 0.67 at $\lambda = 650 \text{ nm}$). If the value of $V_{\text{LIA}}(i_{ph})$ is used as the scaling factor within the microscope software (instead of the system gain factor), then the resulting SPCM images appear in units of external quantum efficiency rather than specimen current.

C.2 Operating procedures

The following procedures were followed to perform SPCM measurements on single-wire devices in this thesis work. These are written to serve as instructions for future users. Typical conditions and instrument settings are shown in Table C.1.

Safety: *Proper laser safety protocol must be followed at all times. Particular attention is required whenever an eyepiece is used with the microscope (instead of or in addition to the video camera). High-power excitation sources should be turned off or disabled before looking into the microscope, and the eyepiece(s) should be removed prior to using dangerous illumination levels.*

Sample preparation: Devices are mounted and wire bonded in ceramic DIP16 packages (CSB01652, Spectrum Semiconductor Materials, Inc.). The device wafers are elevated within the cavity to sit flush with the top surface of the packages. (Recessed devices cannot be approached by short-working-distance objectives or NSOM tips.) Low-profile wire bonds are carefully placed so as not to interfere with contact-mode NSOM measurements (if

*The SR830 should usually be configured to display/output “R” on CH1.

desired), as well as to fit within the limited working distance of the higher-power microscope objectives. Oversize devices can be accommodated on custom circuit boards rather than ceramic packages. Alternatively, a small probe stage can be used in place of the DIP socket stage, permitting non-wire-bonded devices to be measured, but precluding the use of high-power objectives or near-field excitation.

Source alignment: The desired laser source is coupled into the microscope via a single-mode optical fiber. A dedicated fiber and fiber coupler are provided for the $\lambda = 650$ nm laser source. A second fiber coupler is available for other sources, requiring the selection of an appropriate single-mode fiber and coupling objective. A handheld fiber optic power meter (PM20A, Thorlabs) is used to maximize the coupling efficiency.

The ends of unused fibers are kept covered at all times because they are easily ruined by dust or scratches. Similar care is taken to protect the microscope objectives.

Specimen loading: The microscope arm is first fully extended (upwards) using the handheld controller (“focus up”) or the blue buttons on the microscope controller. The black knob at the base of the handheld controller determines the rate of motion. With the objective(s) rotated to the side, the device is inserted into the ZIF socket and the pins are tightened by rotating the actuator with a flathead screwdriver. The device should be mounted as level as possible, using shims if necessary. The objective is then brought into place and the device is coarsely positioned beneath it using the stage translation knobs. The appropriate pins are then selected by toggling the DIP switches within the switch box, completing the circuit to the transimpedance amplifier and bias source (if used).

Coarse focusing: The field aperture diaphragm is first contracted to ensure that its projection will cast an easily identifiable feature on the device, so that the focal plane can be identified even if no device features are present. The microscope arm is then lowered while monitoring the eyepiece video feed. The image increases in brightness as the focal point is approached,

Table C.1. Typical conditions and instrument settings for SPCM measurements.

Incident beam photocurrent (i_{ph})	100 nA
Chop rate (f)	180 Hz
LIA sensitivity (V_{sens})	1 V
LIA filter settings	Synchronous, $\tau = 1$ ms
Pixel delay time	10 ms
Pixel size	250 × 250 nm
Acquisition time	3–10 min

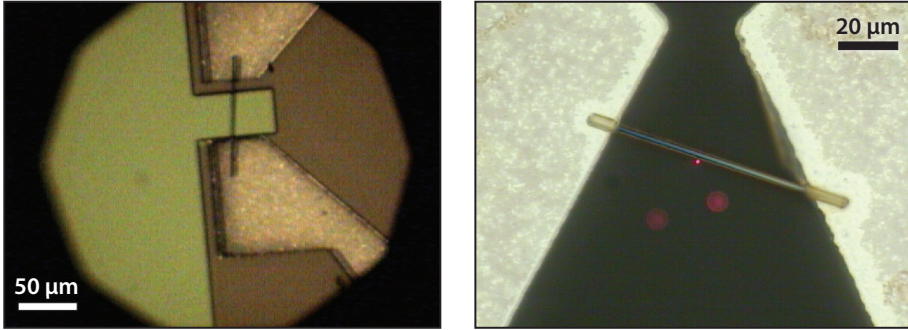


Figure C.5. Confocal SPCM focusing procedures. **Left:** the field aperture diaphragm is contracted to assist in coarse focusing (20× objective shown). The apparent astigmatism indicates a mild specimen tilt (corrected by shimming the lower left-hand side of the device). **Right:** for fine focusing, the beam is incident immediately adjacent to (but not striking) a single-wire device (50× objective shown). The two defocused beam spots are reflections from internal microscope optics and do not actually strike the specimen.

converging to an image of the field aperture when focused. The field aperture can then be dilated to provide a larger field of view. The device of interest is located using the stage translation knobs, the microscope arm is re-focused to produce optimal image quality in the eyepiece camera, and then the excitation beam is focused to a minimal apparent spot size using the focusing micrometer on the microscope’s fiber input port.

Lock-in configuration: With the beam incident on the device of interest, the illumination intensity and LIA settings are adjusted to produce the desired signal quality. For signals exceeding ~ 1 mV, the TIA output can be directly monitored on the oscilloscope (using averaging if necessary). The LIA sensitivity range (V_{sens}) is chosen so that illumination of the ‘brightest’ specimen area produces 40–90% of the full-scale reading. The LIA time constant and filter settings are chosen to yield the fastest response speed that still produces suitable output stability. We targeted an output stability of 1–2% over the course of several seconds, as displayed on the LIA front panel or observed on the oscilloscope. Our experience indicates that the LIA’s synchronous filter alone provides suitable noise rejection, permitting arbitrarily short time constants to be used in the normal filter stage.*

Fine focusing: The specimen stage is translated so that the laser spot narrowly misses an active device region (i.e., 1–2 μm away from the edge of a metal contact or to either side of a single-microwire device). While monitoring the LIA output channel on the oscilloscope (~ 1 s per division time

*This was true so long as the chopper wheel phase jitter was low. A 2-aperture chopper wheel yielded optimal performance in this regard.

base, zooming as necessary) the beam focus knob is then adjusted so as to produce the minimum LIA output value, corresponding to an optimal focusing of the beam into the inactive region of the device. If no minimum is found, the beam is visually re-focused and the procedure is repeated at a slightly different spatial location.

Scan configuration: The x - y piezo scanners are centered (“go to” tab in software) and the device is translated (using the stage knobs) so as to fit within the piezo scan range (indicated by the red square overlaid in the video feed). The scan parameters (width, height, timing, and pixel density) are specified in the microscope control software (first ensuring that the software is in ‘confocal’ mode). Within the input configuration tab (“ADC” button), the channel corresponding to the LIA output voltage (channel 3) must be selected, specifying the correct scaling factor if desired. The scan speed for SPCM measurements must not exceed the system response speed, which depends on the time constant and filter settings on the LIA. In general, the pixel delay time should be at least 6 times the LIA time constant value (for 24 dB/octave filtering). For synchronous filtering, the pixel delay time should be at least as long as the optical chopping period.

Upon starting each scan, the software automatically activates the APD within the lower microscope assembly. Users should ensure that the APD is protected from stray light sources prior to starting measurements.

Near-field excitation: Near-field SPCM measurements are performed with the microscope configured for NSOM. Briefly, the NSOM tip/objective assembly is installed and the excitation laser is coupled through the tip aperture. The deflection laser and photodiode are aligned and the feedback parameters are configured. The device is then coarsely positioned beneath the tip using the stage translation knobs, then the approach procedure is performed. Once in contact mode, the stage translation knobs should not be used. A coarse topography scan is performed to locate the device. The tip is then placed upon the active device region (using the software “go to” feature) to configure the LIA settings prior to SPCM scans.

C.3 Extended capabilities

The following types of experiments and equipment upgrades have been investigated or proposed in the course of this thesis work.

Excitation sources. As of this writing, the $\lambda = 650$ nm semiconductor diode laser remains the only permanently installed excitation source for SPCM measurements. However, the microscope’s fiber-coupled excitation port permits a broad range of potential excitation sources—for example, the $\lambda = 405$ nm laser that was temporarily installed in the course of this thesis work. In 2008, René de Waele et al. established a beam path for the use of a supercontinuum laser (Fianium SC400-series) as either a broadband or

tunable monochromatic excitation source. The supercontinuum laser itself is shared between several instruments (including our integrating-sphere photospectrometer); however, the optics and monochromator remain installed and available for use with the SPCM instrument. In theory, the SC400-series supercontinuum lasers provide useful excitation energy from $\lambda = 400$ nm to beyond $2 \mu\text{m}$. In practice, the accessible excitation wavelengths are limited by the microscope optics (most of which are optimized and AR-coated for visible wavelengths) as well as the optical fiber (which should support a single mode for optimal SPCM imaging). Furthermore, the microscope includes a series of beamsplitters and filters for the NSOM tip deflection laser ($\lambda \sim 780$ nm). These must be temporarily removed to enable near-infrared excitation or collection for confocal-mode SPCM measurements. Because the microscope controller provides front-panel access to analog signals within the system, a broad variety of experiments can be envisioned. For example, the “ z -height” DAC channel that is normally connected to the z -axis piezo driver, can instead be connected to a system that varies the excitation wavelength. In this configuration, instructing the software to perform a three-dimensional (height-resolved) confocal microscopy scan will instead collect a series of wavelength-resolved SPCM scans. We also note that excitation-source instabilities can be corrected by using an external reference photodetector to monitor the source intensity as a separate image channel. The specimen photocurrent image can be normalized to the source intensity image within the microscope software. A similar procedure was used to improve the accuracy of our integrating sphere photo spectrometer.

Probe stage. The combination of packaged (wire-bonded) devices and the low-profile DIP-socket SPCM stage provide a robust platform for high-resolution, low-noise SPCM measurements. However this approach is not feasible for all types of devices—such as the Si microwire-array solar cells fabricated by Morgan Putnam et al. (see Figure 6.1), which had fragile ITO top contacts that were not amenable to wire bonding. To enable SPCM measurements on these devices, Putnam built a small probe stage that can be affixed to the piezo scanner in place of the DIP-socket stage. This precludes the use of high-resolution objectives or NSOM tips, but nonetheless produces excellent results using a $20\times$ long-working-distance objective. A similar approach was employed to perform SPCM on micro-pillar solar cells fabricated by Brendan Kayes. [39, § 5.6]

Four-probe biasing. The devices studied in this thesis typically had low contact resistance that could be safely neglected in the analysis of the SPCM results. However, devices with larger contact resistance or more complex behavior can, in theory, be characterized by SPCM using a feedback loop to bias the device using separate source/sense electrodes (analogous to four-probe I - V measurements). Although such measurements could be performed using the same four-probe source-measure units used for our I - V measurements (Keithley 236), these instruments lack an analog output channel for direct interconnection to a lock-in amplifier or the microscope

controller's auxiliary input channels. The potentiostat employed in our photoelectrochemical absorption studies (Gamry Reference 600) seems to offer a promising combination of sensitivity, speed, and analog output capabilities. Alternatively, the design of our transimpedance amplifier could be modified to include the device segment enclosed by adjacent source/sense electrodes within its the feedback path; adding a differential voltage sensor across the feedback resistor to determine the specimen current.

Enlarged scan area. The utility of our SPCM instrument is presently limited by the $100 \times 100 \mu\text{m}$ x - y range of the piezo scanners—requiring many SPCM images to be manually stitched together to study even the small ($\sim 0.1 \text{ mm}^2$) microwire-array solar cells fabricated by Putnam et al. Future studies may benefit from a large-area scan stage. We note that this will also necessitate means to null or correct for specimen tilt. In our work it was difficult (but not impossible) to manually align the packaged devices within the focal plane of the microscope, requiring an iterative shimming/refocusing process to obtain suitable alignment over $100 \mu\text{m}$ length scales. A micrometer-driven tilt stage would likely be required to null specimen tilt over larger scan areas. Alternatively, specimen tilt could be corrected by varying the height of the z piezo stage as a function of x - y scan position. This can be easily accomplished by affixing the appropriate voltage dividers and adders between the analog (x,y) DAC channels and the z piezo driver, or by incorporating a similar correction within the software. A $1'' \times 1''$ scan stage and a controller module that supports tilt correction are offered by WITec.

Optical microscopy. Although the extent of our single-wire devices was directly evident from their SPCM images, the structure of other devices may prove more difficult to correlate with SPCM data. We note that confocal microscopy data can be recorded at the same time as SPCM data by connecting the microscope's APD or suitable photodetector to the reflection-mode confocal collection port. Confocal microscopy will provide substantially higher resolution images than the eyepiece video camera, and will circumvent any spatial mapping errors between the cursor positions on the video camera feed and the SPCM data within the software. Partially transparent devices would also permit transmission-mode confocal or near-field microscopy (with a clear-field stage). For planar devices with specular surfaces, this could (in theory) permit simultaneous measurements of reflection, transmission, and external quantum efficiency; all with the approximate resolution of confocal microscopy.

Spectrophotometer instrument

In this thesis work, the optical absorption of Si microwire arrays was characterized using a custom-built spectrophotometer instrument (see Chapter 3). Hemispherical reflection and transmission measurements were performed using an integrating sphere, and external quantum efficiency measurements were performed using a photoelectrochemical cell. This appendix provides details on the design and operation of the spectrophotometer instrumentation.

The spectrophotometer system consists of four basic components: A tunable light source, a motorized specimen stage, computer control software, and a light-detection system. All experiments share largely similar configurations for the light source, stage, and computer software; however, by changing the type or configuration of the light detection system, a variety of measurements are possible. The most commonly used light detection system consists of an integrating sphere with a photodiode, which can be configured for either *transmission mode* or *reflection mode* measurements. Alternatively, photovoltaic or photoconductive devices may themselves serve as the light detector—for example, using a photoelectrochemical cell to measure the external quantum efficiency (E.Q.E.) of a Si wire-array photocathode, thereby determining its optical absorption and charge-collection properties. For each measurement type, the computer software permits a variety of one- or two-dimensional parametric sweeps, including wavelength, incidence angle, and illumination position. The data acquisition software is written in LabVIEW (v.7, National Instruments), and can be easily extended to perform unforeseen types of measurements or parameter sweeps by those familiar with the programming environment.

Figure D.1 shows a simplified schematic of the spectrophotometer system configured for transmission-mode integrating sphere measurements. The diagram has not been drawn to scale, but does show the approximate position and size of the optical system components as viewed from above, and also shows the configuration of the electronic instrumentation located beneath the optics bench. The following sections discuss the components of the spectrophotometer system as they relate to each type of measurement. Step-by-step operating procedures are presented in section D.7.

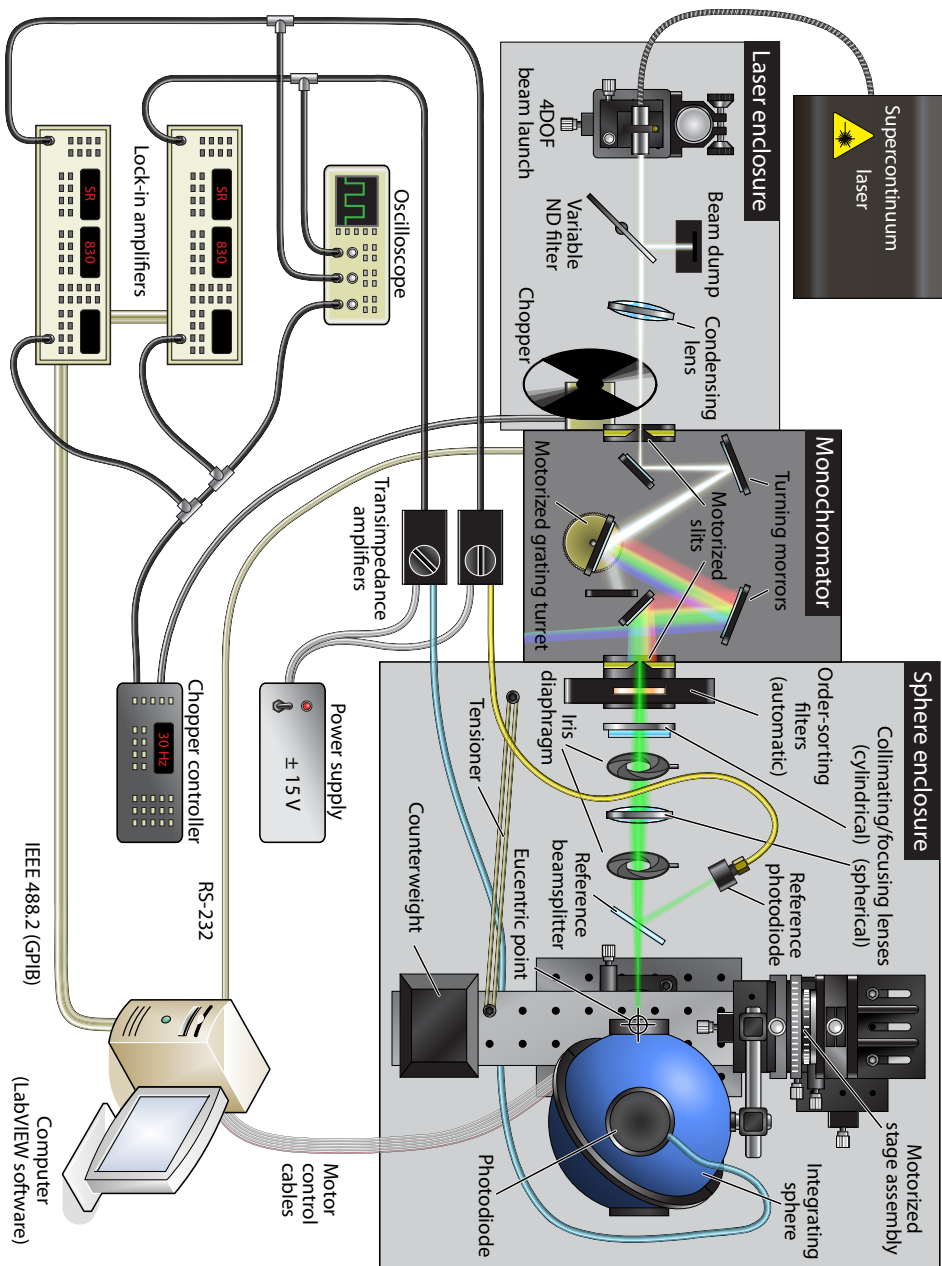


Figure D.1. Schematic illustration of spectrophotometer instrumentation.

D.1 Illumination source and optical path

Supercontinuum laser. A supercontinuum laser provides broadband (white) illumination in a highly collimated beam. For spectrophotometry, this enables a substantially greater combination of spectral, spatial, and angular resolution than possible using diffuse light sources (incandescent or arc lamps) of comparable power levels. Most measurements for this thesis were performed using a 2 W* “blue-enhanced” supercontinuum laser (Fianium SC400-2). This laser is rated to produce $>1 \text{ mW}\cdot\text{nm}^{-1}$ of spectral power density from $\lambda < 420 \text{ nm}$ to $\lambda > 2 \text{ }\mu\text{m}$, and in our system, can be used for measurements from $\lambda \sim 400 \text{ nm}$ to $\lambda \sim 1800 \text{ }\mu\text{m}$ (limited by detector sensitivity at longer wavelengths). A 4 W, “standard” spectrum laser (Fianium SC450-4) is also available for use, which provides slightly higher illumination power at most wavelengths, but whose useful spectral range does not extend below $\lambda \sim 450 \text{ nm}$. The increased power level might be useful for performing measurements with extreme spectral resolution; however in typical operation modes, the accuracy of measurements is not limited by a lack of source intensity. Either supercontinuum laser must be operated at full power to achieve the rated spectral range. The supercontinuum lasers can be connected to the computer via a serial port (over USB) for diagnostic purposes, but are generally operated manually.

Note: The supercontinuum lasers are damaged if light is allowed to reflected back into the source. For this reason, all optics in the source beam path are intentionally tilted slightly off-axis to prevent the specular beam reflection from re-entering the laser.

Laser enclosure. The high-power beam path is fully enclosed to prevent accidental exposure to (or disruption of) the supercontinuum laser source. The enclosure is only opened for initial beam alignment, or to attenuate the source brightness using a variable neutral-density (ND) filter wheel. The chopper wheel assembly is bolted to the input flange of the monochromator within the laser enclosure.

Monochromator. The supercontinuum laser source is coupled into a 1/4 m grating monochromator (Oriel MS257). The monochromator features motorized input/output slits, a 4-position motorized grating turret, and an automatic order-sorting filter assembly. The operation of this monochromator is controlled from the computer via RS-232 (serial port) communication. During measurements, the monochromator controller will automatically select the appropriate order-sorting filter for each wavelength. However, our spectrophotometry software does not explicitly instruct the monochromator to alter the grating or exit slit width settings. Users may manually select the appropriate grating and

*The power ratings reflect the continuous optical output power. Although we consider the illumination to be continuous here, the output from the supercontinuum lasers is in fact pulsed (20 MHz for the 2 W unit, 40 MHz for the 4 W unit).

Table D.1. Monochromator gratings.

Position	Line density (per mm)	Blaze wavelength (nm)	Max wavelength (nm)
1	150	800	11,200
2 ^a	1200	350	1400
3	1200	750	1400
4	600	1000	2800

^a Used in this work.

Table D.2. Monochromator passband values for symmetric entrance/exit slits.^a

Slit width (μm)	Passband ^b (nm)	
	1200-line grating	600-line grating
2000	6.5	12.9
1000	3.2	6.5
500	1.6	3.2
320	1.0 ^c	2.1
100 ^d	0.32	0.65
50 ^d	0.16	0.32

^a This assumes that the illumination source fills the entrance slit. In our system, the effective input slit width is actually the minimum of either the mechanical slit width or the width of the focused laser beam. The reported passband values are thus upper limits.

^b The passband varies slightly with wavelength. Peak values are shown.

^c Typical operating conditions.

^d With the present condenser lens, the beam cannot be focused to pass through such narrow entrance slit widths. Reflections from the beam striking either side of the slits could damage the laser source.

slit width before beginning measurements, or instruct the monochromator controller to automatically select the grating based on user-programmable crossover points. The monochromator can also be operated in “constant passband” mode, in which the controller modulates the slit width depending on wavelength. Our measurements typically use a fixed exit slit width of 320 μm and a 1200 line/mm grating, which provide a ~ 1 nm passband and excitation to $\lambda = 1400$ nm. The available gratings are listed in Table D.1, and typical system passband values are listed in Table D.2.

A lens focuses the laser source beam between the entrance slits of the monochromator, at an estimated focal ratio of F/30. This under-fills the

monochromator's grating optics (F/3.9) but produces a less divergent beam at output. From a bandpass perspective, the size of the focused laser spot at the entrance port (estimated $< 300 \mu\text{m}$) serves as the effective entrance slit width. The physical input slits are kept slightly wider than the beam (typically fixed at $320 \mu\text{m}$) so that the laser beam can be easily focused without striking either side of the slit. This prevents reflection of light from the slit assembly, which could be destructive to the laser source or the eyes of an observer. Because of this potential hazard, the input slit motors are normally disabled (unplugged) to prevent inadvertent closure of the slits during alignment (or, for example, during system power-up routines).

Sphere enclosure. The illumination beam path and the motorized stage assembly are fully enclosed to prevent stray light from entering the light detection system. This was originally necessitated because measurements were performed at D.C. Measurements are now performed using chopped illumination with phase-sensitive detection, which rejects most stray light. However the system's light detectors are extremely sensitive, and typically saturate due to stray illumination at levels well below that of ambient room lighting.

Collimating/focusing optics. A series of lenses and apertures collimate and focus the monochromatic light beam to produce the desired spot size striking the specimen. The adjustable aperture diaphragms are mounted on micrometer-driven bases for precise positioning. With the diaphragms fully contracted, the two-lens configuration shown in Figure D.1 can produce a beam spot size of $\sim 1 \text{ mm}$, although other lens configurations can produce much smaller beam sizes at shorter working distance. For example, Figure D.2 shows a two-dimensional spatial transmission map performed using a $10\times$ microscope objective to focus the illumination to a $< 200 \mu\text{m}$ beam spot size at the entrance of the integrating sphere. Several polarizing filters are also available for insertion in the beam path near the exit of the monochromator. Explicit control of the polarization state is generally required for varied angle-of-incidence measurements (particularly for planar structures).

Reference detector. A reference photodiode continuously monitors the relative illumination intensity during measurements.* By normalizing the specimen response to the relative incidence intensity (see, e.g., equation D.1), the effects of virtually all fluctuations in source intensity can be eliminated. This greatly improves the accuracy of the spectrophotometer system, as the output spectrum of the supercontinuum source can potentially drift during the course of measurements (some of which can last several (>12) hours).

The reference detector assembly includes the beam splitter (microscope slide cover slip), the photodiode, and a baffle to prevent light reflected from the

*The *reference detector* should not be confused with *reference-position measurements*. The reference detector is used at all times—for both reference- and specimen-position measurements.

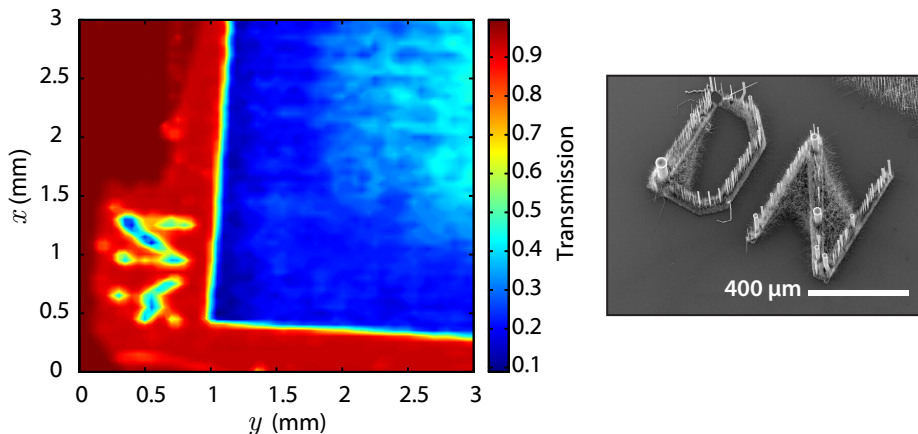


Figure D.2. Spatial transmission map of the edge of a Si wire-array film obtained using a $10\times$ microscope objective to focus $\lambda = 550$ nm illumination to a spot size of <200 μm at the entrance of the integrating sphere. The wire array's fiducial markings ("YN") can be seen. Right: SEM image (45 tilt) showing the structure of similar fiducial markings on a *different* wire array ("DN"). (The actual fiducial markings on the "YN" array were not imaged by SEM.)

specimen from striking the detector. In order to minimize interference with the rotation of the specimen stage, the beam splitter and baffle are mounted on an adjustable arm protruding from the diode. Two interchangeable reference diodes are available: a 3.6×3.6 mm Si photodiode (Thorlabs SM05PD1A) for $\lambda = 400$ nm to 1150 nm, and a $\phi 3.0$ mm Ge photodiode (Thorlabs SM05PD6A) for $\lambda = 800$ nm to 1800 nm.

In this thesis work, reference-detector normalization eliminated all measurement artifacts due to varying source intensity except for a region of anomalous behavior near $\lambda = 1064$ nm, the wavelength of the supercontinuum lasers' master source. Our approach was to "deglitch" the measured data by discarding measurements near $\lambda = 1064$ nm and interpolating the values from either edge of the anomalous behavior (typically ± 5 nm to ± 20 nm). The master source of the SC400-2 laser has recently been replaced, and preliminary measurements seem to indicate that the source of the artifact has been largely reduced.

The above components provide a referenced, monochromatic illumination beam for spectrophotometry measurements with a high degree of specular and spatial resolution. Figure D.3 plots the normalized reference photodiode signal observed during typical measurements performed in the course of this thesis. Our experience indicates that accurate measurements can be obtained when the signal levels are within ~ 60 dB of the peak value. The dynamic range of the system is presently limited by stray (broadband) light transmission through the monochromator (rather than the detection instrumentation).

For example, measurements performed at $\lambda < 400$ nm can produce seemingly stable readings from the photodiodes despite a lack of excitation energy at these wavelengths. This does not indicate that valid measurements can be obtained for these wavelengths—the system is simply measuring the stray light passing through the monochromator. Care must be taken not to attempt measurements beyond the spectral range of the source or detectors. Cleaning the monochromator optics by prove useful in extending the dynamic range of the system.

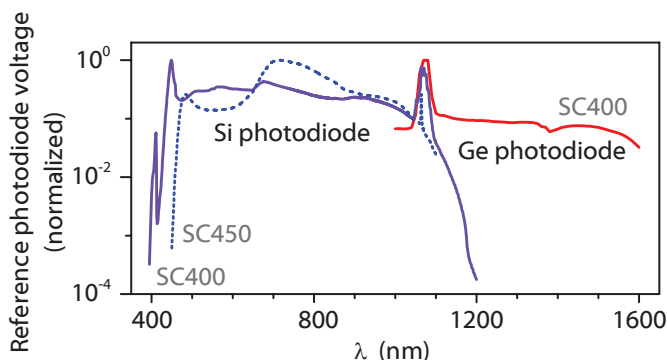


Figure D.3. Illumination spectra for spectrophotometry measurements. Spectra are plotted for both supercontinuum lasers and both reference photodiodes.

D.2 Specimen stage

The stage assembly enables specimen to be translated and tilted in two dimensions within the beam path. This requires four axes of kinematic articulation: a pair of rotation axes (Azimuth, Elevation) for specimen tilt, and a pair of linear translation axes (A_y , E_y) for specimen translation. Four additional axes of kinematic articulation are provided to align the system in a feasible manner. A pair of linear translation axes (A_d , E_h) permit each rotation axis to be aligned to the incident beam, and another pair of linear translation axes (A_x , E_x) permit the specimen to be aligned to the system eucentric plane. Table D.3 summarizes the type and purpose of each axes of the specimen stage. The specimen stage axes are illustrated in Figure D.4, as well as in the sections describing integrating sphere measurements (Figs. D.6 and D.7) and photoelectrochemical measurements (Fig. D.9).

Eucentric alignment is a key requirement for angle-resolved spectrophotometry measurements on small or nonhomogeneous specimen. Once eucentric alignment is reached, the specimen can be independently tilted and translated without affecting the beam focal length: tilting does not change the point of beam incidence on the specimen, while translation does not affect the beam incidence angle. In theory, the eight-axis stage configuration should be able to produce

Table D.3. Specimen stage axes.

Axis	Type	Operation (typ.)	Purpose
A_d	Linear	Manual ^a	Beam alignment ^b
E_h	Linear, 1''	Motorized	
A_x	Linear, 1''	Manual	Eucentric alignment
E_x ^c	Linear, 1/2''		
A_y (y) ^d	Linear, 1''	Motorized	Specimen translation
E_y (x) ^{c,d}	Linear, 1/2''	Manual ^e	
Azimuth (θ_y) ^d	Rotation	Motorized	Specimen tilt
Elevation (θ_x) ^d			

^a A_d is adjusted by sliding the entire stage assembly within guides at its base.

^b E_h is typically used instead of E_x for normal-incidence specimen translation due to the greater range and speed of the 1'' stage.

^c Not used for reflection mode.

^d Over the years, our convention of (θ_x, θ_y) and (x, y) has varied with respect to elevation and azimuth.

^e E_y is nominally motorized, but has been disconnected due to a lack of a functioning controller channel.

perfect eucentric alignment. In practice, system lash (free play) and misalignment will limit the degree to which true eucentric alignment can be reached. The primary mechanical culprit limiting tilt eucentricity is the shaft runout of the rotation axes. To reduce shaft runout, the azimuth axis is counterweighted to minimize the load imbalance over the rotation stage. Similarly, when the elevation rotation stage bears a heavier load (e.g., the integrating sphere assembly for transmission-mode measurements), a tensioning spring can be affixed to the sphere pivot point to alleviate the some or all of its weight. When maximal eucentric alignment is required (i.e., for the smallest specimen), some of the linear translation stages (E_x , E_y) can be removed, as each stage inevitably introduces mild hysteretic free play into the system. (Note, however, that alignment will be more difficult without these micrometer-driven translation stages.) With careful counterbalancing and specimen alignment, we have achieved two-dimensional eucentric positioning yielding < 2 mm of beam spot variation at the specimen, over the rotational limits of both tilt stages. Achieving one-dimensional eucentric alignment is generally much easier.

The resolution of the specimen stage is also limited by mechanical free play and hysteresis. Individually, each stage has relatively tight mechanical tolerance, but combined, the seven kinematic stages can lead to significant free play at the specimen. To mitigate lash, each rotational stage is tensioned with a rubber band during measurements. This yields $< 0.1^\circ$ of bi-directional repeatability in angular positioning. The linear translation stages are preloaded with internal

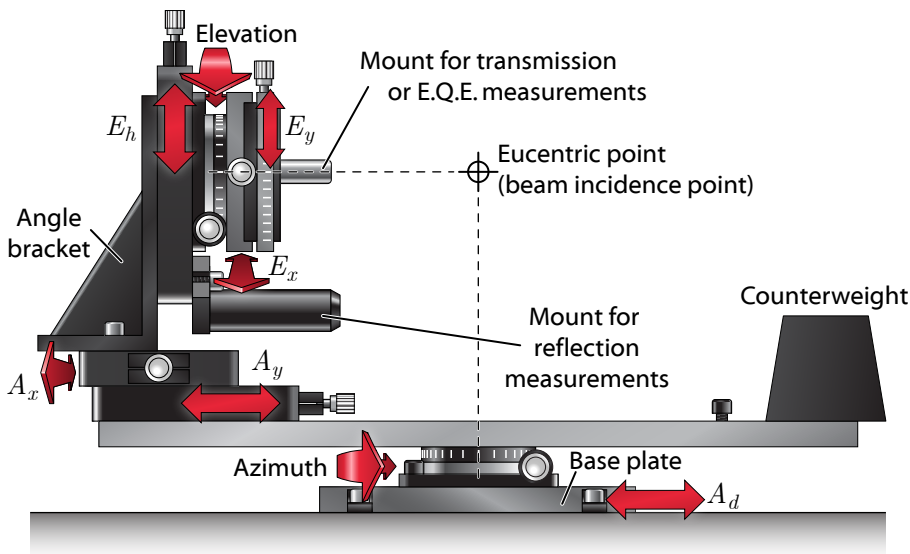


Figure D.4. Specimen stage (front view).

springs, and the more problematic axes have been outfitted with rubber-band tensioners to reduce out-of-plane lash. Hysteresis is largely mitigated by performing standard monotonic (vs. serpentine) rasters for two-dimensional scans. As shown in Figure D.2, we have achieved x - y positioning with apparent resolution of $<200\mu\text{m}$. In general, the lateral resolution of the system is limited by the size of the beam spot rather than the positioning accuracy of the specimen stage.

All rotation and linear translation stages are capable of motorized operation, depending on experimental requirements. The motorized axes are operated from the computer using an 8-channel PCI motor control card (DCX-PCI 100 Series Motion Controller, PMC). The rotation and $1/2''$ linear translation stages share interchangeable motors, as do all $1''$ linear translation stages. It appears that only four channels of the motor control card are operational following a recent failure of the computer's power supply. Manual micrometers can be installed in place of the motor-driven units on any of the $1''$ linear stages, and the worm-gear mechanisms of the rotation and $1/2''$ stages can be turned by hand using an appropriate hex key at the end of the shaft opposite the planetary gears.

D.3 Detection instrumentation

The following instrumentation is employed to perform spectrophotometry measurements. An overview of the equipment configuration is shown in Figure D.1.

Optical chopper. The optical chopper wheel is attached to the monochromator input slit assembly using a standard 1.5" flanged connection. The front panel of the chopper controller (Newport 75150) provides controls to adjust the chop speed. The "stop open" and "stop closed" buttons are particularly useful for alignment procedures, and can be used to temporarily block the beam without turning off the laser or opening the source enclosure. Measurements are typically performed at a chop frequency of $f = 30$ Hz. A two-aperture chopper wheel is used to minimize cyclic phase jitter.

Transimpedance amplifiers. A pair of transimpedance amplifiers (TIAs; DL Instruments Model 654) provide adjustable biasing (0 to -10 V) and gain (10^4 to 10^{10} Ω) for the reference and specimen photodetectors.* The amplifiers are powered by an external ± 15 V D.C. power supply.

The TIA gain is set using switches on the amplifier housing. Generally, measurements benefit from using the highest gain settings that provide adequate time response and avoid saturation of the lock-in amplifiers at the peak signal value.[†] In practice, the gain almost never needs to be adjusted, due to the fixed operating range of the instrument and high dynamic range of the lock-in amplifiers. Typical hemispherical reflection and transmission measurements (using Si photodiodes) are performed with gain settings of 10^5 Ω for the reference photodiode and 10^7 Ω for the integrating sphere photodiode. The gain might need to be adjusted if switching photodetectors (Ge vs. Si), substantially increasing or decreasing the illumination intensity, or if changing the detection configuration (e.g., for solid-state E.Q.E. measurements, in which the specimen-channel TIA can be connected to a photovoltaic or photoconductive device rather than the integrating-sphere photodiode).

Note: *The system is unaware of the TIA gain settings and does not correct for them. If the gain settings are changed between the specimen-position and reference-position measurements, the data will need to be manually corrected.*

The photodiode bias can be adjusted by turning a small potentiometer accessible through the side of the TIA housing. Reverse-biasing the photodiodes can improve their linearity, sensitivity, and speed; but also increases their dark noise. A bias is also required to measure the response of photoconductive devices. We generally obtain better system performance *without* reverse-biasing the photodiodes; thus, the bias is normally set to 0 V for both TIAs. However, users should check the bias before connecting the amplifiers to sensitive devices.

The bias voltage is applied to the *outer* conductor of the amplifiers' "current input" BNC connectors. For this reason, it is most convenient to measure the bias with a handheld multimeter, as most benchtop equipment measures the

*A potentiostat is used in place of the specimen-channel TIA for photoelectrochemical measurements.

[†]The input stage of the lock-in amplifiers will overload before the TIA amplifiers saturate.

voltage of the *inner* conductor while grounding the outer.* It is also important that the photodiodes do not form a chassis ground loop through the outer BNC conductor (common for laboratory equipment). Because the TIAs can only supply negative bias voltages, it is necessary to select the correct photodiode polarity to enable reverse-biasing. A small “coaxial polarity reverser” can be attached to the TIA input connector to reverse-bias some of the photodiodes.

Oscilloscope. An oscilloscope monitors the signals from the transimpedance amplifiers (or from the potentiostat for photoelectrochemical measurements). Observing the signal waveforms is generally only required for alignment or diagnostic purposes. Both detector channels should appear as nondistorted square waves on the oscilloscope display. Averaging is helpful to resolve weaker signals.

Lock-in amplifiers. A pair of digital lock-in amplifiers (LIAs; Stanford Research Systems SR830) measure the signals from the reference and specimen photodetectors. The operation of these instruments is similar to that described for SPCM measurements in section C.2. Unlike the SPCM system, however, the spectrophotometer system interacts with the LIAs digitally, using the IEEE 488.2 bus (GPIB). This enables our spectrophotometry software to employ an adaptive algorithm (described below) to dynamically adjust the integration time and sensitivity range during measurements. This results in greater dynamic range and also alleviates the need to select a fixed sensitivity range for the LIA. For most measurements, the user need only select the desired time constant prior to beginning measurements—the other settings will be adjusted by the computer.† In this thesis work, most spectrophotometry measurements used second-order filtering with a time constant of 30 or 100 ms (in addition to synchronous filtering) on both LIAs.

LIA measurement algorithm. Although the computer communicates with the lock-in amplifiers digitally, the measurement resolution can still be limited by the sensitivity range of the LIAs. For example, using the 1 V sensitivity range, the LIAs do not report measurements with enough digits to resolve μV signal levels. Because the detector signals can vary over several orders of magnitude during wavelength sweeps, it is difficult to select a fixed sensitivity range for spectrophotometry measurements: choosing too low a sensitivity range will cause the LIAs to overload at “bright” wavelengths, while choosing too high a sensitivity range will produce inaccurate or noisy measurements for “dim” wavelengths. Thus, it is useful to dynamically alter the range of each LIA during measurement sequences.

Another dilemma facing lock-in measurements is the relatively long integrating time required to filter the D.C. output from the phase sensitive detector.

*If the impedance of the multimeter is not high enough, the TIA will saturate when it is connected to the input terminal. If so, the TIA gain should be temporarily reduced to prevent saturation when adjust the bias.

†The LIA’s input configuration and filters must also be set manually; however, these settings are not normally changed.

As a rule of thumb, a LIA require 5 time constants (per filter stage*) for the reading to settle to within 1% of its final value (from its *initial* value). However during spectrophotometric scans, there are many wavelength ranges where the signal values change only slightly between consecutive wavelengths. As an example, consider a transmission measurement where the signal values change by 2% between consecutive wavelengths. If 1% *absolute* accuracy is desired, the LIA reading need only settle to within 50% of its final value—which occurs in less than 1 time constant. Thus, by carefully monitoring the stability of the LIA output, it is possible to eliminate most of the integration (delay) time in “smooth” spectral regions, while still providing sufficient settling time in spectral regions where the signals vary greatly between consecutive data points.†

The above observations motivated our development of an adaptive measurement subroutine for the SR830 lock-in amplifiers. The algorithm is implemented in LabVIEW and is used by most of the spectrophotometer data acquisition programs, as well as in other instruments developed by this author. The subroutine begins by determining the LIA time constant setting, τ . When a measurement is requested, the LIA is polled every τ seconds until a minimum number of consecutive measurements (by default, 3) agree within a certain *settling threshold* (by default, 0.2%), in which case the average of the three values is returned. Measurements are repeated until suitable agreement is obtained, or by default, for up to 10 time constants per filter stage, after which the latter half of the readings are averaged to produce the result. The extended averaging time improves the accuracy of measurements for very weak signals, without slowing down the response speed for stronger signals.

During the measurement sequence, the program also adjusts the LIA sensitivity so that at least 10% (by default) of the full scale is utilized, ranging as low as 10 μV by default. The range is immediately increased whenever an overload condition occurs, discarding several subsequent readings before resuming the measurement procedure. If a continuous overload is registered on the maximum sensitivity range (1 V), a system error is issued (by default, halting the top-level program). To prevent range hunting, an overload-induced range-up operation will disable any subsequent range-down operations.‡ The subroutines are written to permit asynchronous (simultaneous) reading of both lock-in amplifiers. Using this algorithm, the typical duration of spectrophotometry measurements was halved with no noticeable loss of accuracy for several control specimen. In fact, the extended averaging helps reduce the noise in regions of weak signal intensity.

*Each low-pass filter stage provides 6 dB/oct roll off. Thus, selecting 12 dB/oct filtering utilizes 2 filter stages, and requires ~ 10 time constants to settle by this rule of thumb.

†A long integration time is also required in “smooth” regions if the signal is temporarily interrupted, e.g., when the order-sorting filter wheel is rotated between certain wavelengths, or following a LIA overload/uprange sequence.

‡If the overload-induced range-up operations place the instrument in a sensitivity range where the algorithm would normally range-down, a warning is issued, suggesting that the user either increase the dynamic reserve setting on the LIA, or increase the minimum permissible range for the auto-ranging algorithm. This condition does not affect the validity of measurements.

The LIA measurement settings typically require no user attention, as the default settings have thus far proven effective for all measurement types. This usually enables “hands-free” configuration of the detection instrumentation. However, users should be aware of the following:

- During measurements, it is normal for the LIAs to momentarily overload in the course of auto-ranging. This will not affect measurement accuracy.
- Selecting too short a time constant on the LIAs can actually *increase* the duration of measurements with this technique. The time constant must be chosen to yield a continuous output stability well within the settling threshold for the adaptive algorithm. If faster, less-accurate measurements are desired, the settling threshold should be increased appropriately. Optimal performance is obtained when the majority of measurements are resolved by quickly satisfying the settling criteria, rather than by extended averaging.
- Many of the spectrophotometry programs include a *delay time* setting (typically 100 ms). This is to ensure that the monochromator/stage motors have stopped moving prior to beginning the measurement subroutine. Users do not need to add lock-in settling delays to this value.

If needed, non-default settings for the adaptive algorithm can be specified within the LabVIEW data acquisition programs.

D.C. measurements. Measurements can also be performed under continuous (nonchopped) illumination by using a pair of D.C. current meters to monitor the photodetector signals. A version of the data acquisition software has been written to monitor the reference and specimen detectors with Keithley model 6430 and 487 current meters. D.C. measurements typically require longer integration times than those performed with chopped illumination and phase-sensitive detection.

D.4 Integrating sphere

Hemispherical transmission and reflection measurements are performed using a 4" integrating sphere that is affixed to the specimen stage to enable motorized tilt and translation. Figure D.5 depicts the internal sphere configuration for either type of measurement.

Sphere. The 4" integrating sphere has four ports: three 1" and one 1/2". All internal sphere components are coated to achieve near-ideal Lambertian reflectance. The sphere itself has been professionally recoated (Labsphere Spectrafect, 12/2009). The other (custom) parts have been sandblasted, cleaned, and coated with a BaSO₄ paint in our labs (Labsphere 6080 White Reflectance Coating).

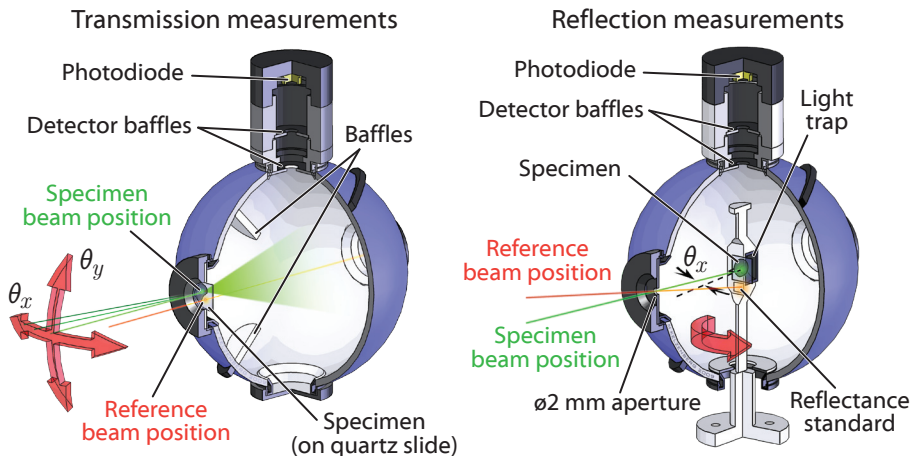


Figure D.5. Internal configuration of integrating sphere. Left: transmission measurements. Right: reflection measurements.

Baffles. The sphere originally included a single baffle that is attached with a screw through the side of the sphere. The second (lower) baffle for transmission measurements consists of a piece of sheet metal that is sandwiched between the sphere halves. Due to the frequent need to open the sphere when changing between transmission and reflection modes, we usually fasten the two halves together using binder clips rather than screws.

Photodiode assembly. The photodiode assembly consists of a photodiode and a series of adapters and baffles required to achieve the desired acceptance angle of light from within the sphere. Some of the custom-machined parts are depicted in section D.8.2. Two photodiodes are available for use with the integrating sphere: a 1 cm^2 Si diode (Newport 818-UV) for wavelengths up to $\sim 1170 \text{ nm}$, and a 0.071 cm^2 ($\phi 3.0 \text{ cm}$) Ge diode (Newport 818-IR) for wavelengths ranging from $\sim 800 \text{ nm}$ to $\sim 1800 \text{ nm}$. Both photodiodes mount to the photodiode assembly via $1''\text{-}40$ threads.

Note: The polarity of the 818-series integrating sphere photodiodes has been reversed to avoid a ground loop condition when biased using the transimpedance amplifier.

D.4.1 Transmission measurements

Figure D.6 depicts the configuration of the integrating sphere and specimen stage used to perform hemispherical transmission measurements. The sphere is attached to the E_y axis stage using a preassembled $1/2''$ post assembly identified as the “transmission mount.” Both baffles are installed for transmission measurements, and the photodiode is attached to the $1/2''$ port using the custom

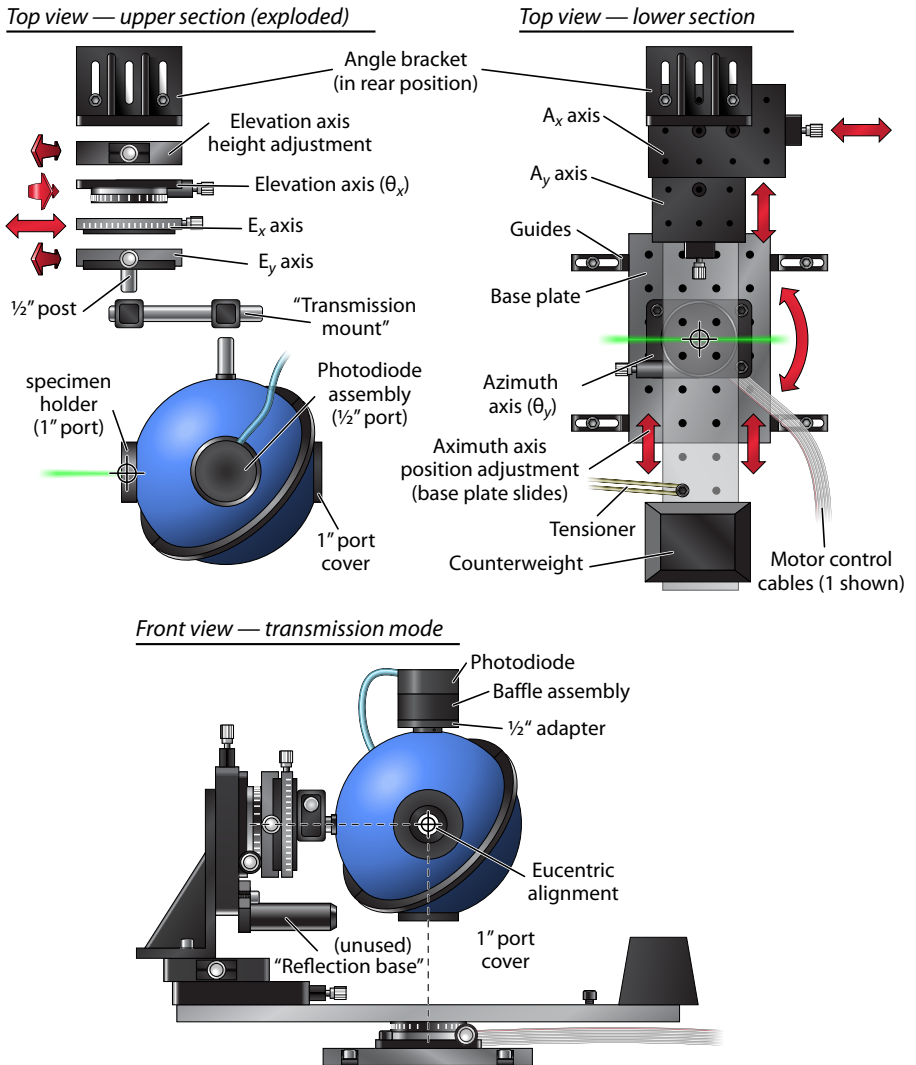


Figure D.6. Transmission-mode integrating sphere configuration.

“photodiode spacer” and “photodiode adapter” parts and the appropriate baffle inserts. The photodiode baffles restrict the acceptance of light to that from the sphere surface directly opposite the photodiode. The specimen is placed in a custom “specimen holder” at the 1" entrance port, and the remaining ports are covered.

During measurements, light that is transmitted into the integrating sphere produces a photocurrent from the sphere photodiode, I_{sph} . To determine the absolute transmission of a specimen, its I_{sph} signal is compared to that of a reference specimen of known transmittance, such as a quartz slide ($T_{\text{ref}} \approx 0.92$) or air ($T_{\text{ref}} = 1$). Both the specimen and reference readings are normalized to

the instantaneous reference photodiode current, I_{inc} . The absolute transmission can be calculated as:

$$T = \left(\frac{I_{\text{sph}}}{I_{\text{inc}}} \right)_{\text{Specimen position}} \cdot \left(\frac{I_{\text{inc}}}{I_{\text{sph}}} \right)_{\text{Reference position}} \cdot T_{\text{ref}} \quad (\text{D.1})$$

For multi-angle transmission scans, the reference position reading is typically only taken at normal incidence.

Because the sensitivity of the integrating sphere is affected by the presence and position of the specimen, the “tightness” of the hemispheres’ assembly, and other physical factors, it is imperative that the sphere configuration not be altered between the specimen and reference readings for accurate transmission measurements. For this reason, the specimen and reference measurements are usually performed under computer automation, using the motorized axes A_y and E_h to translate the sphere between the two positions without user interaction. The two measurement sequences are referred to as *specimen-position* and *reference-position* measurements. The spatial offsets between the specimen and reference beam positions are specified within the software prior to beginning the measurement sequence.

D.4.2 Reflection measurements

Figure D.7 depicts the configuration of the integrating sphere and specimen stage used to perform hemispherical reflection measurements. Unlike transmission measurements, the specimen can only be tilted in one direction (θ_x) during most reflection measurements. The E_x and E_y translation stages are removed, and the angle bracket is moved to the forward position. The sphere is mounted to the “reflection base” (protruding from the E_h axis stage) using a preassembled 1/2” post assembly identified as the “reflection mount.” Neither of the transmission-mode baffles are installed for reflection measurements. The photodiode is attached to a 1” port using the custom “photodiode spacer” (with appropriate baffle inserts) and a 1” adapter ring (Newport 819-DA). The photodiode baffles restrict the acceptance of light to that reflecting from the top surface of the reflection stage (which serves as the only baffle internal to the sphere).

A custom specimen stage holds the specimen at the eucentric point at the center of the sphere for reflection measurements. The reflection specimen stage is mounted directly to the elevation rotation stage, and enters the sphere through the 1/2” port. The specimen is placed over a light trap on the reflection stage: a hollow cavity coated with a diffuse nonreflective paint (Avian Technologies Black-S) that absorbs all transmitted light.* The specimen is typically affixed to the

*The light trap reduces the background reflection reading (i.e., the reading with no specimen loaded) from ~1%–2% to 0.2%–0.5%.

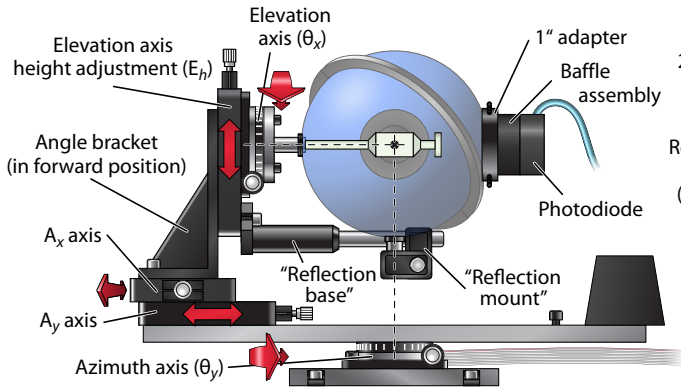
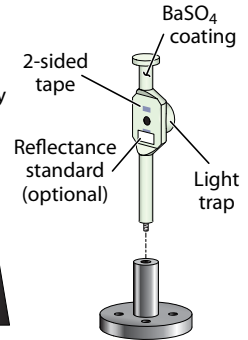
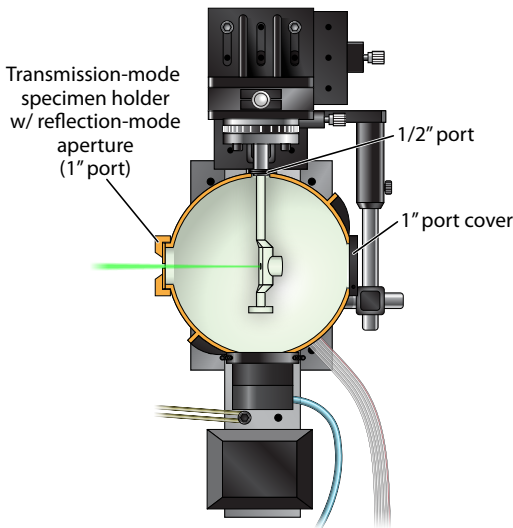
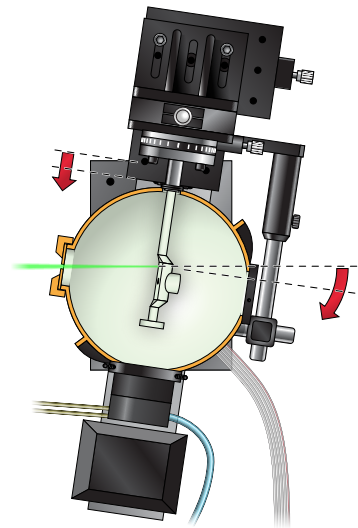
Front view — reflection modeSpecimen stageTop view (cut-away) — specimen positionTop view (cut-away) — reference position

Figure D.7. Reflection-mode integrating sphere configuration.

specimen stage using two-sided tape. Light is incident into the sphere through a $\varnothing 2$ mm aperture placed within the transmission-mode specimen holder. The use of a small-diameter incidence aperture ensures that nearly all reflected light is collected by the sphere. Typically, “normal-incidence” reflection measurements are performed at a slightly off-normal incidence angle ($\theta_y \geq 0.5^\circ$) so that the specular reflection does not exit the sphere through the illumination aperture. The remaining 1” sphere port is covered.

Reflection measurements are performed in a similar fashion to transmission measurements. The signal produced by illuminating the specimen is compared to that produced by illuminating a reference surface of known reflectance, R_{ref} . A small reflection standard (Labsphere) can be affixed to the stage adjacent to the specimen to provide a calibrated reference reading. In most cases, however, the exposed areas of the BaSO_4 -coated reflection stage can provide a reasonably accurate reflectance standard ($R_{\text{ref}} \sim 98\%$). Absolute reflection is calculated as:

$$R = \left(\frac{I_{\text{sph}}}{I_{\text{inc}}} \right)_{\text{Specimen position}} \cdot \left(\frac{I_{\text{inc}}}{I_{\text{sph}}} \right)_{\text{Reference position}} \cdot R_{\text{ref}} \quad (\text{D.2})$$

For multi-angle reflection scans, the reference-position reading is typically only taken at normal incidence. As with transmission measurements, the sequence of specimen- and reference-position reflection readings is performed under computer automation. The motorized azimuth and A_y axes pivot and translate the sphere to illuminate the reference area of the stage, as depicted in Figure D.7. The software must be configured with the correct values of rotation and translation to reach the reference position prior to beginning the measurement sequence. For ease of loading/unloading, the software will return the specimen stage to $\theta_x = 90^\circ$ (horizontal) following measurements.

Although we have not yet needed to perform two-dimensional (x - y) reflection maps, such measurements could be performed using the motorized E_h and A_y axes. The entrance aperture would need to be large enough to accommodate the scan area, requiring that the measurements be performed further from normal incidence in order to collect the specular reflection. A variety of entrance apertures (e.g., slits or dual holes) have been fabricated for different types of reflection-mode parameter sweeps.

D.4.3 Absorption measurements

Calculating absorption from reflection and transmission measurements, although conceptually simple, requires that the measurements be performed in a self-consistent manner in order to produce valid results. This requires that the same specimen area be illuminated in an identical fashion for both reflection and transmission measurements, and that together, the two measurements deterministically account for all non-absorbed light.

Spatial position and incidence angle. The beam should be aligned to strike the same specimen area for both reflection and transmission measurements. The specular reflection from the specimen or an underlying substrate can provide an easy reference point for aligning to normal incidence.

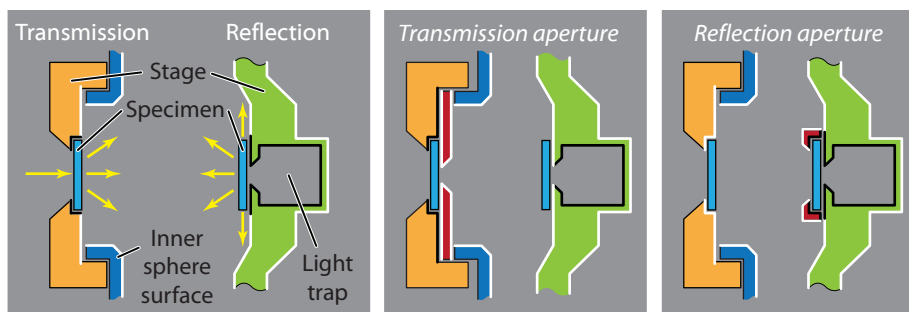


Figure D.8. Integrating sphere absorption measurement configurations. The heavy white and black lines indicate areas of reflective and nonreflective surface coatings, respectively.

Polarization state. For planar structures (particularly those with specular behavior) it is important that the specimen be tilted the same direction with respect to the polarization state of the illumination source. This requires either that the specimen be tilted using the same rotational axis (i.e., elevation) for both reflection and transmission measurements,^{*} or that the polarization state be explicitly controlled using a polarizer filter in the incident beam path. Rigorous absorption studies should independently characterize the specimen response under orthogonal polarization states. However, our experience indicated that Si wire arrays can be suitably characterized without controlling the beam polarization, by ensuring consistent array orientation and using the same tilt axis for both reflection and transmission measurements.

Specimen orientation. For structures with angularly anisotropic optical properties (such as ordered Si microwire arrays), it is also important that each specimen be tilted in a consistent direction with respect to its axis of angular anisotropy. Care should be taken to load each sample in the same orientation for all measurements. In this thesis work, specimen fiducial markings and reflected/transmitted diffraction patterns were used to align the lattice of each wire array to horizontal prior to measurements.

Collection geometry. For specimen with diffuse behavior, particular attention must be paid to the collection geometry. The reflection and transmission measurements must be designed with nominally identical specimen configurations such that combined, they account for all 4π sr of possible light emission directions. In other words, the surfaces surrounding the specimen should be virtually identical for transmission or reflection measurements, and each possible

^{*}The monochromator produces light whose polarization state varies greatly with wavelength (depending on the selected grating). However it can be assumed that, at each wavelength, the polarization state does not vary significantly between each sweep.

direction or light leaving the specimen should be counted as either reflection or transmission (but not both). Figure D.8 depicts three possible sets of collection geometries for diffuse specimen. The configuration on the left is required for highly scattering, nonabsorbing (i.e., ergodic) materials.* The Si microwire arrays of this thesis were only mildly diffuse over large areas, and were measured in a “transmission aperture” configuration. However, the aperture was larger than the specimen area, and served only to hold the quartz slide supporting the specimen in place without tape.

D.5 Photoelectrochemical cell

Photoelectrochemical measurements can be performed using the same illumination source and specimen articulation stage as integrating sphere measurements. The configuration of the system for photoelectrochemical measurements is shown in Figure D.9.

Cell. A ~100 mL rectangular cell was used for the measurements presented in this thesis. The cell was fabricated by Emily Warren, and featured a quartz sidewall and a loose-fitting lid with openings for three electrodes and a purge line. Other cells have also been used with the spectrophotometry equipment. Because of the tendency for the cells’ contents to leak or be spilled, they should be placed in a larger dish when filled with electrolyte.

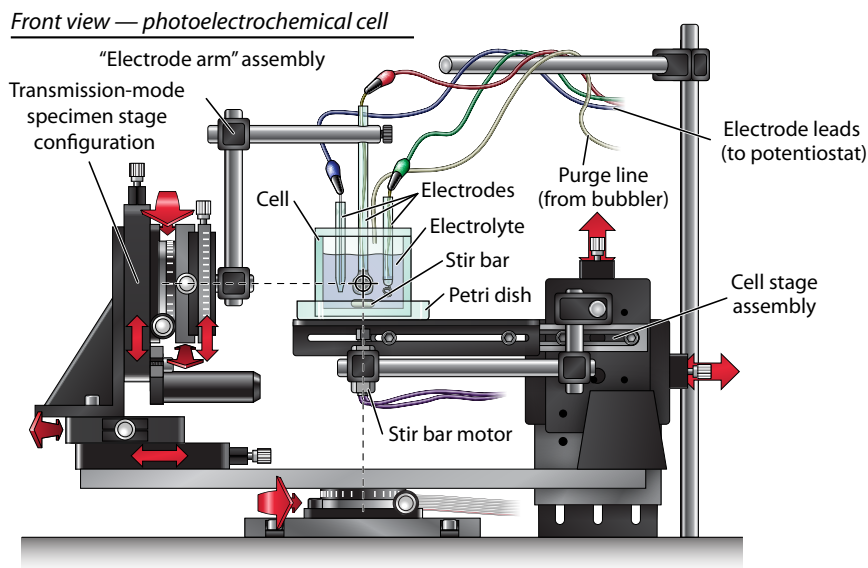


Figure D.9. Photoelectrochemical cell configuration: front view.

*For specimen whose size exceeds that of the light trap opening, this reflection geometry can be achieved by mounting the specimen on a piece of coated (black) sheet metal and placing it on the reflection stage (covering the light trap).

Cell stage. A platform can be pivoted into place above the motorized stage assembly to hold the cell at the correct location for eucentric articulation of the working electrode. Micrometer actuators are provided for adjusting the cell position and height.

Stirring. The cell is continuously stirred using a magnetic stir bar. A small D.C. motor with a magnet attached to its spindle is positioned beneath the cell platform. The motor is powered by a model railroad transformer.

Purging. To prevent oxygen from permeating the electrolyte solution, the cell can be continuously purged with house nitrogen or a bottled gas source (e.g., Ar). The nitrogen line has been plumbed to a regulator next to the sphere enclosure. The purge gas is passed through a bubbler (filled with H₂O for the methyl viologen cell) to prevent evaporation of the electrolyte solution.

Potentiostat. A potentiostat (Gamry Reference 600) is used to bias the cell and amplify the electrode photocurrent signal. The potentiostat is operated from the computer (via a USB connection) using manufacturer-supplied software, which permits a variety of sweep and biasing options. For spectrophotometry measurements, the potentiostat is operated in a continuous (D.C.) bias mode. Its analog output channel (± 3 V full scale) is connected to the input channel of the specimen lock-in amplifier (in place of the TIA). The potentiostat should be operated at the lowest fixed current range that does not cause it to overload (or saturate the LIA) at the peak signal value. The spectrophotometry software is unaware of the bias configuration or the current range of the potentiometer; thus, identical current ranges should be used for specimen (electrode) and reference (photodiode) measurements (or, the measurements must be manually corrected to account for different range settings).

Calibrated photodiode. In order to determine the E.Q.E. of the electrode, a photodetector of known E.Q.E. ($E.Q.E._{ref}$) is positioned in its place within the cell, and its response is measured to calibrate the amount of light striking the electrode at each wavelength.* For this thesis work, Emily Warren prepared an encapsulated, calibrated 3.6×3.6 mm Si photodiode (Thorlabs FDS100-CAL) matching the form factor of our wire-array electrodes, enabling it to be mounted and positioned within the cell using the same electrode holder. We typically used the potentiostat in a two-probe configuration to bias and amplify the response of the calibrated photodiode, although the specimen-channel TIA could also be used for this purpose.

*Note that the *calibrated* photodiode (used as the reference for absolute E.Q.E. measurements) should not be confused with the *reference* photodiode (used to monitor the relative source intensity for all measurements).

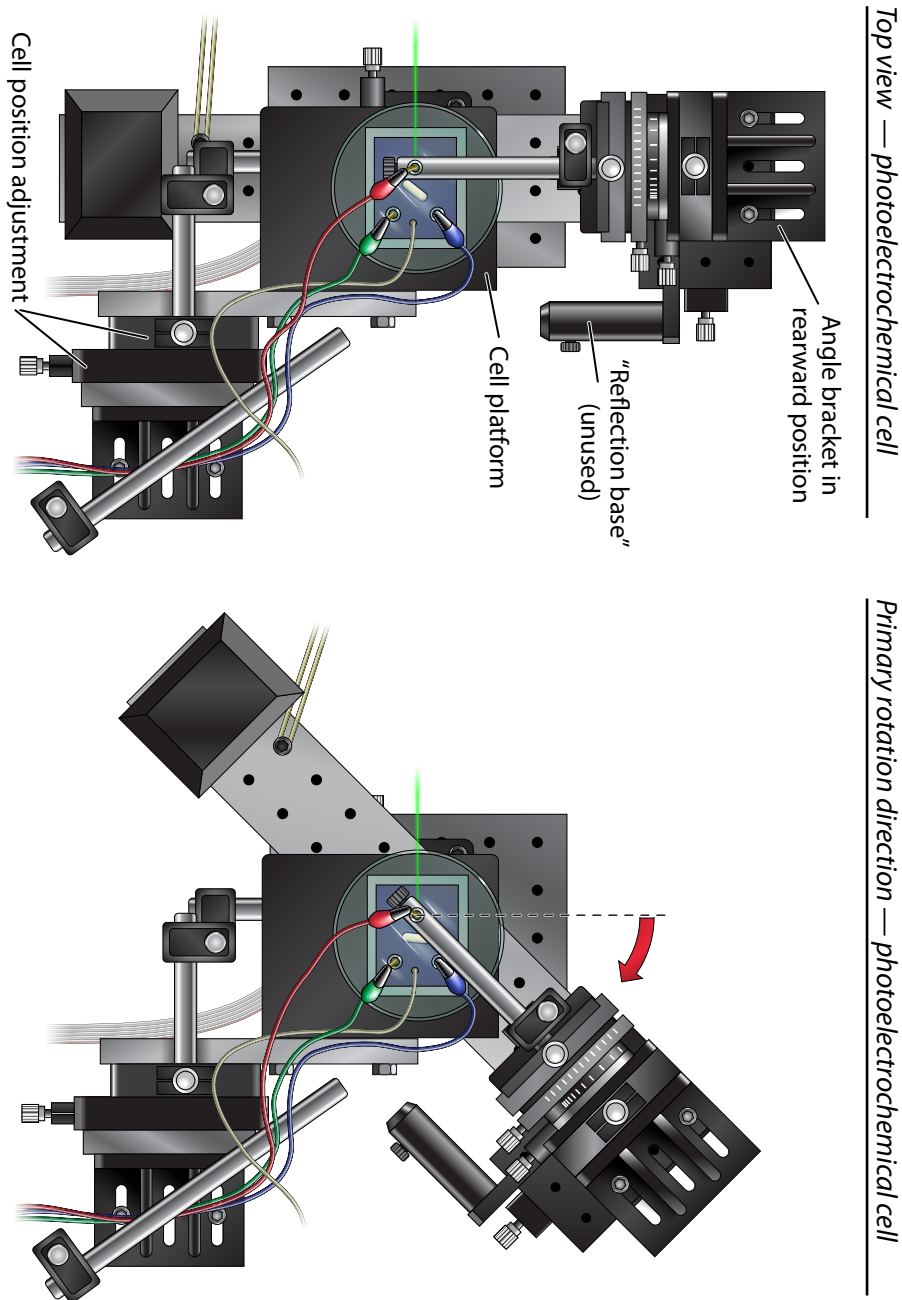


Figure D.10. Photoelectrochemical cell configuration: top view.

D.5.1 E.Q.E. measurements

Using the calibrated photodiode, the E.Q.E. of an electrode can be determined in a similar fashion as reflection and transmission measurements:

$$E.Q.E.(\lambda) = \left(\frac{i_{\text{spec}}}{I_{\text{inc}}} \right)_{\text{Unknown electrode}} \cdot \left(\frac{I_{\text{inc}}}{i_{\text{spec}}} \right)_{\text{Calibrated photodiode}} \cdot E.Q.E._{\text{ref}}(\lambda) \quad (\text{D.3})$$

In the above equation, the wavelength dependence of $E.Q.E._{\text{ref}}$ has been emphasized. Whereas we typically assume constant values for transmission and reflection references, E.Q.E. measurements must usually be normalized on a wavelength-by-wavelength basis using the photodiode calibration data.

D.5.2 Calibration issues

For photoelectrochemical E.Q.E. measurements, most electrolyte solutions are partially absorbing at some wavelengths. Thus, it is critical that the reference photodiode be placed at the exact same position within the cell as the electrode is measured (i.e., the eucentric point). Any positioning errors will alter the path length of the beam in the electrolyte, resulting in a disproportionate attenuation of the light reaching the calibrated photodiode vs. the specimen electrode, and will thus produce erroneous E.Q.E. measurements. Conveniently, the eucentric alignment procedure used to position the electrode prior to measurements can also be used to align the photodiode (in our experience, to within ~ 1 mm of the electrode position). However, E.Q.E. measurements will become increasingly difficult (if not impossible) if the electrolyte absorption is too high—e.g., having an absorption length of a few millimeters or less. Not only does this require positioning repeatability beyond the present alignment capabilities, but ultimately, if too little light reaches the specimen, the measurements will be dominated by noise or stray light at nonattenuated wavelengths. Furthermore, for structures like Si wire arrays, strong parasitic electrolyte absorption will actually change the optical properties of the device: light that would normally be scattered from one wire to another before being absorbed therein might instead be absorbed in the electrolyte between the wires.

For the above reasons, one should generally characterize the absorption of the electrolyte solution to confirm the feasibility of accurate E.Q.E. measurements. This is easily accomplished by measuring the response of the calibrated photodiode positioned within the cell, then removing the cell (or at least emptying it) and remeasuring the response.* The difference between these measurements reveals how much of the light incident on the cell actually reaches the electrode. The result of characterizing our methyl viologen cell in this fashion is shown in

*Logistically, it is easier to perform the latter measurement first, i.e., before the cell is installed or initially filled with electrolyte.

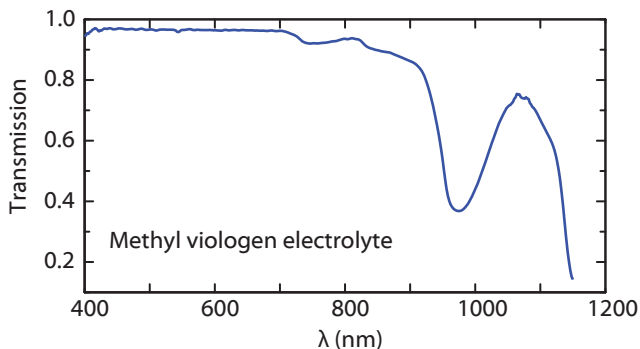


Figure D.11. Opacity of photoelectrochemical cell with methyl viologen electrolyte. Transmission was determined by comparing the light striking a photodiode immersed in the cell to that striking the same photodiode after the cell was removed from the beam path. The $\sim 96\%$ transmission plateau indicates the insertion loss (i.e., front-surface reflectance) of the cell, while the regions of lower transmission indicate absorption by the electrolyte solution. The illumination beam traversed ~ 1 cm of solution before striking the photodiode.

Figure D.11. Although as little as $\sim 40\%$ of the incident beam reached the electrode at some wavelengths (traveling through ~ 1 cm of electrolyte), the ~ 1 mm positioning reproducibility still enabled reasonably accurate E.Q.E. measurements.

Ultimately, one should be able to measure the response of the photodiode positioned in the cell, remove it for electrode measurements, then reinstall/reposition it and obtain the original response spectra within reasonable experimental error. Any deviation will indicate that the electrolyte is too opaque for accurate E.Q.E. measurements, in which case it may be necessary to dilute the electrolyte or otherwise alter the cell configuration.

The shape, encapsulation, and calibration conditions of the photodiode must be considered when using it to normalize photoelectrochemical E.Q.E. measurements. For example, the calibrated photodiode used in this thesis work was furnished in a metal can package (TO-39 type), in which the Si diode is recessed ~ 1.5 mm beneath a transparent front window. It is tempting to position the surface of the Si diode at the system eucentric point for calibration. However, this positioning would reduce the beam path in the electrolyte by 1.5 mm compared to that for electrode measurements, and would thus lead to erroneous E.Q.E. measurements at wavelengths of electrolyte opacity. Furthermore, our visual alignment procedure would prove inaccurate for bringing the Si diode surface to the system eucentric point, due to the refraction of the beam at its front window. Thus, the photodiode should be positioned with the *front window* of the package, rather than the diode surface, aligned to the system eucentric point.

An additional subtlety arises because most photodetectors are calibrated for operation in free space (air), whereas our photodiode is immersed in the



Figure D.12. Photoelectrochemical cell configuration, set up by Elizabeth Santori for characterizing n-type Si wire-array electrodes.

electrolyte solution to provide E.Q.E. reference measurements. Immersion in a liquid will generally change a detector's E.Q.E. For example, the reflectivity of bare Si is reduced by several percent when immersed in water (see Figure 3.2). Thus, the photodiode used for E.Q.E. reference measurements must be either calibrated for immersion in the electrolyte solution, or its free-space calibration data must be corrected to account for the effects of immersion. The correction factor can be measured, or calculated based on knowledge of the diode structure: for example, a diode packaged behind a glass window will exhibit ~3.7% higher E.Q.E. (relative to light striking the window) when immersed in H₂O, due to the decreased front-surface reflectance of the window.

D.5.3 Mass transport issues

Photoelectrochemical measurements can produce erroneous E.Q.E. values if the cell suffers from mass transport issues or other problems related to the electrolyte chemistry. When operating properly, the E.Q.E. readings for typical electrodes should exhibit no dependence on illumination intensity,* chop rate, or stir rate. This behavior should be confirmed prior to beginning measurements. If mass transport issues are identified, they can potentially be resolved by operating at reduced light levels, defocussing the beam, or by changing the cell configuration.

*The neutral density filter wheel in the source enclosure is the preferred means of attenuating the light intensity. Adjusting the supercontinuum laser power setting will reduce the usable wavelengths, while changing the monochromator slits or aperture diaphragms will change the bandwidth and spot size of the beam.

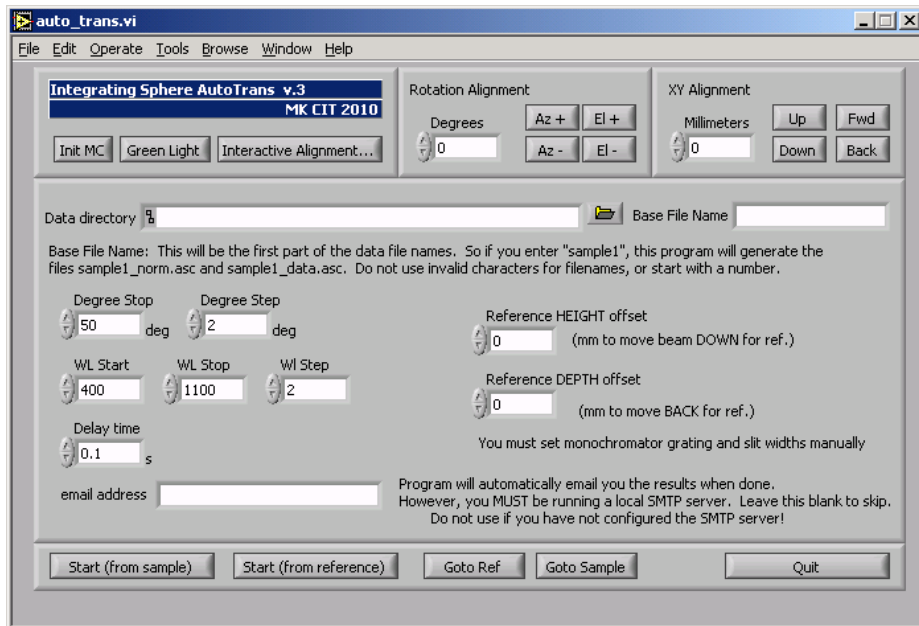


Figure D.13. Screenshot of transmission-mode software.

D.6 Computer software

D.6.1 Data acquisition software

The computer software for performing spectrophotometry measurements is written in LabVIEW (version 7). Each software module or subroutine is known as a *virtual instrument* (VI). Many of the original low-level instrument driver VIs were written by Robb Walters, and some of the spectrophotometry software was written by Jan Petykiewicz.

A screenshot of one of the program modules, `auto_trans` is shown in Figure D.13. This and similar top-level event-driven programs are used to perform most spectrophotometry measurements. They feature controls to align the instrument and configure parameter scans, and will automatically sequence the specimen and reference readings without user interaction (if possible). Each program can also email the results to a user upon completing the experiment (note that this requires a local SMTP server). The following top-level programs are available for measurements:

- `auto_trans` (transmission-mode λ - θ sweeps)
Example: Figure 3.8.
- `auto_refl` (reflection-mode λ - θ sweeps)
Example: Figure 3.8.

- `auto_pecsr` (photoelectrochemical cell λ - θ sweeps)
Example: Figure 3.31.
- `auto_angle` (transmission-mode or PEC θ_x - θ_y sweeps)
Example: Figure 3.32, Figure 3.18.
- `auto_xy` (transmission-mode or PEC x - y sweeps)
Example: Figure 3.30, Figure D.2.

All top-level program modules rely on the same set of subroutines wherever possible. Thus, each generally differs only in which axes are driven and how reference-position measurements are taken.

D.6.2 Alignment utilities

Several alignment tools are available both within and outside of the spectrophotometry software. Within the software, the *green light* button will bring the monochromator back to a visible wavelength for alignment ($\lambda = 550$ nm). The *interactive alignment* button opens a modal dialog window that monitors keystrokes, enabling the motors to be adjusted using the computer's keyboard. There are also several absolute translation/rotation motor controls, which are used to determine the exact distance the integrating sphere should travel between reference and specimen positions.

Outside of the spectrophotometry software modules, a number of VIs are available to control the monochromator, including a serial-port communication terminal (`mono_term`) for manually issuing monochromator commands. To avoid resource conflicts, it is important that operators use this program (as opposed to non-LabVIEW programs such as HyperTerminal) to communicate with the monochromator, especially if other experiments (e.g., photoluminescence) are running concurrently. Another useful monochromator control program is `mono_back_and_forth`, which simply scans the monochromator output across the visible spectrum in an oscillatory manner (from $\lambda = 460$ nm to 650 nm to avoid filter changes). Not only is this useful for beam alignment procedures, but more importantly, it makes for more interesting equipment demonstrations for lab visitors.

D.6.3 Data processing software

The LabVIEW data acquisition programs generate simple text-based output files containing raw experimental data, but do not contain functionality to process or plot this data. Included with this thesis is a simple MATLAB script for loading, normalizing, and plotting most types of measurements. It was written to provide a useful data plotting environment for those unfamiliar with MATLAB, and can be used for most spectrophotometry measurements without modification of the script. The source code is listed at the end of this appendix (section D.8.1), and can be easily copied from the electronic version of this thesis.

Measurement sequences are stored in four-column, tab-delimited text files containing raw measurement data. The first data column records the outer sweep variable (typically θ_x), and the second column records the inner sweep variable (typically λ). The third and fourth columns store the measured signal values for the specimen and source detectors, respectively.*

The files are given a name consisting of a *base file name* (a descriptor specified by the user within the data acquisition program), a measurement identifier (appended automatically by the software), and the extension `.asc` (chosen for ease of associating the files with, e.g., Excel or MATLAB). The MATLAB script parses the file names (and measurement range) to determine how to normalize and plot the data, as well as what to name the imported data within the MATLAB workspace. As an example, the file `wa45_refl_norm.asc` contains the normalization data for a reflection measurement performed on a sample named `wa45`.

Each measurement sequence generates two files: a specimen data file and a normalization data file, recorded with the instrument in specimen and reference positions, respectively. From this, R , T , or E.Q.E. can be calculated from equations (D.1), (D.2), or (D.3), respectively. Most spectrophotometry measurements produce both files in the course of a single automated sequence, whereas the data files for most E.Q.E. measurements must be recorded in two separate sequences (as the calibrated photodiode must be manually positioned in place of the specimen to obtain the normalization data). Thus, in the `auto_pecsr` or other E.Q.E. acquisition programs, the user must manually specify the measurement identifier (`_data` or `_norm`) in the file name.

The data processing script includes options to normalize, crop, smooth, and “deglitch” measurement data using a quasi-GUI interface, as illustrated in Figures D.14 and D.15. The operating procedures are as follows:

1. Execute the script in MATLAB.
2. Select both files (specimen and normalization data) in the file selection dialog. The normalization data file should include the phrase “`norm`” in its file name to be recognized by the script. The script will parse the files and file names to guess the initial plot/import parameters.

Note: Both files are selected at the same time by holding the `Ctrl` key in the file selection dialog box.

3. Change the plot/import parameters as desired.

An important program option is the *normalization type* keyword. This determines the reference value to use in normalizing the data (e.g., T_{ref} in equation D.1). The normalization keywords (as-supplied) are listed in Table D.4. The default normalization options are wavelength-independent, which is reasonable for the listed types of measurement normalizations. In order to normalize E.Q.E. to

*The software records the raw readings (CH1 R) from the lock-in amplifiers. The values are not corrected for detector sensitivity, amplifier gain, etc. . .

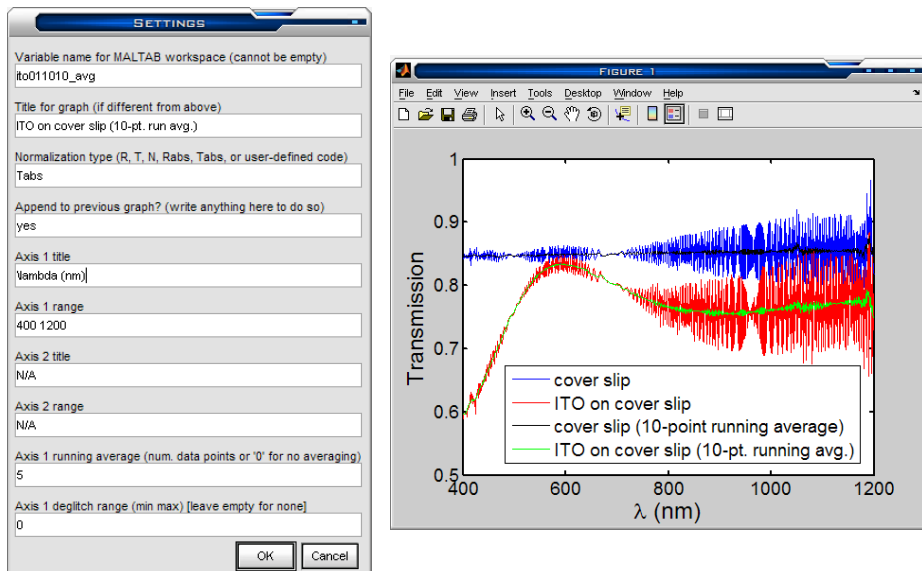


Figure D.14. Use of data processing software utility for one-dimensional sweeps. The plot shown on the right was produced by running the script four times (once per data set). The screenshot (left) depicts the settings used to append the fourth data set to the plot. A 10-point running average was used to suppress the interference fringes observed in the transmission of a microscope cover slip.

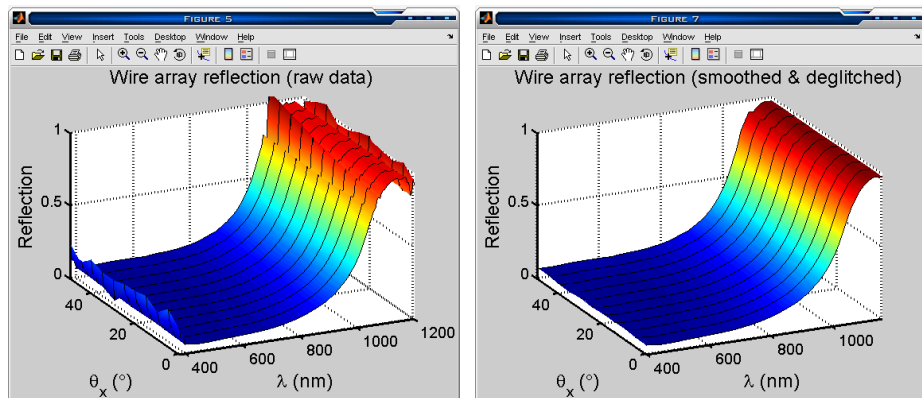


Figure D.15. Use of data processing software utility for two-dimensional sweeps. The plot on the left (raw data) exhibits artifacts due to the $\lambda = 1064$ nm excitation peak as well as measurements taken beyond the usable spectral range of the excitation and detection instrumentation ($\lambda = 380$ – 1200 nm). The plot on the right was obtained by truncating (Axis 1 range: 400 1160), deglitching (Axis 1 deglitch range: 1055 1080), and smoothing (Axis 1 running average: 1) the data using the data processing script.

Table D.4. Default normalization modes of data processing script.

Keyword	Reference value	Graph labeling
T	0.92 (glass slide)	Transmission
Tabs	1.0 (air)	Transmission
R	0.98 (BaSO ₄)	Reflection
Rabs	1.0 (ideal reflector)	Reflection
N	<i>varies</i> ^a	Normalized (A.U.)
EQE	<i>user-defined</i> ^b	E.Q.E.

^a Normalizes result to peak value of 1.0.

^b User must specify $E.Q.E._{ref}(\lambda)$ values within the script.

that of a calibrated photodiode, however, one must modify the script to calculate the value of $E.Q.E._{ref}$ at each wavelength (see comments in source code).

Once the data processing script has been used to plot and import the data into the MATLAB environment, further processing becomes straightforward. For example, after processing the reflection and transmission data for the data set *wa45*, one will find the following variables in the MATLAB workspace:

```
wa45_WL      wa45_Theta      wa45_R      wa45_T
```

One can then calculate and plot absorption as:

```
wa45_A = 1 - wa45_R - wa45_T;
mesh(wa45_Theta, wa45_WL, wa45_A);
```

D.7 Operating procedures

The following procedures are used to align the system and perform basic spectrophotometry measurements.

D.7.1 Laser operation guidelines

The Fianium supercontinuum lasers provide a useful illumination source for spectrophotometry measurements, but have proven to be extraordinarily fragile in operation in our labs. To prevent unnecessary damage to these lasers, and to avoid the downtime and high cost associated with their repair, users should abide by the following guidelines (in addition to standard laser safety protocol):

General handling

- Treat the laser carefully and avoid excessive shock when transporting.
- Always cover the end of the fiber to protect the collimating optics from dust or scratches.
- Do not discard the laser packing materials. They are required to return the unit for repair.

Power-on

1. Before plugging in the laser, verify that the master source and gain stage are switched off.
2. After connecting the power, allow the laser at least 10 minutes to stabilize before energizing the master source.
Note: On our earlier Fianium lasers, the fan operated whenever the unit was plugged in. However, the fan on our most recently refurbished unit appears to be controlled by a thermostat or logic within the laser, and does not always operate during warm-up or idle periods.
3. Attach a high-speed oscilloscope to the SMA connector on the laser. This provides a signal from a photodiode that monitors the output of the laser's master source.
4. Turn on the master source (oscillator).
5. The oscillator button should illuminate green to indicate that the source is operational. Verify that the pulse train is visible on the oscilloscope. Do not proceed if the source is not mode-locked (see Figure [D.16](#)).
6. Allow the master source at least 10 minutes to stabilize.
7. Before energizing the gain stage, verify that the power knob is at its lowest setting (fully counterclockwise).
8. Turn on the gain stage (keyed switch) and increase power to a moderate level (1–4 turns).
9. Operate the laser for an additional ~10 minutes before approaching full power.
10. Operate the laser at full power (10 turns) for measurements.

Standby/shut-down

1. Decrease the power knob fully (10 turns counterclockwise).
2. Turn off the amplifier stage (keyed switch).
3. If the laser will be unused for several hours, turn off the master source.
4. If the laser will be unused for several days, disconnect the power plug.

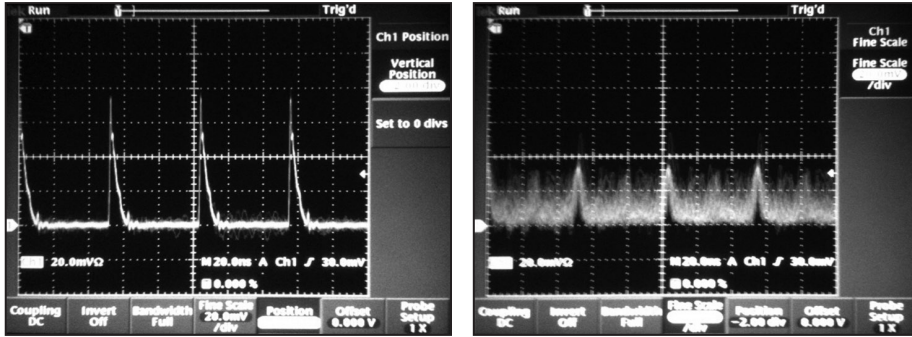


Figure D.16. Fianium laser master source waveforms as viewed on a high-speed oscilloscope. **Left:** normal (modelocked) operation. **Right:** abnormal (q-switching) operation. The laser should not be operated in this state.

Troubleshooting: We have encountered two failure modes for the supercontinuum lasers in our labs: master source failure and damaged splices (i.e., excessive internal back reflections). Diagnosing these conditions requires a high-speed oscilloscope to monitor the SMA connector on the front of the laser, an infrared indicator card, and the USB serial communication port on the laser. Users should consult the laser instruction manual and Fianium technical support at the first signs of trouble.

Master source failure. A master source failure results in rapid and complete loss of laser output. The oscillator button (green light) will usually remain dark even after attempts to reset it. Regardless of the indicator state, the sharp pulse train will not be visible on the oscilloscope (see Fig. D.16), and there will be negligible light output from the fiber (viewed with an infrared indicator card). Do not attempt to operate the amplifier stage if the master source is not working. The laser must be returned to the factory for repair.

Excessive back-reflections. If the laser’s internal detector indicates excessive back-reflections, it will automatically shut down the source and gain stages in an attempt to protect components from further damage. This will be recorded as a back-reflection alarm, which can be read by polling the laser over its USB serial communication port. The cause of the back reflections should be eliminated (e.g., by cleaning and realigning the optics) before returning to full-power operation. The laser can be restarted by turning down the power knob and turning off both switches, then resuming the power-up procedure.

Damaged splices. Over time, some lasers have suffered from reflections at internal splices that trigger the back-reflection alarm even when there are no external reflection sources (e.g., when the beam is sent into a broadband absorber). This causes the laser to shut off whenever the power knob is

turned above a certain threshold (which generally decreases with time), and full-power operation is not possible. One can continue operating the laser at decreased power levels, but the situation will eventually require that the laser be returned to the factory for repair. The USB serial communication port can be used to monitor the back-reflection photodiode value, and with the assistance of Fianium technical support, alter the shutoff threshold to delay the need for repair.

D.7.2 Source alignment

Safety warning: *The spectrophotometer employs a high-power supercontinuum laser source that must be operated at full power (2 or 4 W continuous) to achieve full spectral range. This is a pulsed, broadband laser that produces dangerous levels of visible and infrared radiation, and is capable of causing immediate and permanent blindness. No non-opaque goggles can protect against direct exposure to this laser. Users should be trained in laser safety procedures and comfortable working with high-power sources. Not all safety hazards are identified in these instructions.*

Source alignment is required if the supercontinuum laser has been exchanged or removed from the system, or if the optics have been disturbed. If the system has not been disturbed since the previous measurement session, users need only verify that the beam is properly focused between the monochromator slits prior to bringing the laser to full power. After turning the laser up to a low (but visible) power level, look at the monochromator input slit assembly. Confirm that the symmetric halo of a properly focused beam is visible at the edge of the slits (see Fig. D.17). The source enclosure can then be closed and the laser can be brought to full power for measurements. If, however, the halo appears highly asymmetric (or the beam falls somewhere other than between the slits) the source should be aligned by the following procedure.

1. Open the source and sphere enclosures. Mount the end of the laser fiber securely in the beam launch assembly. Unless the system has been disassembled, the beam launcher should already be near the correct alignment position.
2. Within the source enclosure, move the condenser lens out of the beam path and rotate the neutral density filter (NDF) to its minimum attenuation setting. The chopper should be set to “stop open” so that the monochromator input slits can be seen.

The condenser lens is supported by a magnetic base assembly that provides sufficient mass to hold the lens in place without fasteners. Note that the magnet itself is largely ineffective within the source enclosure as it rests on an aluminum breadboard.

3. Within the sphere enclosure, pivot the focusing lens out of the beam path and open all aperture diaphragms. Remove the integrating sphere (if installed) and set it aside.

4. Following the laser operation guidelines, turn on the laser and increase the power until a faint red beam is visible exiting the laser (1–4 turns).

Although the beam does not appear bright at this point, the laser is emitting dangerous levels of infrared light. For each of the remaining steps, always use as low a power level as possible for alignment.

5. Verify that the beam stop is properly placed to absorb light deflected by the neutral density filter. Recheck this whenever the source alignment is altered.
6. Use the pitch and yaw knobs on the beam launch assembly to direct the laser onto the input slits of the monochromator. The beam should be centered vertically within the slit opening, and should symmetrically straddle the slits.

The monochromator input slits are typically set to 320 μm , which with a 1200 line grating yields a ~ 1 nm passband. The input slit motors are sometimes disabled (unplugged) to prevent inadvertent closure or adjustment of the slits, which could damage the laser source. If unplugged, commands to read or change the slit width will return an E0200 error.

7. Set the monochromator to a red wavelength.

Monochromator commands can be issued using the *Mono_terminal* LabVIEW program. The command to change the wavelength to $\lambda = 650$ nm is:

```
!gw 650 
```

8. Temporarily increase the monochromator entrance slit width to 2 mm. (This is to prevent back-reflection into the laser source when the power is increased without the condenser lens in place.)

The command to set the entrance slit width to 2000 μm is:

```
!slita 2000 .
```

9. Decrease the room lights, increase the laser power, or increase the exit slit width until a beam spot is visible at the output side of the monochromator.

The exit slit width is set with the `!slitb` command. The value may be as large as 2000 μm . We generally use an exit slit width of 320 μm for measurements.

10. Using a ruler to measure the beam height, determine whether or not the beam is level within the sphere enclosure. The beam should deviate in height by no more than 1 cm from the front to the back of the enclosure.
11. If the beam is not level, slightly increase (or decrease) the height of the beam launch assembly using the cog wheel on the 1.5" post. Decrease (or increase) the pitch knob to recenter the beam (vertically) within the input slits. Recheck the output beam slope and iterate as necessary.

Remember to keep laser power to a minimum at each alignment step.

12. Follow a similar iterative procedure of horizontal translation/yaw adjustment of the beam launcher to align the beam horizontally. The aperture diaphragms in the sphere enclosure (which can be contracted as needed for alignment) should provide a target for the horizontal placement of the beam as it exits the monochromator.

If the established path in the sphere enclosure has been disturbed, and prior reference points such as the aperture diaphragms are not available, the monochromator user's manual should be consulted to determine the correct beam incidence and exit angles. A simple horizontal alignment check can be performed by opening the input slits fully (to prevent back-reflections), increasing the laser power to obtain broadband emission, and then running the *monochromator back and forth* alignment program, which continuously sweeps the beam wavelength across the visible spectrum. If the source is substantially misaligned, we have observed that the output spot will move back and forth with wavelength. The position and yaw of the beam launcher should be adjusted to eliminate any observed wobble in beam position as the wavelength is varied.

The laser power should always be reduced before manipulating the beam adjustment knobs.

13. Reduce the laser power to the lowest setting that produces visible light, and set the monochromator input and output slit widths to the values desired for measurements. Insert the condensing lens in the beam path. Vary its position along the beam path to obtain optimal focus onto the monochromator slits. Then move it back or forth to center the focused laser spot so that it disappears between the monochromator slits. The spot can be easily focused between 320 μm slits, with room on either side.

Because the supercontinuum laser is damaged by back-reflected light, keep the condensing lens tilted slightly off-axis to prevent its specular reflection from re-entering the laser (see Fig. D.1). Never close the monochromator input slits while the laser is operating at high power levels.

14. Repeat the above vertical and horizontal alignment procedures, now adjusting the height and position of the condenser lens (rather than the beam launcher) to produce a beam that emerges from the monochromator along the same path as the original beam.

Never manipulate the condenser lens at high laser power levels. The focused beam spot becomes blindingly bright if cast onto either slit.

15. The source beam is now aligned; the laser can be brought to full power. As the power is increased, there should be no visible sources of reflection within the source enclosure. The beam should fall completely between the monochromator input slits, casting only a dim, symmetric halo onto either side of the slits (see Fig. D.17).
16. Close the source enclosure and start the chopper wheel.

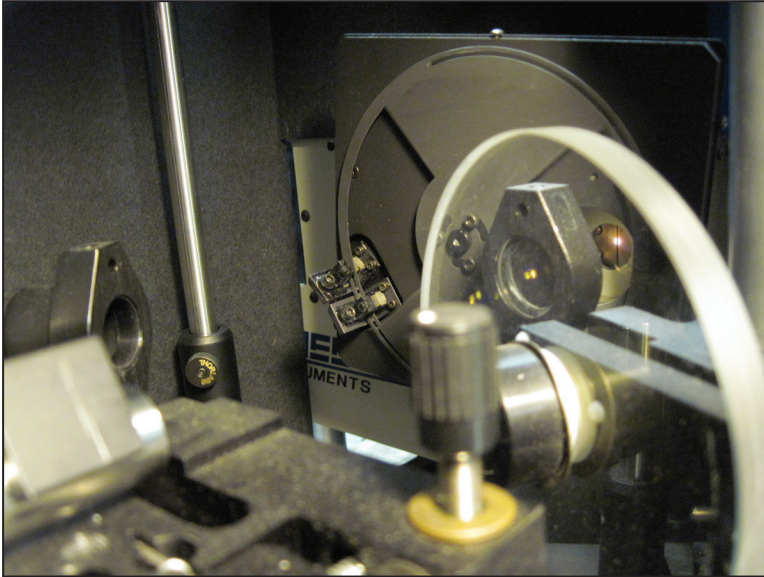


Figure D.17. Aligning the laser to the monochromator input slits. The beam halo can be seen straddling the monochromator input slit.

Following this procedure, the laser source can be run at full power without the need to open the source enclosure (with the possible exception of manipulating the neutral density filter to attenuate the illumination intensity).

D.7.3 Illumination beam alignment

Illumination beam alignment is most easily performed with the laser at full operating power* and the monochromator set to a visible wavelength (e.g., $\lambda = 550$ nm). The monochromator grating and exit slit width should be set as desired for measurements.

1. Within the sphere enclosure, open the aperture diaphragms and pivot the focusing lens out of the beam path. (The cylindrical lens assembly, however, remains attached the monochromator output flange at all times.)
2. Center the first aperture diaphragm in the beam path and contract it slightly until a clipped beam halo is visible.
3. Contract the second aperture diaphragm and precisely center it in the beam path.

*The laser power can be attenuated using the NDF wheel in the source enclosure, but the source must be operated at full power to obtain full spectral bandwidth.

4. Open the second aperture diaphragm fully and pivot the focusing lens into position. Vary its position along the optical axis to produce optimal focus at the specimen plane. The reflection-mode specimen stage can provide a convenient target for focusing.
5. Contract the second aperture diaphragm fully. Move the focusing lens laterally to center the focused beam onto this aperture. Then open the aperture, but only as wide as necessary to fit the beam. This will block stray light and the beam halo from reaching the specimen.
6. Ensure that the beam passes through the reference beamsplitter, replacing the microscope slide cover slip if it has been broken. The posts holding the beam splitter and reference diode are snug but not tight so that they may be adjusted by hand. Pivot the beamsplitter holder to direct the reference beam into the center of the reference detector. Inspect the placement of the baffle to ensure that stray light will not reach the reference photodiode.

Make sure the correct reference photodiode (Si or Ge) is installed.

Following this procedure, a focused, referenced beam having the desired spatial and spectral resolution is striking the specimen plane. If the detection instrumentation is powered on, the reference photodiode signal should be visible on the oscilloscope and the reference-channel lock-in amplifier.

D.7.4 Specimen stage alignment

The specimen stage alignment procedure brings the specimen tilt axes (elevation and azimuth) into alignment with the beam. In order to achieve eucentric alignment, the axes of azimuthal and elevational rotation must precisely coincide with one another, and with the beam path, at a single point in space—the system eucentric point.

Before starting these procedures, the source and illumination beam paths should be aligned as described above. The azimuth axis should be oriented at its “normal incidence” position. During this alignment procedure, the position of the motorized axes can be adjusted from the computer keyboard using the *interactive alignment* LabVIEW program (accessed from the front panel of the reflection, transmission, or E.Q.E. data acquisition programs).

1. Remove the integrating sphere or photoelectrochemical cell stage if present.
2. Bolt a vertical post holder to the base rotational element, directly centered above the azimuth rotation stage. Insert a post that extends to the height of the beam. This will be called the *vertical alignment post*.
3. The beam should strike the vertical alignment post exactly at its center. If not, the entire stage must be translated within its guides (A_d axis). A handful of clamps must be loosened to enable A_d translation; these should be retightened following the alignment.

4. Retract the vertical alignment post into its post holder so that it does not extend to the height of the beam.
5. Remove the E_x and E_y stages (if installed) and move the angle bracket to the forward position (i.e., reflection mode, see Fig. D.7).

The E_x and E_y stages are removed as an assembly. Translate the E_x stage to the fully extended position (to the left) to reveal the two screws holding it to the elevation rotation stage.

To move the angle bracket to the forward position, loosen the two screws holding it to the A_x stage (3/16" hex socket), pull it forward to the end of its travel, and re-tighten the screws.

6. Bolt the reflection-mode specimen stage base to the elevation rotation stage, and attach an alignment post (or the rest of the specimen stage). This will be called the *horizontal alignment post*.

Use short screws to bolt the reflection-mode specimen stage in place. Longer screws will bind the elevation rotation stage.

7. Translate the E_h axis (`[Page ↑]` / `[Page ↓]` in the in the *interactive alignment* program) as necessary so that the horizontal alignment post is exactly centered within the illumination beam.

If the horizontal post is not long enough to reach the beam path, translate the A_y axis as necessary (`[Home]` / `[End]`).

8. Extend the vertical alignment post to reach the horizontal alignment post. The two axes should coincide at the beam position. If not, adjust A_x until the axes are coincident.
9. Remove the horizontal and vertical alignment posts. If performing reflection measurements, the reflection-mode specimen stage base can remain attached to the elevation stage.




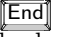


Following this procedure, the A_d , E_h , and A_x axes are properly aligned for eucentric tilt. If two-dimensional eucentric tilt measurements are required, do not further alter the positioning of these three axes.

D.7.5 Reflection-mode configuration

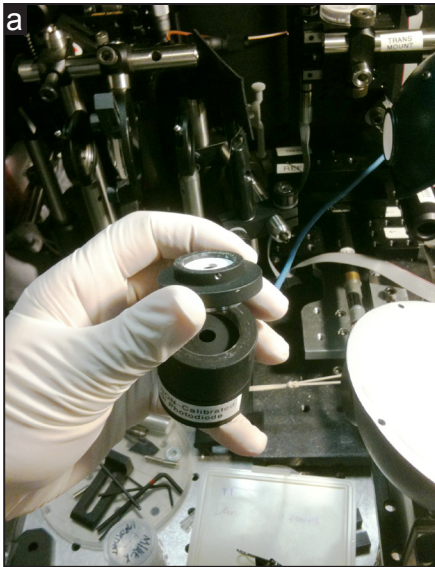
This procedure describe how the integrating sphere is configured and aligned for reflection measurements. The state of the system is assumed to be that following the above specimen stage alignment procedure, i.e., in eucentric alignment, with the angle bracket in the forward position, and with the E_x and E_y translation stages removed. Users may use the `auto_refl` program for alignment and data collection.

Note: *Wear clean gloves whenever handling internal sphere components. Efforts should be made to minimize physical contact with the $BaSO_4$ -coated components. These coatings are easily chipped away by mild physical abrasion, and*

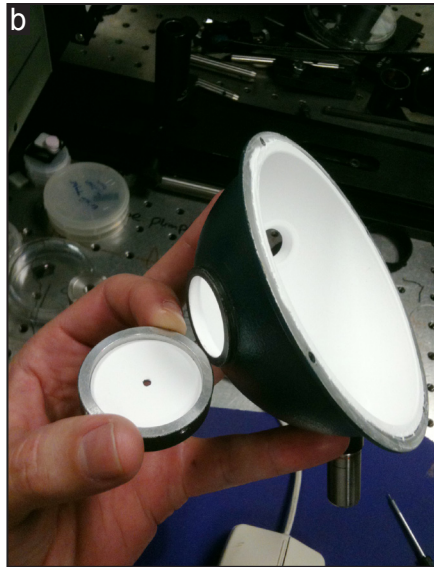
their reflectivity is reduced by contact with dust or oils. Always store the unused components appropriately.

1. Install the reflection-mode specimen stage onto the elevation rotation stage, and rotate the elevation axis so that the specimen stage faces the incident beam ( /  in the *interactive alignment* program).
2. Translate the A_y axis until the incident beam falls directly into the center of the light trap within the specimen stage ( / ). The height of the elevation axis (E_h) should have been set correctly during the stage alignment procedure; however, this should be adjusted if necessary to center the beam in the light trap.
3. Unscrew the upper part of the reflection-mode specimen stage and set it aside.
4. Open the integrating sphere. Remove and store the interior baffles. The upper baffle is held in place by a screw, whereas the lower baffle is simply sandwiched between the hemispheres.
5. Prepare the *mounted* hemisphere (that is, the hemisphere attached to the 1/2" mounting post) by mounting the $\phi 2$ mm reflection aperture over the 1" port using one of the transmission-mode specimen holders. The BaSO₄-coated (white) surface of the aperture faces into the sphere (see Fig. D.18b).
6. Using the "reflection mount" (a 1/2" post assembly), affix the mounted hemisphere to the "reflection base" protruding from the E_h stage, as depicted in Figure D.7. The sphere should be aligned such that the reflection-mode specimen stage fits through the 1/2" port of the mounted hemisphere. Position the sphere at a depth such that its inner surface is approximately flush with the end of the reflection-mode specimen stage base. Lightly tighten the reflection mount and sphere assembly in place.
7. Rethread the reflection-mode specimen stage onto its base (see Fig. D.18c).
8. Adjust the azimuth axis ( / ) as necessary so that the incident beam passes through the center of the $\phi 2$ mm entrance aperture. The beam should now pass through both the entrance aperture and the light trap in the specimen stage. The iris diaphragms should be opened fully so that the beam halo can serve as a guide in centering the beam in the entrance aperture. In the event that the entrance aperture is at the wrong height for the beam, the reflection mount/base assembly can be loosened to permit the sphere to be more precisely aligned to the incident beam.

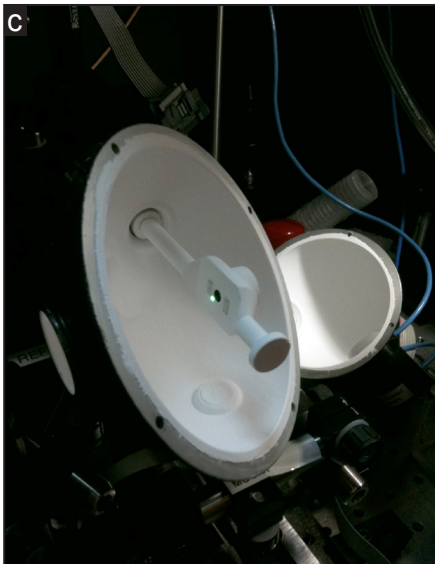
Note: *Aligning the sphere and reflection mount/base assembly from scratch requires a time consuming iterative adjustment approach. For this reason, the reflection mount and base components should not be adjusted or disassembled when not in use. It should be generally possible to archive proper alignment by loosening only the reflection base post-holder thumb-screw as well as the integrating sphere post holder.*



Photodiode assembly: removing the 1/2" adapter from the photodiode spacer



Reflection mode: installing the 2 mm-dia. entrance aperture on the 1" sphere port



Reflection mode: aligning the reflection stage (intentionally misaligned to show beam)



Illumination alignment: centering the reference beam on the reference photodiode

Figure D.18. Reflection-mode configuration.

9. The photodiode assembly is prepared as follows: the 818-series photodiode of choice (Si or Ge) is threaded onto the “photodiode spacer” with a nonreflecting (black) baffle installed between the two. A second baffle is mounted at the bottom of the photodiode spacer. Remove the 1/2” photodiode adapter from the photodiode spacer, if present (see Fig. D.18a).
10. Use the 1” photodiode adapter to affix the photodiode assembly to the 1” port of the other hemisphere (known as the *removable* hemisphere) that will be located opposite the 1/2” port when the sphere is assembled. A third baffle is sandwiched between the port opening and the photodiode spacer. This baffle has BaSO₄ (white) coating on the sphere-facing side, and nonreflective (black) coating on the diode-facing side.
11. Install a 1” port cover on the remaining port of the removable hemisphere.
12. The sphere can now be assembled for a test fit. Attach the removable hemisphere to the mounted hemisphere with 3 or more binder clips, using the original screw holes as guides to align the hemispheres. The four ports should lie in a perfectly horizontal plane, with the specimen stage exactly centered at the eucentric point within the sphere.
13. Check the alignment of the beamsplitter and reference photodiode. The reference beam should strike the center of the diode (see Fig. D.18d).



The integrating sphere is now aligned and prepared for hemispherical reflection measurements. The sphere mounting components should be tightened in place so that the alignment isn’t inadvertently disturbed while opening/closing the sphere, which is required for loading and unloading each sample.

D.7.6 Reflection measurements

Reflection measurements are typically performed as a function of wavelength (λ) and a single incidence angle (θ_x) using the LabVIEW program `auto_refl.vi`.

1. Open the integrating sphere and set the removable hemisphere (with attached photodiode) aside to facilitate loading/unloading the specimen. The specimen exchange is most easily performed with the stage facing upward.
2. Affix the specimen to the reflection stage within the sphere (usually, using two-sided tape). The area of interest should be centered over the light trap.

If desired, also affix a reflectance standard adjacent to the specimen. Most measurements do not require a reflectance standard, and are instead normalized to the reflectance of a clean area of the specimen stage.

3. Rotate the specimen stage ( / ) so that the specimen is illuminated at near-normal incidence. The specular reflection from the beam striking the specimen can be used as a guide.

The *Load* button in the software rotates the stage 90° toward the source, and is usually appropriate for bringing the specimen to normal incidence after loading.

4. Verify that the reference-position rotation and translation offsets within the program are valid. The *Goto Ref* or *Goto Sample* buttons should move the system between the reference and specimen positions as desired when actuated. The numerical adjustment controls may prove useful in fine-tuning the positioning offsets.

It is imperative that the incident beam does not strike the entrance aperture in either measurement position. The iris diaphragms should be opened for alignment so that the beam halo is visible on the entrance aperture (to facilitate centering the beam in the aperture). However for measurements, the diaphragms should be closed to produce a tightly focused beam that passes completely through the aperture.

Once the system is aligned with valid reference-position offsets, subsequent reflection measurements can be taken with relative ease as this alignment does not need to be independently established for each specimen.

5. Enter the scan parameters (wavelengths and angles) and specimen data (name and folder for data) in the software user interface.

To perform a measurement at a single angle only, set *Degree Stop* to 0.

6. To initiate the scan, press *Start (from sample)* or *Start (from reference)*, depending on the current system position.

The software will collect the reference-position spectra (at normal incidence only), then progress to the specimen-position scans. After the first scan, the software will provide an estimated time of completion. After the last scan, the specimen stage will be returned to the upright (90° elevation) position to facilitate unloading.

D.7.7 Transmission-mode configuration

This procedure describe how the integrating sphere is configured and aligned for transmission measurements. The initial state of the system is assumed to be that following reflection measurements.

Note: *Wear clean gloves whenever handling internal sphere components. Efforts should be made to minimize physical contact with the BaSO_4 -coated components. These coatings are easily chipped away by mild physical abrasion, and their reflectivity is reduced by contact with dust or oils. Always store the unused components appropriately.*

1. Open the sphere. Set the removable hemisphere aside.
2. Unscrew and remove the upper part of the reflection-mode specimen stage.
3. Loosen the “reflection base” thumbscrew and slide the sphere assembly forward. Remove the “reflection mount” from the sphere and stow it.

***Note:** Due to the difficulty of assembling and aligning these components, do not disassemble the reflection mount assembly, and leave the reflection base assembly attached to the stage. If the reflection base assembly interferes (collides) with the photoelectrochemical cell stage, the post holder can be removed while leaving its base bolted in place.*

4. Unbolt the reflection-mode specimen stage base from the elevation rotation stage. Reassemble and stow the reflection-mode specimen stage.
5. Move the angle bracket to the rearward position (i.e., the transmission-mode position, see Fig. D.6) as follows: loosen the two screws holding it to the A_x stage (3/16" hex socket), then push it rearward to the end of its travel and retighten the screws.
6. Install the E_x and E_y stages as an assembly. The E_x stage is bolted to the elevation rotation stage using the two rightmost screws. Translate both stages to be approximately centered in their travel. The post protruding from the E_y stage should be approximately concentric with the elevation rotation axis.

***Note:** Be certain to properly thread and tighten the screws holding the E_x stage to the rotation stage. If a screw becomes loose, it can become stuck beneath the stage, making it nearly impossible to translate or remove the stage.*

7. Install the “transmission mount” on the post protruding from the E_y stage (see Fig. D.6).
8. Install the upper baffle in the mounted hemisphere. It is screwed in place from above (see Fig. D.20b).
9. Mount the hemisphere to the transmission mount, with the 1/2" port facing up. The bubble level may be helpful in positioning the sphere. Tighten the thumbscrews with a hex driver to hold the sphere securely.
10. Remove the photodiode assembly from the removable hemisphere and stow the 1" port adapter and its baffle. Thread the 1/2" port adapter onto the photodiode spacer (see Fig. D.18a) and mount it to the top of the integrating sphere. Sandwich a 1/2" baffle between the photodiode adapter and the port opening, with the white (BaSO_4 -coated) side facing the sphere's interior.
11. Install a 1" port cover over the remaining port of the removable hemisphere.

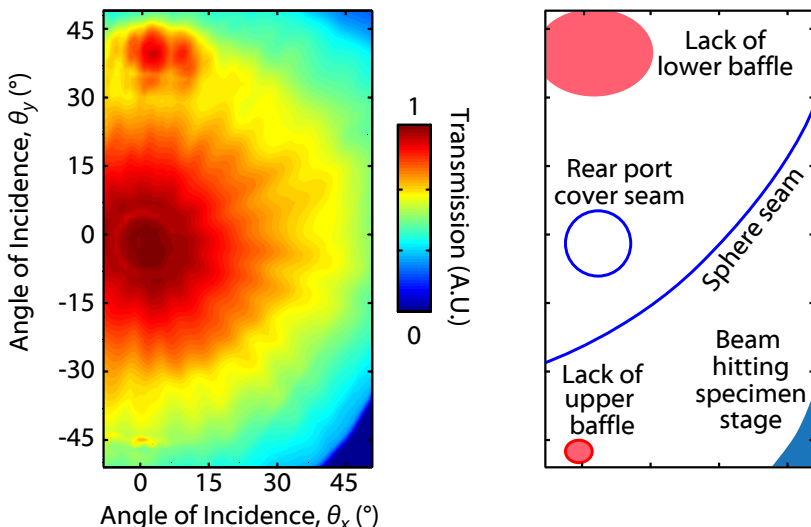
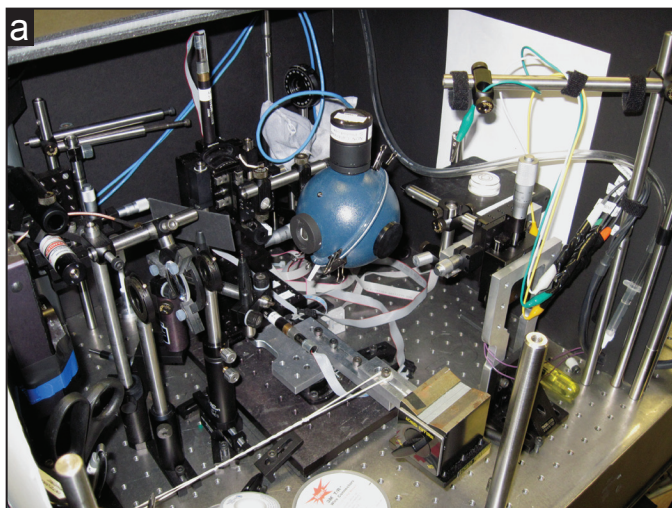


Figure D.19. Artifacts in two-angle transmission scans. **Left:** Two-angle (θ_x – θ_y) transmission measurements performed on a dodecagonally tiled Si wire array. **Right:** Diagram depicting the location and source of artifacts in the measured data. The array was intentionally measured without either baffle in place.

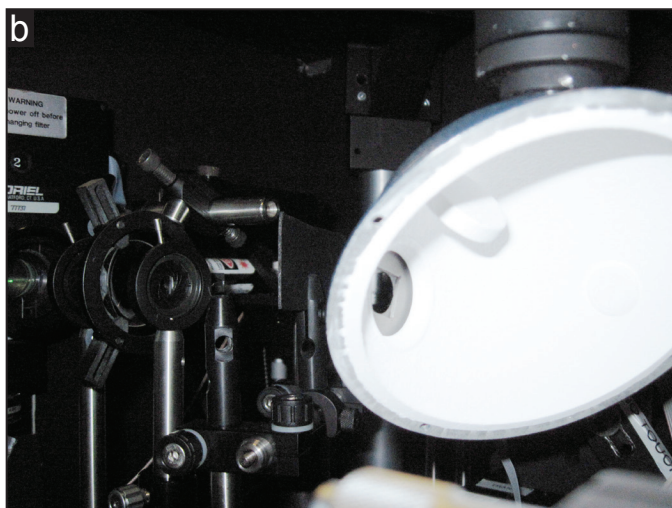
12. Assemble the hemispheres using binder clips. During assembly, position the lower baffle (the thin BaSO₄-coated sheet metal cutout) so that it is sandwiched between the two hemispheres at the appropriate location.

Unlike the reflection-mode configuration, the hemispheres do not need to be aligned such that the ports oppose one another. In fact, for two-angle transmission measurements, it may be advantageous to rotate the removable hemisphere so that the ports are as far as possible from the back side of the sphere. This is true for specimen with non-ideally diffuse behavior such as wire arrays, which transmit a significant amount of the incident beam without scattering or absorbing it. When this beam is cast directly onto a port cover seam (or the sphere seam), some light escapes the sphere and the transmission appears artificially low. Thus, a port cover positioned directly opposite the specimen port can produce a circular artifact at the center of the data set (i.e., near normal incidence). Figure D.19 shows an example of such an artifact. The port seam artifact can be removed from the center of the scan by rotating the removable hemisphere so that the ports occupy other areas of the sphere. Careful inspection will reveal several seam artifacts in the data shown in Figure 3.18.

13. Check the alignment of the beamsplitter and reference photodiode. The reference beam should strike the center of the diode (see Fig. D.18d).



Transmission-mode integrating sphere configuration



Transmission-mode configuration—view inside sphere.

Figure D.20. Transmission-mode configuration.

14. Remove the specimen holder from the 1" port at the front of the sphere. Stow the $\phi 2$ mm reflection-mode entrance aperture. Load a sample or a blank slide in the specimen holder (using tape or a baffle to secure it) and reattach it to the sphere.
15. Move the A_y and E_y axes to illuminate an identifiable feature on the specimen (or mark the point of incidence with a marker). Rotate the azimuth to $\sim 45^\circ$ incidence angle. Adjust the E_x axis as necessary so that the beam strikes the identified specimen feature again. This translates the specimen plane to coincide with the system eucentric point, and ensures that the beam will strike the same spot on the specimen at all incidence angles.

D.7.8 Transmission measurements

Performing two-dimensional angular (θ_x - θ_y) transmission or E.Q.E. sweeps (e.g., Fig. 3.18) requires that the system be in precise eucentric alignment. Single-angle sweeps (i.e., θ_x - λ) can be performed more easily, and only require that one axis be aligned to the beam. Spatial (x - y) scans can be performed without either axis in eucentric alignment.

Two-angle transmission (or E.Q.E.) sweeps are performed using the `auto_angle.vi` program. To preserve eucentric alignment, users should not move the E_h (motorized) or the A_x (manual) axes during setup or measurements. Only the E_y (manual) and A_y (motorized) axes can be used to translate the specimen without disturbing eucentric alignment. Presently, however, the E_h axis is used for motorized translation between specimen- and reference-position measurements. This allows greater range of motion than the smaller E_y axis, but it also disturbs eucentric alignment. Thus, users should use the E_y and A_y stages to translate the specimen to the region of interest, reserving operation of the motorized E_h stage only for translating between this and the reference position. Because the software always returns the stage to the specimen position after measurements, the eucentric alignment of E_h will not be lost.

Single-angle transmission (or E.Q.E.) sweeps are performed using the `auto_trans.vi` (or `aut_pecsr.vi`) program. Only the azimuthal rotation axis needs to be in eucentric alignment for single-angle transmission sweeps. Conveniently, this is almost always the case, as the azimuthal rotation stage is bolted to the (stationary) base plate. Users may simplify the operating procedures for such measurements: the motorized E_h axis can be used to pan the specimen, and either the A_x or E_x stages can be used to bring the specimen plane to the eucentric point.

Spatial transmission (or E.Q.E.) sweeps are performed using the `auto_xy.vi`. The user need not check the eucentric alignment of either rotational axis before starting measurements.

The following procedures describe how to perform single-angle transmission sweeps:

1. Mount the specimen in one of the transmission-mode specimen holders, using two-sided tape or one of the apertures to hold it in place. Attach the specimen holder to the front port of the integrating sphere.

The specimen mounting configuration must allow for a reference reading to be taken (see Figure D.5). Thus, the specimen cannot occupy the entire open area of the specimen holder. Wire-array films, for example, can be mounted on a slide (leaving a portion of the slide uncovered to serve as the reference point), whereas brittle specimen can be cut to occupy only a portion of the specimen holder area.

Samples that are too large to fit the 1/2" form factor of the specimen holders can be taped directly to the entrance port of the sphere.

2. Adjust the E_y and A_y axes so that the desired area of the specimen is illuminated.
3. To verify that the specimen is aligned to the system eucentric point, rotate the azimuth axis by $\sim 45^\circ$. The beam incidence point should not move on the specimen. Adjust the E_x stage if necessary and return the stage to normal incidence.
4. Use the numerical motor controls at the top of the software window (*Up*, *Down*, *Fwd*, and *Back*) to translate the sphere to the reference alignment. Keep track of the total distance traveled in each direction, and set the reference-position translation offsets in the software accordingly. If these values are entered correctly, pressing *Goto Sample* should return the sphere exactly to the starting point (illuminating the specimen area of interest).
5. Enter the scan parameters (wavelengths and angles) and specimen data (name and folder for data) in the software user interface.

To perform a measurement at a single angle only, set *Degree Stop* to 0.

6. To initiate the scan, press *Start (from sample)* or *Start (from reference)*, depending on the current system position.

The software will collect the reference-position spectra (at normal incidence only), then progress to the specimen-position scans. After the first scan, the software will provide an estimated time of completion.

D.8 Supplementary information

D.8.1 Data processing program

The following MATLAB script can be used to process and plot the data taken by the spectrophotometer instrument. Use of the program is described in section D.6.3. The listing has been typeset to facilitate copying from this PDF file.

Listing D.1. Data plotting program for spectrophotometer system.

```
% Prompt user for file location
global mksearchpath
if (~isempty(mksearchpath))
    [FileName,PathName] = uigetfile({'*.asc;*.dat;*.txt;*.csv' '*'},...
    'Select norm and data file - norm file must include 'norm' in name.',...
    'MultiSelect','on',mksearchpath);
else
    [FileName,PathName] = uigetfile({'*.asc;*.dat;*.txt;*.csv' '*'},...
    'Select norm and data file - norm file must include 'norm' in name.',...
    'MultiSelect','on');
end

% Figure out which file is which, and determine sweep settings
if (~isempty(FileName))
    if( iscell(FileName))

        normfilename = [PathName FileName{1}];
        [pathstr, name, ext, versn] = fileparts(normfilename);
        one_data = dlmread( normfilename );

        samplefilename = [PathName FileName{2}];
        [pathstr, name, ext, versn] = fileparts(samplefilename);
        two_data = dlmread( samplefilename );

        if isempty( strfind( [name ext], 'norm' ) )
            norm_data = one_data; sample_data = two_data;
        else
            sample_data = one_data; norm_data = two_data;
        end

        probablename = name;
        nameend = strfind(name, '_');
        if (~isempty(nameend))
            probablename = name(1:nameend(1)-1);
        end

        probabletype = 'T';
        if (~isempty(strfind(name,'refl')) || ~isempty(strfind(name,'br')))
            probabletype = 'R';
        end

        sampleWL = sample_data(:,2);
        wl_range = [ min(sampleWL) (sampleWL(2)-sampleWL(1)) max(sampleWL)];
                                                % (min step max)
        numbersweep = length(wl_range(1):wl_range(2):wl_range(3));
        numsweeps = length(sampleWL)/numbersweep;
        sampleTheta = sample_data(:,1);

        normWL = norm_data(:,2);
        WL_max = min(max(normWL),wl_range(3)); % truncate data range to that
```

```

WL_min = max(min(normWL),wl_range(1)); % available in normalization file
alname = '\lambda (nm)';
if (WL_max < 400) alname = '\theta_y (\circ)'; end
if (WL_max < 10 ) alname = 'x (mm)'; end

if (numsweeps > 1)
    a2name = '\theta_x (\circ)';
    a2range = [num2str(min(sampleTheta)) ' ' num2str(max(sampleTheta))];
    dTheta = sampleTheta (numersweep+1)-sampleTheta(1);
    if (max(sampleTheta) < 10) a2name = 'y (mm)'; end
else
    a2name = 'N/A'; a2range = 'N/A'; dTheta = 0;
end

global mkrunavg mkdeglitch;
if (isempty(mkrunavg) || isempty(mkdeglitch))
    mkdeglitch = '1054 1074'; mkrunavg = '0';
end

%Now prompt user for user input
defAns = {probablename '' probabletype '' '\lambda (nm)' ...
    [num2str(WL_min) ' ' num2str(WL_max)] a2name a2range ...
    mkrunavg mkdeglitch };
sampleinfo = inputdlg({ ...
    'Variable name for MALTB workspace (cannot be empty)'...
    'Title for graph (if different from above)' ...
    'Normalization type (R, T, N, Rabs, Tabs, or user-defined code)'...
    'Append to previous graph? (write anything here to do so)' ...
    'Axis 1 title' 'Axis 1 range' 'Axis 2 title' 'Axis 2 range' ...
    'Axis 1 running average (num. data points or ''0'' for no averaging)'...
    'Axis 1 deglitch range (min max) [leave empty for none]', ...
    'Settings', 1, defAns);
end
mksearchpath = samplefilename; % remember folder for next time.
end

%Parse user input
if (isempty(sampleinfo{2})) titlename = sampleinfo{1}; %graph title name
else titlename = sampleinfo{2}; end
shouldhold = ~isempty(sampleinfo{4}); %whether to open new window
userwlrangle = str2num(sampleinfo{6});
userthetarange = str2num(sampleinfo{8});
WL_max = min(userwlrangle(2),WL_max); %truncate wavelength range?
WL_min = max(userwlrangle(1),WL_min);
if (numsweeps > 1) %truncate theta range?
    Theta_min = max(min(sampleTheta),userthetarange(1));
    Theta_max = min(max(sampleTheta),userthetarange(2));
end
deglitchrange = 0; %whether or not to deglitch the noisy peak at ~1064 nm
if ~isempty(sampleinfo{10})
    deglitchrange = str2num(sampleinfo{10});
    if (deglitchrange)
        deglitchrange = min(WL_max, deglitchrange);
        deglitchrange = max(WL_min, deglitchrange);
    end
end
runavg = floor(abs(str2num(sampleinfo{9}))); % running average
exptype = sampleinfo{3}; %What type of normalization (T, R, or other?)
samplename = sampleinfo{1}; %base name for workspace variable

%Save deglitch/avg settings for next time program is run
mkrunavg = num2str(runavg); mkdeglitch = mat2str(deglitchrange);

%Initialize arrays for normalized data
WL = WL_min:wl_range(2):WL_max;

```

```

nWL = length(WL);

if ( numsweeps > 1)
    Theta = Theta_min:dTheta:Theta_max;
    nT = length(Theta);
else
    Theta = 0; nT = 1; Theta_min = 0; Theta_max = 0;
end

normalizedData = zeros(nT,nWL);
sampleReading = sample_data(:,3)./sample_data(:,4);

%Re-sample the normalization data
normReadingOrig = norm_data(:,3)./norm_data(:,4);
normWLOrig = normWL;
normReading = interp1(normWLOrig, normReadingOrig, WL);

%Iterate through the file data to construct the 2D array of normalized data
ThetaIndex = 1;
WLIndex = 1;
recognizedNormalization = 1;
for n=1:length(sampleReading)
    thisWL = sampleWL(n);
    thisTheta = sampleTheta(n);

    if (thisTheta < Theta_min || thisTheta > Theta_max) continue
    elseif (thisWL < WL_min || thisWL > WL_max) continue
    end

    thisRelative = sampleReading(n)/normReading(WLIndex);

    %%%%%%%%%%%%%%%%%%%%%%%%%%%%%%%%%%%%%%%%%%%%%%%%%%%%%%%%%%%%%%%%%%%%%%%%%
    % Normalization - this is where we determine what the "reference"
    % value is. We can add additional experiment types here, e.g. for a
    % reference photodiode (which must be interpolated by wavelength):
    %
    % if (strcmp(exptype,'EQE'))
    %     refValue = interp1(diodeWL,diodeEQE,thisWL);
    % end
    %%%%%%%%%%%%%%%%%%%%%%%%%%%%%%%%%%%%%%%%%%%%%%%%%%%%%%%%%%%%%%%%%%%%%%%%%
    if (strcmp(exptype,'T'))
        refValue = 0.92; %approx transmission through quartz slide
    elseif (strcmp(exptype,'R'))
        refValue = 0.98; %approx reflectivity of BaSO4 coating on refl. stage
    elseif (strcmp(exptype,'N'))
        refValue = 1; % (Data is divided by max value later)
    elseif (strcmp(exptype,'Tabs') || strcmp(exptype,'Rabs'))
        refValue = 1; %Data is normalized to unity
    else
        refValue = 1; %default case
        recognizedNormalization = 0; %This will issue a warning after the loop
    end

    normalizedData(ThetaIndex, WLIndex) = thisRelative * refValue;

    WLIndex = WLIndex + 1;
    if (WLIndex > nWL)
        WLIndex = 1;
        ThetaIndex = ThetaIndex + 1;
        if (ThetaIndex > nT)
            break;
        end
    end
end
end
end

```

```

if (~recognizedNormalization)
    warndlg(['The experiment type '' exptype '' does not have an '...
        'associated normalization spectrum in this program. Data have '...
        'been normalized to unity.']);
end

%apply deglitching
if(deglitchrange)
    numdeglitches = size(deglitchrange); numdeglitches = numdeglitches(1);
    for nd = 1:numdeglitches
        temp_ND = normalizedData;
        deglitchFromIndex=max(floor((deglitchrange(nd,1)-WL_min)/wl_range(2)+1),1);
        deglitchToIndex=min(ceil((deglitchrange(nd,2)-WL_min)/wl_range(2)+1),nWL);
        for nTheta = 1:nT
            for nWavelen = deglitchFromIndex:deglitchToIndex;
                temp_ND(nTheta, nWavelen) = ...
                    interp1([deglitchFromIndex deglitchToIndex], ...
                        [normalizedData(nTheta,deglitchFromIndex) ...
                        normalizedData(nTheta,deglitchToIndex)], nWavelen);
            end
        end
        normalizedData = temp_ND;
    end
end

%apply running average
if (runavg)
    temp_ND = normalizedData;
    for nTheta = 1:nT
        for nWavelen = 1:length(WL)
            temp_ND(nTheta, nWavelen) = ...
                mean(normalizedData(nTheta, ...
                    (max(nWavelen-runavg,1):(min(nWavelen+runavg,nWL)))));
        end
    end
    normalizedData = temp_ND;
end

%Normalize data to unity for experiment type 'N':
if (strcmp(exptype,'N'))
    normalizedData = normalizedData./max(max(normalizedData));
end

%Prepare figure for plot
if(shouldhold)
   (gcf; hold on; legend(gca,'off')
    prettycolors = {'b' 'r' 'k' 'g' 'c' 'y' 'm'};
    linespec = prettycolors{mod(length(get(gca,'Children')),7)+1};
else
    figure; linespec = 'b'; %Note: linespec only affects 2D (line) plots.
end

%Determine human-readable experiment type for plots
if (exptype(1) == 'T')
    measuredQuantity = 'Transmission';
elseif (exptype(1) == 'R')
    measuredQuantity = 'Reflection';
elseif (strcmp(exptype,'EQE'))
    measuredQuantity = 'External Quantum Efficiency';
elseif (strcmp(exptype,'N'))
    measuredQuantity = '(Normalized)';
else
    measuredQuantity = [exptype ' (rel. to reference reading)'];
end

```

```

%Make 3-D plot for 2-dimensional data sets
if ( nT > 1 )
    hmesh = mesh(Theta, WL, normalizedData, 'DisplayName', titlename);
    xlabel(sampleinfo{7}, 'FontName', 'Helvetica', 'FontSize', 18)
    ylabel(sampleinfo{5}, 'FontName', 'Helvetica', 'FontSize', 18)
    zlabel(measuredQuantity, 'FontName', 'Helvetica', 'FontSize', 18)
    view(65, 30)
    set(hmesh, 'FaceColor', 'interp', 'EdgeColor', [0 0 0], 'MeshStyle', 'column')
    set(gca, 'FontSize', 14, 'FontName', 'Helvetica', 'LineWidth', 2)
    set(gca, 'YLim', [WL_min WL_max], 'XLim', [Theta_min Theta_max])
    title(titlename, 'FontName', 'Helvetica', 'FontSize', 18);
    if (exptype(1) == 'R')
        set(gca, 'XDir', 'reverse'); %This usually looks better
    end

%2D line plot for 1-dimensional data set
else
    plot(WL, normalizedData, linespec, 'DisplayName', titlename);
    xlabel(alname, 'FontName', 'Helvetica', 'FontSize', 18);
    title(titlename, 'FontName', 'Helvetica', 'FontSize', 18);
    ylabel(measuredQuantity, 'FontName', 'Helvetica', 'FontSize', 18);
    set(gca, 'LineWidth', 2, 'FontName', 'Helvetica', 'FontSize', 14);
end

hold on;
if (shouldhold) legend('show'); title(''); end

% Save data to workspace:
assignin('base', [samplename '_' exptype], normalizedData);
assignin('base', [samplename '_WL'], WL);
assignin('base', [samplename '_Theta'], Theta);

```

D.8.2 Diagrams of custom parts

This section provides the mechanical drawings of the two key custom parts that were machined for the integrating sphere by the Caltech instrument shop.

- Reflection-mode specimen stage

The reflection specimen stage bolts to the elevation rotation stage and suspends the specimen at the center of the sphere. It can be separated at the base to allow it to be threaded through the 1/2" sphere port. A cup-shaped light-trap seals the back of the cavity beneath the sample.
- Transmission-mode specimen holder

The transmission specimen holders affix to the 1" integrating sphere ports. Two have been built: one has a 1 cm diameter circular field while the second has a 1/2" diameter (slightly larger) field. They are designed to hold 1/2" square specimen. They can also hold a baffle or aperture over the sphere port (e.g., as used for reflection-mode measurements). A variety of aperture discs that fit within the transmission-mode specimen holders have been fabricated.

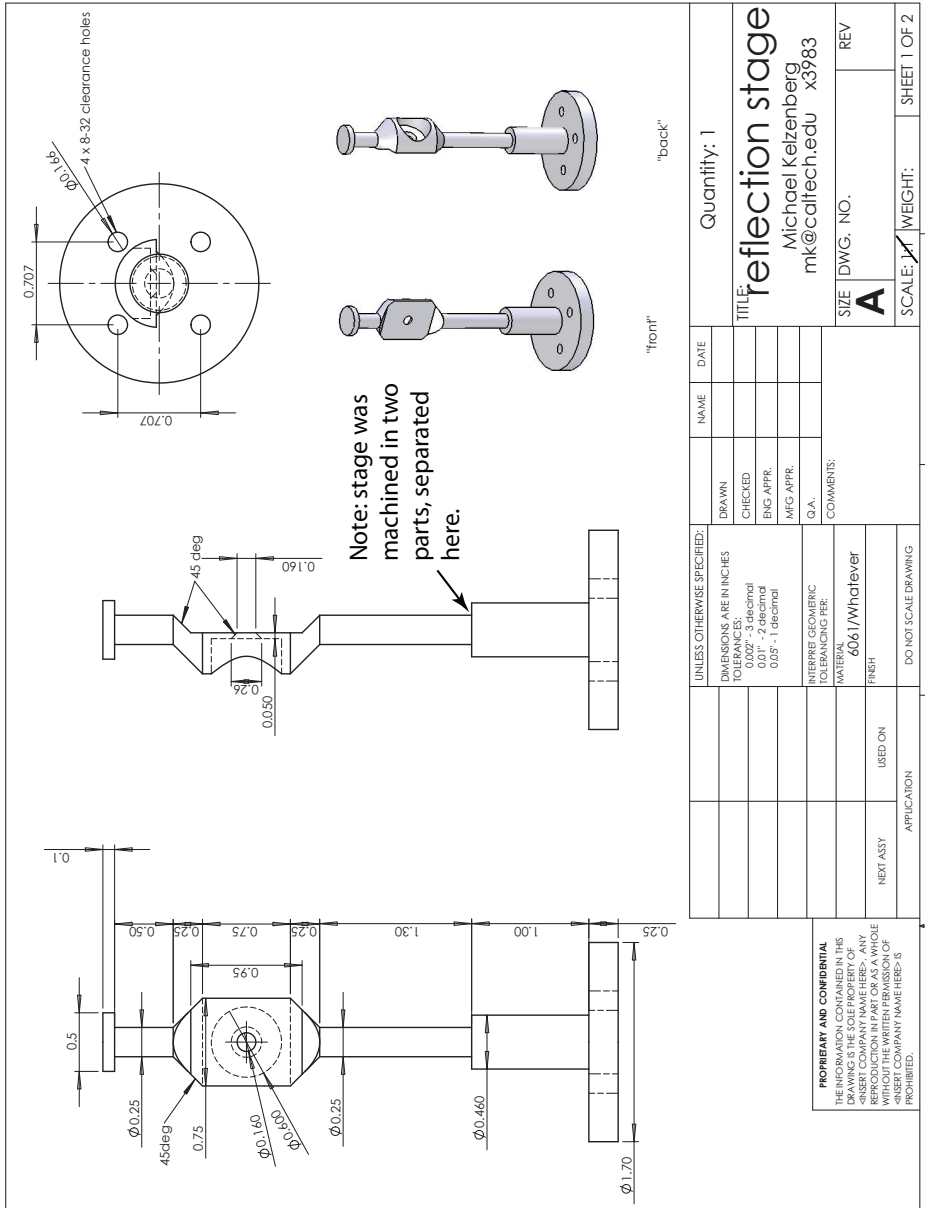


Figure D.21. Mechanical drawing: Reflection-mode specimen stage.

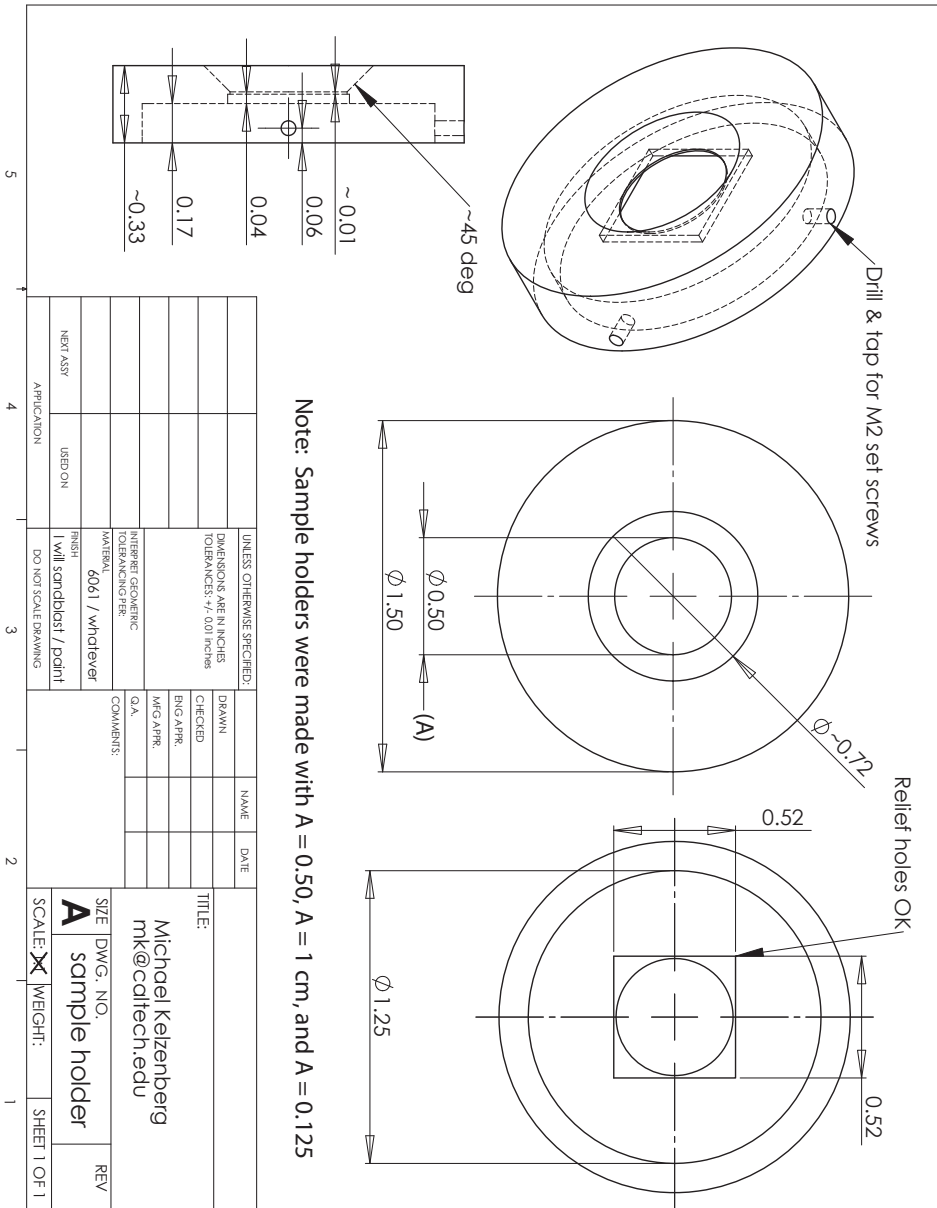


Figure D.22. Mechanical drawing: Transmission-mode specimen holder.

Bibliography

- [1] R. E. Smalley. Future global energy prosperity: The terawatt challenge, *MRS Bulletin*, 30(6):412–417, **2005**. [□](#)
- [2] D. Goodstein. *Out of Gas: The End of the Age of Oil*. New York, W. W. Norton & Company, Inc., **2004**.
- [3] N. S. Lewis. Powering the planet, *MRS Bulletin*, 32(9):808–820, **2007**. [□](#)
- [4] N. S. Lewis. Toward cost-effective solar energy use, *Science*, 315(5813):798–801, **2007**. [□](#)
- [5] International Energy Agency. Technology Roadmaps—Solar photovoltaic energy. Technical report, **2010**. [□](#)
- [6] G. Nemet. Learning curves for photovoltaics. Technical report, International Energy Agency, **2007**.
- [7] J. Perlin. The silicon solar cell turns 50. Technical Report NREL Report No. BR-520-33947, **2004**. [□](#)
- [8] R. M. Swanson. Device physics for backside-contact solar cells. In *Conference Record of the Thirty-third IEEE Photovoltaics Specialists Conference*, **2008**.
- [9] A. Luque and S. Hegedus. *Handbook of Photovoltaic Science and Engineering*. Wiley, **2003**.
- [10] C. del Cañizo, G. del Coso, and W. C. Sinke. Crystalline silicon solar module technology: Towards the 1 Euro per watt-peak goal, *Progress in Photovoltaics: Research and Applications*, 17(3):199–209, **2009**. [□](#)
- [11] First Solar. Fast Facts: Company Overview, **2010**. [□](#)
- [12] A. Shah, P. Torres, R. Tscharnner, N. Wyrsh, and H. Keppner. Photovoltaic technology: The case for thin-film solar cells, *Science*, 285(5428):692–698, **1999**. [□](#)
- [13] R. Brendel. *Thin-Film Crystalline Silicon Solar Cells - Physics and Technology*. Wiley, **2003**. [□](#)
- [14] G. Beaucarne and A. Slaoui. Thin film polycrystalline silicon solar cells. In Poortmans and Arkhipov, editors, *Thin Film Solar Cells*. John Wiley & Sons, **2006**. [□](#)

- [15] ASTM. ASTM G173 - 03e1 Standard tables for reference solar spectral irradiances: Direct normal and hemispherical on 37° tilted surface, **2003**. [□](#)
- [16] W. Shockley and H. J. Queisser. Detailed balance limit of efficiency of p-n junction solar cells, *Journal of Applied Physics*, 32(3):510–519, **1961**. [□](#)
- [17] R. M. Swanson. Approaching the 29% limit efficiency of silicon solar cells. In *Conference Record of the Thirty-First IEEE Photovoltaic Specialists Conference*, pages 889–894, **2005**. [□](#)
- [18] T. Tiedje, E. Yablonovitch, G. D. Cody, and B. G. Brooks. Limiting efficiency of silicon solar-cells, *IEEE Transactions on Electron Devices*, 31(5):711–716, **1984**. [□](#)
- [19] M. A. Green, K. Emery, Y. Hishikawa, and W. Warta. Solar cell efficiency tables (Version 34), *Progress in Photovoltaics: Research and Applications*, 17(5):320–326, **2009**. [□](#)
- [20] P. Campbell and M. A. Green. The limiting efficiency of silicon solar cells under concentrated sunlight, *IEEE Transactions on Electron Devices*, 33(2):234–239, **1986**. [□](#)
- [21] M. A. Green and S. R. Wenham. Novel parallel multijunction solar cell, *Applied Physics Letters*, 65(23):2907–2909, **1994**. [□](#)
- [22] W. P. Rahilly. Vertical multijunction solar cells. In *Conference Record of the Ninth IEEE Photovoltaic Specialists Conference*, pages 44–52, Silver Spring, MD, USA, **1972**. IEEE.
- [23] T. B. S. Chadda and M. Wolf. Comparison of vertical multi-junction and conventional solar cell performance. In *Conference Record of the Tenth IEEE Photovoltaic Specialists Conference*, pages 52–57, **1974**.
- [24] A. Gover and P. Stella. Vertical multijunction solar-cell one-dimensional analysis, *IEEE Transactions on Electron Devices*, 21(6):351–356, **1974**. [□](#)
- [25] W. W. Lloyd. Fabrication of an improved vertical multijunction solar cell. In *Conference Record of the Eleventh IEEE Photovoltaic Specialists Conference*, pages 349–355, Scottsdale, AZ, **1975**. Conference Record. (A76-14727 04-44) New York, Institute of Electrical and Electronics Engineers, Inc.
- [26] R. M. Swanson, S. K. Beckwith, R. A. Crane, W. D. Eades, K. Young Hoon, R. A. Sinton, and S. E. Swirhun. Point-contact silicon solar cells, *IEEE Transactions on Electron Devices*, 31(5):661–664, **1984**. [□](#)
- [27] R. M. Swanson. Point-contact solar cells: Modeling and experiment, *Solar cells*, 17(1):85–118, **1986**. [□](#)

- [28] K. J. Weber, A. W. Blakers, M. J. Stocks, J. H. Babaei, V. A. Everett, A. J. Neuendorf, and P. J. Verlinden. A novel low-cost, high-efficiency micromachined silicon solar cell, *IEEE Electron Device Letters*, 25(1):37–39, **2004**. [□](#)
- [29] J. Yoon, A. J. Baca, S. I. Park, P. Elvikis, J. B. Geddes, L. F. Li, R. H. Kim, J. L. Xiao, S. D. Wang, T. H. Kim, M. J. Motala, B. Y. Ahn, E. B. Duoss, J. A. Lewis, R. G. Nuzzo, P. M. Ferreira, Y. G. Huang, A. Rockett, and J. A. Rogers. Ultrathin silicon solar microcells for semitransparent, mechanically flexible and microconcentrator module designs, *Nature Materials*, 7(11):907–915, **2008**. [□](#)
- [30] Z. Liu, A. Masuda, T. Nagai, T. Miyazaki, M. Takano, M. Takano, H. Yoshigahara, K. Sakai, K. Asai, and M. Kondo. A concentrator module of spherical Si solar cell, *Solar Energy Materials and Solar Cells*, 91(19):1805–1810, **2007**. [□](#)
- [31] A. A. Shchetinin, A. I. Drozhzhin, N. K. Sedykh, and E. P. Novokreshchenova. Photoconverters based on silicon-crystal whiskers, *Measurement Techniques*, 41(4):502–204, **1978**. [□](#)
- [32] H. Diepers. Method of manufacturing solar cells, utilizing single-crystal whisker growth, *U.S. Patent Number 4,155,781*, **1979**.
- [33] R. S. Wagner and W. C. Ellis. Vapor-liquid-solid mechanism of single crystal growth, *Applied Physics Letters*, 4(5):89–90, **1964**. [□](#)
- [34] R. S. Wagner and C. J. Doherty. Controlled vapor-liquid-solid growth of silicon crystals, *Journal of the Electrochemical Society*, 113(12):1300–1305, **1966**. [□](#)
- [35] R. S. Wagner. Defects in silicon crystals grown by the VLS technique, *Journal of Applied Physics*, 38(4):1554–1560, **1967**. [□](#)
- [36] V. Schmidt, J. V. Wittemann, and U. Gösele. Growth, thermodynamics, and electrical properties of silicon nanowires, *Chemical Reviews*, 110(1):361–388, **2010**. [□](#)
- [37] B. M. Kayes, M. A. Filler, M. C. Putnam, M. D. Kelzenberg, N. S. Lewis, and H. A. Atwater. Growth of vertically aligned Si wire arrays over large areas ($>1 \text{ cm}^2$) with Au and Cu catalysts, *Applied Physics Letters*, 91(10):103110, **2007**. [□](#)
- [38] A. E. Cha. Solar energy firms leave waste behind in China, *Washington Post*, **9 March 2008**.
- [39] B. M. Kayes. *Radial pn junction, wire array solar cells*. PhD thesis, California Institute of Technology, **2008**. [□](#)
- [40] L. Tsakalakos, J. Balch, J. Fronheiser, B. A. Korevaar, O. Sulima, and J. Rand. Silicon nanowire solar cells, *Applied Physics Letters*, 91(23):233117, **2007**. [□](#)

- [41] B. M. Kayes, H. A. Atwater, and N. S. Lewis. Comparison of the device physics principles of planar and radial p-n junction nanorod solar cells, *Journal of Applied Physics*, 97(11):114302, **2005**. [□](#)
- [42] K. E. Plass, M. A. Filler, J. M. Spurgeon, B. M. Kayes, S. Maldonado, B. S. Brunschwig, H. A. Atwater, and N. S. Lewis. Flexible polymer-embedded Si wire arrays, *Advanced Materials*, 21(3):325–328, **2009**. [□](#)
- [43] J. M. Spurgeon, K. E. Plass, B. M. Kayes, B. S. Brunschwig, H. A. Atwater, and N. S. Lewis. Repeated epitaxial growth and transfer of arrays of patterned, vertically aligned, crystalline Si wires from a single Si(111) substrate, *Applied Physics Letters*, 93(3):032112, **2008**. [□](#)
- [44] J. O. Schumacher and W. Wettling. Device physics of silicon solar cells. In Archer and Hill, editors, *Clean Electricity from Photovoltaics*. Imperial College Press, London, **2001**.
- [45] P. P. Altermatt, G. Heiser, A. G. Aberle, A. Wang, J. Zhao, S. J. Robinson, S. Bowden, and M. A. Green. Spatially resolved analysis and minimization of resistive losses in high-efficiency Si solar cells, *Progress in Photovoltaics: Research and Applications*, 4(6):399–414, **1996**. [□](#)
- [46] J. Zhao, A. Wang, P. P. Altermatt, S. R. Wenham, and M. A. Green. 24% efficient perl silicon solar cell: Recent improvements in high efficiency silicon cell research, *Solar Energy Materials and Solar Cells*, 41–42:87–99, **1996**. [□](#)
- [47] S. M. Sze and K. N. Kwok. *Physics of Semiconductor Devices*. Hoboken, NJ, John Wiley & Sons, 3rd edition, **2007**.
- [48] A. L. Fahrenbruck and R. H. Bube. *Fundamentals of Solar Cells: Photovoltaic Solar Energy Conversion*. Academic Press, New York, **1983**.
- [49] C. Zechner, P. Fath, G. Willeke, and E. Bucher. Two- and three-dimensional optical carrier generation determination in crystalline silicon solar cells, *Solar Energy Materials and Solar Cells*, 51(3-4):255–267, **1998**. [□](#)
- [50] R. Bisconti and H. A. Ossenbrink. Optical modelling of silicon cells in spherical shape, *Solar Energy Materials and Solar Cells*, 48(1-4):1–6, **1997**. [□](#)
- [51] L. Hu and G. Chen. Analysis of optical absorption in silicon nanowire arrays for photovoltaic applications, *Nano Letters*, 7(11):3249–3252, **2007**. [□](#)
- [52] L. Tsakalacos, J. Balch, J. Fronheiser, M.-Y. Shih, S. F. LeBoeuf, M. Pietrzykowski, P. J. Codella, B. A. Korevaar, O. V. Sulima, J. Rand, A. Davuluru, and U. Rapol. Strong broadband optical absorption in silicon nanowire films, *Journal of Nanophotonics*, 1(1):013552–10, **2007**. [□](#)

- [53] P. P. Altermatt, Y. Yang, T. Langer, A. Schenk, and R. Brendel. Simulation of optical properties of Si wire cells. In *Proceedings of the Thirty-Fourth IEEE Photovoltaic Specialists Conference*, pages 1–6, Philadelphia, PA, **2009**. [□](#)
- [54] J. Li, H. Yu, S. M. Wong, X. Li, G. Zhang, P. G.-Q. Lo, and D.-L. Kwong. Design guidelines of periodic Si nanowire arrays for solar cell application, *Applied Physics Letters*, 95(24):243113–3, **2009**. [□](#)
- [55] C. Lin and M. L. Povinelli. Optical absorption enhancement in silicon nanowire arrays with a large lattice constant for photovoltaic applications, *Optics Express*, 17(22):19371–19381, **2009**. [□](#)
- [56] L. Cao, P. Fan, A. P. Vasudev, J. S. White, Z. Yu, W. Cai, J. A. Schuller, S. Fan, and M. L. Brongersma. Semiconductor nanowire optical antenna solar absorbers, *Nano Letters*, 10(2):439–445, **2010**. [□](#)
- [57] S. M. Wong, H. Y. Yu, J. S. Li, G. Zhang, P. Lo, and D. L. Kwong. Design high-efficiency Si nanopillar-array-textured thin-film solar cell, *IEEE Transactions on Electron Devices*, 31(4):335–337, **2010**. [□](#)
- [58] H. K. Gummel. A self-consistent iterative scheme for one-dimensional steady state transistor calculations, *IEEE Transactions on Electron Devices*, 11(10):455–465, **1964**. [□](#)
- [59] D. L. Scharfetter and H. K. Gummel. Calculation of large-signal transients in avalanche diode oscillators. In *Proceedings of the 1965 International Electron Devices Meeting*, volume 11, pages 15–15, **1965**. [□](#)
- [60] J. G. Fossum. Computer-aided numerical analysis of silicon solar cells, *Solid-State Electronics*, 19(4):269–277, **1976**. [□](#)
- [61] D. T. Rover, P. A. Basore, and G. M. Thorson. Solar cell modeling on personal computers. In *Conference Record of the Eighteenth IEEE Photovoltaic Specialists Conference*, pages 703–709, **1985**. [□](#)
- [62] P. J. McElheny, J. K. Arch, and S. J. Fonash. Assessment of the surface-photovoltage diffusion-length measurement, *Applied Physics Letters*, 51(20):1611–1613, **1987**. [□](#)
- [63] A. Froitzheim, R. Stangl, L. Elstner, M. Kriegel, and W. Fuhs. AFORS-HET: A computer-program for the simulation of heterojunction solar cells to be distributed for public use. In *Proceedings of Third World Conference on Photovoltaic Energy Conversion*, volume 1, pages 279–282, **2003**. [□](#)
- [64] P. P. Altermatt, G. Heiser, and M. A. Green. Numerical quantification and minimization of perimeter losses in high-efficiency silicon solar cells, *Progress in Photovoltaics: Research and Applications*, 4(5):355–367, **1996**. [□](#)

- [65] A. G. Aberle, G. Heiser, and M. A. Green. Two-dimensional numerical optimization study of the rear contact geometry of high-efficiency silicon solar cells, *Journal of Applied Physics*, 75(10):5391–5405, **1994**. [□](#)
- [66] H. Ohtsuka, Y. Ohkura, T. Uematsu, and T. Warabisako. Three-dimensional numerical analysis of contact geometry in back-contact solar cells, *Progress in Photovoltaics: Research and Applications*, 2(4):275–285, **1994**. [□](#)
- [67] R. E. Bank, D. J. Rose, and W. Fichtner. Numerical methods for semiconductor device simulation, *IEEE Transactions on Electron Devices*, 30(9):1031–1041, **1983**. [□](#)
- [68] Synopsys Inc. *Sentaurus Device User Guide*. Version a-2009.06.sp2 edition, **2009**.
- [69] G. Masetti, M. Severi, and S. Solmi. Modeling of carrier mobility against carrier concentration in arsenic-, phosphorus-, and boron-doped silicon, *IEEE Transactions on Electron Devices*, 30(7):764–769, **1983**. [□](#)
- [70] Synopsys Inc. Optimizer User Guide. (Sentaurus TCAD Version C-2009.06), **2009**.
- [71] M. J. Keevers and M. A. Green. Efficiency improvements of silicon solar cells by the impurity photovoltaic effect. In *Conference Record of the Twenty-Third IEEE Photovoltaic Specialists Conference*, pages 140–146, **1993**. [□](#)
- [72] E. C. Garnett and P. Yang. Silicon nanowire radial p-n junction solar cells, *Journal of the American Chemical Society*, 130(29):9224–5, **2008**. [□](#)
- [73] O. L. Muskens, J. G. m. Rivas, R. E. Algra, E. P. A. M. Bakkers, and A. Lagendijk. Design of light scattering in nanowire materials for photovoltaic applications, *Nano Letters*, 8(9):2638–2642, **2008**. [□](#)
- [74] R. A. Street, P. Qi, R. Lujan, and W. S. Wong. Reflectivity of disordered silicon nanowires, *Applied Physics Letters*, 93(16):163109, **2008**. [□](#)
- [75] D. E. Aspnes. Optical properties of Si. In Hull, editor, *Properties of Crystalline Silicon*, page 677. INSPEC, IEE, London UK, **1999**.
- [76] J. A. Woollam, W. A. McGahan, and B. Johs. Spectroscopic ellipsometry studies of indium tin oxide and other flat-panel display multilayer materials, *Thin Solid Films*, 241(1-2):44–46, **1994**. [□](#)
- [77] E. D. Palik. *Handbook of Optical Constants of Solids*. New York, Academic Press, **1997**.
- [78] J. G. Fossum, R. P. Mertens, D. S. Lee, and J. F. Nijs. Carrier recombination and lifetime in highly doped silicon, *Solid-State Electronics*, 26(6):569–576, **1983**. [□](#)

- [79] M. S. Tyagi and R. Van Overstraeten. Minority carrier recombination in heavily-doped silicon, *Solid-State Electronics*, 26(6):577–597, **1983**. [□](#)
- [80] M. C. Putnam, M. A. Filler, B. M. Kayes, M. D. Kelzenberg, Y. Guan, N. S. Lewis, J. M. Eiler, and H. A. Atwater. Secondary ion mass spectrometry of vapor-liquid-solid grown, Au-catalyzed, Si wires, *Nano Letters*, 8(10):3109–3113, **2008**. [□](#)
- [81] D. K. Schroder, R. N. Thomas, and J. C. Swartz. Free carrier absorption in silicon, *IEEE Journal of Solid-State Circuits*, 13(1):180–187, **1978**. [□](#)
- [82] M. J. Keevers and M. A. Green. Extended infrared response of silicon solar cells and the impurity photovoltaic effect, *Solar Energy Materials and Solar Cells*, 41–42:195–204, **1996**. [□](#)
- [83] G. R. Fowles. *Introduction to Modern Optics*. New York. (Dover reprint), Holt, Rinehart, and Winston, 2nd edition, **1975**.
- [84] S. Ping. Optical absorption of thin film on a Lambertian reflector substrate, *IEEE Transactions on Electron Devices*, 31(5):634–636, **1984**. [□](#)
- [85] E. Yablonovitch. Statistical ray optics, *Journal of the Optical Society of America*, 72(7):899–907, **1982**. [□](#)
- [86] P. Campbell. Enhancement of light absorption from randomizing and geometric textures, *Journal of the Optical Society of America B: Optical Physics*, 10(12):2410–2415, **1993**. [□](#)
- [87] J. M. Gee. Optically enhanced absorption in thin silicon layers using photonic crystals. In *Conference Record of the Twenty-Ninth IEEE Photovoltaic Specialists Conference*, pages 150–153, **2002**.
- [88] P. Bermel, C. Luo, L. Zeng, L. C. Kimerling, and J. D. Joannopoulos. Improving thin-film crystalline silicon solar cell efficiencies with photonic crystals, *Optics Express*, 15(25):16986–17000, **2007**. [□](#)
- [89] R. S. Wagner and W. C. Ellis. Vapor-liquid-solid mechanism of crystal growth and its application to silicon, *Transactions of the Metallurgical Society of AIME*, 233(6):1053–1064, **1965**.
- [90] Z.-P. Yang, L. Ci, J. A. Bur, S.-Y. Lin, and P. M. Ajayan. Experimental observation of an extremely dark material made by a low-density nanotube array, *Nano Letters*, 8(2):446–451, **2008**. [□](#)
- [91] W. Shockley. Electrons, holes, and traps, *Proceedings of the IRE*, 46(6):973–990, **1958**. [□](#)
- [92] J. Zhu, Z. Yu, G. F. Burkhard, C.-M. Hsu, S. T. Connor, Y. Xu, Q. Wang, M. McGehee, S. Fan, and Y. Cui. Optical absorption enhancement in amorphous silicon nanowire and nanocone arrays, *Nano Letters*, 9(1):279–282, **2009**. [□](#)

- [93] C. Wu, C. H. Crouch, L. Zhao, J. E. Carey, R. Younkin, J. A. Levinson, E. Mazur, R. M. Farrell, P. Gothoskar, and A. Karger. Near-unity below-band-gap absorption by microstructured silicon, *Applied Physics Letters*, 78(13):1850–1852, **2001**. [□](#)
- [94] M. J. Bierman and S. Jin. Potential applications of hierarchical branching nanowires in solar energy conversion, *Energy & Environmental Science*, 2(10):1050–1059, **2009**. [□](#)
- [95] T. Stelzner, M. Pietsch, G. Andra, F. Falk, E. Ose, and S. Christiansen. Silicon nanowire-based solar cells, *Nanotechnology*, 19(29):295203, **2008**. [□](#)
- [96] O. Gunawan and S. Guha. Characteristics of vapor-liquid-solid grown silicon nanowire solar cells, *Solar Energy Materials and Solar Cells*, 93(8):1388–1393, **2009**. [□](#)
- [97] J. A. Jacquez and H. F. Kuppenheim. Theory of the integrating sphere, *Journal of the Optical Society of America*, 45(6):460–466, **1955**. [□](#)
- [98] D. K. Edwards, J. T. Gier, K. E. Nelson, and R. D. Roddick. Integrating sphere for imperfectly diffuse samples, *Journal of the Optical Society of America*, 51(11):1279–1288, **1961**. [□](#)
- [99] G. A. Zerlaut and T. E. Anderson. Multiple-integrating sphere spectrophotometer for measuring absolute spectral reflectance and transmittance, *Applied Optics*, 20(21):3797–3804, **1981**. [□](#)
- [100] B. Marion, B. Kroposki, K. Emery, J. del Cueto, D. Myers, and C. Osterwald. Validation of a photovoltaic module energy ratings procedure at NREL. Technical Report NREL/TP-520-26909, **1999**. [□](#)
- [101] J. L. Balenzategui and F. Chenlo. Measurement and analysis of angular response of bare and encapsulated silicon solar cells, *Solar Energy Materials and Solar Cells*, 86(1):53–83, **2005**. [□](#)
- [102] Y. Miyakea, R. Shimokawab, Y. Nakanishia, and Y. Hamakawac. Global radiation model and angular distribution of the diffuse irradiance, *Solar cells*, 20(2):127, **1987**. [□](#)
- [103] A. Parretta, P. P. Altermatt, and J. Zhao. Transmittance from photovoltaic materials under diffuse light, *Solar Energy Materials and Solar Cells*, 75(3-4):387–395, **2003**. [□](#)
- [104] J. I. Pankove. *Optical Processes in Semiconductors*. Englewood Cliffs, New Jersey. (Dover reprint), Prentice-Hall, Inc., **1971**.
- [105] M. Wolf. Limitations and possibilities for improvement of photovoltaic solar energy converters: Part I: Considerations for Earth’s surface operation, *Proceedings of the IRE*, 48(7):1246–1263, **1960**. [□](#)

- [106] M. J. Keevers and M. A. Green. Efficiency improvements of silicon solar cells by the impurity photovoltaic effect, *Journal of Applied Physics*, 75(8):4022–4031, **1994**. [□](#)
- [107] A. S. Brown and M. A. Green. Impurity photovoltaic effect: Fundamental energy conversion efficiency limits, *Journal of Applied Physics*, 92(3):1329–1336, **2002**. [□](#)
- [108] Z. Huang, J. E. Carey, M. Liu, X. Guo, E. Mazur, and J. C. Campbell. Microstructured silicon photodetector, *Applied Physics Letters*, 89(3):033506, **2006**. [□](#)
- [109] C. T. Sah, A. F. Tasch, and D. K. Schroder. Recombination properties of the gold acceptor level in silicon using the impurity photovoltaic effect, *Physical Review Letters*, 19(2):71, **1967**. [□](#)
- [110] G. Guttler and H. J. Queisser. Photovoltaic effect of gold in silicon, *Journal of Applied Physics*, 40(12):4994–4995, **1969**. [□](#)
- [111] G. Guttler and H. J. Queisser. Impurity photovoltaic effect in silicon, *Energy Conversion*, 10(2):51–55, **1970**. [□](#)
- [112] N. Ferralis, R. Maboudian, and C. Carraro. Temperature-induced self-pinning and nanolayering of AuSi eutectic droplets, *Journal of the American Chemical Society*, 130(8):2681–2685, **2008**. [□](#)
- [113] C. M. Hessel, A. T. Heitsch, and B. A. Korgel. Gold seed removal from the tips of silicon nanorods, *Nano Letters*, 10(1):176–180, **2009**. [□](#)
- [114] M. Seibt and K. Graff. Characterization of haze-forming precipitates in silicon, *Journal of Applied Physics*, 63(9):4444–4450, **1988**. [□](#)
- [115] W. J. Shattes and H. A. R. Wegener. Lifetime and nickel precipitation in silicon, *Journal of Applied Physics*, 29(5):866–866, **1958**. [□](#)
- [116] A. A. Istratov, C. Flink, H. Hieslmair, S. A. McHugo, and E. R. Weber. Diffusion, solubility and gettering of copper in silicon, *Materials Science and Engineering B*, 72(2-3):99–104, **2000**. [□](#)
- [117] M. A. Green, Z. Jianhua, A. Wang, and S. R. Wenham. Very high efficiency silicon solar cells-science and technology, *IEEE Transactions on Electron Devices*, 46(10):1940–1947, **1999**. [□](#)
- [118] B. Kumar, T. Baskara Pandian, E. Sreekiran, and S. Narayanan. Benefit of dual layer silicon nitride anti-reflection coating. In *Conference Record of the Thirty-first IEEE Photovoltaic Specialists Conference*, pages 1205–1208, **2005**. [□](#)
- [119] C. C. Johnson, T. Wydeven, and K. Donohoe. Plasma-enhanced CVD silicon-nitride anti-reflection coatings for solar-cells, *Solar Energy*, 31(4):355–358, **1983**. [□](#)

- [120] J. Schmidt, M. Kerr, and A. Cuevas. Surface passivation of silicon solar cells using plasma-enhanced chemical-vapour-deposited SiN films and thin thermal SiO₂/plasma SiN stacks, *Semiconductor Science and Technology*, 16(3):164–170, **2001**. [□](#)
- [121] A. G. Aberle and R. Hezel. Progress in low-temperature surface passivation of silicon solar cells using remote-plasma silicon nitride, *Progress in Photovoltaics: Research and Applications*, 5(1):29–50, **1997**. [□](#)
- [122] K. R. McIntosh, R. M. Swanson, and J. E. Cotter. A simple ray tracer to compute the optical concentration of photovoltaic modules, *Progress in Photovoltaics: Research and Applications*, 14(2):167–177, **2006**. [□](#)
- [123] O. Berger, D. Inns, and A. G. Aberle. Commercial white paint as back surface reflector for thin-film solar cells, *Solar Energy Materials and Solar Cells*, 91(13):1215–1221, **2007**. [□](#)
- [124] E. Garnett and P. Yang. Light trapping in silicon nanowire solar cells, *Nano Letters*, 10(3):1082–1087, **2010**. [□](#)
- [125] S. W. Boettcher, J. M. Spurgeon, M. C. Putnam, E. L. Warren, D. B. Turner-Evans, M. D. Kelzenberg, J. R. Maiolo, H. A. Atwater, and N. S. Lewis. Energy-conversion properties of vapor-liquid-solid-grown silicon wire-array photocathodes, *Science*, 327(5962):185–187, **2010**. [□](#)
- [126] J. M. Spurgeon, S. W. Boettcher, M. D. Kelzenberg, B. S. Brunschwig, H. A. Atwater, and N. S. Lewis. Flexible, polymer-supported, Si wire array photoelectrodes, *Advanced Materials*, 22(30):3277–3281, **2010**. [□](#)
- [127] J. Kupec and B. Witzigmann. Dispersion, wave propagation and efficiency analysis of nanowire solar cells, *Optics Express*, 17(12):10399–10410, **2009**. [□](#)
- [128] Z. Fan, H. Razavi, J. w. Do, A. Moriwaki, O. Ergen, Y.-L. Chueh, P. W. Leu, J. C. Ho, T. Takahashi, L. A. Reichertz, S. Neale, K. Yu, M. Wu, J. W. Ager, and A. Javey. Three-dimensional nanopillar-array photovoltaics on low-cost and flexible substrates, *Nature Materials*, 8(8):648–653, **2009**. [□](#)
- [129] J. R. Davis Jr., A. Rohatgi, R. H. Hopkins, P. D. Blais, P. Rai-Choudhury, J. R. McCormick, and H. C. Mollenkopf. Impurities in silicon solar cells, *IEEE Transactions on Electron Devices*, 27(4):677–687, **1980**. [□](#)
- [130] R. H. Hopkins and A. Rohatgi. Impurity effects in silicon for high-efficiency solar-cells, *Journal of Crystal Growth*, 75(1):67–79, **1986**. [□](#)
- [131] H. Savin, M. Yli-Koski, and A. Haarahiltunen. Role of copper in light induced minority-carrier lifetime degradation of silicon, *Applied Physics Letters*, 95(15):152111–3, **2009**. [□](#)
- [132] T. Saitoh, H. Hashigami, S. Rein, and S. Glunz. Overview of light degradation research on crystalline silicon solar cells, *Progress in Photovoltaics: Research and Applications*, 8(5):537–547, **2000**. [□](#)

- [133] A. Goetzberger, C. Hebling, and H.-W. Schock. Photovoltaic materials, history, status and outlook, *Materials Science and Engineering: R: Reports*, 40(1):1–46, **2003**. [□](#)
- [134] R. Hull. *Properties of crystalline silicon*. London, INSPEC, **1999**.
- [135] T. F. Ciszek. Silicon material quality and throughput: the high and the low, the fast and the slow. In *Conference Record of the Twentieth IEEE Photovoltaic Specialists Conference*, pages 31–38 vol.1, **1988**. [□](#)
- [136] V. L. Dalal and P. Sharma. Defect density and diffusion length of holes in nanocrystalline silicon devices, *Applied Physics Letters*, 86(10):103510–3, **2005**. [□](#)
- [137] E. Vallat-Sauvain, A. Shah, and J. Bailat. Advances in microcrystalline silicon solar cell technologies. In Poortmans and Arkhipov, editors, *Thin Film Solar Cells*. John Wiley & Sons, **2006**. [□](#)
- [138] R. A. Street. *Hydrogenated Amorphous Silicon*. Cambridge University Press, **1991**. [□](#)
- [139] M. Zeman. Advanced amorphous silicon solar cell technologies. In Poortmans and Arkhipov, editors, *Thin Film Solar Cells*. John Wiley & Sons, Ltd., **2006**. [□](#)
- [140] B. Chalmers. *Principles of Solidification*. New York, Wiley, **1964**.
- [141] A. A. Istratov, T. Buonassisi, R. J. McDonald, A. R. Smith, R. Schindler, J. A. Rand, J. P. Kalejs, and E. R. Weber. Metal content of multicrystalline silicon for solar cells and its impact on minority carrier diffusion length, *Journal of Applied Physics*, 94(10):6552–6559, **2003**. [□](#)
- [142] A. A. Shchetinin, V. A. Nebol'sin, O. D. Kozenkov, A. F. Tatarenkov, A. I. Dunaev, and E. P. Novokreshchenova. Distribution coefficient of the initiating impurity and its influence on the electrical-resistivity of filamentary silicon-crystals, *Inorganic Materials (Translation of Neorganicheskie Materialy)*, 27(7):1342–1344, **1991**.
- [143] Y. Wang, V. Schmidt, S. Senz, and U. Gösele. Epitaxial growth of silicon nanowires using an aluminium catalyst, *Nature Nanotechnology*, 1(3):186–189, **2006**. [□](#)
- [144] Y. Ke, X. Weng, J. M. Redwing, C. M. Eichfeld, T. R. Swisher, S. E. Mohny, and Y. M. Habib. Fabrication and electrical properties of Si nanowires synthesized by Al catalyzed vapor-liquid-solid growth, *Nano Letters*, 9(12):4494–4499, **2009**. [□](#)
- [145] R. S. Wagner, W. C. Ellis, K. A. Jackson, and S. M. Arnold. Study of the filamentary growth of silicon crystals from the vapor, *Journal of Applied Physics*, 35(10):2993–3000, **1964**. [□](#)

- [146] M. I. den Hertog, J. L. Rouviere, F. Dhalluin, P. Gentile, P. Ferret, C. Termon, and T. Baron. Gold catalyzed silicon nanowires: Defects in the wires and gold on the wires. In *Microscopy of Semiconducting Materials 2007*, pages 217–220. Springer Netherlands, **2008**. [□](#)
- [147] J. E. Allen, E. R. Hemesath, D. E. Perea, J. L. Lensch-Falk, Z. Y. Li, F. Yin, M. H. Gass, P. Wang, A. L. Bleloch, R. E. Palmer, and L. J. Lauhon. High-resolution detection of Au catalyst atoms in Si nanowires, *Nature Nanotechnology*, 3(3):168–173, **2008**. [□](#)
- [148] D. E. Perea, J. E. Allen, S. J. May, B. W. Wessels, D. N. Seidman, and L. J. Lauhon. Three-dimensional nanoscale composition mapping of semiconductor nanowires, *Nano Letters*, 6(2):181–185, **2005**. [□](#)
- [149] Y. Cui, Z. H. Zhong, D. L. Wang, W. U. Wang, and C. M. Lieber. High performance silicon nanowire field effect transistors, *Nano Letters*, 3(2):149–152, **2003**. [□](#)
- [150] Y. Gu, E. S. Kwak, J. L. Lensch, J. E. Allen, T. W. Odom, and L. J. Lauhon. Near-field scanning photocurrent microscopy of a nanowire photodetector, *Applied Physics Letters*, 87(4):043111, **2005**. [□](#)
- [151] T. Hanrath and B. A. Korgel. Influence of surface states on electron transport through intrinsic Ge nanowires, *Journal of Physical Chemistry B*, 109(12):5518–5524, **2005**. [□](#)
- [152] A. Yeonghwan, J. Dunning, and J. Park. Scanning photocurrent imaging and electronic band studies in silicon nanowire field effect transistors, *Nano Letters*, 5(7):1367–1370, **2005**. [□](#)
- [153] J. E. Allen, G. Yi, J. P. Romankiewicz, J. L. Lensch, S. J. May, T. W. Odom, B. W. Wessels, and L. J. Lauhon. Measurement of minority carrier diffusion lengths in semiconductor nanowires. In *IEEE Device Research Conference*, pages 289–290, University Park, PA, USA, 26–28 June 2006, **2006**. IEEE, Piscataway, NJ, USA. [□](#)
- [154] Y. Gu, J. P. Romankiewicz, J. K. David, J. L. Lensch, and L. J. Lauhon. Quantitative measurement of the electron and hole mobility-lifetime products in semiconductor nanowires, *Nano Letters*, 6(5):948–952, **2006**. [□](#)
- [155] Y. Gu, J. P. Romankiewicz, J. K. David, J. L. Lensch, L. J. Lauhon, E. S. Kwak, and T. W. Odom. Local photocurrent mapping as a probe of contact effects and charge carrier transport in semiconductor nanowire devices, *Journal of Vacuum Science & Technology, B: Microelectronics Processing and Phenomena*, 24:2172–2177, **2006**. [□](#)
- [156] Y. Gu, J. P. Romankiewicz, and L. J. Lauhon. Quantitative characterization of carrier transport in nanowire photodetectors, *Proceedings of SPIE*, 6479:64790C, **2007**. [□](#)

- [157] B. Tian, X. Zheng, T. J. Kempa, Y. Fang, N. Yu, G. Yu, J. Huang, and C. M. Lieber. Coaxial silicon nanowires as solar cells and nanoelectronic power sources, *Nature*, 449(7164):885–889, **2007**. [□](#)
- [158] A. Colli, A. Fasoli, C. Ronning, S. Pisana, S. Piscanec, and A. C. Ferrari. Ion beam doping of silicon nanowires, *Nano Letters*, 8(8):2188–2193, **2008**. [□](#)
- [159] T. J. Kempa, B. Tian, D. R. Kim, J. Hu, X. Zheng, and C. M. Lieber. Single and tandem axial p-i-n nanowire photovoltaic devices, *Nano Letters*, 8(10):3456–3460, **2008**. [□](#)
- [160] B. Tian, T. J. Kempa, and C. M. Lieber. Single nanowire photovoltaics, *Chemical Society Reviews*, 38(1):16, **2008**. [□](#)
- [161] J. E. Allen, E. R. Hemesath, and L. J. Lauhon. Scanning photocurrent microscopy analysis of Si nanowire field-effect transistors fabricated by surface etching of the channel, *Nano Letters*, 9(5):1903–1908, **2009**. [□](#)
- [162] J. E. Allen, D. E. Perea, E. R. Hemesath, and L. J. Lauhon. Nonuniform nanowire doping profiles revealed by quantitative scanning photocurrent microscopy, *Advanced Materials*, 21(30):3067–3072, **2009**. [□](#)
- [163] Y. Dong, B. Tian, T. J. Kempa, and C. M. Lieber. Coaxial group III nitride nanowire photovoltaics, *Nano Letters*, 9(5):2183–2187, **2009**. [□](#)
- [164] P. Xie, Y. Hu, Y. Fang, J. Huang, and C. M. Lieber. Diameter-dependent dopant location in silicon and germanium nanowires, *Proceedings of the National Academy of Sciences*, 106(36):15254–15258, **2009**. [□](#)
- [165] E. Koren, N. Berkovitch, and Y. Rosenwaks. Measurement of active dopant distribution and diffusion in individual silicon nanowires, *Nano Letters*, **2010**. [□](#)
- [166] A. S. Walton, C. S. Allen, K. Critchley, M. L. Górzny, J. E. McKendry, R. M. D. Brydson, B. J. Hickey, and S. D. Evans. Four-probe electrical transport measurements on individual metallic nanowires, *Nanotechnology*, 18(6):065204, **2007**. [□](#)
- [167] K. Kyung-Hwan, K. Kihyun, J. Dong-Young, M. Byungdon, C. Kyoungah, K. Hyunsuk, M. Byung-Moo, N. Taeyong, P. Jucheol, S. Minchul, and K. Sangsig. Photocurrent of undoped, n- and p-type Si nanowires synthesized by thermal chemical vapor deposition, *Japanese Journal of Applied Physics*, 45(5A):4265–4269, **2006**. [□](#)
- [168] K.-I. Seo, S. Sharma, A. A. Yasseri, D. R. Stewart, and T. I. Kamins. Surface charge density of unpassivated and passivated metal-catalyzed silicon nanowires, *Electrochemical and Solid-State Letters*, 9(3):G69–G72, **2006**. [□](#)

- [169] C. Colombo, M. Heibeta, M. Gratzel, and A. Fontcuberta i Morral. Gallium arsenide p-i-n radial structures for photovoltaic applications, *Applied Physics Letters*, 94(17):173108–3, **2009**. [□](#)
- [170] D. R. Khanal and J. Wu. Gate coupling and charge distribution in nanowire field effect transistors, *Nano Letters*, 7(9):2778–2783, **2007**. [□](#)
- [171] X. Ou, P. D. Kanungo, R. Kögler, P. Werner, U. Gösele, W. Skorupa, and X. Wang. Carrier profiling of individual Si nanowires by scanning spreading resistance microscopy, *Nano Letters*, 10(1):171–175, **2009**. [□](#)
- [172] F. M. Ross, J. Tersoff, and M. C. Reuter. Sawtooth faceting in silicon nanowires, *Physical Review Letters*, 95(14):146104–4, **2005**. [□](#)
- [173] W. M. Bullis. Properties of gold in silicon, *Solid-State Electronics*, 9(2):143–168, **1966**. [□](#)
- [174] S. K. Ghandhi and F. L. Thiel. The properties of nickel in silicon, *Proceedings of the IEEE*, 57(9):1484–1489, **1969**. [□](#)
- [175] A. A. Istratov and E. R. Weber. Electrical properties and recombination activity of copper, nickel and cobalt in silicon, *Applied Physics A: Materials Science & Processing*, 66(2):123–136, **1998**. [□](#)
- [176] J. R. I. Maiolo, B. M. Kayes, M. A. Filler, M. C. Putnam, M. D. Kelzenberg, H. A. Atwater, and N. S. Lewis. High aspect ratio silicon wire array photoelectrochemical cells, *Journal of the American Chemical Society*, 129(41):12346–12347, **2007**. [□](#)
- [177] I. Park, Z. Li, A. P. Pisano, and R. S. Williams. Selective surface functionalization of silicon nanowires via nanoscale Joule heating, *Nano Letters*, 7(10):3106–3111, **2007**. [□](#)
- [178] D. J. Thomson, M. A. Matiowsky, and H. C. Card. Stability of aluminium-polysilicon photovoltaic junctions, *Electronics Letters*, 17(11):382–383, **1981**. [□](#)
- [179] D. J. Thomson, S. Mejia, and H. C. Card. The influence of surface preparation on rectification in aluminum-polycrystalline silicon solar cells, *Journal of Power Sources*, 7(2):191–194, **1982**.
- [180] D. L. Meier, H. P. Davis, R. A. Garcia, J. Salami, A. Rohatgi, A. Ebong, and P. Doshi. Aluminum alloy back p-n junction dendritic web silicon solar cell, *Solar Energy Materials and Solar Cells*, 65(1-4):621–627, **2001**. [□](#)
- [181] H. C. Card. Aluminum-silicon Schottky barriers and ohmic contacts in integrated-circuits, *IEEE Transactions on Electron Devices*, 23(6):538–544, **1976**. [□](#)

- [182] K. Chino. Behavior of Al:n-Si Schottky barrier diodes under heat treatments, *Electrical Communication Laboratories Technical Journal*, 21(9):1765–1780, **1972**.
- [183] R. A. Gudmundsen and J. Maserjian. Semiconductor properties of recrystallized silicon in aluminum alloy junction diodes, *Journal of Applied Physics*, 28(11):1308–1316, **1957**. [□](#)
- [184] D. V. Lang and C. H. Henry. Scanning photocurrent microscopy: A new technique to study inhomogeneously distributed recombination centers in semiconductors, *Solid-State Electronics*, 21(11-12):1519–1524, **1978**. [□](#)
- [185] G. Bemski. Recombination properties of gold in silicon, *Physical Review*, 111(6):1515–1518, **1958**. [□](#)
- [186] W. D. Davis. Lifetimes and capture cross sections in gold-doped silicon, *Physical Review*, 114(4):1006, **1959**. [□](#)
- [187] J. M. Fairfield and B. V. Gokhale. Control of diffused diode recovery time through gold doping, *Solid-State Electronics*, 9(9):905–907, **1966**. [□](#)
- [188] K. Watanabe and C. Munakata. Recombination lifetime in a gold-doped p-type silicon crystal, *Semiconductor Science and Technology*, 8(2):230, **1993**. [□](#)
- [189] D. J. Michalak and N. S. Lewis. Use of near-surface channel conductance and differential capacitance versus potential measurements to correlate inversion layer formation with low effective surface recombination velocities at n-Si/liquid contacts, *Applied Physics Letters*, 80(23):4458–4460, **2002**. [□](#)
- [190] M. C. Putnam, D. B. Turner-Evans, M. D. Kelzenberg, S. W. Boettcher, N. S. Lewis, and H. A. Atwater. 10 μm minority-carrier diffusion lengths in Si wires synthesized by Cu-catalyzed vapor-liquid-solid growth, *Applied Physics Letters*, 95(16):163116–3, **2009**. [□](#)
- [191] A. Goetzberger and W. Shockley. Metal precipitates in silicon p-n junctions, *Journal of Applied Physics*, 31(10):1821–1824, **1960**. [□](#)
- [192] P. Nash and A. Nash. The Ni–Si (nickel-silicon) system, *Journal of Phase Equilibria*, 8(1):6–14, **1987**. [□](#)
- [193] R. Olesinski and G. Abbaschian. The Cu–Si (copper-silicon) system, *Journal of Phase Equilibria*, 7(2):170–178, **1986**. [□](#)
- [194] Y. Yamaguchi, M. Yoshida, and H. Aoki. Solid solubility of nickel in silicon determined by use of ^{63}Ni as a tracer, *Japanese Journal of Applied Physics*, 2:714, **1963**. [□](#)
- [195] J. H. Aalberts and M. L. Verheijke. The solid solubility of nickel in silicon determined by neutron activation analysis, *Applied Physics Letters*, 1(1):19–20, **1962**. [□](#)

- [196] J. D. Struthers. Solubility and diffusivity of gold, iron, and copper in silicon, *Journal of Applied Physics*, 27(12):1560–1560, **1956**. [□](#)
- [197] V. Nebol'sin, A. Shchetinin, A. Dolgachev, and V. Korneeva. Effect of the nature of the metal solvent on the vapor-liquid-solid growth rate of silicon whiskers, *Inorganic Materials*, 41(12):1256–1259, **2005**. [□](#)
- [198] J. S. Kang and D. K. Schroder. Gettering in silicon, *Journal of Applied Physics*, 65(8):2974–2985, **1989**. [□](#)
- [199] C. Kendrick, S. Eichfeld, J. Redwing, Y. Yuwen, H. Yoon, T. Mayer, G. Barber, and T. Mallouk. Effects of surface preparation on the diode characteristics of radial p-n junction silicon wire array solar cells. (Presented at MRS Spring 2010 Meeting; P12.2), **2010**.
- [200] T. J. Kempa, J. F. Cahoon, B. Z. Tian, Y. Dong, and C. M. Lieber. Probing efficiency limits for nanowire photovoltaics. (Presented at MRS Spring 2010 Meeting, P11.4), **2010**.
- [201] W. I. Park, G. Zheng, X. Jiang, B. Tian, and C. M. Lieber. Controlled synthesis of millimeter-long silicon nanowires with uniform electronic properties, *Nano Letters*, 8(9):3004–3009, **2008**. [□](#)
- [202] T. Buonassisi, M. A. Marcus, A. A. Istratov, M. Heuer, T. F. Ciszek, B. Lai, Z. Cai, and E. R. Weber. Analysis of copper-rich precipitates in silicon: Chemical state, gettering, and impact on multicrystalline silicon solar cell material, *Journal of Applied Physics*, 97(6):063503–9, **2005**. [□](#)
- [203] M. Kittler, J. Larz, W. Seifert, M. Seibt, and W. Schroter. Recombination properties of structurally well defined NiSi₂ precipitates in silicon, *Applied Physics Letters*, 58(9):911–913, **1991**. [□](#)
- [204] Z. Xi, J. Chen, D. Yang, A. Lawrenz, and H. J. Moeller. Copper precipitation in large-diameter Czochralski silicon, *Journal of Applied Physics*, 97(9):094909–4, **2005**. [□](#)
- [205] R. Sachdeva, A. A. Istratov, and E. R. Weber. Recombination activity of copper in silicon, *Applied Physics Letters*, 79(18):2937–2939, **2001**. [□](#)
- [206] T. F. Ciszek, T. H. Wang, R. W. Burrows, and X. Wu. Growth of thin crystalline silicon layers for photovoltaic device use, *Journal of Crystal Growth*, 128(1-4):314–318, **1993**. [□](#)
- [207] S. Takayama, E. Ostuni, X. Qian, J. C. McDonald, X. Jiang, P. LeDuc, M. H. Wu, D. E. Ingber, and G. M. Whitesides. Topographical micropatterning of poly(dimethylsiloxane) using laminar flows of liquids in capillaries, *Advanced Materials*, 13(8):570–574, **2001**. [□](#)
- [208] E. Yablonovitch, D. L. Allara, C. C. Chang, T. Gmitter, and T. B. Bright. Unusually low surface-recombination velocity on silicon and germanium surfaces, *Physical Review Letters*, 57(2):249–252, **1986**. [□](#)

- [209] S. Dauwe, J. Schmidt, and R. Hezel. Very low surface recombination velocities on p- and n-type silicon wafers passivated with hydrogenated amorphous silicon films. In *Conference Record of the Twenty-Ninth IEEE Photovoltaic Specialists Conference*, pages 1246–1249, **2002**. [□](#)
- [210] E. Maruyama, A. Terakawa, M. Taguchi, Y. Yoshimine, D. Ide, T. Baba, M. Shima, H. Sakata, and M. Tanaka. Sanyo's challenges to the development of high-efficiency HIT solar cells and the expansion of HIT business. In *Conference Record of the Fourth IEEE World Conference on Photovoltaic Energy Conversion*, volume 2, pages 1455–1460, **2006**. [□](#)
- [211] P. Doshi, G. E. Jellison, and A. Rohatgi. Characterization and optimization of absorbing plasma-enhanced chemical vapor deposited antireflection coatings for silicon photovoltaics, *Applied Optics*, 36(30):7826–7837, **1997**. [□](#)
- [212] W. J. Royea, A. Juang, and N. S. Lewis. Preparation of air-stable, low recombination velocity Si(111) surfaces through alkyl termination, *Applied Physics Letters*, 77(13):1988–1990, **2000**. [□](#)
- [213] L. Cao, J. S. White, J.-S. Park, J. A. Schuller, B. M. Clemens, and M. L. Brongersma. Engineering light absorption in semiconductor nanowire devices, *Nature Materials*, 8(8):643–647, **2009**. [□](#)
- [214] C. F. Bohren and D. R. Huffman. *Absorption and Scattering of Light by Small Particles*. New York, Wiley, **1983**.
- [215] A. K. Sharma, S. K. Agarwal, and S. N. Singh. Determination of front surface recombination velocity of silicon solar cells using the short-wavelength spectral response, *Solar Energy Materials and Solar Cells*, 91(15–16):1515–1520, **2007**. [□](#)
- [216] J. Lindmayer and J. F. Allison. The violet cell: An improved silicon solar cell, *Solar cells*, 29(2-3):151–166, **1990**. [□](#)
- [217] M. C. Putnam. *Si Microwire-Array Solar Cells*. PhD thesis, California Institute of Technology, **2010**.
- [218] M. C. Putnam, S. W. Boettcher, M. D. Kelzenberg, D. B. Turner-Evans, J. M. Spurgeon, E. L. Warren, R. M. Briggs, N. S. Lewis, and H. A. Atwater. Si microwire-array solar cells, *Energy & Environmental Science*, Submitted, **2010**.
- [219] V. Sivakov, G. Andrä, A. Gawlik, A. Berger, J. Plentz, F. Falk, and S. H. Christiansen. Silicon nanowire-based solar cells on glass: Synthesis, optical properties, and cell parameters, *Nano Letters*, 9(4):1549–1554, **2009**. [□](#)
- [220] A. R. Forouhi and I. Bloomer. Optical dispersion relations for amorphous semiconductors and amorphous dielectrics, *Physical Review B*, 34:7018–7026, **1986**. [□](#)